UNIVERSITEIT·STELLENBOSCH·UNIVERSITY
jou kennisvennoot • your knowledge partner

Flight Control System for a Variable Stability Blended-Wing-Body Unmanned Aerial Vehicle

by

Deon Blaauw

Thesis presented at Stellenbosch University in partial
fulfilment of the requirements for the degree of

Master of Science in Electrical & Electronic Engineering

Department of Electrical & Electronic Engineering
University of Stellenbosch
Private Bag X1, 7602 Matieland, South Africa

Supervisor: Dr. I.K. Peddle

March 2009

Declaration

By submitting this thesis electronically, I declare that the entirety of the work contained therein is my own, original work, that I am the owner of the copyright thereof (unless to the extent explicitly otherwise stated) and that I have not previously in its entirety or in part submitted it for obtaining any qualification.

Date: 30 January 2009

Abstract

This thesis presents the analysis, design, simulation and practical implementation of a novel control system for a variable stability blended-wing-body unmanned aerial vehicle. The aircraft has a moveable centre of mass that allows it to operate in an aerodynamically optimised minimum drag configuration during cruise flight. The primary purpose of the control system is thus to regain nominal static stability for all centre of mass positions, and then to further regulate motion variables for autonomous way point navigation. A thorough analysis of the parameters affected by the varying centre of mass position leads to the identification of the main control problem. It is shown that a recently published acceleration based control methodology can be used with minor modification to elegantly solve the variable stability control problem. After providing the details of the control system design, the customised avionics used for their practical implementation are presented. The results of extensive hardware in the loop simulations verify the functionality of the controllers. Finally, flight test results illustrate the practical success of the autopilot and clearly show how the control system is capable of controlling the variable stability aircraft at centre of mass locations where a human pilot could not.

Opsomming

Hierdie tesis bied die analise, ontwerp, simulasie en praktiese implementering van ’n unieke beheerstelsel vir ’n vlerk-en-bak-in-een onbemande lugvaartuig met wisselende stabiliteit aan. Die vliegtuig het ’n beweegbare massamiddelpunt wat dit toelaat om in ’n optimale minimum-sleurkonfigurasie tydens kruisvlug te werk. Die primêre doel van hierdie beheerstelsel is dus om die nominale statiese stabiliteit vir alle massamiddelpunt-posisies te herwin om sodoende bewegingsveranderlikes vir outonome wegpuntnavigasie te reguleer. ’n Deeglike analise van die aerodinamiese eienskappe wat meestal deur die wisselende massamiddelpunt-posisie beïnvloed word, lei tot die identifisering van die primêre probleem rondom beheer. Daar word aangedui dat ’n onlangs gepubliseerde beheermetodiek wat op versnellingsterugvoer gebaseer is, gebruik kan word om die wisselende stabiliteit beheerprobleem op ’n knap, dog eenvoudige manier op te los. Nadat die beheerargitektuur bespreek is, word die ontwerp van die doelgemaakte lugvaartelektronika wat die beheerder prakties implementeer, uitgelê. Hardeware-in-die-lus-simulasies toon die korrekte werking van die beheerders. Laastens illustreer vlugtoetsresultate die praktiese sukses van die outoloods en wys duidelik dat die beheerstelsel daartoe in staat is om ’n vliegtuig met wisselende stabiliteit by ’n massamiddelpunt-posisie te beheer waar ’n menslike loods nie kan nie.

Acknowledgements

I would like to extend my sincere gratitude to the following people/organisations for their contributions towards this thesis,

- The CSIR DPSS for funding the project.
- Dr. I.K. Peddle for your support, guidance and advice throughout the project. Thank you for providing me with valuable insight and deeper understanding on so many topics.
- Dr. B.A. Broughton for his extensive aerodynamic research which led to this project.
- Dr. R. Heise for your passionate approach towards the project. Your friendship made the long hours spent working late nights at the CSIR much more bearable!
- My lovely girlfriend Sonja for understanding and bearing with all the days spent working. Your love and support really helped me tremendously through the tough times.
- Abrie Vermeulen, Ian Burger and Francois Haasbroek, for always being there for me and providing invaluable distraction through music!
- Francois Haasbroek and Carla-Marie Spies for linguistic assistance during the write-up of this thesis.
- Steven Kriel and Rudi Gaum for technical assistance during the write-up of this thesis. Your advice and friendship are much appreciated.
- Smous, Ruan de Hart, Bernard Visser and Philip Smit for providing both valuable inputs during the project and distracting me from my work when I needed it!
- Wessel Kroukamp, Johan Arendse, Quintis Brandt and Lincoln Saunders for providing technical assistance with various aspects of the project.
- My mom and dad, for the crucial support network I needed allowing me to perform to the best of my ability.

Dedications

This thesis is dedicated to my family.

Contents

Nomenclature

Physical:

b	Wing Span
c	Reference Chord
$\bar{c}$	Mean Aerodynamic Chord
m	Mass
S	Surface Area
A	Aspect Ratio
e	Efficiency
cg_p	Aircraft Centre of Mass Position
$\mathbf{I}$	Moment of Inertia Matrix
I_{xx}	Moment of Inertia around roll axis
I_{yy}	Moment of Inertia around pitch axis
I_{zz}	Moment of Inertia around yaw axis

Natural Constants:

ρ	Air Pressure
g	Gravitational Acceleration

Aerodynamic:

$\bar{q}$	Dynamic Pressure
C_L	Aerodynamic Lift Coefficient
C_D	Aerodynamic Drag Coefficient
C_l	Aerodynamic Roll Coefficient
C_m	Aerodynamic Pitch Coefficient
C_n	Aerodynamic Yaw Coefficient
C_x	Aerodynamic Axial Force Coefficient
C_y	Aerodynamic Lateral Force Coefficient

C_z	Aerodynamic Normal Force Coefficient

Linear Quadratic Regulator:

$\mathbf{J}$	Cost Function
$\mathbf{Q}_1$	State weighting matrix
$\mathbf{Q}_2$	Actuator weighting matrix

Position and Orientation:

$\boldsymbol{P}$	Position Vector
N	North Position
E	East Position
D	Down Position
h	Height
α	Angle of Attack
β	Angle of Side slip
ϕ,θ,ψ	Euler Angles (roll, pitch and yaw)
$\boldsymbol{i}$,$\boldsymbol{j}$,$\boldsymbol{k}$	Basis Vectors
$\mathbf{DCM}$	Direction Cosine Matrix

Velocity and Rotation:

$\boldsymbol{V}$	Velocity Vector
$\overline{V}$	Velocity Vector Magnitude
u	Axial Velocity
$\boldsymbol{\omega}$	Angular Velocity Vector
p	Roll Rate
q	Pitch Rate
r	Yaw Rate

Forces, Moments and Accelerations:

$\boldsymbol{M}$	Moment Vector
L	Roll Moment
M	Pitch Moment
N	Yaw Moment
$\boldsymbol{F}$	Force Vector
X	Axial Force

Y	Lateral Force
Z	Normal Force
a_a	Axial Specific Acceleration
a_n	Normal Specific Acceleration

Actuation:

a_{n_c}	Normal Specific Acceleration Virtual Actuator
T_c	Thrust Command
T	Thrust State
τ_T	Thrust Time Constant
δ_E	Elevator Deflection
δ_A	Aileron Deflection
δ_R	Rudder Deflection
δ_T	Thrust Deflection
δ_s	Steering Deflection

System:

$\mathbf{A}, \mathbf{F}$	Continuous System Matrix
$\mathbf{B}, \mathbf{G}$	Continuous Input Matrix
$\mathbf{C}, \mathbf{H}$	Output Matrix
Φ	Discrete System Matrix
Γ	Discrete Input Matrix
T_S	Sampling Time
$\mathbf{K}$	Feedback Gain Matrix

Subscripts:

B	Coordinated in Body Axes
I	Coordinated in Inertial Axes
W	Coordinated in Wind Axes
G	Gravitational force or acceleration
T	Thrust force or acceleration
0	Static or Initial value

Superscripts:

BI	Body relative to Inertial

BW	Body relative to Wind
WI	Wind relative to Inertial

Acronyms:

ADC	Analog to Digital Converter
BWB	Blended Wing Body
CAD	Computer Aided Design
CSIR	Council for Scientific and Industrial Research
DPSS	Defence, Peace, Safety and Security
ESL	Electronic Systems Laboratory
GUI	Graphical User Interface
LQR	Linear Quadratic Regulator
MIMO	Multi-Input-Multi-Output
MOI	Moment Of Inertia
MIPS	Million Instructions Per Second
NSA	Normal Specific Acceleration
SPM	Short Period Mode
SU	Stellenbosch University
UAV	Unmanned Aerial Vehicle
VSA	Variable Stability Aircraft
VTOL	Vertical Take Off and Landing

List of Figures

List of Tables

Chapter 1

Introduction

Over the past number of years, the South African government has been committed to building the aerospace industry towards a sustainable, growing, empowered and internationally recognised industry sector. Minister of Trade and Industry, Mandisi Mpahlwa, recently unveiled three government endorsed aerospace initiatives, the Centurion Aerospace Village (CAV), the Aerospace Industry Support Initiative (AISI) and the establishment of the National Aerospace Centre of Excellence (NACoE). The aforementioned initiatives are only a few examples aimed at repositioning the South African aerospace sector in terms of higher value-added participation in the global aerospace market, working towards a globally competitive South African aerospace industry.

The Unmanned Air Vehicle (UAV) sector is arguably the fastest growing sector of the aerospace industry world wide. Numerous organisations within the aerospace sector are systematically working towards the integration of UAV systems into civil controlled airspace. The primary driver for this is economics, as UAVs can perform a number of missions such as prolonged flight (i.e. in excess of days and months) and those involving danger to human pilots (i.e. search and rescue in extreme weather conditions) more cost effectively than manned aircraft. Some examples of non-military UAV missions include earth observation, maritime surveillance, mobile telecommunication extension, natural fire management, border patrol, pipeline monitoring, power line maintenance and law enforcement. Most of these missions involve long-range flights, an aspect that could cause fatigue and strain on a human pilot. UAVs therefore provide a cost effective and low risk solution to the requirements of these and other missions.

1.1 Background

Research into aerodynamic efficiency becomes of paramount importance, especially when it is desired to arrive at a practically feasible solution regarding long-range UAV applications. To this end, the aeronautic systems competency area at the Defence, Peace, Safety and Security (DPSS) branch of the South African Council for Scientific and Industrial

Research (CSIR) launched the Sekwa program. The main task of this project was to research and demonstrate the advantages of using reduced natural stability on a UAV for the purpose of drag reduction.

Figure 1.1: (a) Sekwa CAD model. (b) Constructed Sekwa UAV.

The Sekwa research vehicle (figure 1.1) was aimed at investigating the possible advantages of using reduced natural stability for increased aerodynamic efficiency, especially for tail-less flying wing or blended-wing-body aircraft designs. According to the CSIR DPSS, the reduced wetted area and low interference drag of these designs in theory allow for lower parasitic drag (and therefore increased aerodynamic performance), but the need for natural aerodynamic stability on blended-wing-body aircraft generally leads to penalties in aerodynamic efficiency. Therefore, it was desired to relax the requirement for natural stability during the design and optimisation of the vehicle, which allowed for a more efficient platform to be designed.

With a relaxed stability margin, the aircraft becomes extremely difficult, if not impossible, to control manually by a human pilot. Therefore, the Centre of Expertise in Autonomous Systems, a subdivision of the Electronic Systems Laboratory (ESL) at Stellenbosch University (SU), was contracted to research methodologies for augmenting the aircraft's stability artificially through the application of control system theory. Since its establishment in 2001, the ESL research group demonstrated its competence on both practical and theoretical fronts regarding the application of flight control systems. Some of the recently completed projects by the ESL Autonomous Systems research group include:

- Autonomous navigation systems for both fixed-wing aircraft and helicopters.
- Autonomous take-off and landing systems for fixed-wing aircraft.

- Aggressive aerobatic manoeuvre flight control systems for fixed-wing aircraft.
- Vertical take-off and landing flight control systems for VTOL aircraft.
- Naval decoy ducted fan demonstrator.

With a collaborative effort, both competency areas (CSIR DPSS and the ESL) embarked on a multi-phase project aimed at demonstrating flight of South Africa's first variable stability UAV. Such a technology demonstrator will have an immediate and positive impact on the South African Aerospace Industry as a whole.

1.2 Task Description and Project Outcomes

The variable stability aircraft designed by the CSIR DPSS is a tailless aircraft with a moveable centre of mass. The moveable centre of mass was designed such that the natural static stability of the aircraft can be varied from sufficiently stable for human piloted flight to highly unstable conditions. The purpose of the control system was to augment the natural stability of the aircraft such that the nominal static stability is restored and then furthermore, to regulate motion variables for autonomous flight. The main project outcomes are listed below:

- From a control systems perspective, analyse the implications of a varying centre of mass on aircraft stability and controllability.
- Develop the control methodology needed to control a variable stability aircraft.
- Design further control systems to enable full autonomous flight of the variable stability aircraft.
- Develop the necessary avionics needed to facilitate practical implementation of the flight control system designed.
- Demonstrate that the flight control system is capable of controlling a variable stability aircraft, especially when the aircraft is unstable to the point where an experienced human pilot cannot control it anymore.
- Continue to build on the partnership developed between SU and the CSIR, thereby strengthening the South African Aerospace *Network of Excellence*.
- Demonstrate that UAV technology can be developed in a coordinated manner between different institutions. Such a symbiotic relationship between different institutions within the South African aerospace sector will undoubtedly contribute in a positive manner to the South African aerospace sector.

1.3 Thesis Outline

With reference to figure 1.2, the thesis is conceptually divided into two sections. The first four chapters are aimed at Modelling, Problem Identification and Control System Development. The last four chapters are mainly concerned with Simulation and Practical Implementation of the flight control system developed.

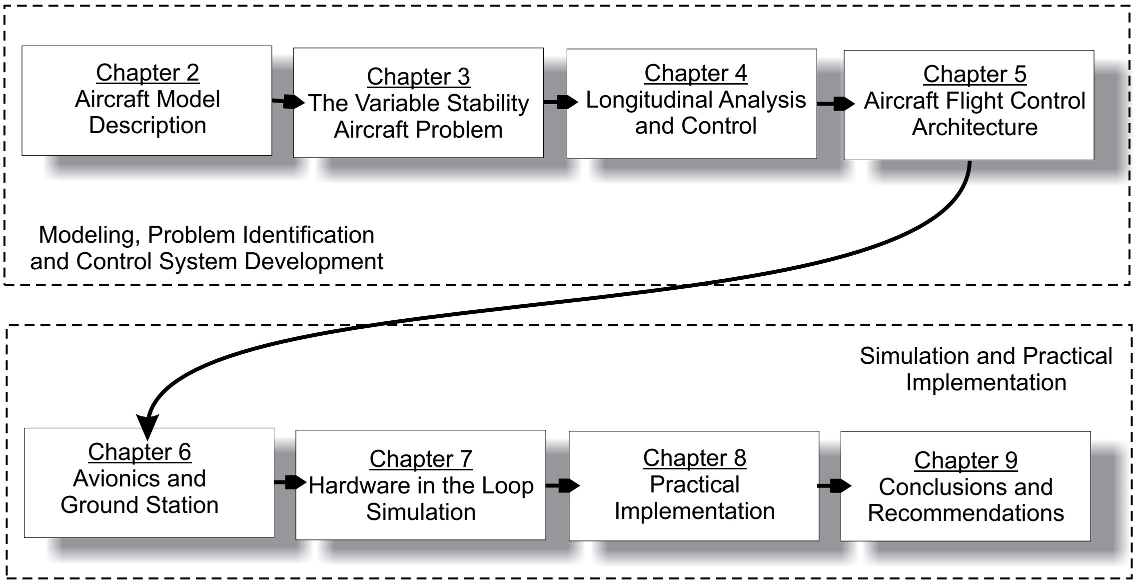

Figure 1.2: Thesis Outline

1.3.1 Modelling, Problem Identification and Control System Development

In Chapter 2, a non-linear aircraft model is developed. The aircraft model developed was adopted from [15], and presents the aircraft dynamics in a form that reduces the complexity of the autopilot design architecture for the variable stability aircraft problem. Due to the general nature of the aircraft model derived, its application is not restricted to blended-wing-body aircraft, and could be applied to a wide variety of more conventional aircraft as well.

Chapter 3 investigates the effect of varying the aircraft centre of mass position on the parameters that describe the natural dynamics of the aircraft. The chapter argues that the airframe can be considered a completely different vehicle with unique stability characteristics and dynamic response at each new centre of mass position, which leads to both an interesting and challenging control problem. The analyses presented in chapter 3 were kept as general as possible, to allow for the intended flight control system designed (based on conclusions drawn in this chapter) to be applied directly to a wide variety of blended-wing-body aircraft.

Chapter 4 isolates the variable stability aircraft problem, and identifies the aircraft mode of motion most influenced by centre of mass variations. With the fundamental control problem identified, an *inner-loop* stability augmentation design strategy is formulated. The stability augmentation design strategy ensures a dynamically invariant closed loop response to centre of mass variations.

Chapter 5 follows with the design of further outer loop flight control systems, allowing for full autonomous flight. Note that, with the nominal static stability regained for all centre of mass positions by the control system designed in chapter 4, the controllers designed in chapter 5 could be based on a statically stable aircraft.

1.3.2 Simulation and Practical Implementation

Chapter 6 presents the design of the avionics system capable of practically implementing the flight control system on the blended-wing-aircraft mentioned earlier. A general avionics system was developed specifically for the project, and was developed in such a way so as to ensure that it can be applied and extended for numerous future UAV projects within the ESL Autonomous Systems research group.

Chapter 7 outlines the hardware in the loop simulation environment, used to test both the flight control system and hardware, in a non-linear simulation environment. The purpose of the hardware in the loop simulation environment is to evaluate the flight control system and to ensure the validity of the assumptions made during the development of the various control systems.

Chapter 8 provides the results of some of the practical flight tests conducted. This chapter proves that the flight control system is capable of practically controlling a variable stability aircraft, at centre of mass positions where an experienced human pilot can not.

Chapter 2

Aircraft Model Description

Many different methods exist to formally define an aircraft model as put forth by [2], [1] and [3]. However, in light of the discussions presented in [15], the control system architecture can be simplified dramatically by appropriately formulating the aircraft dynamics and carefully selecting the states to be controlled. In this way, the complexity of the autopilot design is dramatically reduced, and existing control system design techniques can be applied to elegantly, efficiently and robustly solve the variable-stability control problem as will be shown in chapter 4.

This chapter begins by presenting the axis systems and actuator sign conventions and defines some of the notation used throughout the thesis. Next, the aircraft is modelled as a rigid body assuming a fixed centre of mass position to simplify the analysis. The chapter concludes by investigating the effect of moving the centre of mass on the aircraft dynamics presented.

2.1 Definitions and Notations

This section introduces some of the notations and definitions used throughout the modelling and control system design chapters in this project. It starts by defining the axis systems, then introduces the actuator sign convention and notation as defined for this thesis.

2.1.1 Axis Systems

Before developing mathematical models of the aeroplane, it is necessary to define a framework in which the equations of motion can be developed. A complete description of aircraft motion can be obtained by splitting it into that of a reference frame capturing the gross motion and attitude relative to inertial space, as well as that of a body-fixed frame that rotates relative to the reference frame, as argued by [15]. An appropriate choice for the reference frame is the wind axis system as stated in [16]. Therefore, three axis systems are defined, namely inertial, body and wind axis systems.

2.1.1.1 Inertial Axes

Newton's laws can only be applied in an inertial reference frame. Therefore, it is assumed that the surface of the earth is *flat* and *non-rotating*. Given typical durations and distances of localised (non trans-global) flight, and that angular velocities of the airframe will be much greater than the earth's angular rotation, the flat non-rotating earth assumption is adequate. This axis system defines a horizontal plane tangential to the surface of the earth, as shown in figure 2.1, with its centre chosen at some convenient point usually located on the runway.

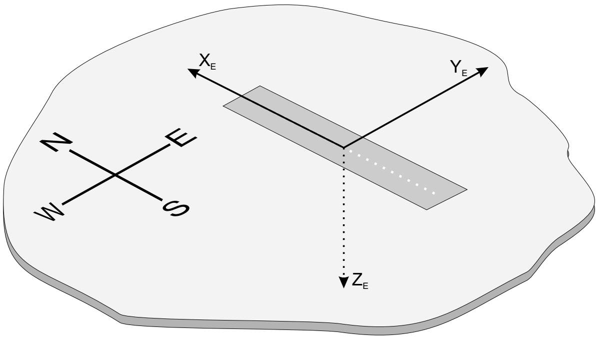

Figure 2.1: Inertial axis system [18]

2.1.1.2 Body Axis System

This right-handed orthogonal axis system is attached to the vehicle with the origin located at the centre of mass. Gravity is assumed to be uniform, hence the centre of mass and the centre of gravity are the same point. The definition of this axis system is shown in figure 2.2 as well as the positive directions for yaw, pitch and roll motions of the aircraft. The symbols and positive directions for the aircraft body axes forces and moments are also given in figure 2.2.

2.1.1.3 Aerodynamic Axes

Wind Axes: This right handed orthogonal axis system shares its origin with the body axes, but differs in orientation as its X-axis is always aligned with the total velocity vector. The Z-axis of the wind axes is defined to reside within the aircraft's plane of symmetry,

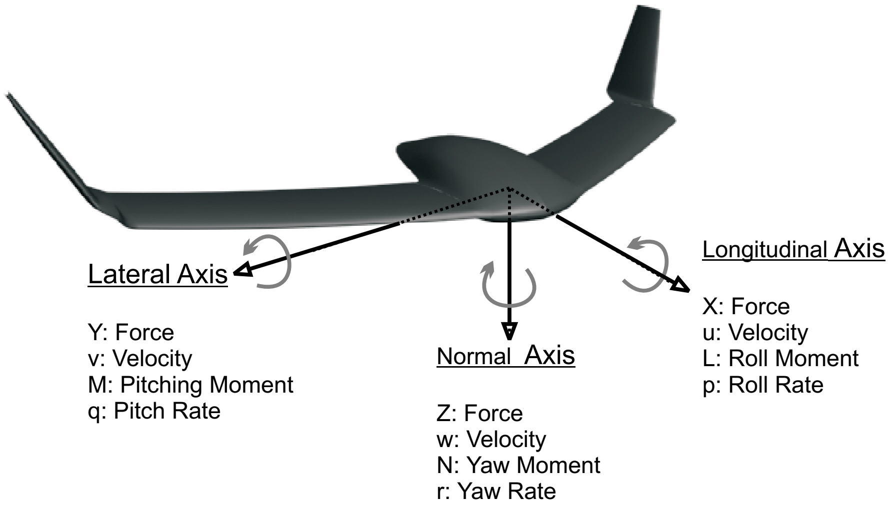

Figure 2.2: Body Axes Force, Moment, Velocity and Angular Rate Definitions

with the Y-axis pointing out the aircraft starboard wing [15]. The wind axis system is particularly useful during aerodynamic modelling since stability derivatives[1] are modelled in this axis system.

Stability Axes: A variation of the wind axis system arises when β (sideslip angle) is assumed to be zero during a pure longitudinal analysis. This axis system is referred to as the stability axes.

2.1.2 Aircraft Aerodynamic Actuators

The aircraft is equipped with a set of six aerodynamic actuators ($\delta_1, \delta_2, \delta_3, \delta_4, \delta_5, \delta_6$) shown in figure 2.3. Additionally the aircraft is equipped with retractable landing gear (δ_G) and a steerable nose wheel (δ_S). The thrust propulsion source actuator is denoted by δ_T. Note that the notation δ_ζ represents a perturbation of the actuator ζ by some small amount δ.

During conventional aircraft modelling, standard actuator definitions are used describing the elevators (δ_E), ailerons (δ_A) and rudders (δ_R) respectively. To simplify the derivation of the aircraft model, a relationship between the six aerodynamic actuators, shown in figure 2.3, and the three conventional aerodynamic actuators ($\delta_E, \delta_A, \delta_R$) has to be established.

The deflection of a control surface is defined in radians with a *positive* deflection causing a *negative* moment. With reference to figure 2.3, the rudders located on the wing tips must work in unison[2]. Furthermore, figure 2.3 indicates that the port and starboard

---

[1] Parameters describing aircraft aerodynamic forces and moments

[2] A negative rudder (δ_R) deflection results in a positive yaw moment

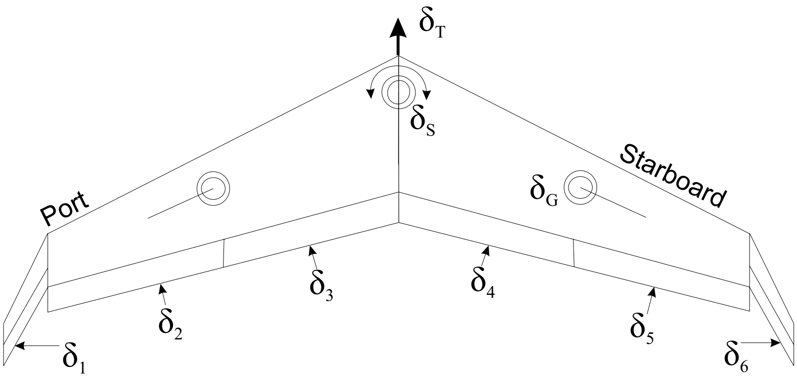

Figure 2.3: Aircraft Actuator Setup

wings each have two independent actuators per wing. It is desired to work with one actuator per wing for control purposes, therefore δ_2 and δ_3 should move together and δ_4 and δ_5 should move together. The previous arguments produce the following set of constraint equations,

$$\delta_1 = \delta_6 \tag{2.1.1}$$
$$\delta_2 = \delta_3 \tag{2.1.2}$$
$$\delta_4 = \delta_5 \tag{2.1.3}$$

To relate the six aerodynamic actuators of figure 2.3 to the three classic aerodynamic actuators ($\delta_E, \delta_A, \delta_R$), the following virtual actuators are defined,

$$\delta_E = (\delta_2 + \delta_3 + \delta_4 + \delta_5)/4 \tag{2.1.4}$$
$$\delta_A = (-\delta_2 - \delta_3 + \delta_4 + \delta_5)/4 \tag{2.1.5}$$
$$\delta_R = (\delta_1 + \delta_6)/2 \tag{2.1.6}$$

By combining equations (2.1.1) to (2.1.6) , the relationship between the actual aerodynamic actuators and the virtual actuators can be written in matrix form as,

$$\delta^V = [\mathbf{T^{VR}}]\delta^R \tag{2.1.7}$$

where the superscripts denote the virtual (V) and real (R) actuators respectively. Expanding δ^V and δ^R,

$$\delta^V = \begin{bmatrix} \delta_R & \delta_E & \delta_A & \delta_T & \delta_G & \delta_S & 0 & 0 & 0 \end{bmatrix}^T \tag{2.1.8}$$

$$\delta^R = \begin{bmatrix} \delta_1 & \delta_2 & \delta_3 & \delta_4 & \delta_5 & \delta_6 & \delta_7 & \delta_8 & \delta_9 \end{bmatrix}^T \tag{2.1.9}$$

The transformation matrix transforming the *real* actuators to the *virtual* actuators is given by,

$$\mathbf{T^{VR}} = \begin{bmatrix} 1/2 & 0 & 0 & 0 & 0 & 1/2 & 0 & 0 & 0 \\ 0 & 1/4 & 1/4 & 1/4 & 1/4 & 0 & 0 & 0 & 0 \\ 0 & -1/4 & -1/4 & 1/4 & 1/4 & 0 & 0 & 0 & 0 \\ 0 & 0 & 0 & 0 & 0 & 0 & 1 & 0 & 0 \\ 0 & 0 & 0 & 0 & 0 & 0 & 0 & 1 & 0 \\ 0 & 0 & 0 & 0 & 0 & 0 & 0 & 0 & 1 \\ 1 & 0 & 0 & 0 & 0 & -1 & 0 & 0 & 0 \\ 0 & 1 & -1 & 0 & 0 & 0 & 0 & 0 & 0 \\ 0 & 0 & 0 & 1 & -1 & 0 & 0 & 0 & 0 \end{bmatrix} \tag{2.1.10}$$

Note that the throttle and landing gear actuators are simple one-to-one mappings. The virtual *steering* actuator δ_S is connected directly to the rudder signal during take off and disconnected in flight. The relationship between the actual aerodynamic actuators and the defined *virtual* actuators is now shown to be:

$$\delta^R = [\mathbf{T^{VR}}]^{-1}\delta^V \tag{2.1.11}$$

Therefore, during aerodynamic modelling the classically known actuator definitions (elevator, aileron, rudder and throttle) can now be used, thereby simplifying the modelling process. After a model is derived with respect to the *virtual* actuators, they are simply related back to the actual aerodynamic actuators through equation (2.1.11).

2.2 Six degree of freedom equations of motion

This section develops the six degree of freedom equations of motion for a rigid body in a form highlighting the ideas presented in [15]. To simplify the derivation of the aircraft model, a static centre of mass position is initially assumed. The strategy put forth by [15] involves describing the total motion of the body as the superposition of the body's point mass dynamics (kinematics) and its rigid body rotational dynamics (kinetics). The point mass dynamics are described by the position and attitude of the wind axis system over time. The total rigid body motion of the aircraft is then described by the attitude of the body axis system with respect to the wind axis system.

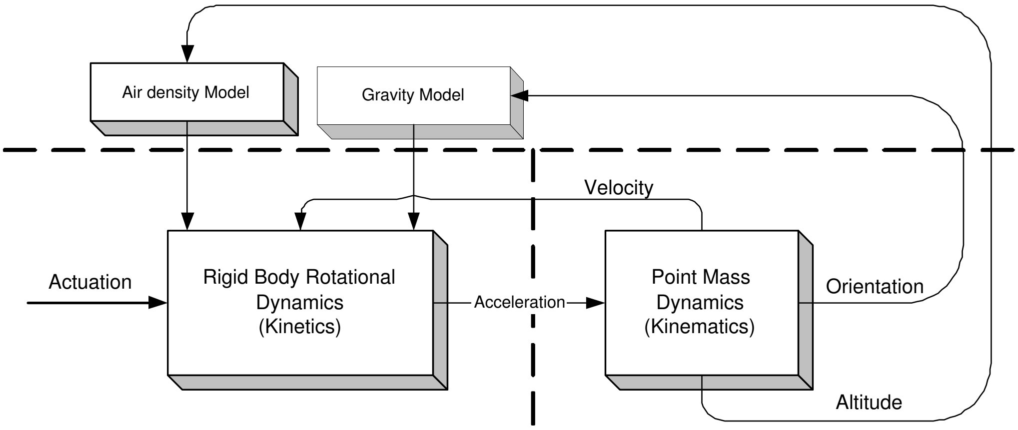

Figure 2.4: Simplified Aircraft model Graphical Representation

To this end, two concepts are introduced namely kinetics and kinematics. Kinematics involve maintaining the attitude, position, velocity and acceleration of a rigid body in three dimensional space. On the other hand, kinetics involve how forces acting on a body (in this case, an aircraft) translates into accelerations. The accelerations provided by the kinetic equations are then used in the kinematic equations to describe how they propagate into velocity, position and attitude over time. Therefore, during rigid body modelling it is only necessary to derive the kinematic equations up to an acceleration level since the kinetic equations relate forces to accelerations. A simplified graphical representation of the aircraft model is shown by figure 2.4. According to [15], it is advantageous to be able to control the aircraft's acceleration as this would simplify the outer control loops, regulating further kinematic states.

2.2.1 Kinematics

This section introduces the topic of kinematics. Note that the derivations presented are based on the work done by [15]. As previously mentioned, kinematics involve the description of attitude, position, velocity and acceleration of a body in three dimensional space. To this end two topics are discussed, namely point mass dynamics and attitude dynamics.

2.2.1.1 Point Mass Dynamics

If the aircraft is considered a rigid body with static centre of mass, it is reduced to a point mass traversing inertial space. There exists a kinematic relationship between the acceleration, velocity and position of the aircraft's centre of mass with respect to inertial space (I). Since the origin of the wind axis system coincides with the aircraft's centre of mass the kinematic relationships can be stated as,

$$\left.\frac{d}{dt}\boldsymbol{P}^{WI}\right|_I = \boldsymbol{V}^{WI} \tag{2.2.1}$$

$$\left.\frac{d}{dt}\boldsymbol{V}^{WI}\right|_I = \boldsymbol{A}^{WI} \tag{2.2.2}$$

where $\boldsymbol{P}^{WI}$, $\boldsymbol{V}^{WI}$ and $\boldsymbol{A}^{WI}$ are the position, velocity and acceleration vectors[3] of the wind axis system with respect to inertial space. If it is assumed that the aircraft's mass (m) is time invariant, the applied resultant force vector ($\boldsymbol{F}$) can be written as,

$$\boldsymbol{F} = m\boldsymbol{A}^{WI} \tag{2.2.3}$$

For the purpose of this thesis, it is more desirable to work with the velocity magnitude and attitude of the wind axis system when describing the aircraft velocity vector. Therefore, equation (2.2.2) can be expanded using equation (B.2.2) defined in appendix B and written in the following form,

$$\left.\frac{d}{dt}\boldsymbol{V}^{WI}\right|_I = \left.\frac{d}{dt}\boldsymbol{V}^{WI}\right|_W + \boldsymbol{\omega}^{WI} \times \boldsymbol{V}^{WI} = \boldsymbol{A}^{WI} \tag{2.2.4}$$

where $\boldsymbol{\omega}^{WI}$ is the angular velocity of the wind axis system with respect to inertial space. Coordinating equation (2.2.4) into the wind axis system yields,

$$\dot{\mathbf{V}}_W^{WI} + \mathbf{S}_{\omega_W^{WI}}\mathbf{V}_W^{WI} = \mathbf{A}_W^{WI} \tag{2.2.5}$$

where the $\mathbf{S}_{\omega_W^{WI}}$ matrix implements the cross product in equation (2.2.4) and is defined as,

$$\mathbf{S}_{\omega_W^{WI}} = \begin{bmatrix} 0 & -R_W & Q_W \\ R_W & 0 & -P_W \\ -Q_W & P_W & 0 \end{bmatrix} \tag{2.2.6}$$

In equation (2.2.6) , P_W, Q_W and R_W denote roll, pitch and yaw rates of the *wind* axis

---

[3] For further information regarding vectors, coordinate vectors and vector notation as used throughout this section refer to appendix B

system (W) with respect to inertial space. By making use of the principle illustrated with equation (2.2.3), equation (2.2.5) can be written as,

$$\dot{\mathbf{V}}_{W}^{WI} = -\mathbf{S}_{\omega_{W}^{WI}}\mathbf{V}_{W}^{WI} + m^{-1}\mathbf{F}_{W} \tag{2.2.7}$$

Expanding equation (2.2.7) and writing it in matrix form provides the kinematic equations describing the velocity vector of the origin of the wind axis system with respect to inertial space,

$$\begin{bmatrix} \dot{\overline{V}}_W \\ 0 \\ 0 \end{bmatrix} = -\begin{bmatrix} 0 & -R_W & Q_W \\ R_W & 0 & -P_W \\ -Q_W & P_W & 0 \end{bmatrix}\begin{bmatrix} \overline{V}_W \\ 0 \\ 0 \end{bmatrix} + m^{-1}\begin{bmatrix} X_W \\ Y_W \\ Z_W \end{bmatrix} \tag{2.2.8}$$

where X_W, Y_W and Z_W denote the coordinates of the force vector and $\overline{V}_W$ the velocity vector magnitude in wind axes. The previous result shows how acceleration propagates into velocity over time. To describe how velocity propagates into position over time, equation (2.2.1) is rewritten as follows,

$$\dot{\mathbf{P}}_{I}^{WI} = [\mathbf{DCM}^{WI}]^{T}\,\mathbf{V}_{W}^{WI} \tag{2.2.9}$$

where $[\mathbf{DCM}^{WI}]^{T}$ is the direction cosine matrix defined in appendix B by equation (B.3.6) and is used to transform the velocity coordinate vector $\mathbf{V}_{W}^{WI}$ into the inertial axis system. Equation (2.2.9) is provided below in expanded form,

$$\begin{bmatrix} \dot{P}_x \\ \dot{P}_y \\ \dot{P}_z \end{bmatrix} = \begin{bmatrix} \cos(\psi_W)\cos(\theta_W) \\ \sin(\psi_W)\cos(\theta_W) \\ -\sin(\theta_W) \end{bmatrix}\overline{V}_W \tag{2.2.10}$$

where the subscript W denotes the wind axis system and the parameters P_x, P_y and P_z denotes aircraft position along the X, Y and Z directions of the inertial axis system respectively. In this text P_x, P_y and P_z are often represented by north (N), east (E) and altitude (D) respectively.

2.2.1.2 Attitude and Attitude Dynamics

Attitude: Although several methods exist to quantify aircraft attitude, Euler angles are chosen for their intuitive nature and ease of linearisation. Any Euler representation exhibits a singularity in the resulting attitude dynamics under certain orientations as shown in [9]. Methods to avoid these singularities include interesting Euler switching algorithms or the use of Quaternion representations. However, neither of these methods will be employed because a conventional flight envelope is used in this project and therefore no Euler singularities will be encountered[4]. Aircraft attitude is therefore described by yaw (ψ_W), pitch (θ_W) and roll (ϕ_W) angles of the *wind* axes with respect to inertial space as defined by [15]. Refer to [9] for more information on different Euler sequences and their respective discontinuities. The Euler 321 sequence as used in this thesis is discussed further in appendix B.

Attitude Dynamics: Attitude dynamics are represented by the following equation [15],

$$\begin{bmatrix} \dot{\phi}_W \\ \dot{\theta}_W \\ \dot{\psi}_W \end{bmatrix}_{(321)} = \begin{bmatrix} 1 & \sin\phi_W \tan\theta_W & \cos\phi_W \tan\theta_W \\ 0 & \cos\phi_W & -\sin\phi_W \\ 0 & \sin\phi_W \sec\theta_W & \cos\phi_W \sec\theta_W \end{bmatrix}_{(321)} \begin{bmatrix} P_W \\ Q_W \\ R_W \end{bmatrix} \qquad (2.2.11)$$

where P_W, Q_W and R_W denotes roll, pitch and yaw rates of the *wind* axis system with respect to inertial space. The subscript 321 denotes the state vector using this specific Euler sequence. Equation (2.2.11) allows for the dynamic calculation of the Euler angles and ultimately describes the orientation of the wind axis system with respect to the inertial axis system with the angular rates as inputs.

2.2.2 Kinetics

As previously mentioned, kinetics involve how forces acting on a body (in this case, an aircraft) translates into accelerations. The accelerations provided by the kinetic equations are then used in the kinematic equations derived in section 2.2.1.1 to describe how they propagate into velocity, position and attitude over time.

2.2.2.1 Rigid Body Rotational Dynamics

The equations developed in section 2.2.1.1 described the motion of the aircraft's centre of mass through inertial space by describing the motion of the wind axis system over time. However, with the aircraft modelled as a rigid body, there can also be rotational motion of the body axis system relative to the wind axis system as argued by [15]. This section presents the equations of motion describing the rigid body rotational dynamics of the aircraft by describing the rotational motion of the body axis system relative to the wind axis system.

To arrive at the rotational dynamics for all mass elements in a rigid body, it is sufficient to consider the dynamics of a single mass element along with its attitude. Newton's

---

[4] A singularity in the solution appears for $|\theta_W| = \pi/2$ for the Euler 3-2-1 sequence. Conventional flight ensures that $|\theta_W| \neq \pi/2$

second law regarding moments state that the summation of all external moments ($\boldsymbol{M}$) acting on an object must equal the time of rate of change of the object's angular momentum with respect to inertial space,

$$\boldsymbol{M} = \frac{d}{dt}\boldsymbol{H}\bigg|_{I} \tag{2.2.12}$$

where $\boldsymbol{H}$ denotes the angular momentum, or *moment of momentum* about the centre of mass. The momentum of an arbitrary mass element dm due to the angular velocity $\boldsymbol{\omega}^{BI}$ of the body axes relative to inertial space is equal to its tangential velocity about the centre of mass multiplied by its mass dm, or $dm(\boldsymbol{\omega}^{BI} \times \boldsymbol{r}^{dmB})$. Since $\boldsymbol{H}$ is a *moment of momentum*, it can be determined by[5],

$$\boldsymbol{H} = \int_{v} \boldsymbol{r}^{dmB} \times (\boldsymbol{\omega}^{BI} \times \boldsymbol{r}^{dmB}) dm \tag{2.2.13}$$

where $\boldsymbol{r}^{dmB}$ is the position vector of an arbitrary mass element dm, relative to the centre of mass within the rigid body v.

As argued by [15], the angular momentum vector takes on its simplest form when coordinated into the body axes since the moment arms to all mass elements are fixed and independent of other motion variables. Equation (2.2.12) can be written in the following form by applying equation (B.2.2) defined in appendix B as,

$$\boldsymbol{M} = \frac{d}{dt}\boldsymbol{H}\bigg|_{B} + \boldsymbol{\omega}^{BI} \times \boldsymbol{H} \tag{2.2.14}$$

By combining equation (2.2.13) and (2.2.14) and rearranging the result, the dynamics of the *body* axis angular velocity with respect to inertial space can be expressed as shown in [15] as,

$$\dot{\boldsymbol{\omega}}_{B}^{BI} = \mathbf{I}_{B}^{-1}\left[-\mathbf{S}_{\omega_{B}^{BI}}\mathbf{I}_{B}\boldsymbol{\omega}_{B}^{BI} + \mathbf{M}_{B}\right] \tag{2.2.15}$$

where the subscript B implies that the vectors are *coordinated* in the body axes and $\mathbf{I}_{B}$ is the moment of inertia matrix (see appendix C) referenced to the body axis system. The matrix $\mathbf{S}_{\omega_{B}^{BI}}$ implements a cross product and is defined as,

$$\mathbf{S}_{\omega_{B}^{BI}} = \begin{bmatrix} 0 & -r & q \\ r & 0 & -p \\ -q & p & 0 \end{bmatrix} \tag{2.2.16}$$

---

[5] Entire rigid body volume: v

where p, q and r denotes roll, pitch and yaw rates of the *body* axes with respect to inertial space. If it is assumed that the aeroplane is symmetric about the x-z plane and that the mass is uniformly distributed, the products of inertia simplify to $I_{xy} = I_{yz} = 0$. According to [1], the symmetry of the aircraft determines that I_{xz} is generally much smaller than I_{xx}, I_{yy} and I_{zz}, and can often be neglected for control purposes. $\mathbf{I}_B$ can now be written in simplified form as,

$$\mathbf{I}_B = \begin{bmatrix} I_{xx} & -I_{xy} & -I_{xz} \\ -I_{xy} & I_{yy} & -I_{yz} \\ -I_{xz} & -I_{yz} & I_{zz} \end{bmatrix} \approx \begin{bmatrix} I_{xx} & 0 & 0 \\ 0 & I_{yy} & 0 \\ 0 & 0 & I_{zz} \end{bmatrix} \tag{2.2.17}$$

Equation (2.2.15) governs the rotational motion of the body axis system with respect to inertial space as a function of the applied moment vector. However, the body axes rotational motion ($\boldsymbol{\omega}^{BI}$) is a superposition of the angular velocity of the wind axis system relative to inertial space ($\boldsymbol{\omega}^{WI}$) and the angular velocity of the body axis system relative to the wind axis system ($\boldsymbol{\omega}^{BW}$), as argued by [15]. This argument is written mathematically as,

$$\boldsymbol{\omega}^{BI} = \boldsymbol{\omega}^{BW} + \boldsymbol{\omega}^{WI} \tag{2.2.18}$$

Furthermore, from the definition of the wind axes the wind Z-axis lies in the aircraft's symmetry plane resulting in,

$$\boldsymbol{k}^{W} \cdot \boldsymbol{j}^{B} = 0 \quad \forall t \tag{2.2.19}$$

where $\boldsymbol{j}^B$ and $\boldsymbol{k}^W$ is the body axis system Y-axis unit vector and the wind axis system Z-axis unit vector respectively. Since this condition must hold for all time, the derivative of equation (2.2.19) must also be zero. This constraint only holds when $\boldsymbol{\omega}^{BW}$ is written in the following form as stated in [15],

$$\boldsymbol{\omega}^{BW} = a\boldsymbol{j}^{B} + b\boldsymbol{k}^{W} \tag{2.2.20}$$

implying that $\boldsymbol{\omega}^{BW}$ must lie in the plane spanned by the basis vectors[6] $\boldsymbol{j}^B$ and $\boldsymbol{k}^W$. From the standard definition of the aircraft angle of attack (α) and angle of sideslip (β), with equations (2.2.20) and (2.2.18), the following relationship holds when coordinated in the body axes,

---

[6] For perpendicular unit vectors: $\boldsymbol{j}^B \cdot \boldsymbol{j}^B = 1$, $\boldsymbol{k}^W \cdot \boldsymbol{j}^B = 0$ and $\boldsymbol{j}^B \times \boldsymbol{j}^B = 0$

$$\boldsymbol{\omega}_{B}^{BI} = \dot{\alpha}\mathbf{j}_{B}^{B} - \dot{\beta}\mathbf{k}_{B}^{W} + \boldsymbol{\omega}_{B}^{WI} \tag{2.2.21}$$

The above equation can be expressed as,

$$\boldsymbol{\omega}_{B}^{BI} = \dot{\alpha}\mathbf{j}_{B}^{B} - \dot{\beta}\left[\mathbf{DCM}^{BW}\right]\mathbf{k}_{W}^{W} + \left[\mathbf{DCM}^{BW}\right]\boldsymbol{\omega}_{W}^{WI} \tag{2.2.22}$$

Expanding and rearranging equation (2.2.22) results in,

$$\begin{bmatrix} p \\ q \\ r \end{bmatrix} - \begin{bmatrix} C_\alpha C_\beta & -C_\alpha S_\beta & -S_\alpha \\ S_\beta & C_\beta & 0 \\ S_\alpha C_\beta & -S_\alpha S_\beta & C_\alpha \end{bmatrix} \begin{bmatrix} P_W \\ Q_W \\ R_W \end{bmatrix} = \begin{bmatrix} 0 & S_\alpha \\ 1 & 0 \\ 0 & -C_\alpha \end{bmatrix} \begin{bmatrix} \dot{\alpha} \\ \dot{\beta} \end{bmatrix} \tag{2.2.23}$$

where C_α and S_β denote $\cos(\alpha)$ and $\sin(\beta)$ respectively. The equations are rearranged to make $\begin{bmatrix} \dot{\alpha} & \dot{\beta} & P_W \end{bmatrix}^T$ the subject of the formula and Q_W and R_W are replaced by the constraints given in equation (2.2.8). The angular velocity dynamics (equation (2.2.15)) and the α and β dynamics (equation (2.2.23)) are combined to form the complete rotational dynamic equations,

$$\begin{bmatrix} \dot{\alpha} \\ \dot{\beta} \end{bmatrix} = \begin{bmatrix} -C_\alpha T_\beta & 1 & -S_\alpha T_\beta \\ S_\alpha & 0 & -C_\alpha \end{bmatrix} \begin{bmatrix} p \\ q \\ r \end{bmatrix} + \frac{1}{m\overline{V}} \begin{bmatrix} C_\beta^{-1} & 0 \\ 0 & 1 \end{bmatrix} \begin{bmatrix} Z_W \\ Y_W \end{bmatrix} \tag{2.2.24}$$

$$\begin{bmatrix} \dot{p} \\ \dot{q} \\ \dot{r} \end{bmatrix} = \boldsymbol{I}_{B}^{-1} \left(- \begin{bmatrix} 0 & -r & q \\ r & 0 & -p \\ -q & p & 0 \end{bmatrix} \boldsymbol{I}_{B} \begin{bmatrix} p \\ q \\ r \end{bmatrix} + \begin{bmatrix} L \\ M \\ N \end{bmatrix} \right) \tag{2.2.25}$$

$$P_W = \begin{bmatrix} C_\alpha C_\beta^{-1} & 0 & S_\alpha C_\beta^{-1} \end{bmatrix} \begin{bmatrix} p \\ q \\ r \end{bmatrix} + \frac{1}{m\overline{V}} \begin{bmatrix} -T_\beta & 0 \end{bmatrix} \begin{bmatrix} Z_W \\ Y_W \end{bmatrix} \tag{2.2.26}$$

with the constraint on P_W ensuring that condition 2.2.19 remains valid. Equations (2.2.24) to (2.2.26) maintains the attitude of the body axis system with respect to the wind axis system over time, as a function of the applied moment vector coordinates in body axes (L, M and N) and the lateral and normal force vector coordinates in the wind axes. To complete the topic of kinetics, forces and their resulting moments acting on the aircraft are analysed in the next section (2.2.3).

2.2.3 Forces and Moments

For the purpose of this thesis, the aircraft is modelled as a six degree of freedom rigid body with gravitational and specific forces with their corresponding moments acting on it. The specific forces include aerodynamic and propulsion forces. These arise mainly due to the form and motion of the aircraft itself. The gravitational force is applied to the aircraft in proportion to its mass, assuming a uniform gravitational field. These forces are discussed in the section to follow.

2.2.3.1 Propulsion Forces and Thrust Model

The aircraft used in this project was equipped with single brushless DC motors, with the primary thrust vector acting through the aircraft's centre of gravity along $\boldsymbol{i}^B$. The body axis thrust vector can be coordinated into the wind axes (W),

$$\begin{bmatrix} X_W^E \\ Y_W^E \\ Z_W^E \end{bmatrix} = \begin{bmatrix} \cos\alpha\cos\beta \\ -\cos\alpha\sin\beta \\ -\sin\alpha \end{bmatrix} T \tag{2.2.27}$$

where the superscript E denotes a propulsion source vector coordinate, and T is the magnitude of the thrust vector in newton.

Various thrust models exist for different propulsion sources. Considering the significant bandwidth-limited response of most propulsion sources, the engine is modelled as a first order transfer function representing a throttle lag with time constant τ_T. Note that the dynamic effect of velocity magnitude on output thrust is ignored in this model because its effect is often negligible [15] for control purposes. The model is given by,

$$\dot{T} = -\frac{1}{\tau_T}T + \frac{1}{\tau_T}T_c \tag{2.2.28}$$

where the time constant τ_T is approximated experimentally.

2.2.3.2 Aerodynamic Forces

The aerodynamic specific forces and their corresponding moments modelled in the wind axes [3] are presented below,

$$\begin{bmatrix} X_W^A \\ Y_W^A \\ Z_W^A \end{bmatrix} = \bar{q}S \begin{bmatrix} -C_D \\ C_y \\ -C_L \end{bmatrix} \tag{2.2.29}$$

$$\begin{bmatrix} L_W^A \\ M_W^A \\ N_W^A \end{bmatrix} = \bar{q}S \begin{bmatrix} b & 0 & 0 \\ 0 & \bar{c} & 0 \\ 0 & 0 & b \end{bmatrix} \begin{bmatrix} C_l \\ C_m \\ C_n \end{bmatrix} \tag{2.2.30}$$

where,

$$\bar{q} = \frac{1}{2}\rho\overline{V}_a^2 \tag{2.2.31}$$

The above equations state the aerodynamic (A) forces and moments in the wind axes (W). Furthermore, $\bar{q}$ is the dynamic pressure, ρ the air density, and $\overline{V}_a$ is the airspeed magnitude. The dimensionless coefficients C_D, C_y and C_L are *drag*, *lift* and *side-force* coefficients respectively with C_l, C_m and C_n the dimensionless *roll*, *pitch* and *yaw* moment coefficients respectively. To allow for the same surface area and moment arms to be used in the force and moment calculations, reference quantities are used to calculate the aerodynamic coefficients. These are listed in table 2.1.

Physical Value	**Aerodynamic Reference**
Total wing area S	Surface
Mean-aerodynamic chord $\bar{c}$	Pitching moment arm
Wingspan b	Roll and Yaw moment arms

Table 2.1: Aerodynamic References

Note that the rigid body rotational dynamics require forces in the wind axes and moments in the body axes. Transforming the moment coordinate vector from the wind to body axes yields,

$$\begin{bmatrix} L \\ M \\ N \end{bmatrix} = [\mathbf{DCM}^{BW}] \begin{bmatrix} L_W^A \\ M_W^A \\ N_W^A \end{bmatrix} \tag{2.2.32}$$

where $\mathbf{DCM}^{BW}$ is defined in appendix B by equation (B.3.7), and L, M and N are the moment vector coordinates in the body axes.

Stability and Control Derivatives: These are dimensionless quantities describing a change in a force or moment due to a change in a normalised motion variable or actuator. These derivatives can be computed from first principles, computational fluid dynamics methods, wind tunnel measurements or using flight test data and system identification techniques. The derivatives allow for a direct comparison between aircraft of different dimensions. Expressing the dimensionless stability and control derivatives in the wind axis system yields the following results as given in [4],

$$C_D = C_{D_0} + \frac{C_L^2}{\pi A e} \tag{2.2.33}$$

$$\begin{aligned}
\begin{bmatrix} C_y \\ C_L \end{bmatrix} &= \begin{bmatrix} 0 \\ C_{L_0} \end{bmatrix} + \begin{bmatrix} 0 & C_{Y_\beta} & \frac{b}{2V_a}C_{Y_p} & 0 & \frac{b}{2V_a}C_{Y_r} \\ C_{L_\alpha} & 0 & 0 & \frac{\bar{c}}{2V_a}C_{L_q} & 0 \end{bmatrix} \begin{bmatrix} \alpha \\ \beta \\ p \\ q \\ r \end{bmatrix} \\
&+ \begin{bmatrix} C_{Y_{\delta_A}} & 0 & C_{Y_{\delta_R}} \\ 0 & C_{L_{\delta_E}} & 0 \end{bmatrix} \begin{bmatrix} \delta_A \\ \delta_E \\ \delta_R \end{bmatrix}
\end{aligned} \tag{2.2.34}$$

$$\begin{aligned}
\begin{bmatrix} C_l \\ C_m \\ C_n \end{bmatrix} &= \begin{bmatrix} 0 \\ C_{m_0} \\ 0 \end{bmatrix} + \begin{bmatrix} 0 & C_{l_\beta} & \frac{b}{2V_a}C_{l_p} & 0 & \frac{b}{2V_a}C_{l_r} \\ C_{m_\alpha} & 0 & 0 & \frac{\bar{c}}{2V_a}C_{m_q} & 0 \\ 0 & C_{n_\beta} & \frac{b}{2V_a}C_{n_p} & 0 & \frac{b}{2V_a}C_{n_r} \end{bmatrix} \begin{bmatrix} \alpha \\ \beta \\ p \\ q \\ r \end{bmatrix} \\
&+ \begin{bmatrix} C_{l_{\delta_A}} & 0 & C_{l_{\delta_R}} \\ 0 & C_{m_{\delta_E}} & 0 \\ C_{n_{\delta_A}} & 0 & C_{n_{\delta_R}} \end{bmatrix} \begin{bmatrix} \delta_A \\ \delta_E \\ \delta_R \end{bmatrix}
\end{aligned} \tag{2.2.35}$$

For this project, a vortex lattice simulation program (AVL) was used to determine the stability and control derivatives and is discussed further in appendix C. In equation (2.2.33), A is the wing aspect ratio, C_{D_0} is the parasitic drag coefficient and e is the Oswald efficiency factor defined in appendix C. In equations (2.2.34) and (2.2.35), C_{L_0} is the static lift coefficient and C_{m_0} is the static moment coefficient. Small angle approximations were made to transform the roll and yaw rates to the wind axis system as given in [4]. Terms of the form,

$$C_{\lambda_\epsilon} = \frac{\partial C_\lambda}{\partial \epsilon'} \tag{2.2.36}$$

where $\epsilon^{'}$ is defined as,

$$\epsilon^{'} = n\epsilon \tag{2.2.37}$$

represent the non-dimensional stability and control derivatives where n is a normalising coefficient of ϵ. The normalising coefficients makes use of the aerodynamic reference values given in table 2.1. For pitch rate the normalising coefficient is $\frac{\bar{c}}{2V_a}$ and for roll and yaw rates it is $\frac{b}{2V_a}$. Therefore, a change in $\epsilon^{'}$ introduces a change in C_λ and is denoted by C_{λ_ϵ}. In this text λ represents a force or moment and $\epsilon^{'}$ represents a normalised kinematic state.

In the model presented, the stability derivatives for the first time derivative of the states have been ignored. Of the first time derivatives however, only $C_{L_{\dot{\alpha}}}$ and $C_{m_{\dot{\alpha}}}$ are significant, quantifying effects such as downwash lag and added mass according to [3]. For a blended-wing aircraft downwash lag is ignored[7] due to the lack of a tail plane, and added mass is assumed negligible for control design purposes. Furthermore, it is assumed that the stability and control derivatives are not a function of the rigid body rotational dynamics but rather parameters describing these dynamics. This assumption is valid for an aircraft operating within the small incidence angle range and greatly simplifies the design and analysis of the control system.

2.2.3.3 Gravitational Forces

The rigid body rotational dynamics require the gravity vector to be coordinated in the wind axes. Therefore, the direction cosine matrix is used to coordinate the gravity vector (G) fixed in inertial space into the wind axes (W). The moment contributions due to gravity are zero because this force acts through the centre of gravity.

$$\begin{bmatrix} X_W^G \\ Y_W^G \\ Z_W^G \end{bmatrix} = [\mathbf{DCM}^{WI}] \begin{bmatrix} 0 \\ 0 \\ mg \end{bmatrix} \tag{2.2.38}$$

Here g is the gravitational force per unit mass, m the aircraft mass, and $\mathbf{DCM}^{WI}$ is the direction cosine transformation matrix, which is defined in appendix B.

2.2.4 Complete Aircraft Model

The inner loop dynamics are created by substituting the linear force model (equations (2.2.29) to (2.2.35) with equation 2.2.27) into the rotational dynamics (equations (2.2.24) and (2.2.26)). This model can easily be decoupled into axial, normal and lateral compo-

---

[7] Downwash lag is often ignored for control design purposes for conventional aircraft as well.

nents to simplify the control system design and analysis, as shown in [15]. The control architecture however is discussed in detail in chapter 4.

2.3 Dynamic Centre of Mass Position

Up to this point the analysis assumed a fixed centre of mass for a rigid body. This section investigates the effect of varying the aircraft centre of mass position on the aircraft dynamics presented thus far. Aircraft stability effects due to variations in centre of mass position is discussed at length in chapter 3. The aircraft is equipped with a centre of mass constrained to move along $\boldsymbol{i}^B$ by means of moving another mass, in this case the avionics and engine battery located in an *actuator tray*.

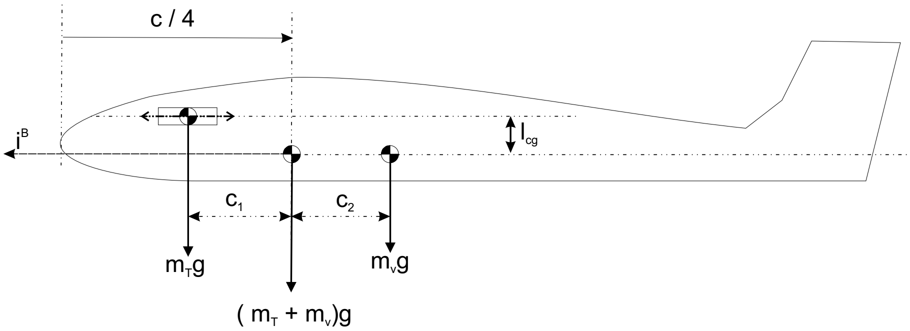

Figure 2.5: Moveable centre of mass dynamics

Consider both the aircraft and linear actuator tray as two separate rigid bodies. By placing the actuator tray in the position shown in figure 2.5, the centre of mass can be placed at the quarter chord point, where m_T and m_v denotes the tray and vehicle mass respectively. During static equilibrium between these two bodies the resulting centre of mass position can be determined by,

$$m_T g C_1 = m_v g C_2 \tag{2.3.1}$$

where C_2 is a known measurable quantity. The linear motion of the actuator tray will affect the aircraft stability derivatives, moment of inertia, and aircraft forces and moments. These factors will now be discussed.

2.3.1 Contributions to Forces and Moments

If the actuator tray (T) is assumed to have its own right handed orthogonal axis system described by the basis unit vectors $\boldsymbol{i}^T$, $\boldsymbol{j}^T$ and $\boldsymbol{k}^T$, the force vector relative to the aircraft is given by,

$$\boldsymbol{F}^{T} = m_T \dot{\boldsymbol{V}}^{TI} \tag{2.3.2}$$

where $\boldsymbol{F}^{T}$ is the actuator tray force vector and $\boldsymbol{V}^{TI}$ the actuator tray velocity vector with respect to inertial space. Expanding the previous equation yields,

$$\begin{bmatrix} X_B^T \\ Y_B^T \\ Z_B^T \end{bmatrix} = m_T \begin{bmatrix} \dot{u}_T \\ 0 \\ 0 \end{bmatrix} \tag{2.3.3}$$

where u_T is the velocity of the tray along the aircraft longitudinal axis. Note the subscript B implies that the actuator tray force vector is coordinated in the aircraft body axes. This is because the tray is constrained to move along $\boldsymbol{i}^{B}$, and the force exerted by the tray can therefore be viewed as a disturbance adding to the aircraft body axes forces. Furthermore, if the actuator tray is located either above or below the native aircraft centre of mass (offset by a distance of l_{cg}) a pitching moment disturbance can be induced as well. However, the actuator tray acceleration $\dot{u}_T$ is very small and its effect is therefore negligible. Consequently the force and moment disturbances in the aircraft body axes caused by the actuator tray acceleration is ignored for control design purposes.

2.3.2 Contributions to the Moment of Inertia

Varying the position of the actuator tray changes the MOI (moment of inertia) values. The total aircraft MOI is the sum of the MOI values calculated for the aircraft with and without the actuator tray, and can be written as,

$$I_{\zeta\zeta} = I'_{\zeta\zeta} + \Delta I_{\zeta\zeta} \tag{2.3.4}$$

where $I_{\zeta\zeta}$ is the aircraft total MOI, $I'_{\zeta\zeta}$ the MOI without the actuator tray and $\Delta I_{\zeta\zeta}$ the tray MOI contribution about the X, Y and Z axes respectively. With reference to table 2.2 and figure 2.5, position one is when the actuator tray is in front of the aircraft native centre of mass. Position two is when the tray centre of mass, aircraft native centre of mass and the resultant centre of mass coincide, and position three is when the tray is located aft of the native aircraft centre of mass.

The value l_{cg} is typically very small ($< 0.1c$ where c is the chord length) and can be ignored. Therefore, it is observed that the biggest contributions to the moment of inertia will be about the pitch and yaw axes when the tray is in its most forward and most rearward positions. Table 2.2 now simplifies to,

Moment of Inertia	**Tray Position 1**	**Tray Position 2**	**Tray Position 3**
ΔI_{xx}	$m_T I_{cg}^2$	$m_T I_{cg}^2$	$m_T I_{cg}^2$
ΔI_{yy}	$m_T(C_1^2 + I_{cg}^2)$	$m_T I_{cg}^2$	$m_T(C_2^2 + I_{cg}^2)$
ΔI_{zz}	$m_T C_1^2$	0	$m_T C_2^2$

Table 2.2: Variable Mass MOI Contributions

Moment of Inertia	**Tray Position 1**	**Tray Position 2**	**Tray Position 3**
ΔI_{xx}	0	0	0
ΔI_{yy}	$m_T C_1^2$	0	$m_T C_2^2$
ΔI_{zz}	$m_T C_1^2$	0	$m_T C_2^2$

Table 2.3: Simplified Variable Mass MOI Contributions

Given that the tray is mechanically constrained to a most forward distance of $C_1 = 0.13c$ and aft distance of $C_2 = 0.19c$, and assuming the actuator tray has a mass given by $m_T = \frac{m_v}{2}$, the forward and aft moment of inertia contributions can be represented by,

$$\Delta I_{\zeta\zeta}^{'} = \frac{m_v}{2}(0.13c)^2 = \frac{0.9}{100} m_v c^2 \times 100 \quad [\%] \tag{2.3.5}$$

$$\Delta I_{\zeta\zeta}^{''} = \frac{m_v}{2}(0.19c)^2 = \frac{1.8}{100} m_v c^2 \times 100 \quad [\%] \tag{2.3.6}$$

In the above equations, $\Delta I_{\zeta\zeta}^{'}$ is the MOI contribution about either the Y or Z-axis for the most forward case, and $\Delta I_{\zeta\zeta}^{''}$ for the most rearward case expressed as a percentage of the product of the aircraft mass m_v and the square of the chord length c. When expressing the moment of inertia values (excluding the actuator tray) obtained experimentally in a similar way, the following results are obtained:

$$I_{yy} = \frac{6.4}{100} m_v c^2 \times 100 \quad [\%] \tag{2.3.7}$$

$$I_{zz} = \frac{29.0}{100} m_v c^2 \times 100 \quad [\%] \tag{2.3.8}$$

where the vehicle mass is 3.2 kg and the reference chord length is 0.52 m. It is shown that the parameter I_{yy} exhibits a 13.4% increase in the most forward position and a 27.5% increase in the aft position. This means that when the actuator tray with mass $\frac{m_v}{2}$ (where m_v is the aircraft mass) is added to the vehicle, I_{yy} is predicted to increase by 13.4% when the tray is in the foremost position; and 27.5% when it is in the most aft position.

In contrast, I_{zz} shows a 3% and 6% increase for the two respective tray positions. In total, I_{yy} changes the most over the entire range with about 28% where I_{zz} changes only 6%. However, since the actuator tray dynamics are mechanically constrained to operate at a bandwidth very much lower than that of the rigid body rotational dynamics, a timescale separation argument can therefore be used to handle the dynamic coupling of moment of inertia back into the rigid body rotational dynamics. With a significant timescale separation between the dynamics, the moment of inertia can be considered parameters in the rigid body rotational dynamics instead of states. This is equivalent of saying that over the timescales of interest in the rigid body rotational dynamics, the moment of inertia remain very close to constant. Therefore, this effect can be taken into account by updating the moment of inertia as a quadratic function of the centre of mass position. The control architecture developed to achieve this is discussed in chapter 4.

2.3.3 Impact on Stability and Control Derivatives

Stability derivatives are often derived from the geometry of an aircraft with the centre of mass taken as a reference point. Therefore, variations in aircraft centre of mass will impact the aircraft stability and control derivatives and consequently affect aircraft stability. Identifying which stability derivatives are affected by variations in centre of mass position is the topic of discussion in chapter 3.

Chapter 3

The Variable Stability Aircraft Problem

As mentioned in chapter 1, the aircraft designed by the CSIR is optimised to deliver minimum drag. During the design and optimisation process the aircraft centre of mass position is taken as a *variable*, providing an extra degree of freedom to the designers when optimising the airframe. Consequently, the performance of the aircraft with respect to drag reduction must be evaluated at some optimal centre of mass location. According to the aircraft designers, the design goals can be achieved when the aircraft's centre of mass is placed slightly aft of the neutral point (defined in section 3.1.2). By moving an *actuator tray*, as discussed in section 2.3, the aircraft is initially made statically stable allowing for manual take-off. The actuator tray is then adjusted in flight to place the centre of mass aft of the neutral point. At this point however, the aircraft is statically unstable (section 3.1.2) and cannot be controlled by a human pilot, therefore a flight control system is necessary to stabilise the airframe as discussed in chapter 4.

However, before a flight control system can be designed, the effect of varying the aircraft centre of mass position on the parameters that describe the natural dynamics of the aircraft must be investigated. Since stability and control derivatives are often derived using the aircraft centre of mass position as a reference point, these derivatives will vary when the centre of mass position is changed.

The aim of this chapter is therefore threefold. Firstly, some classic aerodynamic concepts regarding stability are introduced (section 3.1). Secondly, the stability and control derivatives are analysed to determine which derivatives are affected by varying the centre of mass position (section 3.2). The chapter concludes by providing AVL simulation results showing how the stability and control derivatives vary with centre of mass position, when derived using vortex lattice methods, to confirm the arguments presented (section 3.3).

3.1 Classic Aerodynamic Concepts

Section 3.1.1 presents the classic definition of aerodynamic aircraft stability, introducing the concepts of *static* and *dynamic* stability respectively. Next, section 3.1.2 describes longitudinal static stability in more detail, and introduces an important aerodynamic reference point, i.e. the *neutral point*, used to explain various concepts throughout the chapter.

3.1.1 Aerodynamic Stability in General

Static and Dynamic Stability: Static stability of an aeroplane is classically described as the aircraft's ability to generate a restoring moment following a disturbance from the trim equilibrium condition [1]. Static stability therefore excludes dynamic effects, such as aerodynamic damping and stiffness in pitch and yaw. Dynamic stability on the other hand describes the *transient* motion following a disturbance during recovery to the initial trim condition. Two primary forms of longitudinal oscillations related to dynamic stability classically exists describing the transient motion of the aircraft following a disturbance. These are known as the Phugoid and Short period mode and will be discussed further in chapter 4. Although various definitions for aerodynamic stability exist, the material presented here will be concerned mainly with longitudinal, lateral and directional stability regarding a subsonic aircraft.

Static Directional and Lateral Stability: An aeroplane is said to be *directionally* stable, if a yawing moment is created to restore the aircraft to its equilibrium condition, following a disturbance in angle of sideslip β relative to its current flight path. Furthermore, an aeroplane is said to possess *lateral* static stability, if after undergoing a disturbance that rolls it to some bank angle ϕ, forces and moments are generated reducing the bank angle and restoring the equilibrium flight condition.

3.1.2 Aerodynamic Longitudinal Static Stability

Figure 3.1 shows the normal forces and pitching moments as defined for a blended-wing-body aircraft. Note that because a blended-wing-body aircraft lacks a horizontal tailplane, a *virtual* horizontal tailplane is used throughout this thesis. The *virtual* horizontal tailplane is defined as the section of the blended-wing-body aircraft acting as a conventional horizontal tailplane for the purpose of providing pitch rate damping.

With reference to figure 3.1, the aerodynamic centre (*ac*) of an aerofoil is used as an aerodynamic reference point, and is defined as the point where the pitching moment coefficient remains *constant* regardless of angle of attack. Note however that the lift force acting at an aerodynamic centre is a function of the angle of attack α, i.e. $L_W = f(\alpha_W)$ and $L_T = f(\alpha_T)$, where α_W and α_T are the angles of attack on the main wing (W) and horizontal tailplane (T) respectively. Note that the pitching moment coefficients of the wing M_W and tail M_T are determined by the camber of the respective aerofoils.

Furthermore, the total longitudinal aerodynamic centre of an aircraft is referred to as the *neutral point*, denoted by NP_L. Therefore, the moment M_{NP} is the sum of the moments M_W and M_T, and the force L_{NP} is the sum of the forces L_W and L_T. Consequently, the force acting at the neutral point L_{NP} is also dependent on the angle of attack with the moment M_{NP} remaining invariant to variations in angle of attack.

Equilibrium: The neutral point for a longitudinally statically stable aircraft is located aft of the centre of mass, as shown by figure 3.1. For a given angle of attack, the tailplane actuators (elevators) are adjusted to change the pitching moment about the neutral point until the moments due to aerofoil camber about the centre of mass are zero. The vehicle is now considered *trimmed* for straight and level flight.

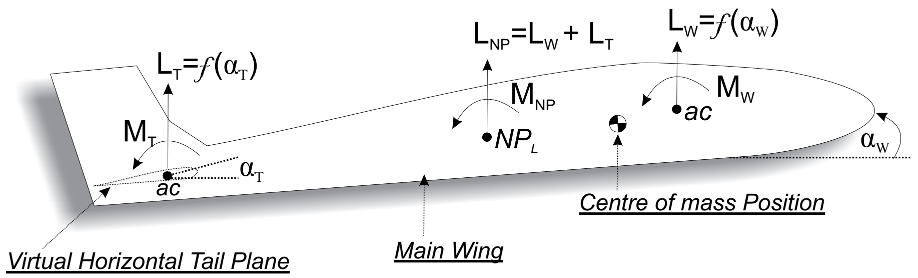

Figure 3.1: Simple Pitching Moment Diagram

Longitudinally Statically Stable Aircraft: With reference to figure 3.2, if a sudden *positive* pitch disturbance q acts on the aircraft, the angle of attack increases by $\alpha_W^{'}$ and consequently the lift force L_{NP} increases. This increase in lift force creates a moment M_α about the aircraft centre of mass inducing a *negative* pitching moment, countering the induced pitch disturbance. The derivative describing a pitching moment due to a perturbation in angle of attack (C_{m_α}) is therefore *negative*.

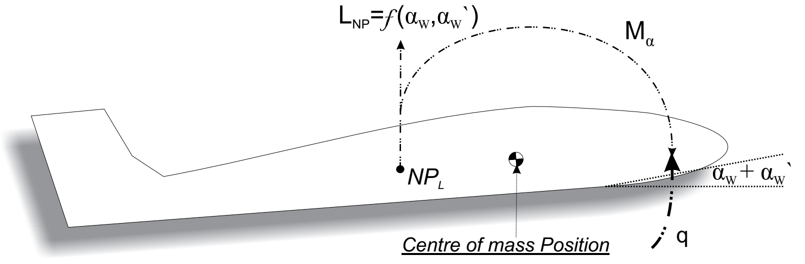

Figure 3.2: Statically Stable Aircraft During Positive Pitch Disturbance

Longitudinally Statically Unstable Aircraft: With reference to figure 3.3, for an aircraft to be statically *unstable* the centre of mass is located behind the aircraft neutral point. If the same positive pitch disturbance acts on this airframe, the larger lift force due to angle of attack creates a further *positive* pitching moment about the centre of mass. No stabilising moment is therefore created and the airframe is deemed statically unstable. The derivative C_{m_α} is therefore *positive*.

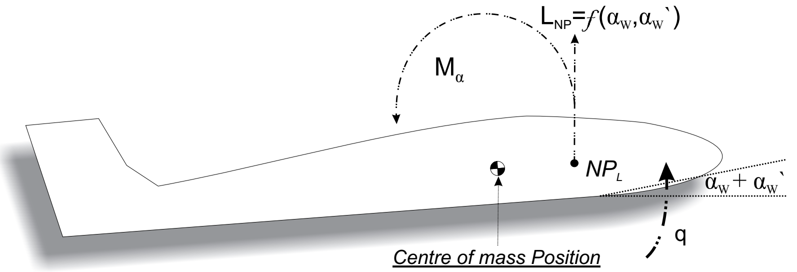

Figure 3.3: Statically Unstable Aircraft During Positive Pitch Disturbance

The aforementioned arguments indicate that a major influence of shifting the aircraft centre of mass position is to change longitudinal static stability. The following section continues with a more thorough analysis.

3.2 Analysis of Selected Stability Derivatives

The aim of this section is to analyse the stability and control derivatives presented in chapter 2 and thereby determine which derivatives are affected by variations in aircraft centre of mass position. As explained by [1], the aerodynamic analysis can be divided into a symmetric flow (longitudinal motion) and asymmetric flow (lateral motion) analysis. Under the symmetric flow condition, the lateral aerodynamic coefficients are *exactly* zero due to the symmetry of the aircraft. Furthermore, for the asymmetric flow condition, all of the aerodynamic coefficients are affected because there is aerodynamic interference between the different aircraft surfaces. However, the effect of asymmetric flow on the longitudinal force and moment coefficients is typically negligibly small compared to that of the symmetric flow condition, and is therefore *assumed* to be zero. This assumption decouples the longitudinal and lateral aerodynamic model. Therefore, the stability derivatives can be divided into lateral and longitudinal stability derivatives respectively, and can consequently be used to separately describe the lateral and longitudinal stability of the vehicle.

Grouping the Derivatives: The stability and control derivatives quantifying aerodynamic lateral and longitudinal forces and moments, as presented in the previous chapter (see section 2.2.3), are now grouped into the following categories:

- Forces due to incidence angles (C_{L_α},C_{Y_β})
- Moments due to incidence angles (C_{m_α},C_{l_β},C_{n_β})
- Forces due to angular velocities (C_{L_q},C_{Y_p},C_{Y_r})
- Moments due to angular velocities (C_{m_q},C_{l_p},C_{n_p},C_{l_r},C_{n_r})
- Forces and Moments due to actuator deflections ($C_{L_{\delta_E}}$,$C_{Y_{\delta_A}}$,$C_{Y_{\delta_R}}$,$C_{m_{\delta_E}}$,$C_{l_{\delta_A}}$,$C_{l_{\delta_R}}$,$C_{n_{\delta_A}}$,$C_{n_{\delta_R}}$)

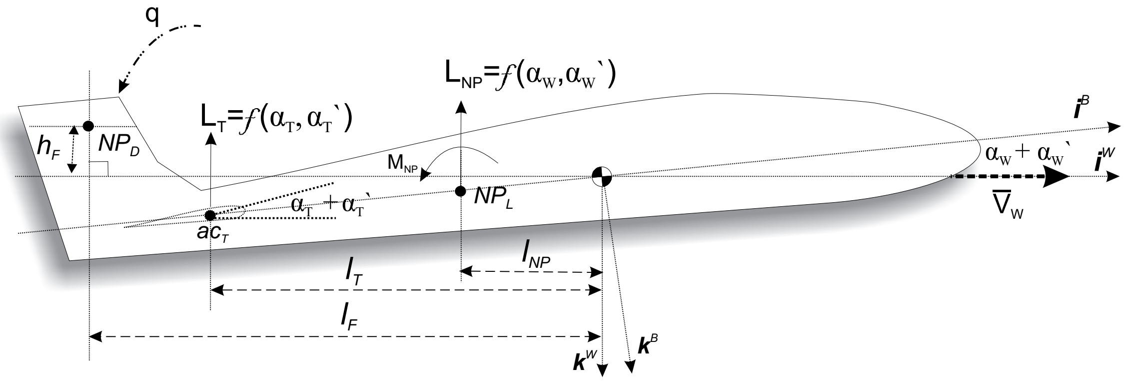

Figure 3.4: Simple Pitching Moment Diagram for a Blended-Wing Aircraft

The above mentioned groups will now be discussed with reference to the simplified pitching moment diagram given by figure 3.4. With reference to figure 3.4, the directional and longitudinal *neutral points* are defined by NP_D and NP_L respectively. The *aerodynamic centre* of the virtual tailplane is denoted by ac_T. As previously mentioned, the induced angle of attack on the wing and tailplane due to a pitch motion q is denoted by $\alpha_W^{'}$ and $\alpha_T^{'}$ respectively. The wind axes X and Z unit vectors are denoted by $\boldsymbol{i}^W$ and $\boldsymbol{k}^W$ respectively, and the body axes unit vectors by $\boldsymbol{i}^B$ and $\boldsymbol{k}^B$. As mentioned earlier, the force acting at the neutral point L_{NP} is a function of the angle of attack α_W, and will therefore increase with induced angle of attack $\alpha_W^{'}$. Similarly, the lift force on the tailplane L_T is a function of the angle of incidence on the tailplane α_T and increases with induced incidence on the tailplane $\alpha_T^{'}$.

Figure 3.4 shows four moment arm lengths between the aircraft centre of mass and the respective aerodynamic reference points. These moment arm lengths are given by:

- l_{NP}: The longitudinal distance between the aircraft centre of mass and the longitudinal neutral point.
- l_F: The longitudinal distance between the aircraft centre of mass and the directional neutral point.
- l_T: The longitudinal distance between the aircraft centre of mass and the aerodynamic centre of the virtual tailplane.
- h_F: The vertical distance between the aircraft centre of mass and the directional neutral point.

In actual fact, a fifth moment arm exists which is used to model the aircraft's natural rate damping ability. This moment arm length, denoted by l_D, is defined as the longitudinal distance between the aircraft centre of mass and the point where the aerodynamic damping force originates. To simplify the analysis presented in the chapter, the following assumption is made,

$$l_D \approx l_T \tag{3.2.1}$$

With respect to aerodynamic damping, the above simplifying assumption presumes that the dominating aerodynamic properties, are mainly those of the section of the blended-wing-body aircraft acting as a conventional horizontal tailplane. It is acknowledged that the wing contribution may not necessarily be small and that its omission will reduce the accuracy of the analysis to follow. However, section 3.3 will show that the error incurred by adopting this assumption is acceptably small for the blended-wing-body aircraft used in this project.

3.2.1 Forces due to incidence angles (C_{L_α},C_{Y_β})

If the aircraft is flying straight and level at a constant angle of attack α_W (i.e. $\alpha_W^{'} = 0$ and $q = 0$) as shown in figure 3.4, the total lift generated at the neutral point L_{NP} is dependent only on α_W which is determined by the lift curve slope of the wing as defined by equation D.2.2 in appendix D.

Furthermore, the lift curve slope of an aerofoil depends on the aerofoil aspect ratio, thickness, chord length and sweep angle, not on the centre of mass position. Therefore, the stability derivatives concerned with lift due to an angle of incidence α_W remains constant with variations in aircraft centre of mass position for small angles of incidence. The same argument is made for the lateral case with angle of sideslip β and the vertical fin.

3.2.2 Moments due to incidence angles (C_{m_α},C_{l_β},C_{n_β})

An aerodynamic moment due to an incidence angle is created because an aerodynamic force due an incidence angle acts about a moment arm to the centre of mass. Here, the moment arms of concern are (figure 3.4) $l_{_{NP}}$, l_F and h_F. The percentage change in the moment arm h_F due to variations in aircraft centre of mass position along $\boldsymbol{i}^B$ is negligibly small for small angles of attack, therefore this length is assumed to remain constant. Consequently, only l_F and $l_{_{NP}}$ will change with variations in centre of mass position along $\boldsymbol{i}^B$. When the aircraft centre of mass position changes, the moment arm lengths (l_f and $l_{_{NP}}$) change linearly, therefore this group of stability derivatives are affected linearly with centre of mass position.

Exception to the aforementioned arguments: The roll moment due to sideslip angle β on the vertical fin (described by C_{l_β}) is created about the h_F moment arm. Because the moment arm length h_F is assumed to remain constant with centre of mass variations, and because C_{l_β} is dominated by wing dihedral and wing sweep angle [1], this derivative is not dependent on aircraft centre of mass variations.

3.2.3 Forces due to angular velocities (C_{L_q},C_{Y_p},C_{Y_r})

An aeroplane pitching through its equilibrium attitude with pitch rate perturbation q is shown in figure 3.4. Since the effect of the pitch rate is to cause the aircraft to experience a normal velocity component due to rotation about the centre of mass, the resultant effect is a change in the effective incidence of the tailplane denoted by $\alpha_T^{'}$. The total angle of incidence perturbation [1] is given by,

$$\alpha_T^{'} \approx \frac{q l_T}{\overline{V}_W} \tag{3.2.2}$$

As previously mentioned, the force L_T is a function of incidence, and as a result will increase with induced angle of incidence $\alpha_T^{'}$. This increase in force at $ac_{_T}$ consequently damps the pitching motion. Furthermore, because $\alpha_T^{'}$ is linearly dependent on the distance l_T, and because the resultant lift force L_T is a function of $\alpha_T^{'}$, the derivative describing an induced lift force due to pitch rate (C_{L_q}) will depend linearly on the aircraft centre of mass position. Additionally, variations in aircraft centre of mass position will therefore linearly affect the aircraft's natural rate damping. The previous arguments can also be extended to the derivative C_{Y_r}, with the moment arm length l_F and the lateral force Y acting at NP_D.

Exception to the aforementioned arguments: The derivative describing a lateral force due to a roll rate (C_{Y_p}) is dominated by the fin lift curve slope and geometry, as shown in [1], and therefore is completely independent of aircraft centre of mass variations along $\boldsymbol{i}^B$.

3.2.4 Moments due to angular velocities (C_{m_q},C_{l_p},C_{n_p},C_{l_r},C_{n_r})

An aerodynamic moment due to an angular velocity is created when a force due to an angular velocity acts about a moment arm to the centre of mass. As previously argued, a force due to an angular velocity is already linearly dependent on a moment arm length. To create the moment due to an angular velocity, this force is again multiplied by the arm length (l_T or l_F), resulting in the moment becoming quadratically dependent on the length between the centre of mass and the lifting surface where the force originates. Therefore, this group of stability derivatives will change *quadratically* with variations in centre of mass position.

Exceptions to the aforementioned arguments: During a positive yaw motion, the port-side wing moves with a greater velocity than the starboard-side wing. This results in more lift being generated on the port-side wing than on the starboard wing, and consequently this difference in lift induces a roll rate. The roll rate magnitude is influenced mainly by the wing semi-span length, and therefore the derivative C_{l_r} is independent of centre of mass variations. Additionally, the derivatives due to roll rate C_{l_p} and C_{n_p} arise largely from the wing geometry [1], and are therefore not dependent on the aircraft centre of mass location.

3.2.5 Forces and Moments due to actuator deflections ($C_{L_{\delta_E}}$,$C_{Y_{\delta_A}}$,$C_{Y_{\delta_R}}$,$C_{m_{\delta_E}}$,$C_{l_{\delta_A}}$,$C_{l_{\delta_R}}$,$C_{n_{\delta_A}}$,$C_{n_{\delta_R}}$)

For this group of derivatives, the following assumptions are made [1]:

1. For a small elevator deflection, the resulting normal force perturbation arises from the lift change associated with the horizontal tailplane only.
2. For a small rudder deflection, the resulting lateral force perturbation arises from the lift change associated with the vertical fin only.
3. For a small aileron deflection, the resulting force perturbation arises from the lift generated differentially across the main wing area.

With reference to figure 3.4, when the elevator is deflected by some small amount, the induced angle of incidence on the horizontal tailplane $\alpha_T^{'}$ increases and consequently a force is induced. The induced lift force is dependent only on the aerofoil lift curve slope of the actuator (section D.2) and is *not* dependent on the aircraft centre of mass position. This argument is also extended to the lateral case with respect to the vertical fin.

A moment due to an actuator deflection is created when a force due to an actuator deflection acts about a moment arm to the centre of mass. Therefore, control derivatives quantifying aerodynamic moments due to actuator deflections are linearly dependent on the aircraft's centre of mass location. The first two assumptions stated above implies that the moment arm length related to the elevator control derivative is l_T, and the moment arm length related to the rudder control derivative is l_F.

Exceptions to the aforementioned arguments: The roll moment due to a rudder perturbation ($C_{l_{\delta_R}}$) is dependent only on the vertical fin moment arm h_f, as shown in [1], and is therefore assumed not to be dependent on variations in aircraft centre of mass position along $\boldsymbol{i}^B$. Furthermore, when the ailerons are deflected, differential drag is induced across the wing surface resulting in a yawing motion, quantified by $C_{n_{\delta_A}}$. Because $C_{n_{\delta_A}}$ is dominated by the effect of the induced differential drag, it is independent of aircraft centre of mass variations. Since the roll moment due to aileron perturbation $C_{l_{\delta_A}}$ is dominated by differential lift across the main wing area, $C_{l_{\delta_A}}$ is independent of centre of mass variations along $\boldsymbol{i}^B$.

3.2.6 Impact of Centre of Mass Variations on Derivatives

The stability and control derivatives presented thus far can now be sub-divided into three categories, namely derivatives that do not change with centre of mass position, derivatives that change *linearly* with centre of mass position and derivatives that change *quadratically* with the centre of mass position. The results are given in table 3.1.

Independent	Linearly dependent	Quadratically dependent
C_{L_α}	C_{m_α}	C_{m_q}
C_{Y_β}	C_{n_β}	C_{n_r}
$C_{L_{\delta_E}}$	$C_{m_{\delta_E}}$	
$C_{Y_{\delta_A}}$	$C_{n_{\delta_R}}$	
$C_{Y_{\delta_R}}$	C_{Y_r}	
C_{Y_p}	C_{L_q}	
C_{l_p}		
C_{n_p}		
C_{l_β}		
$C_{l_{\delta_R}}$		
$C_{l_{\delta_A}}$		
C_{l_r}		
$C_{n_{\delta_A}}$		

Table 3.1: The dependency of stability and control derivatives on centre of mass position

As previously argued, when the aircraft centre of mass is varied along $\boldsymbol{i}^B$, the moment arm lengths $l_{_{NP}}$, l_T and l_F change, and the stability and control derivatives modelled using $l_{_{NP}}$, l_T and l_F change as indicated by table 3.1. Therefore, if it can be shown that the change of a moment arm length due to the longitudinal motion of the aircraft centre of mass is negligible, then the stability and control derivatives modelled using this moment arm length can be considered independent of aircraft centre of mass variations along $\boldsymbol{i}^B$. By identifying which derivatives remain invariant to variations in aircraft centre of mass position, the control system design process is substantially simplified.

3.2.6.1 Variation of the Lateral Moment Arm l_F with Aircraft Centre of Mass Position

The moment arm length between the directional neutral point and centre of mass, denoted by l_F, is used to model C_{n_β}, C_{Y_r} and C_{n_r} (quantifying *natural yaw damping*) as given in [1]. Classically, the directional neutral point NP_D is shown to be located on the vertical fin [1]. It was assumed earlier, that for a small rudder deflection, the resulting lateral force perturbation arises from the lift change associated with the vertical fin only. With this assumption in place, the derivative $C_{n_{\delta_R}}$ is also found to be dependant on the moment arm length l_F.

If it is assumed that the aircraft centre of mass can be placed in the two positions as shown in figure 3.5, denoted by P_1 and P_2 respectively, the moment arm length l_F can be shown to be,

$$l_F^1(\Delta c_1, \Delta c_4) = \Delta c_1 + \Delta c_4 \tag{3.2.3}$$

$$l_F^2(\Delta c_1, \Delta c_2) = \Delta c_1 + \Delta c_2 \tag{3.2.4}$$

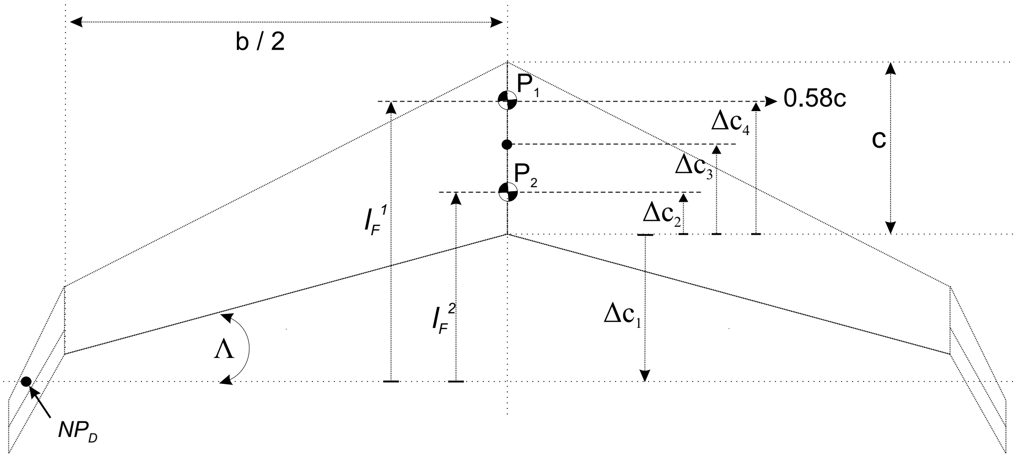

Figure 3.5: Variable Centre of Mass Effect on Lateral Moment Arm l_F

where l_F^1 is the distance from P_1 to NP_D, and l_F^2 is the distance from P_2 to NP_D. Taking position P_1 as a fixed reference point, with Δc_4 (measured from the trailing edge of the main wing chord as indicated by figure 3.5) expressed as a fraction of the chord length c such that $\Delta c_4 = 0.58c$, equations (3.2.3) and (3.2.4) can be used to determine the percentage variation of the lateral moment arm l_F as a function of centre of mass position,

$$l_F^{\%}(\Delta c_1, \Delta c_2, \Delta c_4) \quad = \quad \frac{l_F^1(\Delta c_1, \Delta c_4) - l_F^2(\Delta c_1, \Delta c_2)}{l_F^1(\Delta c_1, \Delta c_4)} \times 100 \quad [\%] \tag{3.2.5}$$

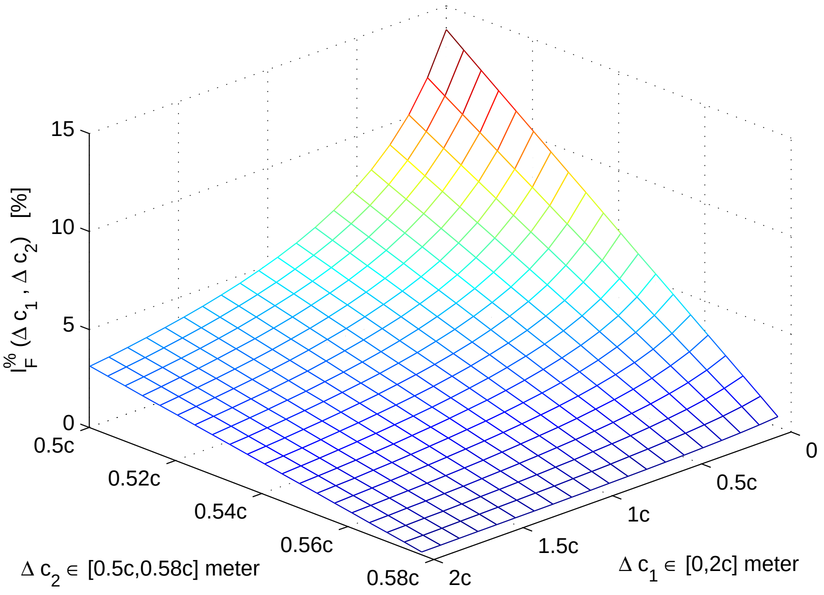

Figure 3.6: Percentage Change of Lateral Moment Arm l_F Due to Variations in Aircraft Centre of Mass Position

With reference to figure 3.6, equation (3.2.5) is evaluated for $\Delta c_2 \in [0.5c, 0.58c]$, resulting in a centre of mass position change of 8% of the aircraft chord length c. Varying the aircraft centre of mass position 8% of the chord length is more than what is required to take the aircraft from a well controllable, statically stable condition to a severely statically unstable condition. This significant range of centre of mass variation is deliberately used in the analysis to investigate possible variations of l_F for a fairly large range of centre of mass positions.

Furthermore, note that Δc_1 is evaluated for $\Delta c_1 \in [0, 2c]$. The distance Δc_1 is a lumped parameter, quantifying both the angle Λ and the wing-span b. The relationship between Δc_1, Λ and b is given by,

$$\Delta c_1 = \frac{b \tan \Lambda}{2} \tag{3.2.6}$$

Figure 3.6 clearly shows that the percentage variation in l_F is less than 10% for values of $\Delta c_1 > 0.2c$, when the centre of mass position is varied 8% of the chord length. Therefore, the percentage variation in l_F is proven to be negligibly small for the centre of mass position range investigated. This implies that the lateral stability and control derivatives dependent on the moment arm l_F can be *assumed* to remain acceptably constant for control design purposes, if the centre of mass is moved less than 8% of the chord length, with the constraint $\Delta c_1 > 0.2c$.

3.2.6.2 Variation of the Longitudinal Moment Arm l_T with Aircraft Centre of Mass Position

As previously mentioned, the moment arm length between the virtual horizontal tailplane and centre of mass, denoted by l_T, is used to model C_{L_q} and C_{m_q} (quantifying *natural pitch damping*). It was assumed earlier, for small elevator deflections, that the resulting normal force perturbations arise from the lift change associated with the *virtual tailplane* only. With this assumption in place, the derivative $C_{m_{\delta_E}}$ is also found to be linearly dependant on the moment arm length l_T.

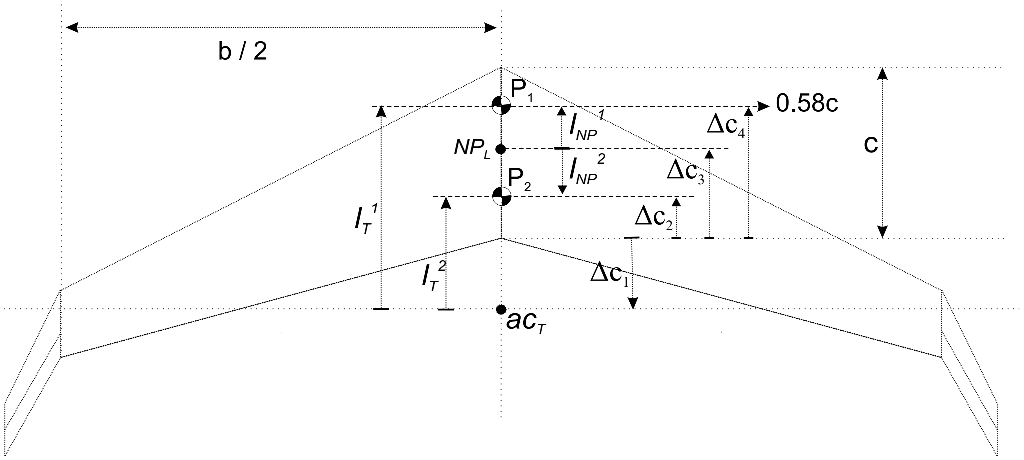

Figure 3.7: Variable Centre of Mass Effect on Longitudinal Moment Arms l_T and l_{NP}

If it is assumed that the aircraft centre of mass can be placed in the two positions as shown in figure 3.7, denoted by P_1 and P_2 respectively, the moment arm length l_T can be shown to be,

$$l_T^1(\Delta c_1, \Delta c_4) = \Delta c_1 + \Delta c_4 \tag{3.2.7}$$

$$l_T^2(\Delta c_1, \Delta c_2) = \Delta c_1 + \Delta c_2 \tag{3.2.8}$$

where l_T^1 is the distance from P_1 to ac_T, and l_T^2 is the distance from P_2 to ac_T. Taking position P_1 as a fixed reference point, with Δc_4 expressed as a fraction of the chord length c such that $\Delta c_4 = 0.58c$, equations (3.2.7) and (3.2.8) can be used to determine the percentage variation of the longitudinal moment arm l_T as a function of centre of mass position,

$$l_T^{\%}(\Delta c_1, \Delta c_2, \Delta c_4) = \frac{l_T^1(\Delta c_1, \Delta c_4) - l_T^2(\Delta c_1, \Delta c_2)}{l_T^1(\Delta c_1, \Delta c_4)} \times 100 \quad [\%] \tag{3.2.9}$$

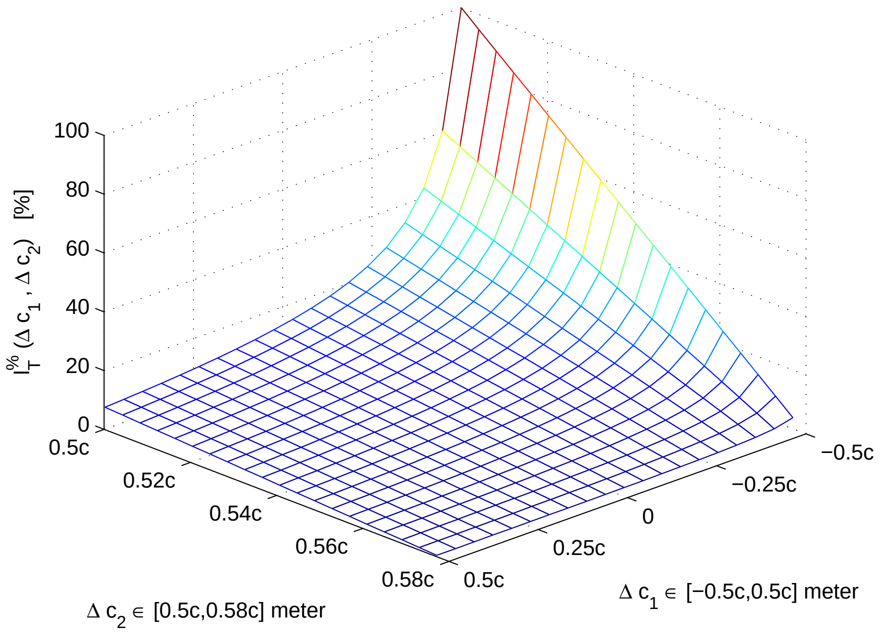

Figure 3.8: Percentage Change of Longitudinal Moment Arm l_T Due to Variations in Aircraft Centre of Mass Position

With reference to figure 3.8, equation (3.2.9) is evaluated for $\Delta c_2 \in [0.5c, 0.58c]$, resulting in a centre of mass position change of 8% of the aircraft chord length c. As previously mentioned, this significant range of centre of mass variation is deliberately used in the analysis to investigate possible variations of l_T for a fairly large range of centre of mass positions.

Furthermore, note that Δc_1 is evaluated for $\Delta c_1 \in [-0.5c, 0.5c]$. The distance Δc_1 quantifies the distance the aerodynamic centre of the virtual tailplane ($ac_{_T}$) is aft of the trailing edge of the main wing chord. However, it is quite possible for $ac_{_T}$ to lie in front of the trailing edge of the main wing chord as well, therefore Δc_1 is evaluated for negative values up to 0.5c, which places $ac_{_T}$ a distance of 50% of the chord length in *front* of the *trailing edge* of the main wing chord.

Figure 3.8 clearly shows that the percentage variation in l_T is less than 20% when $ac_{_T}$ is assumed to be aft of the trailing edge of the main wing chord, and more than 30% when it is assumed that $ac_{_T}$ is more than 35% in front of the trailing edge of the main wing chord. Since it is difficult to accurately determine the exact location of $ac_{_T}$ for a blended-wing-body aircraft from first principles, it cannot be safely assumed that $ac_{_T}$ lies aft of the trailing edge of the main wing chord. Therefore, derivatives modelled using l_T must be assumed to vary with centre of mass position, and taken into account during the design of the longitudinal flight control system.

3.2.6.3 Variation of the Longitudinal Moment Arm $l_{_{NP}}$ with Aircraft Centre of Mass Position

The only derivative left in table 3.1 that needs to be analysed is C_{m_α}. As mentioned earlier, this derivative is dependent on the moment arm length $l_{_{NP}}$. With reference to figure 3.7, the longitudinal moment arm length $l_{_{NP}}$ can be shown to be,

$$\begin{aligned} l^1_{_{NP}}(\Delta c_3, \Delta c_4) &= \Delta c_4 - \Delta c_3 & (3.2.10)\\ l^2_{_{NP}}(\Delta c_2, \Delta c_3) &= -(\Delta c_3 - \Delta c_2) & (3.2.11) \end{aligned}$$

where $l^1_{_{NP}}$ is the distance from P_1 to NP_L, and $l^2_{_{NP}}$ is the distance from P_2 to NP_L. Position P_1 is taken as a fixed reference point as previously stated, and the centre of mass position is again varied a total of 8% of the chord length. Equations (3.2.10) and (3.2.11) are used to determine the percentage variation of the longitudinal moment arm $l_{_{NP}}$ as a function of the centre of mass and neutral point position,

$$l^{\%}_{_{NP}}(\Delta c_2, \Delta c_3, \Delta c_4) = \frac{l^1_{_{NP}}(\Delta c_3, \Delta c_4) - l^2_{_{NP}}(\Delta c_2, \Delta c_3)}{l^1_{_{NP}}(\Delta c_3, \Delta c_4)} \times 100 \quad [\%] \qquad (3.2.12)$$

With reference to figure 3.9, the neutral point is assumed to be in the range $\Delta c_3 \in [0.54c, 0.56c]$ to investigate the variation in the longitudinal moment arm length for various possible neutral point positions. The results show that the longitudinal moment arm $l_{_{NP}}$ changes between 200% and 400% if the aircraft centre of mass is moved 8% of the chord length. Figure 3.9 suggest that C_{m_α}, dependent on the moment arm length to the

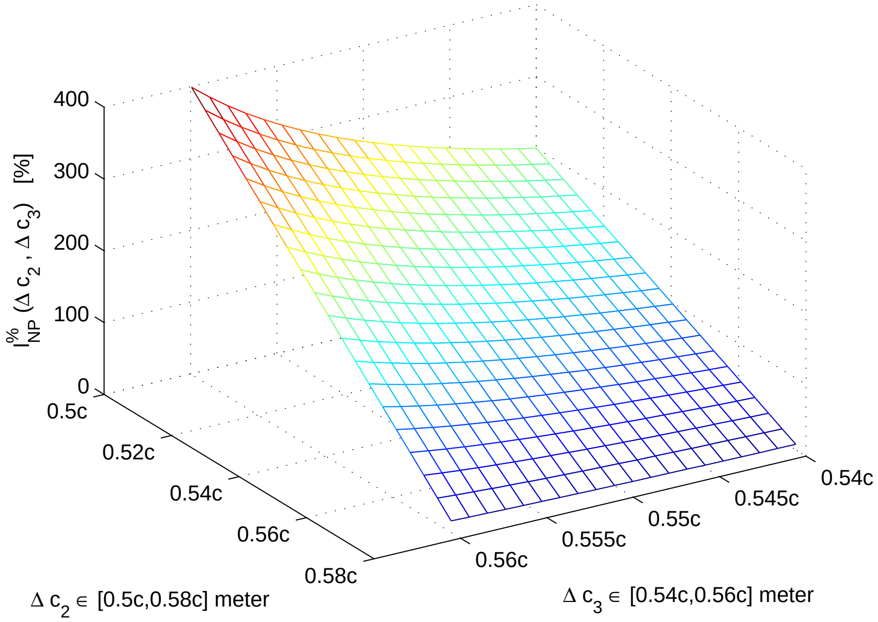

Figure 3.9: Percentage Change of Longitudinal Moment Arm Due to Variations in Aircraft Centre of Mass Position

longitudinal neutral point NP_L, is greatly affected when the centre of mass is varied even as little as 1% of the chord length.

3.2.6.4 Summary

Table 3.1 can now be considerably simplified due to the previously stated arguments with respect to the moment arm lengths l_{NP}, l_T and l_F. The result is given in table 3.2.

Linearly dependent	**Quadratically dependent**
C_{m_α}	C_{m_q}
C_{L_q}	
$C_{m_{\delta_E}}$	

Table 3.2: Simplified dependency of stability and control derivatives on centre of mass position

Using AVL, a vortex lattice simulation and modelling software package, the following section continues to verify the arguments presented thus far by presenting the percentage variation in stability and control derivatives, as a function of the aircraft centre of mass position.

3.3 AVL Simulation Results

As previously mentioned AVL, a software package using vortex-lattice modelling methods, is used to model the aircraft and calculate the stability and control derivatives for various centre of mass positions as outlined in appendix C. Figures 3.10 to 3.13 shows how the stability and control derivatives, discussed in section 3.2, vary as the aircraft centre of mass position is changed linearly from a statically stable position to a statically unstable position. With reference to figures 3.10 to 3.13, 0% centre of mass variation is when the aircraft is statically stable, and 100% centre of mass variation is when the centre of mass is in the aft, statically unstable position. All of the data presented in this section is based on the Sekwa aircraft.

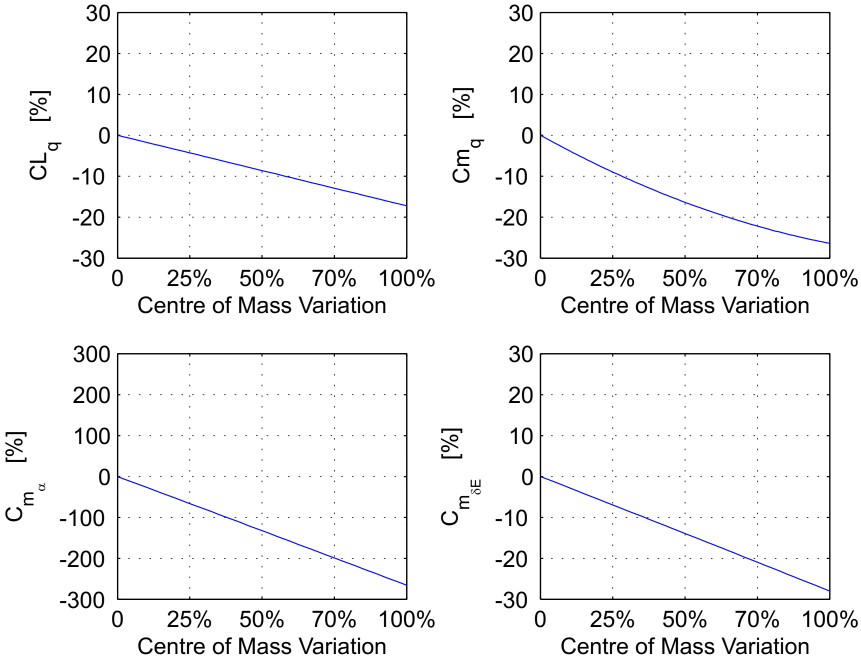

Figure 3.10: Percentage Change of C_{L_q},C_{m_q},C_{m_α},$C_{m_{\delta_E}}$ with centre of mass position

With reference to figure 3.10, the derivatives C_{L_q}, C_{m_α} and $C_{m_{\delta_E}}$ all vary linearly with centre of mass position, and C_{m_q} shows a quadratic change over the centre of mass position range investigated. The simulation data therefore confirms the results listed in table 3.2. Furthermore, $C_{m_{\delta_E}}$ and C_{m_q}, dependent on the moment arm length l_T, shows roughly a 25% change over the centre of mass range investigated, implying that the aerodynamic centre of the *virtual* horizontal tailplane must lie in front of the trailing edge of the main wing chord (see section 3.2.6.2).

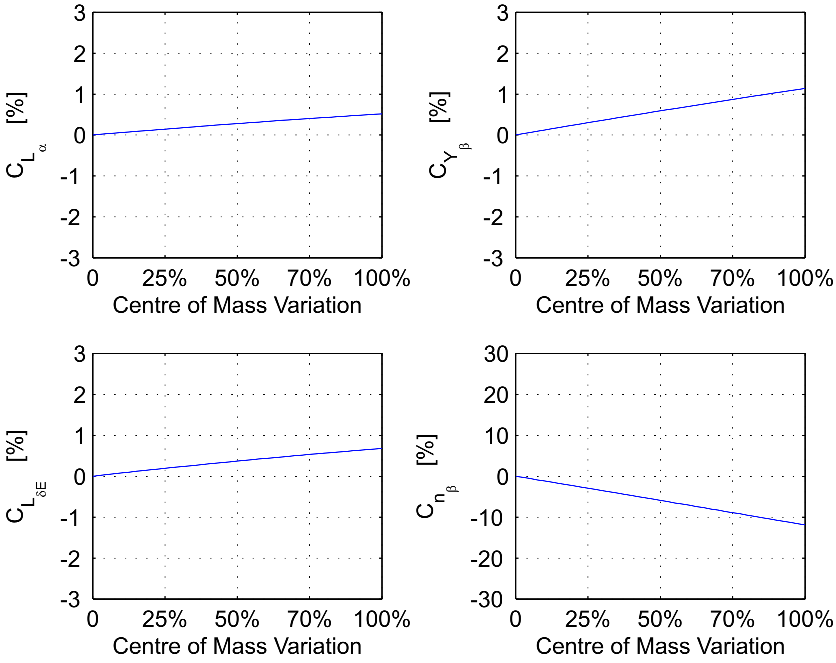

Figure 3.11: Percentage Change of C_{L_α},C_{Y_β},$C_{L_{\delta_E}}$,C_{n_β} with centre of mass position

Figure 3.11 confirms the arguments presented in section 3.2 with modelling data showing that C_{L_α}, C_{Y_β} and $C_{L_{\delta_E}}$ essentially remain invariant to variations in aircraft centre of mass position. Furthermore, C_{n_β} exhibits approximately a 10% change over the centre of mass position range investigated, and is therefore assumed to remain constant with centre of mass variations for *control design* purposes.

With reference to figure 3.12, the derivatives $C_{Y_{\delta_R}}$, $C_{l_{\delta_R}}$ and $C_{l_{\delta_A}}$ all essentially remain constant with centre of mass variations since they change less than 4% over the centre of mass range investigated, confirming the arguments presented in section 3.2. The derivative $C_{Y_{\delta_A}}$ however shows a less than 15% change, and consequently is *assumed* to remain constant with variations in aircraft centre of mass position for control design purposes.

The modelling data presented by figure 3.13 proves to be in accord with the arguments presented in section 3.2, since $C_{n_{\delta_R}}$, C_{Y_r}, C_{l_p} and C_{l_r} all vary less than 10% with centre of mass position, and therefore are assumed to remain constant with centre of mass variations.

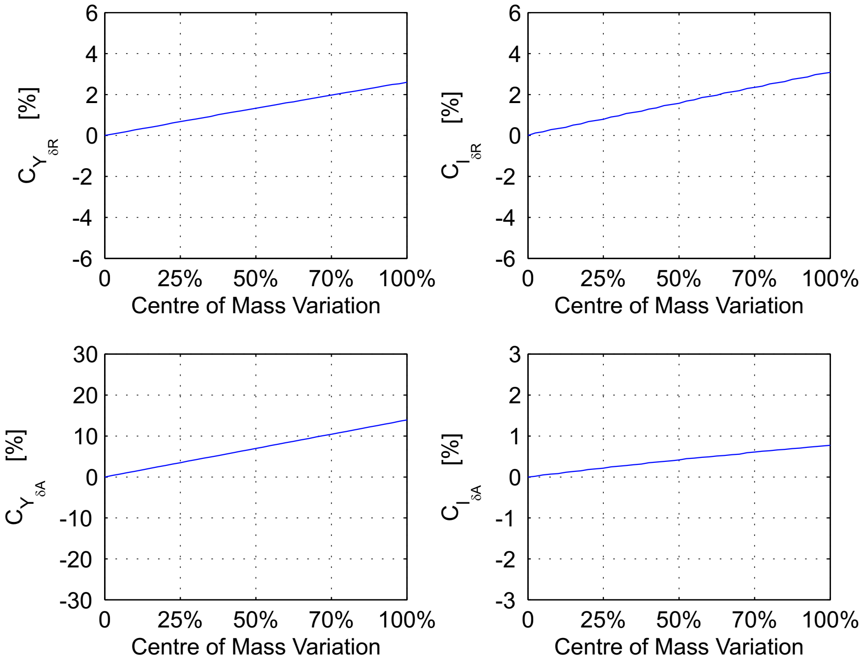

Figure 3.12: Percentage Change of $C_{Y_{\delta_R}}$,$C_{l_{\delta_R}}$,$C_{Y_{\delta_A}}$,$C_{l_{\delta_A}}$ with centre of mass position

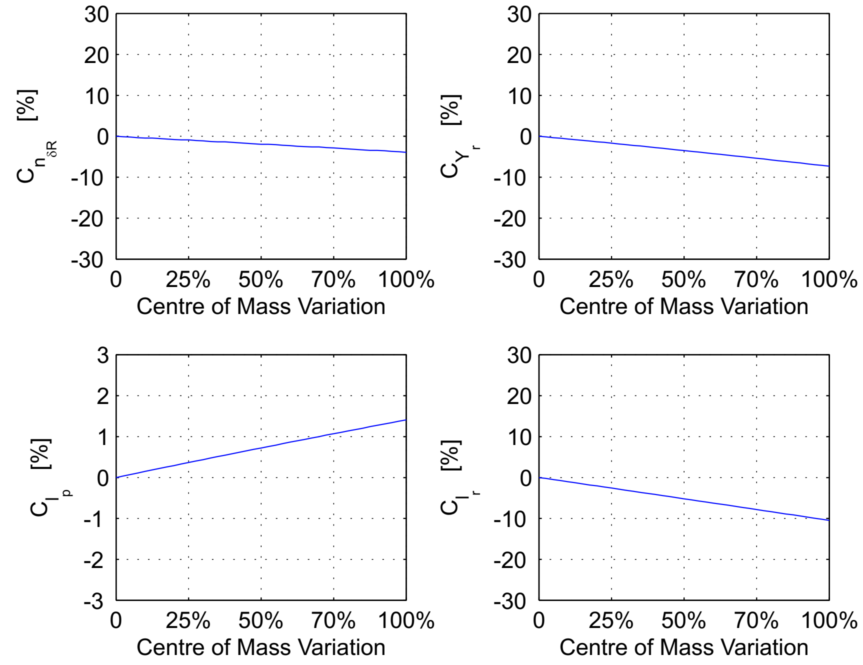

Figure 3.13: Percentage Change of $C_{n_{\delta_R}}$,C_{Y_r},C_{l_p},C_{l_r} with centre of mass position

3.3.1 AVL Modelling Limitations

Like any computational method, AVL has limitations on what it can do. Induced drag is extremely difficult to accurately simulate in AVL [11], especially when the induced drag is dependent on incidence angles, and therefore derivatives dominated by drag carries a high amount of uncertainty. This explains the counter-intuitive nature of the derivatives $C_{n_{\delta_A}}$ (quantifying adverse yaw), C_{n_p} and C_{n_r} shown by figure 3.14.

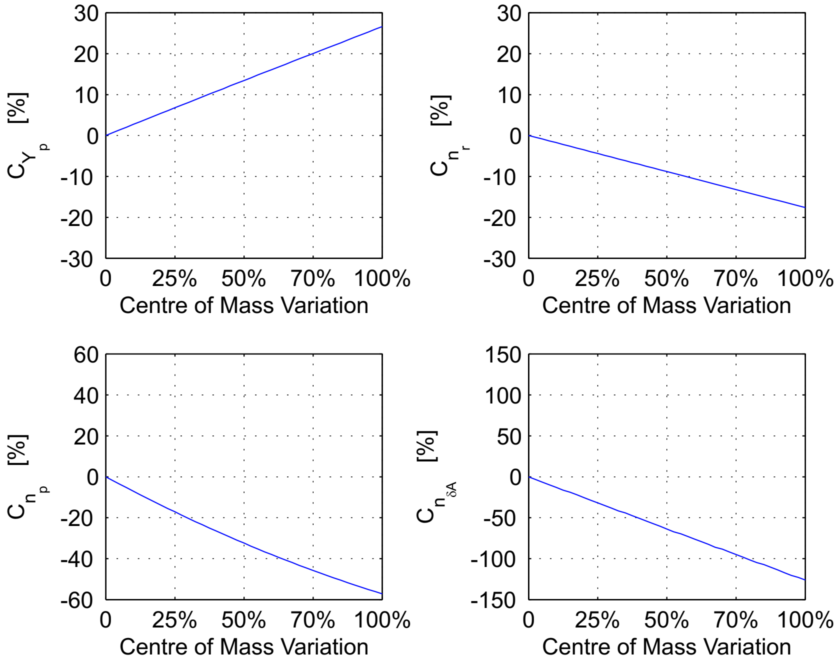

Figure 3.14: Percentage Change of C_{Y_p},C_{n_r},C_{n_p},$C_{n_{\delta_A}}$ with centre of mass position

Furthermore, derivatives that are numerically very small and classically difficult to estimate may exhibit numerical errors that produce counter-intuitive results to the arguments presented in section 3.2. This explains the apparent significant variation in the derivatives $C_{Y_{\delta_A}}$ and C_{Y_p} with aircraft centre of mass position.

Values with higher certainty with respect to drag dependent derivatives can be obtained through more accurate modelling methods, or the values can be adjusted after practical flight test data is obtained. However, because these derivatives are numerically very small and classically don't have a significant effect on aircraft dynamics, they are assumed constant for *control design* purposes. The change of these derivatives with centre of mass position however is taken into account in the simulation environment (see chapter 7).

3.3.2 The aerodynamic damping moment arm length l_D

Recall that the moment arm l_T was assumed to be equal to the damping moment arm l_D for the aircraft used in this thesis (i.e. $l_D \approx l_T$). This assumption was given by equation (3.2.1). Theoretically these moment arms can be expressed as [15],

$$l_T = -\bar{c}\frac{C_{m_{\delta_E}}}{C_{L_{\delta_E}}} \tag{3.3.1}$$

$$l_D = -\bar{c}\frac{C_{m_q}}{C_{L_q}} \tag{3.3.2}$$

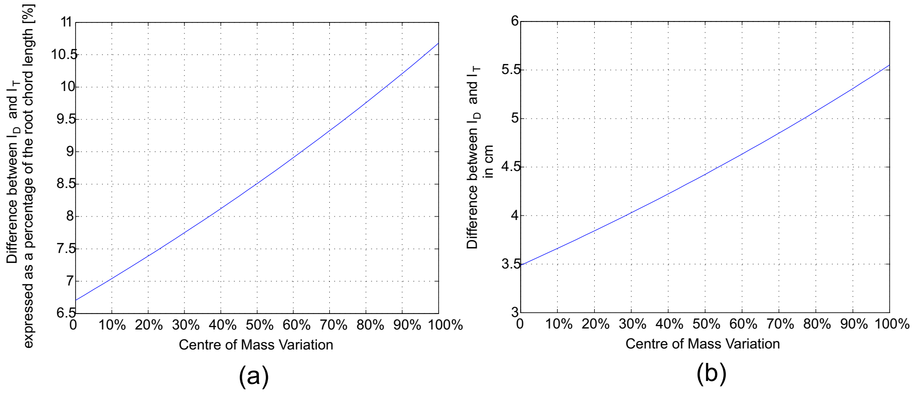

Figure 3.15: (a) Percentage difference between l_D and l_T expressed as a percentage of the chord length c. (b) Difference in length between l_D and l_T expressed in cm

With reference to figure 3.15 (b), when evaluating the above equations for the blended-wing-body aircraft used in this project, the difference between the lengths l_T and l_D is revealed to be between 3.5 cm and 5.5 cm. When expressed as a percentage of the root chord length c (figure 3.15 (a)), this translates into roughly a 7% to 10.5% difference. Therefore, it can be assumed that $l_D \approx l_T$, thereby verifying the assumption stated by equation (3.2.1).

3.3.3 Classic Aerodynamic Stability Conditions

The conditions for static directional stability (equation (3.3.3)) and static longitudinal stability (equation (3.3.4)) [1] are classically expressed as,

$$C_{n_\beta} > 0 \tag{3.3.3}$$

$$C_{m_\alpha} < 0 \tag{3.3.4}$$

With reference to figure 3.16, the above static stability condition for the lateral dynamics hold for the entire centre of mass position range, therefore the aircraft will remain statically stable in the lateral sense at all times. However, when the centre of mass moves aft of the longitudinal neutral point, the longitudinal static stability condition is violated (i.e. $C_{m_\alpha} > 0$) and the aircraft becomes statically *unstable* in the longitudinal sense.

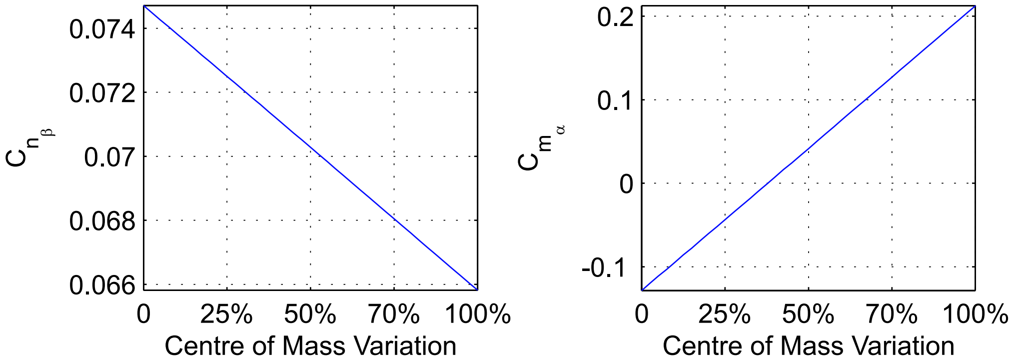

Figure 3.16: Linear Variation of C_{m_α} and C_{n_β} with centre of mass position

This is in accord with the arguments presented in section 3.1.2, since a *negative* C_{m_α} implies that a stabilising moment is created during a perturbation in angle of attack, while the converse is true for a *positive* C_{m_α}.

3.4 Summary

The arguments provided by section 3.2 with the results given in section 3.3 suggest that the stability and control derivatives most *prominent* in the lateral dynamics can be confidently assumed to remain invariant with centre of mass variations for *control design* purposes. It is also shown that the lateral stability of the aircraft remains acceptably constant, while the longitudinal stability varies dramatically with centre of mass position. Hence, the lateral control problem of the variable stability aircraft becomes that of a conventional aircraft. Therefore, conventional lateral flight control systems are designed, the details of which are discussed in depth in appendix A so as not to distract from the main problem at hand, i.e. the longitudinal variable stability problem. Furthermore, all of the stability and control derivatives are included as either linear or quadratic functions of centre of mass position (as stated in section 3.2) in the simulation environment outlined in chapter 7. The reason for this is to verify that a conventional lateral flight control system can in fact be designed under these assumptions, and still perform adequately when applied to the complete lateral dynamics of the variable stability aircraft. The lateral control strategy is only briefly outlined in section 5.4, and the full design is provided in appendix A.

The following section re-states some of the key results regarding the longitudinal stability and control derivatives discussed in this chapter, and motivates why the majority of this project is dedicated to analysis and control of the longitudinal aircraft dynamics with emphasis on longitudinal stability.

3.4.1 Fundamental Control Problem Identification

The arguments provided by section 3.2 illustrated that the stability and control derivatives most *prominent* in the longitudinal aircraft dynamics vary dramatically with centre of mass position. Section 3.3 showed that the aircraft's degree of longitudinal static stability also depends significantly on the aircraft centre of mass position relative to the neutral point position.

Furthermore, section 3.3 indicated that the aircraft becomes statically unstable (figure 3.16) at centre of mass positions aft of the neutral point due to the positive value of the C_{m_α} stability derivative. Following a perturbation in incidence angle α, a positive value of C_{m_α} implies that a destabilising moment acts about the aircraft centre of mass position, rendering the vehicle almost impossible to control manually. As the centre of mass continues to move aft of the neutral point, the value of C_{m_α} increases, and consequently the vehicle suffers severe longitudinal divergence from the trim flight equilibrium condition following even the slightest disturbance in pitch attitude.

At each new centre of mass position, the airframe can be considered a completely different vehicle with unique stability characteristics and dynamic response, posing both an interesting and challenging control problem. Therefore, chapter 4 is dedicated to a thorough analysis of the *longitudinal* aircraft dynamics, with emphasis on longitudinal stability. After the effect of varying the centre of mass on the longitudinal dynamics is analysed, the control architecture responsible for regaining static stability at all centre of mass locations is developed.

Chapter 4

Longitudinal Analysis and Control

The arguments presented in chapter 3 concluded that the longitudinal stability and control derivatives presented in chapter 2 vary dramatically with centre of mass position, whereas the lateral derivatives can be confidently assumed to remain almost constant. As previously mentioned, the variable stability aircraft problem therefore presents itself primarily in the longitudinal dynamics presented in chapter 2. The aim of this chapter is to consider the longitudinal dynamics under the variable centre of mass condition to gain further insight into the problem (section 4.1). This will allow for an elegant control solution to be formulated in order to regain static stability at all centre of mass positions (section 4.4). Once the aircraft is stabilised, chapter 5 continues with the design of further outer-loop flight control systems allowing for full autonomous flight, and presents the design of a control system capable of adjusting the aircraft's static stability margin in flight in order to meet the project design goals.

4.1 Isolating the Variable Stability Aircraft Problem

This section is aimed at analysing the longitudinal aircraft dynamics in order to gain deeper insight into the variable stability aircraft problem. A prerequisite to the analysis however is that the longitudinal dynamics be formally stated in a linear form. As mentioned in chapter 2, the aircraft dynamics can be decoupled into longitudinal and lateral dynamics. When analysing the longitudinal dynamics exclusively, the lateral forces, moments, angles and angular velocities are set to zero. Equations (2.2.8), (2.2.24), (2.2.25), (2.2.27), (2.2.29) and (2.2.30) are then used to create the non-linear, decoupled longitudinal dynamic equations of motion. These non-linear differential equations of the following form,

$$\dot{\mathbf{x}} = f(\mathbf{x}, \mathbf{u}) \tag{4.1.1}$$

$$\mathbf{y} = h(\mathbf{x}) \tag{4.1.2}$$

are linearised about the trim equilibrium condition by calculating the respective *Jacobian* matrices and evaluating them at the trim condition (denoted by $\mathbf{x}_0$ and $\mathbf{u}_0$),

$$\mathbf{F}^{'} = \left[\frac{\partial f(\mathbf{x},\mathbf{u})}{\partial \mathbf{x}}\right]_{\mathbf{x}_0,\mathbf{u}_0} \tag{4.1.3}$$

$$\mathbf{G}^{'} = \left[\frac{\partial f(\mathbf{x},\mathbf{u})}{\partial \mathbf{x}}\right]_{\mathbf{x}_0,\mathbf{u}_0} \tag{4.1.4}$$

$$\mathbf{H}^{'} = \left[\frac{\partial h(\mathbf{x})}{\partial \mathbf{x}}\right]_{\mathbf{x}_0,\mathbf{u}_0} \tag{4.1.5}$$

$$\mathbf{J}^{'} = \left[\frac{\partial h(\mathbf{x})}{\partial \mathbf{x}}\right]_{\mathbf{x}_0,\mathbf{u}_0} \tag{4.1.6}$$

resulting in a linearised, multi-variable state space representation of the form,

$$\dot{\mathbf{x}}^{'} = \mathbf{F}^{'}\mathbf{x}^{'} + \mathbf{G}^{'}\mathbf{u}^{'} \tag{4.1.7}$$

$$\mathbf{y}^{'} = \mathbf{H}^{'}\mathbf{x}^{'} + \mathbf{J}^{'}\mathbf{u}^{'} \tag{4.1.8}$$

where $\mathbf{F}^{'}$ is the $n \times n$ *state* matrix, $\mathbf{G}^{'}$ is the $n \times m$ *input* matrix, $\mathbf{H}^{'}$ is the $n \times n$ *output* matrix and $\mathbf{J}^{'}$ is often referred to as the *direct* matrix. Assuming that the velocity magnitude of the wind axis system is equal to the aircraft's airspeed, the longitudinal equations linearised about the trim equilibrium condition (straight and level flight) are presented below,

$$\begin{bmatrix} \dot{\alpha}^{'} \\ \dot{q}^{'} \\ \dot{\overline{V}}_W^{'} \\ \dot{\theta}_W^{'} \\ \dot{T}^{'} \end{bmatrix} = \begin{bmatrix} -\frac{\overline{q}SC_{L_\alpha}}{m\overline{V}_{W_0}} & 1-\frac{\overline{q}S\overline{c}C_{L_q}}{2m\overline{V}_{W_0}^2} & -\frac{\overline{q}SC_L}{m\overline{V}_{W_0}^2} - \frac{g}{\overline{V}_{W_0}^2} - \frac{\overline{q}SC_{L_{\overline{V}_{W_0}}}}{m\overline{V}_{W_0}^2} & 0 & 0 \\ \frac{\overline{q}S\overline{c}C_{m_\alpha}}{I_{yy}} & \frac{\overline{q}S\overline{c}^2C_{m_q}}{2I_{yy}\overline{V}_{W_0}} & \frac{\overline{q}S\overline{c}C_{m_{\overline{V}_{W_0}}}}{I_{yy}\overline{V}_{W_0}} & 0 & 0 \\ -\frac{\overline{q}SC_{D_\alpha}}{m} & -\frac{\overline{q}SbC_{D_q}}{2m\overline{V}_{W_0}} & -\frac{\overline{q}SC_{D_{\overline{V}_{W_0}}}}{m\overline{V}_{W_0}} - \frac{2\overline{q}SC_D}{m\overline{V}_{W_0}} & -g & \frac{1}{m} \\ \frac{\overline{q}SC_{L_\alpha}}{m\overline{V}_{W_0}} & \frac{\overline{q}ScC_{L_q}}{2m\overline{V}_{W_0}^2} & \frac{\overline{q}SC_L}{m\overline{V}_{W_0}^2} + \frac{g}{\overline{V}_{W_0}^2} + \frac{\overline{q}SC_{L_{\overline{V}_{W_0}}}}{m\overline{V}_{W_0}^2} & 0 & 0 \\ 0 & 0 & 0 & 0 & -\frac{1}{\tau_c} \end{bmatrix} \begin{bmatrix} \alpha^{'} \\ q^{'} \\ \overline{V}_W^{'} \\ \theta_W^{'} \\ T^{'} \end{bmatrix}$$

$$+ \begin{bmatrix} -\frac{\sin\alpha}{m\overline{V}_{W_0}} & -\frac{\overline{q}SC_{L_{\delta_E}}}{m\overline{V}_{W_0}} \\ 0 & \frac{\overline{q}S\overline{c}C_{m_{\delta_E}}}{I_{yy}} \\ \frac{\cos\alpha}{m} & -\frac{\overline{q}SC_{D_{\delta_E}}}{m} \\ \frac{\sin\alpha}{m\overline{V}_{W_0}} & \frac{\overline{q}SC_{L_{\delta_E}}}{m\overline{V}_{W_0}} \\ \frac{1}{\tau_c} & 0 \end{bmatrix} \begin{bmatrix} T^{'} \\ \delta_E^{'} \end{bmatrix} \tag{4.1.9}$$

where $\left[\begin{array}{ccccc} \alpha' & q' & \overline{V}_W' & \theta_W' & T' \end{array}\right]^T$ is the linearised longitudinal control state vector, and $\overline{V}_{W_0}$ is the trim airspeed. In the above equation m is the total aircraft mass, $\overline{q}$ the dynamic pressure as defined by equation (2.2.31) and the stability and control derivatives are expressed as defined by equation (2.2.36). Writing the longitudinal dynamics in the form given by equation (4.1.9) allows for the calculation of the longitudinal *eigenvalues* describing the longitudinal dynamic response of the aircraft. When excluding the throttle state, equation (4.1.9) describes a fourth-order system, and therefore four distinct eigenvalues can be found, classically forming two complex pole pairs. These complex pole pairs in turn describe the two classically defined longitudinal modes of motion, namely the *Short period* and *Phugoid* modes of motion as mentioned in [2], which are discussed in the section to follow. After this discussion, the primary control problem for the variable stability aircraft will be identified.

4.1.1 Classic Longitudinal Aircraft Modes of Motion

The Phugoid Mode: This mode is commonly a lightly damped, low frequency oscillation in velocity which couples into the flight path angle (θ_W) and altitude. Within the timescale of this mode, incidence (α) remains acceptably constant when this mode is excited. In actual fact, the Phugoid appears to a greater or lesser extend in all of the longitudinal motion variables, but the relative magnitudes of the Phugoid components in α and pitch rate q are negligibly small. For small unmanned aircraft, the undamped natural frequency of this mode is typically in the range of 0.1 rad/s to 1 rad/s according to [1], often with very poor damping. This mode is furthermore often approximated by an undamped harmonic motion in which potential and kinetic energy are exchanged as the aircraft flies a gentle sinusoidal flight path about the nominal trimmed altitude.

The Short Period Mode: This is typically a damped oscillation in pitch about $\boldsymbol{j}^B$. Whenever an aircraft is disturbed from its pitch equilibrium state, this mode is excited and classically manifests itself as a second order oscillation in which the principal variables are incidence (α) and pitch rate (q). Typically, the undamped natural frequency of this mode is in the range 1 rad/s to 12 rad/s, according to [1], and the damping is usually stabilising, although the damping ratio might often be lower than desired. As the period of this mode is short, inertia and momentum effects ensure that changes in velocity magnitude, longitudinal flight path angle (θ_W), altitude and climb rate in the time scale of *this mode* are negligible. The physical effect of this mode can be interpreted by a comparison with a torsional spring-mass-damper system as is often done in classic aircraft literature [1].

With reference to figure 4.1, the aircraft behaves as if it were restrained by a torsional spring about $\boldsymbol{j}^B$. A pitch disturbance from the trim equilibrium condition causes the "spring" to produce a **restoring moment** thereby giving rise to an oscillation in pitch [1].

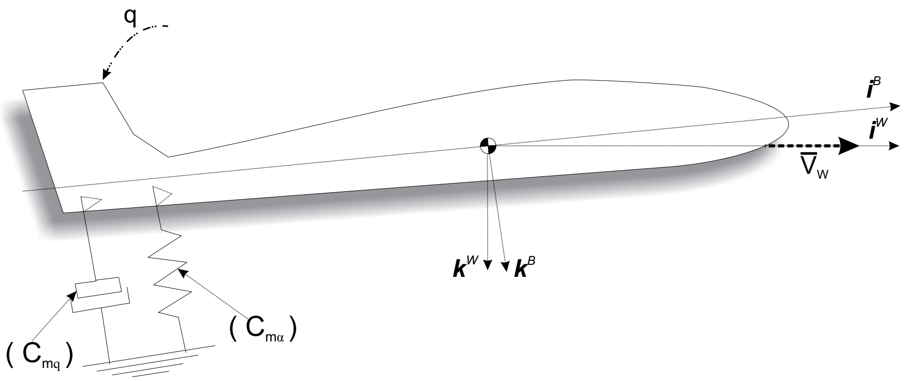

Figure 4.1: Short Period Mode Spring-Mass-Damper Relationship

If the aircraft is statically stable, the oscillation is damped and this can be represented by a viscous damper as suggested in figure 4.1 [1].

4.1.2 Core Control Problem Identification

Section 3.1.2 argued that the dimensionless derivative C_{m_α} classically describes the natural tendency of the aircraft to generate a **restoring moment** following a pitch disturbance, and therefore C_{m_α} quantifies the aircraft "spring" stiffness as discussed in [1]. As mentioned in section 3.2, the derivative C_{m_q} quantifies the aircraft's natural *rate* damping ability, and therefore C_{m_q} represents the conceptual aerodynamic viscous damper [1] of the Short period mode shown in figure 4.1.

The aerodynamic viscous damping coefficient: Chapter 3 (see section 3.2) argued that C_{m_q} is quadratically dependent on l_T, which is the distance between the aircraft centre of mass and the aerodynamic centre of the virtual horizontal tailplane. Recall that, as the centre of mass moves aft, the moment arm length l_T is decreased, consequently decreasing the aerodynamic damping by roughly 25% over the centre of mass position range investigated (see section 3.3). This implies that the blended-wing-body aircraft used in this project always shows some degree of positive damping, albeit a degraded damping response when the centre of mass is shifted aft.

These results are only valid for blended-wing-body aircraft with a swept-back wing configuration as is used in this project. With less sweep back, the aerodynamic damping will be influenced more when shifting the centre of mass aft from its stable position, due to a more significant change in the moment arm length l_T (refer to chapter 3 sections 3.3 and 3.2).

The aerodynamic spring stiffness coefficient: Chapter 3 (section 3.2) argued that C_{m_α} is linearly dependent on l_{NP}, which is the distance between the aircraft centre of mass and the longitudinal neutral point. Recall that, as the centre of mass moves aft, the moment arm length l_{NP} is significantly decreased, consequently decreasing the aerodynamic spring stiffness by roughly 250% over the centre of mass position range investigated (see section 3.3).

An obvious problem is encountered when the spring stiffness is substantially decreased (i.e. centre of mass is close to the neutral point), as a small negative spring coefficient means that little restoring spring force is generated to effectively counter pitch disturbances, consequently failing to *naturally* stabilise the aircraft. It then becomes the responsibility of the human pilot to *artificially* stabilise the vehicle, which ends in catastrophe if the vehicle suffers pitch rate disturbances at frequencies higher than the bandwidth of an average human pilot[1]. This phenomenon can occur even for a slight reduction in the aerodynamic "spring" stiffness, as was observed during one of the practical flight tests (see chapter 8).

Furthermore, when the centre of mass is aft of the neutral point (section 3.3.3), the moment arm length changes sign and the spring effect, quantified by C_{m_α}, is *destabilising* because a positive C_{m_α} is analogous to a mechanical spring with a *positive* spring constant, driving in the *same* direction as the applied disturbance. With the aerodynamic "spring" force essentially amplifying even the slightest disturbance in pitch (which couples into the longitudinal flight path angle θ_W) the aircraft is extremely difficult to control manually by a human pilot at this point.

On the other hand, when the centre of mass is placed a considerable distance in front of the neutral point, a large negative spring stiffness coefficient implies that the aircraft will be very resistant to any upsets. This in turn means that greater actuation[2] is required to encourage the aircraft to change its trim state or to manoeuvre. An obvious consequence of this is that too much stability can be as hazardous as too little stability since typically only a finite amount of actuation is available. The problems caused by excessive stability must therefore be kept in mind when placing the centre of mass position at the initial statically stable location during manual take-off.

The aforementioned arguments suggest that the variation in C_{m_α} is the major contributor towards the problems associated with the variable stability aircraft, as the vehicle becomes difficult if not impossible to control *manually* when the centre of mass is close to or aft of the neutral point. Since the aerodynamic "spring" parameter C_{m_α} is linked to the Short period mode of motion, it is concluded that the variable stability problem manifests itself primarily in the aircraft Short period mode dynamics. Therefore, if the effect of the changing C_{m_α} derivative could be negated through proper feedback control by stabilising the Short period mode, static stability will be regained for all centre of mass positions. This will allow for simple outer-loop controllers to be designed for a statically stable aircraft which remains invariant to variations in centre of mass position, and will

---

[1] Pilot modelling can be found in [2].

[2] The amount a control surface is deflected

also allow for a human pilot to control the aircraft even when the centre of mass is in the most aft position. The following section (section 4.2) continues with an analysis of the aircraft longitudinal eigenvalues using equation (4.1.9), to provide additional insight into the effect of the variable centre of mass on the aircraft longitudinal dynamic response.

4.2 Impact of Centre of Mass Variations on Longitudinal Dynamics

The following analysis is based on Sekwa modelling data. For the specific stability and control derivative data, refer to appendix C.

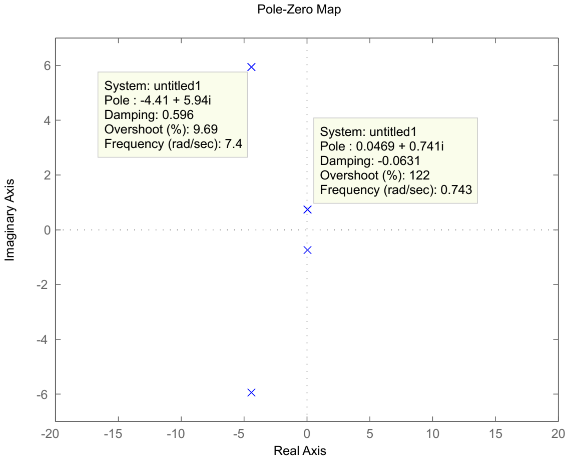

Figure 4.2: Longitudinal Dynamics Pole Plot when the Aircraft is Statically Stable

Figure 4.2 shows the open-loop longitudinal poles of equation (4.1.9), when the aircraft is statically stable, i.e. the centre of mass is placed in front of the neutral point and $C_{m_\alpha} < 0$. As expected, four poles are seen, forming two sets of complex pole pairs. The low frequency complex pole pair (0.743 rad/s) indicates a very slow damped sinusoidal oscillation, and is consequently classically identified as the Phugoid mode of motion. As mentioned earlier, the Phugoid mode is often poorly damped, which is the case for most aircraft. Note however that a highly damped Phugoid mode increases drag, and because Sekwa was especially designed to reduce drag the Phugoid mode will be damped less than that of a conventional aircraft. The higher frequency complex pole pair (7.4 rad/s) indicates a higher frequency damped oscillatory response, and is therefore classically identified as the Short period mode of motion.

Figure 4.3 (a) shows *all* of the Short period and Phugoid mode poles when the centre of mass is moved 15% aft of the total range investigated, in increments of 7% of the total chord length. Seven distinctive pole locations are shown by figure 4.3 (a) each related to a

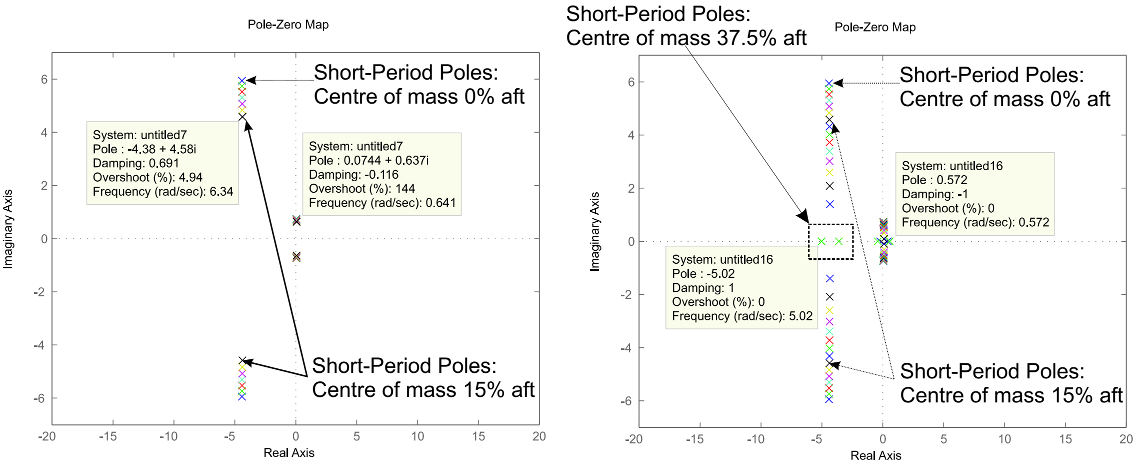

(a) (b)

Figure 4.3: (a) Pole Plot with Centre of mass 0% to 15% aft of stable position. (b) Pole Plot with Centre of mass 0% to 37.5% aft of stable position.

specific centre of mass position. The percentage change in the Phugoid and Short period mode frequencies with centre of mass position is 14.32% and 13.73% respectively. Note that both modes exhibits relatively the same change in frequency, and that the Phugoid mode is still well controllable manually with a frequency of 0.641 rad/s, and the Short period mode poles indicate that the aircraft remains acceptably statically stable.

With reference to figure 4.3 (b), if the centre of mass is moved aft 37.5% of the total range investigated, the centre of mass is slightly aft of the AVL predicted neutral point. At this point, the Short period mode poles change from a complex pole pair to a real pole pair, and the Phugoid mode becomes an unstable "saddle point", i.e. two real poles, one stable, the other unstable. Note that one real pole is unstable with a frequency of 0.572 rad/s, and therefore the aircraft becomes difficult to control at this point. Furthermore, due to the absence of second order complex pole pairs, figure 4.3 (b) indicates that there is no clear distinction between the classically defined, second order Short period and Phugoid modes of motion anymore for centre of mass positions beyond this point.

Figure 4.4 (a) shows the longitudinal poles when the aircraft centre of mass is moved aft 45% of the total centre of mass range investigated. With the centre of mass 45% aft of the most forward position, a complex pole pair once again forms. This complex pole pair is low in frequency, and one might argue that this complex pole pair describes the Phugoid mode, according to the definition of the Phugoid mode stated earlier. Without analysing the eigenvectors, for centre of mass positions at and beyond this point, it becomes extremely difficult if not impossible to intuitively relate a given pole position back to a motion variable (e.g. $\overline{V}_W$, θ_W , α , q), and therefore it is not clear whether or not this complex pole pair is quantifying the Phugoid mode. Figure 4.4 (b) shows only one set of longitudinal poles when the aircraft centre of mass is 100% aft of the stable position (i.e.

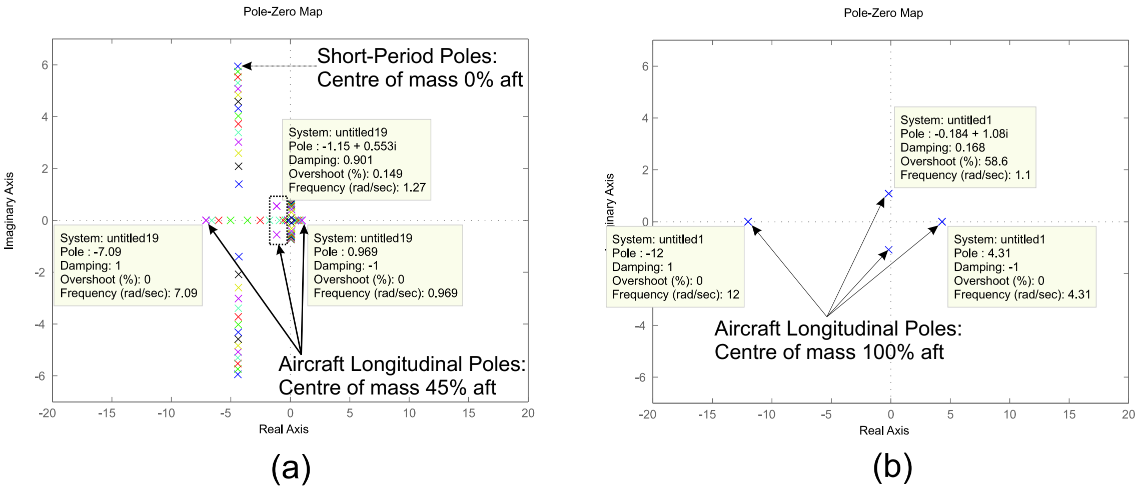

Figure 4.4: (a) Pole Plot with Centre of mass 0% to 45% aft of stable position. (b) Pole Plot with Centre of mass 100% aft of stable position.

at the aft limit) to avoid clutter. This shows that a 4.31 rad/s unstable pole dominates the longitudinal aircraft response at this centre of mass location.

To intuitively understand the physical phenomenon pertaining to the variable stability aircraft problem, it is clear from the previous results that a pure open-loop eigenvalue analysis obscures the underlying mechanisms involved. With the eigenvalue analysis, no true insight into the longitudinal modes of motion can be gained when the centre of mass is moved close to or aft of the AVL predicted neutral point, as the classic definitions concerning both the Short period and Phugoid modes of motion are no longer valid at these centre of mass locations. Therefore, to intuitively visualise the physical interaction between the aircraft variable centre of mass position and associated stability characteristics, the spring-mass-damper analogy presented in section 4.1.2 is used throughout the remainder of this thesis.

A very interesting result is given by figure 4.5, when the aerodynamic "spring" parameter C_{m_α} is kept *constant* in equation (4.1.9), while all of the other derivatives vary with centre of mass position over the range investigated. It is observed that the aircraft remains acceptably statically stable, implying that the change in the aerodynamic "spring" parameter C_{m_α} is the *main* factor influencing the dramatic change in the longitudinal dynamic response given by figures 4.3 to 4.4.

According to the results summarised in table 3.2 (see chapter 3, section 3.2), the aerodynamic "viscous damping" parameter C_{m_q} along with C_{L_q} and $C_{m_{\delta_E}}$ were found to vary with centre of mass variations. However, because of the relatively small percentage variation in the moment arm l_T used to model these derivatives, C_{m_q} along with C_{L_q} and $C_{m_{\delta_E}}$ were shown to vary less than 30% over the entire centre of mass range investigated. This in turn explains the result given by figure 4.5.

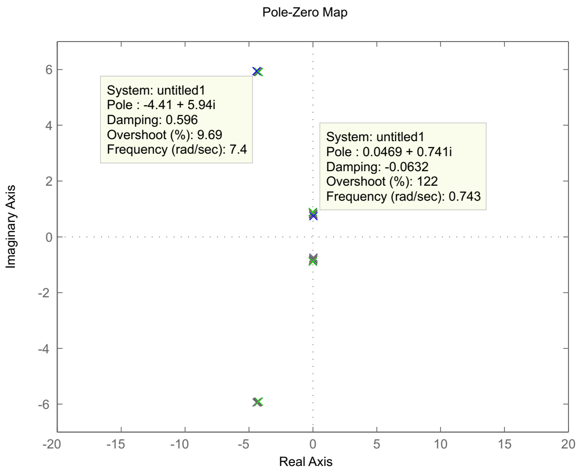

Figure 4.5: Pole Plot with Centre of mass 0% to 100% aft of stable position, with C_{m_α} kept constant

The previous results are in accord with the intuitive arguments presented in section 4.1.2, arguing that the variable stability aircraft problem manifests itself primarily in the Short period mode of motion, and more specifically in the aerodynamic "spring" parameter C_{m_α}. The following section continues with the design of a stability augmentation control strategy, which negates the effect of the changing aerodynamic spring coefficient on the aircraft's longitudinal dynamics through the application of feedback control.

4.3 Stability Augmentation Design Strategy

As previously mentioned, this section aims to develop a flight control strategy that remains invariant to centre of mass position changes, to effectively and elegantly regain static stability for all centre of mass positions in the range investigated. Since the variable stability aircraft problem was found to reside in the Short period mode dynamics, these dynamics must be *isolated* from the rest of the aircraft dynamics to allow for an effective control strategy to be formulated. This task is accomplished in the next section.

4.3.1 Conceptual Arguments

The aircraft model presented in chapter 2 was originally derived by [15] to allow for the design of a full 3D flight aerobatic manoeuvre autopilot using acceleration based inner-loop controllers. Figure 4.6 shows the decoupled longitudinal aircraft model initially developed by [15], with the rigid body rotational dynamics, as discussed in chapter 2, separated at an acceleration level from the point mass kinematics. With reference to figure 4.6, a_a, a_n and cg_p denotes the axial specific acceleration, normal specific acceleration and centre of mass position respectively. The term C_{λ_ϵ} denotes the non-dimensional stability and control derivatives, as defined in section 2.2.3, changing as a function of the centre of mass position (cg_p).

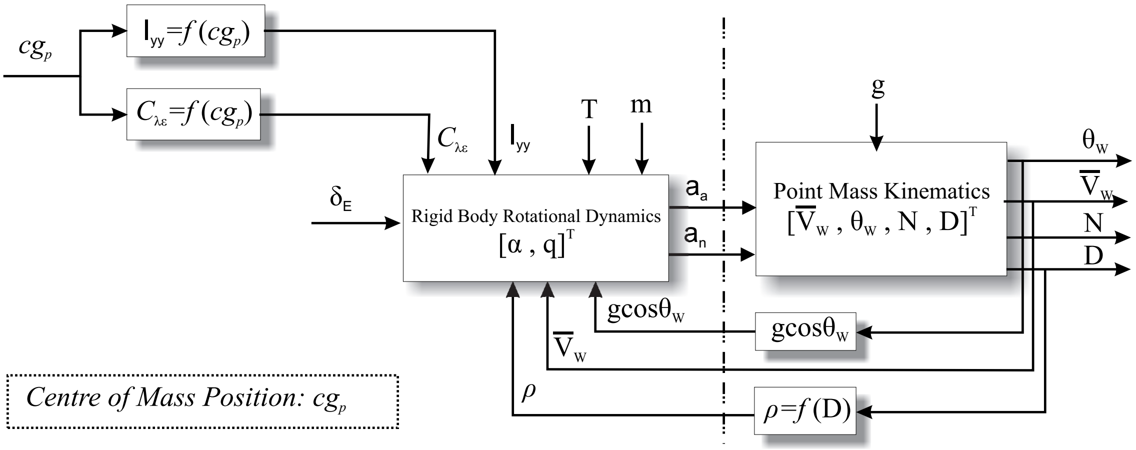

Figure 4.6: Split between the Rigid Body Rotational Dynamics and Point Mass Kinematics

Upon further investigation of the longitudinal aircraft model derived in [15], it was found that a consequence of arranging the equations of motion specifically in this form allowed for all the aircraft parameters (changing with centre of mass position) to be encapsulated behind the specific acceleration interface (see section 4.3.2). Furthermore, it is shown by [15] that the *normal* dynamics behind the specific acceleration interface are simply the dynamics generated by the standard Short period mode approximation, commonly found in aircraft modelling and control literature [1]. This is the *main* reason for using the model derived by [15], since this modelling strategy conveniently removes the Short period mode dynamics from the rest of the aircraft dynamics.

4.3.2 Mathematical Analysis

This section continues with a mathematical analysis of the arguments presented in the previous section, and outlines some crucial points to be taken into account during the construction of the stability augmentation flight control system. The point mass kinematics ($\overline{V}_W$,θ_W) and position dynamics (N,D) derived in chapter 2 are stated in expanded form below as,

$$\dot{\theta}_W = -\left(\frac{a_n + g\cos\theta_W}{\overline{V}_W}\right) \tag{4.3.1}$$

$$\dot{\overline{V}}_W = a_a - g\sin\theta_W \tag{4.3.2}$$

$$\dot{N} = \overline{V}_W\cos\theta_W \tag{4.3.3}$$

$$\dot{D} = -\overline{V}_W\sin\theta_W \tag{4.3.4}$$

Separated from the above dynamics at an acceleration level are the rigid body rotational dynamics given by,

$$\dot{q} = \frac{\overline{q}SC_m}{I_{yy}} \tag{4.3.5}$$

$$\dot{\alpha} = q + \frac{a_n + g\cos\theta_W}{V_W} \tag{4.3.6}$$

A commonly used aircraft force and moment model for pre-stall flight [16] is used to expand the specific acceleration terms above. For small angles of incidence and typical aircraft lift to drag ratios [16], equations (4.3.7) and (4.3.8) shows the specific acceleration terms in simplified expanded form,

$$a_a = \frac{T\cos\alpha - \overline{q}SC_D}{m} \approx \frac{T - \overline{q}SC_D}{m} \tag{4.3.7}$$

$$a_n = -\frac{T\sin\alpha + \overline{q}SC_L}{m} \approx -\frac{\overline{q}SC_L}{m} \tag{4.3.8}$$

The above simplifying assumptions removes the coupling of thrust into the normal dynamics. Analysis of the aforementioned dynamics and the associated dynamics diagram given by figure 4.6 reveals the following results,

1. All of the aircraft parameters changing with centre of mass position, *including* C_{m_α}, are contained within the rigid body rotational dynamics, isolating the variable stability aircraft problem behind a *normal* specific acceleration interface.
2. The point mass kinematics couple back into the rigid body rotational dynamics through the velocity magnitude, air density (as a function of altitude) and flight path angle (through the gravity coupling term in equation (4.3.6))
3. The only uncertainty that exists in the point mass dynamics is that introduced through the gravitational acceleration coupling term as argued by [16] in equations (4.3.1) and (4.3.2). This uncertainty is typically very low.

The significance of point 1 above is that all of the parameters dependent on the aircraft centre of mass position, determining the aircraft's degree of static stability, are contained within the normal dynamics encapsulated behind a normal specific acceleration interface. As previously mentioned, it is shown by [15] that the normal dynamics are simply the dynamics generated by the standard Short period mode approximation. Therefore the Short period mode dynamics, and consequently the primary variable stability aircraft problem, is found to be isolated from the rest of the aircraft dynamics.

The mathematical analysis above supports the conceptual arguments of section 4.3.1 and strongly motivates the design of a control system regulating normal specific acceleration. To this end however, it is necessary to remove the feedback coupling between the rigid body rotational dynamics and the point mass kinematics. The following assumptions are made to handle the dynamic feedback couplings,

1. The rigid body rotational dynamics states operate on a timescale much faster than the velocity magnitude and air density (as a function of altitude) states.
2. The flight path angle (through the gravity coupling term in equation (4.3.6)) reduces only to gravitational acceleration entering the system as a well modelled bias.

The dynamics of most aircraft is such that the first assumption above, made by [15], is either naturally validated or easily enforced through feedback control. The second assumption above was made specifically for this project, and holds when the flight envelope remains within small angles of θ_W, which is the case for the non-aerobatic flight envelope used in this project. Furthermore, integral control can then be employed to negate this constant bias entering the rigid body rotational dynamics. With assumptions 1 and 2 in place, the normal dynamics (encapsulating the Short period mode) and the point mass kinematics (encapsulating the rest of the aircraft longitudinal dynamics) are decoupled.

For the purpose of this project, it is *assumed* that the states of the Short period mode dynamics operate on a timescale much greater than the centre of mass position state. This assumption is largely validated by mass and inertia effects of the actuator tray as well as mechanical constraints such as the speed of the actuation mechanism used, and can easily be enforced through proper feedback control to ensure its validity. Furthermore, with this assumption in place the Short period mode dynamics reduce from being dynamically dependent on the stability and control derivatives, changing with centre of mass position, to being only *statically* dependent on these parameters. This means that the stability and control derivatives can be treated as parameters instead of states in the Short period mode dynamics, thereby dramatically simplifying the inner-loop control architecture.

These dynamic decoupling assumptions allow for the design of a specific acceleration control law that acts as a function of the stability and control derivatives, and in doing so yield an invariant dynamic response to changes in these parameters at all times. With the variable stability problem identified to be contained within the Short period mode dynamics, and with these dynamics isolated from the rest of the aircraft longitudinal dynamics through the *normal* specific acceleration interface, an acceleration based control strategy designed around the ideas presented in [15] can be used to elegantly solve the variable stability aircraft problem.

4.3.3 Investigation of the Normal Specific Acceleration Dynamics

This section investigates the normal specific acceleration dynamics to determine whether or not the control law designed by [15] can be implemented on a blended-wing-body aircraft. According to [15], the design of the normal specific acceleration controller can be significantly simplified if the following condition holds,

$$\omega_n \;<\; \frac{1}{3}\left|\sqrt{\frac{\bar{q}S\bar{c}C_{L_\alpha}}{I_{yy}}\left(\frac{C_{m_\alpha}}{C_{L_\alpha}} - \frac{C_{m_{\delta_E}}}{C_{L_{\delta_E}}}\right)}\right| \tag{4.3.9}$$

establishing an upper frequency bound for the normal specific acceleration controller, where ω_n is the Short period mode natural frequency. If this condition holds, the term quantifying the elevator to normal specific acceleration non-minimum phase nature of the aircraft, $C_{L_{\delta_E}}$, can be ignored thereby simplifying the derivation of this controller significantly [15].

For this project, equation (4.3.9) implies that the upper frequency bound of the normal specific acceleration controller lies between 5.965 rad/s and 5.981 rad/s, for the centre of mass range investigated. Furthermore, the normal dynamics must operate at a timescale at least 5 times faster than the point mass kinematics according to [15] in order to be statically dependent on air density and velocity magnitude, and in doing so adhere to the dynamic decoupling assumption stated earlier.

It was found (see chapter 5) that the closed loop point mass kinematics must operate at a frequency of around 1 rad/s to achieve a desirable dynamic response. This in turn limits the allowable pole placement region for the normal specific acceleration controller significantly, as the upper bound is between 5.965 rad/s and 5.981 rad/s, and the lower bound is 5 rad/s to maintain the dynamic decoupling assumption between the normal and point mass dynamics as previously mentioned. Therefore, given that modelling inaccuracies will almost certainly inhibit accurate pole placement within this extremely narrow bound, the assumptions proposed by [15] cannot be confidently applied to a tailless aircraft.

The following section continues with the derivation of the normal specific acceleration controller based on the ideas given in [15], but without the associated simplification assumptions ignoring the aircraft's non-minimum phase nature.

4.4 Short Period Mode Stability Augmentation System

This section builds on the previous section, and presents the design and associated analysis of the novel **N**ormal **S**pecific **A**cceleration (**NSA**) controller that yields an invariant dynamic response for all centre of mass positions in the range investigated. From equations (4.3.6) and (4.3.5), with the assumptions given by equations (4.3.7) and (4.3.8), the resulting normal dynamics augmented by an integrator state is given by,

$$\begin{bmatrix} \dot{\alpha} \\ \dot{q} \\ \dot{E}_{a_n} \end{bmatrix} = \begin{bmatrix} -\frac{\overline{q}SC_{L_\alpha}}{m\overline{V}_W} & 1-\frac{\overline{q}S\overline{c}C_{L_q}}{2m\overline{V}_W^2} & 0 \\ \frac{\overline{q}S\overline{c}C_{m_\alpha}}{I_{yy}} & \frac{\overline{q}S\overline{c}^2C_{m_q}}{2I_{yy}\overline{V}_W} & 0 \\ -\frac{\overline{q}SC_{L_\alpha}}{m} & -\frac{\overline{q}S\overline{c}C_{L_q}}{2m\overline{V}_W} & 0 \end{bmatrix} \begin{bmatrix} \alpha \\ q \\ E_{a_n} \end{bmatrix} + \begin{bmatrix} -\frac{\overline{q}SC_{L_{\delta_E}}}{m\overline{V}_W} \\ \frac{\overline{q}S\overline{c}C_{m_{\delta_E}}}{I_{yy}} \\ -\frac{\overline{q}SC_{L_{\delta_E}}}{m} \end{bmatrix} \delta_E + \begin{bmatrix} 0 \\ 0 \\ -1 \end{bmatrix} a_{n_c} \quad (4.4.1)$$

where a_{n_c} is the normal specific acceleration command. Note that for the purpose of this project, it is assumed that the velocity magnitude of the wind axis system is approximately equal to the aircraft's airspeed. This assumption simplifies the derivation of the control system, and the validity thereof will be tested in hardware in the loop simulations. Furthermore, the zero angle of attack lift (C_{L_0}) and moment (C_{m_0}) coefficients along with the gravitational acceleration term (g) are static effects on the aircraft normal dynamics and are consequently omitted from equation (4.4.1). Typically, the C_{L_0} and C_{m_0} terms can be considered zero due to the symmetrical camber of the wings of most conventional aircraft. If C_{L_0} and C_{m_0} are not exactly zero however, a steady state error is incurred on normal specific acceleration which the integrator will remove. Furthermore, gravitational acceleration enters the system as an unwanted bias, which the integrator on normal specific acceleration will remove provided that the flight path angle θ_W remains within small angles. The compensator integrator state is given by,

$$\dot{E}_{a_n} = a_n - a_{n_c} \quad (4.4.2)$$

and the system output equations are given as follows,

$$\begin{bmatrix} a_n \\ q \\ E_{a_n} \end{bmatrix} = \begin{bmatrix} -\frac{\overline{q}SC_{L_\alpha}}{m} & -\frac{\overline{q}S\overline{c}C_{L_q}}{2m\overline{V}_W} & 0 \\ 0 & 1 & 0 \\ 0 & 0 & 1 \end{bmatrix} \begin{bmatrix} \alpha \\ q \\ E_{a_n} \end{bmatrix} + \begin{bmatrix} -\frac{\overline{q}SC_{L_{\delta_E}}}{m} \\ 0 \\ 0 \end{bmatrix} \delta_E \quad (4.4.3)$$

The normal dynamics operate at a frequency more than 30 times smaller than the chosen sample frequency (50Hz), therefore accurate design by emulation can be achieved according to [6]. This means that the control system can be designed in the continuous time domain, and directly applied in the discrete time domain at the selected sample frequency.

With reference to figure 4.7, the normal specific acceleration stability augmentation controller is designed using the pole placement method. The methodology is to obtain the characteristic polynomial of the closed-loop normal dynamics (see equation (4.4.8)), and solving the feedback gains K_{a_n}, K_Q and K_I by comparing the coefficients of the characteristic polynomial of the closed-loop normal dynamics to a desired polynomial equa-

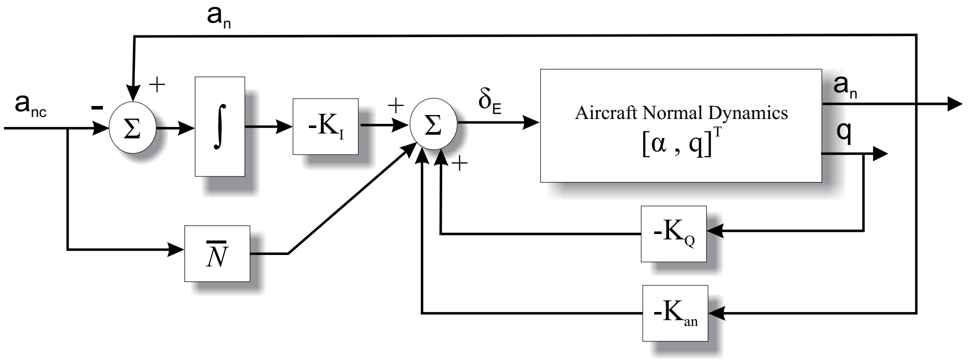

Figure 4.7: Normal Specific Acceleration Controller Conceptual Diagram

tion. This will ensure that the feedback gains obtained drive the system in the correct manner to match the dynamic response defined by the desired polynomial equation.

Note that all of the parameters given in table 3.2 shown to vary with the aircraft centre of mass position are contained in the dynamics given by equation (4.4.1). The feedback gains will be a function of the aircraft parameters which in turn will be a function of the centre of mass position. Therefore, the control system will work to ensure the same dynamic response for normal specific acceleration commands regardless of the centre of mass position, solving the variable stability aircraft problem through the inner-loop **NSA** control system.

The desired third order polynomial equation is given below,

$$\alpha_c(s) = s^3 + \alpha_2 s^2 + \alpha_1 s + \alpha_0 \tag{4.4.4}$$

With the desired third order polynomial equation stated and the control methodology discussed, a solution to the feedback gains can now be found. An integral type control law using feedback from both pitch rate and normal specific acceleration has enough degrees of freedom to arbitrarily place the closed loop poles. This control law is given by,

$$\delta_E = -K_Q q - K_{a_n} a_n - K_I E_{a_n} + \overline{N} a_{n_c} \tag{4.4.5}$$

where $\overline{N}$ is used to place a zero on the closed-loop integrator pole, preventing the integrator dynamics from being seen from the reference input, and will be discussed further in section 4.4.1.2. By substituting the normal specific acceleration output equation a_n given by equation (4.4.3) into to control law above and expanding the result, the control law can be expressed as,

$$\delta_E = \begin{bmatrix} \Omega K_{a_n}\frac{\overline{q}SC_{L_\alpha}}{m} & \Omega K_{a_n}\frac{\overline{q}S\overline{c}C_{L_q}}{2m\overline{V}_W} - \Omega K_Q & -\Omega K_I \end{bmatrix} \begin{bmatrix} \alpha \\ q \\ E_{a_n} \end{bmatrix} + \Omega \overline{N} a_{n_c} \tag{4.4.6}$$

where Ω is given by,

$$\Omega = \frac{1}{1 - K_{a_n}\left(\frac{\overline{q}SC_{L_{\delta_E}}}{m}\right)} \tag{4.4.7}$$

When substituting equation (4.4.6) into equation (4.4.1), the closed loop system matrix $\mathbf{A}_{cl}$ becomes,

$$\mathbf{A}_{cl} = \begin{bmatrix} -\varsigma_1 - \Omega K_{a_n}\overline{V}_W\varsigma_1\varsigma_3 & 1 - \varsigma_2 - \varsigma_3\left(\Omega K_{a_n}\overline{V}_W\varsigma_2 - \Omega K_Q\right) & \varsigma_3\Omega K_I \\ \varsigma_4 + \varsigma_6\Omega K_{a_n}\overline{V}_W\varsigma_1 & \varsigma_5 + \varsigma_6\left(\Omega K_{a_n}\overline{V}_W\varsigma_2 - \Omega K_Q\right) & -\varsigma_6\Omega K_I \\ -\overline{V}_W\varsigma_1 - \Omega K_{a_n}\overline{V}_W\overline{V}_W\varsigma_1\varsigma_3 & -\overline{V}_W\varsigma_2 - \overline{V}_W\varsigma_3\left(\Omega K_{a_n}\overline{V}_W\varsigma_2 - \Omega K_Q\right) & \overline{V}_W\varsigma_3\Omega K_I \end{bmatrix} \tag{4.4.8}$$

where the lumped parameters ς_1 to ς_6 are defined in table 4.1 below.

Lumped Parameter	Definition	Lumped Parameter	Definition
ς_1	$\frac{\overline{q}SC_{L_\alpha}}{m\overline{V}_W}$	ς_2	$\frac{\overline{q}S\overline{c}C_{L_q}}{2m\overline{V}_W^2}$
ς_3	$\frac{\overline{q}SC_{L_{\delta_E}}}{m\overline{V}_W}$	ς_4	$\frac{\overline{q}S\overline{c}C_{m_\alpha}}{I_{yy}}$
ς_5	$\frac{\overline{q}S\overline{c}^2C_{m_q}}{2I_{yy}\overline{V}_W}$	ς_6	$\frac{\overline{q}S\overline{c}C_{m_{\delta_E}}}{I_{yy}}$

Table 4.1: Longitudinal Lumped Parameter Definitions

To determine the characteristic polynomial of equation (4.4.8), the following relationship is used,

$$|\lambda\mathbf{I} - \mathbf{A}_{cl}| = 0 \tag{4.4.9}$$

When equating the coefficients of equation (4.4.4) and (4.4.9) the following results are obtained,

$$\begin{aligned}
\alpha_2 &= \Omega K_{a_n}\overline{V}_W\varsigma_1\varsigma_3 - \varsigma_5 - \Omega K_{a_n}\overline{V}_W\varsigma_2\varsigma_6 + \Omega K_Q\varsigma_6 - \overline{V}_W\varsigma_3\Omega K_I + \varsigma_1 \qquad (4.4.10)\\
\alpha_1 &= \Omega\overline{V}_W\left(K_I\left(\varsigma_3\varsigma_5 - \varsigma_2\varsigma_6\right) + K_{a_n}\left(\varsigma_2\varsigma_3\varsigma_4 - \varsigma_1\varsigma_3\varsigma_5 - \varsigma_1\varsigma_6\right)\right)\\
&\quad + \left(\Omega K_Q\left(\varsigma_1\varsigma_6 - \varsigma_3\varsigma_4\right) - \varsigma_1\varsigma_5 - \varsigma_4 + \varsigma_4\varsigma_2\right) \qquad (4.4.11)\\
\alpha_0 &= \Omega\overline{V}_W K_I\varsigma_3\varsigma_4 - \Omega\overline{V}_W K_I\varsigma_1\varsigma_6 \qquad (4.4.12)
\end{aligned}$$

Since there are three equations with three unknowns, the control gain can be found by simultaneously solving the above equations. The results are given below,

$$\begin{aligned}
K_I &= \frac{\alpha_0 - \alpha_0 K_{a_n}\overline{V}_W\varsigma_3}{\overline{V}_W\left(\varsigma_3\varsigma_4 - \varsigma_1\varsigma_6\right)} \qquad (4.4.13)\\
K_{a_n} &= \frac{1}{\overline{V}_W C_4}\left(\alpha_1 - \frac{C_1C_3\alpha_1 - C_1C_3C_5 + \overline{V}_W C_3C_4C_2 - \overline{V}_W C_3C_4\alpha_2}{\left(C_1C_3 - \overline{V}_W C_4\varsigma_6\right)} - C_5\right) \qquad (4.4.14)\\
K_Q &= \frac{C_1\alpha_1 - C_1C_5 + \overline{V}_W C_4C_2 - \overline{V}_W C_4\alpha_2}{\left(C_1C_3 - \overline{V}_W C_4\varsigma_6\right)} \qquad (4.4.15)
\end{aligned}$$

The coefficients C_1 to C_5 are given as,

$$\begin{aligned}
C_1 &= \alpha_2\overline{V}_W\varsigma_3 + \overline{V}_W\varsigma_3\varsigma_5 - \overline{V}_W\varsigma_2\varsigma_6 + \frac{\alpha_0\overline{V}_W\varsigma_3\varsigma_3}{\left(\varsigma_3\varsigma_4 - \varsigma_1\varsigma_6\right)} \qquad (4.4.16)\\
C_2 &= \varsigma_1 - \varsigma_5 - \frac{\varsigma_3\alpha_0}{\left(\varsigma_3\varsigma_4 - \varsigma_1\varsigma_6\right)} \qquad (4.4.17)\\
C_3 &= \varsigma_1\varsigma_6 - \varsigma_3\varsigma_4 \qquad (4.4.18)\\
C_4 &= \varsigma_3\varsigma_4 - \varsigma_1\varsigma_6 - \frac{\varsigma_3\alpha_0\varsigma_3\varsigma_5}{\left(\varsigma_3\varsigma_4 - \varsigma_1\varsigma_6\right)} + \frac{\varsigma_3\alpha_0\varsigma_2\varsigma_6}{\left(\varsigma_3\varsigma_4 - \varsigma_1\varsigma_6\right)} + \alpha_1\varsigma_3 \qquad (4.4.19)\\
C_5 &= \frac{\alpha_0\varsigma_3\varsigma_5}{\left(\varsigma_3\varsigma_4 - \varsigma_1\varsigma_6\right)} - \frac{\alpha_0\varsigma_2\varsigma_6}{\left(\varsigma_3\varsigma_4 - \varsigma_1\varsigma_6\right)} - \varsigma_1\varsigma_5 - \varsigma_4 + \varsigma_4\varsigma_2 \qquad (4.4.20)
\end{aligned}$$

Therefore, to solve the feedback gains K_{a_n}, K_Q and K_I, equations (4.4.13) to (4.4.15) are used with the coefficients C_1 to C_5 defined above by setting the values of α_2, α_1 and α_0 in the equations below,

$$\begin{aligned}
\alpha_2 &= 2\zeta\omega_n + R_I \qquad (4.4.21)\\
\alpha_1 &= \omega_n^2 + 2R_I\zeta\omega_n \qquad (4.4.22)\\
\alpha_0 &= R_I\omega_n^2 \qquad (4.4.23)
\end{aligned}$$

where ζ is the desired Short period mode damping ratio, ω_n the desired Short period mode frequency in radians per second, and R_I the frequency of the integrator on normal specific acceleration. The value for $\overline{N}$ is selected by [8],

$$\overline{N} = \frac{K_I}{R_I} \tag{4.4.24}$$

The following section is aimed at discussing the allowable pole placement options ensuring a feasible and robust closed loop solution.

4.4.1 Closed Loop Analysis and Pole Placement Considerations

Section 4.4.1.1 considers various frequency bounds imposed on the normal specific acceleration controller. Section 4.4.1.2 follows with a closed loop analysis and investigates various pole placement options with the frequency bounds in mind, and concludes by analysing the effect of delays on the closed loop system.

4.4.1.1 Frequency Bounds

Timescale Separation - The Lower Frequency Bound: The solution derived allows for the Short period poles to be placed arbitrarily, as long as ω_n is at least a factor 5 greater than the poles of the point mass kinematics states. As previously mentioned, this is done to enforce the timescale separation assumed between the rigid body rotational dynamics and the point mass kinematics dynamics, imposing a lower frequency bound on the closed loop Short period mode pole locations.

Servo Response - The Upper Frequency Bound: The upper bound for the placement of the Short period mode poles will be influenced by the response ability of the servo actuator. A simple first order low-pass filter was used in modeling the dynamics from the control surface deflection command to the *actual* deflection, and is included in the simulation environment discussed in chapter 7. The cutoff frequency was chosen based on the slew-rate limitation from the specifications of the servo motors used in this project. In the frequency range less than the cutoff frequency, the sinusoidal deflection of a servo arm according to [17] can be expressed as,

$$\delta(t) = A\sin\omega t \Rightarrow \dot{\delta}(t) = A\omega\cos\omega t \tag{4.4.25}$$

Since the maximum of $\dot{\delta}(t)$ is limited, the corresponding critical frequency where the servo begins to reach its maximum speed is given by,

$$\omega_{cr} = \frac{|\dot{\delta}(t)|_{max}}{A} \tag{4.4.26}$$

where A is the amplitude of the servo arm deflection. The servos used in this project has a $260°/s$ slew rate, and assuming extreme servo deflections of ±10°, the *maximum* servo speed is found to be,

$$\omega_{cr} = \frac{260°/s}{20°} = 13 \quad [\text{rad/s}] \tag{4.4.27}$$

Therefore, the frequency bounds on ω_n is found to be,

$$5\omega_n^k < \omega_n < 13 \quad [\text{rad/s}] \tag{4.4.28}$$

where ω_n^k is the point mass kinematics frequency, which was determined to be less than 1 rad/s. The above constraint must be taken into account when designing further outer-loop controllers as discussed in chapter 5.

Closed Loop Pole Locations: The closed loop poles are placed at the open loop frequency when the aircraft centre of mass is in the most forward (most stable) position. This frequency can be determined by,

$$\omega_n = \sqrt{\varsigma_4(\varsigma_2 - 1) - \varsigma_1\varsigma_5} = 7.4 \quad [\text{rad/s}] \tag{4.4.29}$$

where ς_2, ς_5, ς_1 and ς_4 are defined as given in table 4.1, and the values of these parameters are chosen for the most stable case. The proposed closed loop pole locations at the frequency stated in the above equation (equation (4.4.29)), are well within the upper and lower frequency bounds given by equation (4.4.28).

4.4.1.2 Closed Loop Analysis

In order to investigate the effect of the control law derived in the previous section on the normal dynamics, the closed loop solution must be derived. The normal dynamics open-loop state and output equations, given by equations (4.4.1) and (4.4.3) respectively, can be written in the following summarised form,

$$\dot{\mathbf{x}} = \mathbf{A}\mathbf{x} + \mathbf{B}\mathbf{u} \tag{4.4.30}$$

$$\mathbf{y} = \mathbf{C}\mathbf{x} + \mathbf{D}\mathbf{u} \tag{4.4.31}$$

where $\mathbf{A}$ is the 3×3 system matrix (which includes the augmented integrator state), $\mathbf{B}$ is the 3×1 input matrix, $\mathbf{C}$ is the 3×3 output matrix and $\mathbf{D}$ is 3×1. The control law using output feedback is defined as,

$$\mathbf{u} \;=\; -\mathbf{K}\mathbf{y} + \overline{N} a_{n_c} \tag{4.4.32}$$

where a_{n_c} is the reference input. Substituting equation (4.4.31) into equation (4.4.32), and writing the input vector $\mathbf{u}$ as the subject of the formula,

$$\mathbf{u} \;=\; -\left(1 + \mathbf{K}\mathbf{D}\right)^{-1} \mathbf{K}\mathbf{C}\mathbf{x} + \left(1 + \mathbf{K}\mathbf{D}\right)^{-1} \overline{N} a_{n_c} \tag{4.4.33}$$

Equation (4.4.33) is substituted into equation (4.4.30) to obtain the closed loop equation,

$$\dot{\mathbf{x}} = \left[\mathbf{A} - \mathbf{B}\left(1 + \mathbf{K}\mathbf{D}\right)^{-1} \mathbf{K}\mathbf{C}\right] \mathbf{x} + \left[\mathbf{B}\left(1 + \mathbf{K}\mathbf{D}\right)^{-1}\right] \overline{N} a_{n_c} \tag{4.4.34}$$

By substituting equation (4.4.33) into equation (4.4.31), the closed loop output equation is given by,

$$\mathbf{y} \;=\; \left(\mathbf{C} - \mathbf{D}(1 + \mathbf{K}\mathbf{D})^{-1}\mathbf{K}\mathbf{C}\right) \mathbf{x} + \left[\mathbf{D}(1 + \mathbf{K}\mathbf{D})^{-1}\right] \overline{N} a_{n_c} \tag{4.4.35}$$

Closed Loop Evaluation: Using the previous results, the closed loop system response can now be investigated. Figure 4.8 (b) shows the desired and actual closed loop pole locations when the non-minimum phase nature of the normal specific acceleration dynamics is ignored, as suggested by [15]. Figure 4.8 (a) shows the case where the non-minimum phase nature is taken into account through the control architecture developed in this thesis. It is clear from figure 4.8 (a) that the non-minimum phase nature must be taken into account, as accurate pole placement is achieved and the closed loop poles are placed in exactly the same locations over the entire centre of mass range investigated.

Figure 4.8 (b) shows the upper allowable frequency bound set by equation (4.3.9) allowing the non-minimum phase nature of the aircraft to be ignored. When the non-minimum phase zero is ignored (i.e. $C_{L_{\delta_E}} \approx C_{L_q} \approx 0$), the closed loop response is still stable, but the poles do *not* end up in the desired locations.

Furthermore, figure 4.8 (b) shows the upper bound for the placement of the closed-loop Short period mode poles, determined by the maximum response speed of the servo actuators used in this project. Note that at a certain point the algorithm *ignoring* the non-minimum phase zero attempts to place the closed loop poles at a frequency beyond the capability of the actuation mechanism. This induces a severe non-linearity in the system since the output of the controller will continually be driven into saturation. The

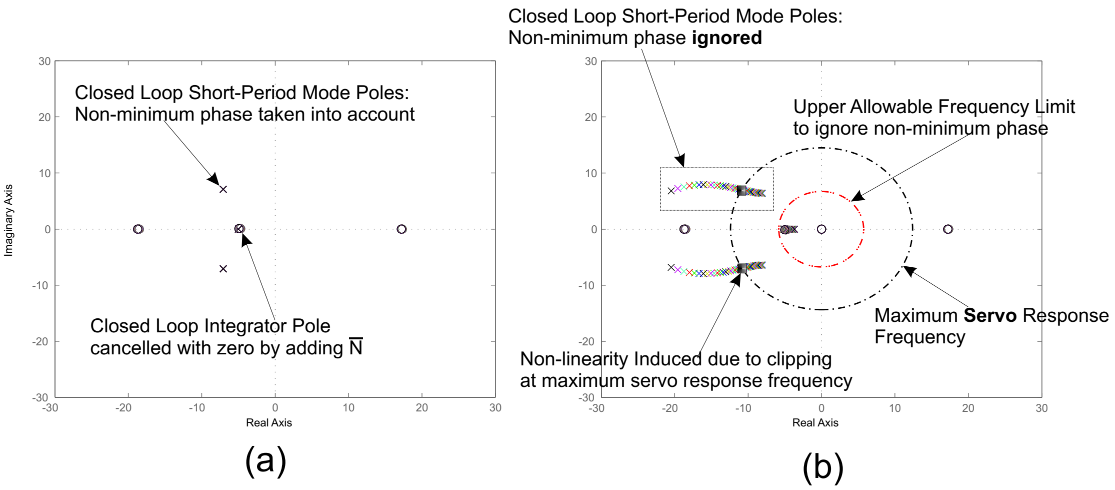

Figure 4.8: (a) Closed Loop Pole Locations: Non-minimum phase taken into account. (b) Closed Loop Pole Locations: Non-minimum phase ignored.

non-linear behaviour will produce undesired results as the control system will fail to adequately stabilise the Short period mode when the aircraft is statically unstable.

The aforementioned analysis confirms the need to include the parameters describing the elevator to normal specific acceleration non-minimum phase nature in the control system designed. It must be stressed however that the results given by figure 4.8 (b) only apply to aircraft violating the condition given by equation (4.3.9), as is the case for this project.

System Delays: Now that the pole placement strategy for the closed-loop Short period poles have been analysed, it remains to investigate the effect of delays on the closed loop system. The avionics package designed uses a full sample period to calculate the control signals and relay the information to the actuation mechanisms at the start of the next cycle. Since the system operates at a sample frequency of 50Hz, this implies a 0.02s delay in the system.

With reference to figure 4.9, it is clear that when the closed loop poles are selected at too high a frequency ($\omega_n = 13$, $R_I = 13$), in this case at the maximum servo frequency, that the delay in the system drives the system unstable when the centre of mass is in the most aft position. Even when the integrator pole is placed at a lower frequency ($\omega_n = 13$, $R_I = 10$), the resulting delay-integrator complex pole pair dominates the response leading to an undesired dynamic response.

Figure 4.10 continues the analysis showing when $\omega_n = 10$ and $R_I = 8$, that the delay-integrator complex pole pair causes the closed-loop Short period poles to become a real pole pair when the aircraft is statically unstable, delivering improved but still fairly poor results. However, when the closed loop poles are placed at the open-loop stable fre-

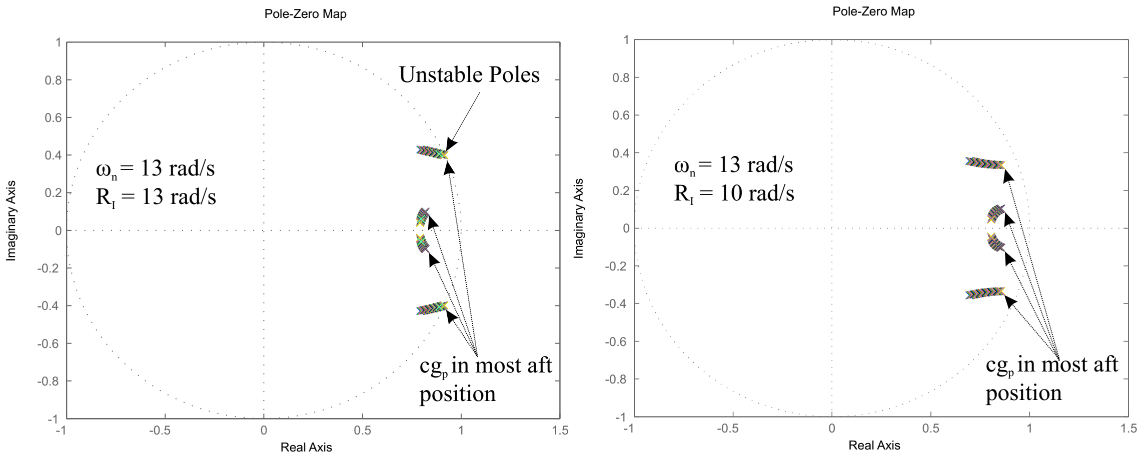

Figure 4.9: The Effect of Delays on the Closed Loop System (a)

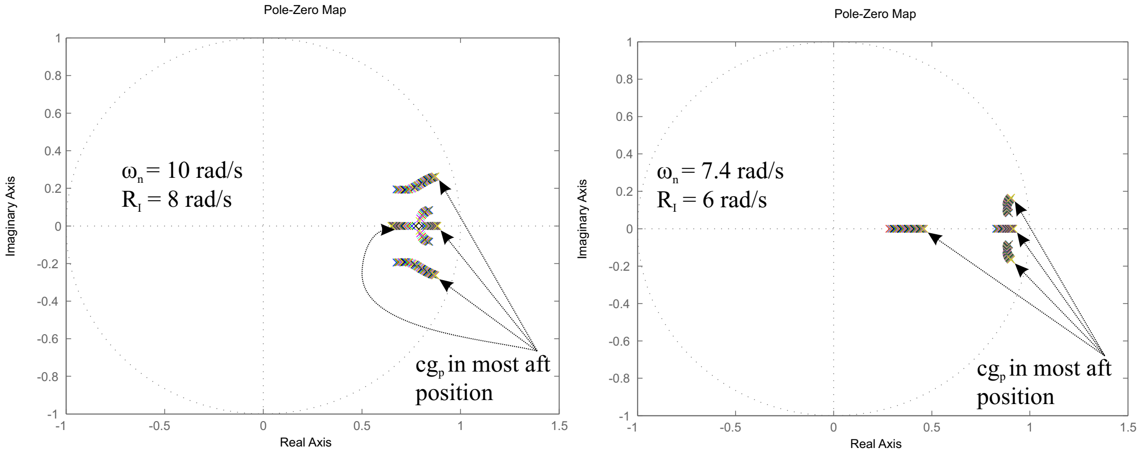

Figure 4.10: The Effect of Delays on the Closed Loop System (b)

quency ($\omega_n = 7.4$, $R_I = 6$) with the integrator at a slightly lower frequency, the delay influences the Short period damping by a maximum of 35% and the closed-loop frequency by 25%. Although the delay still influences the placement of the closed loop Short period poles, a 25% change in the frequency and 35% change in the damping over the entire centre of mass range is still acceptable. It should be noted however that the delay will start to play a more significant role if more control effort is needed to stabilise the vehicle.

Closed Loop Step Response: Figure 4.11 shows the closed loop step response of the normal specific acceleration controller with and without $\overline{N}$. When $\overline{N}$ is included, the integrator dynamics is not seen from the reference input, and the feed-forward term $\overline{N}$ increases the closed loop system response to reference inputs. Because the integrator pole must be placed at a slightly lower frequency than the rest of the dynamics for the reasons stated earlier, $\overline{N}$ must be included to improve the overall closed loop dynamic response. The rise time improves from about 0.8 seconds to less than 0.3 seconds.

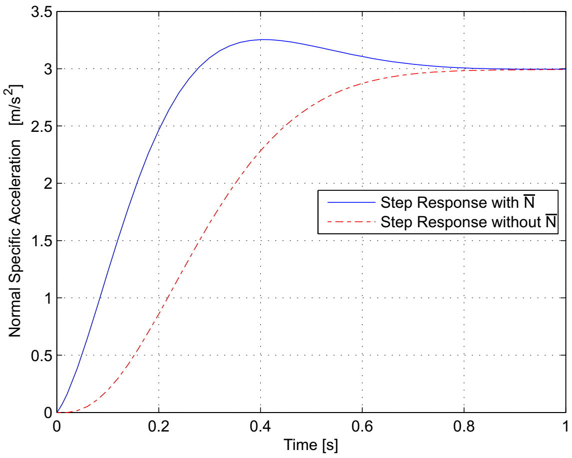

Figure 4.11: Normal Specific Acceleration Controller Closed Loop Step Response

4.4.2 Integrators and Integrator Windup

Compensator integrators provide infinite steady-state gain, and are capable of promptly removing steady-state errors induced due to both modelling errors and unmodelled dynamics. An integrator tends to keep increasing or decreasing its output until its input reaches zero. When a large reference value is commanded such that the actuator is driven into saturation, the integrator state builds up over time, and can cause significant overshoot after the actuator returns from saturation. The continuous increase in the integrator state during actuator saturation is often referred to as *integrator windup*.

Therefore, integrator anti-windup was implemented on all of the compensator integrators used in this project. Anti-windup prevents the compensator integration process when an actuator saturates to prevent the build up of large actuation commands over time. This in turn prevents the integrators from causing instability in the system and improves the robustness of the control system.

4.4.3 The Effect of Centre of Mass Position Measurement Errors

Up to now, the analysis and design of the normal specific acceleration controller assumed that the aircraft centre of mass position can be measured with 100% accuracy. Practically however, this might not always be entirely possible.

Figure 4.12 shows the **NSA** control system's closed step response when the centre of mass position is fixed in the most forward position, with measurement errors on cg_p (the centre of mass position). A 0% error is when cg_p is exactly known, and a 100% error is when the control system thinks that the centre of mass is in the most aft (most unstable) position, when it is actually in the most forward (most stable) position.

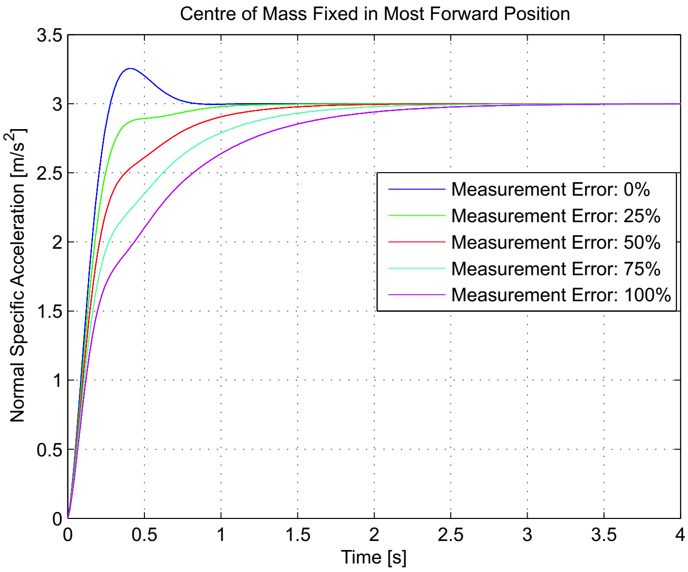

Figure 4.12: NSA Controller Closed Loop Step Response with Centre of Mass Measurement Errors: Statically Stable Case

With reference to figure 4.12, the control system suffers degraded response as the measurement error on cg_p becomes significant. Note however that the closed loop response remains stable, and for measurement errors of below 25% the closed loop response is still acceptable. With reference to figure 4.12, a 25% measurement error implies that the control system thinks that the aircraft is 25% more *unstable* than it actually is. Note that the aircraft is *naturally* stable when the centre of mass in the most forward position. The natural stability consequently helps to stabilise the aircraft Short period mode dynamics, explaining the results given by figure 4.12.

Figure 4.13 shows the **NSA** control system closed step response when the centre of mass position is fixed in the most aft position. Here, a 100% error is when the control system thinks that the centre of mass is in the most forward (most stable) position, when it is actually in the most aft (most unstable) position. Note that as the measurement error on cg_p becomes larger, the closed loop system step response degrades severely, and will eventually become completely unstable. Again, for measurement errors of up to 25% the closed loop response remains acceptable. With reference to figure 4.13, a 25% measurement error implies that the control system thinks that the aircraft is 25% more *stable* than it actually is.

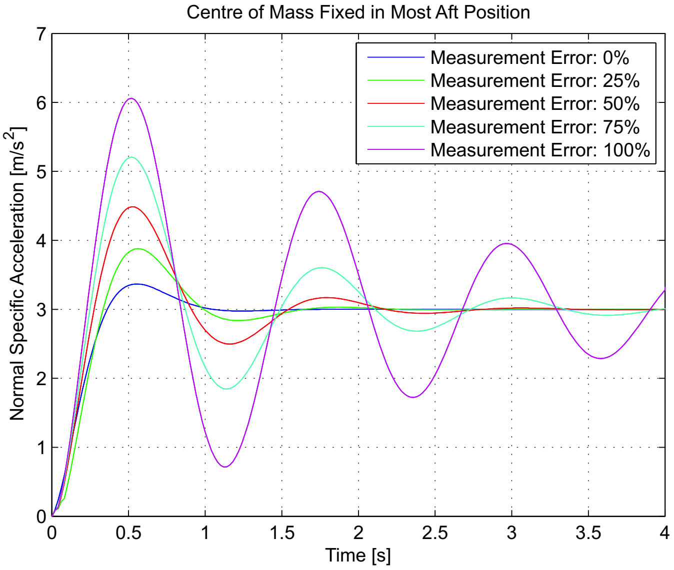

Figure 4.13: NSA Controller Closed Loop Step Response with Centre of Mass Measurement Errors: Statically Unstable Case

It should be noted that a 25% error on the measurement of cg_p is quite significant, and that practically the error is far less than this because a high-precision digital encoder is used to measure cg_p.

4.4.4 Least Squares Curve Approximations for Stability and Control Derivatives

As previously mentioned, the stability and control derivatives are assumed to be parameters in the rigid body rotational dynamics instead of states. However, the derivatives vary as a function of centre of mass position, and must therefore be updated accordingly in the normal specific acceleration controller equations (see equations (4.4.13) to (4.4.20)) derived. AVL produces discrete values for each of the derivatives used. These values are loaded into matrices using MATLAB, and a least squares algorithm computes the coefficients needed to construct either linear or quadratic functions of the derivatives.

A least square algorithm provided by [6] was investigated and applied to estimate both the linear and quadratic derivatives used in the previous section. The algorithm is stated below,

$$\hat{\mathbf{x}}_{LS} = \left[\mathbf{H}^T\mathbf{H}\right]^{-1}\mathbf{H}^T\mathbf{Y} \tag{4.4.36}$$

where the least squares estimate is $\hat{\mathbf{x}}_{LS}$ and $\mathbf{Y}$ is a $n \times 1$ matrix containing the values of an individual derivatives as given by AVL at various centre of mass locations. To obtain a linear curve, the matrix **H** is defined as,

$$\mathbf{H} = \begin{bmatrix} 1 & F_{cg}(1) \\ \vdots & F_{cg}(2) \\ \vdots & \vdots \\ \vdots & F_{cg}(n) \end{bmatrix} \tag{4.4.37}$$

where $\mathbf{F}_{cg}$ is a matrix of the aircraft centre of mass positions in meter. To obtain a quadratic function, **H** is defined as,

$$\mathbf{H} = \begin{bmatrix} 1 & F_{cg}(1) & F_{cg}(1)^2 \\ \vdots & F_{cg}(2) & F_{cg}(2)^2 \\ \vdots & \vdots & \vdots \\ \vdots & F_{cg}(n) & F_{cg}(n)^2 \end{bmatrix} \tag{4.4.38}$$

where n is the length of the available data set used. By using **H** as defined by equation (4.4.37) with equation (4.4.36), a stability or control derivative *linearly* dependent on centre of mass position is expressed as,

$$C_{\lambda_\epsilon} = \hat{x}_{LS}(1) + \hat{x}_{LS}(2) \times cg_p \tag{4.4.39}$$

where cg_p is the centre of mass position in meter. Similarly, by using **H** as defined by equation (4.4.38) with equation (4.4.36), a stability or control derivative *quadratically* dependent on centre of mass position may be expressed as,

$$C_{\lambda_\epsilon} = \hat{x}_{LS}(1) + \hat{x}_{LS}(2) \times cg_p + \hat{x}_{LS}(3) \times cg_p^2 \tag{4.4.40}$$

4.5 Summary

This chapter introduced the two longitudinal modes of motion, namely the Phugoid and Short period modes, and argued that the variable stability problem manifests itself primarily in the *Short period* mode of motion. The aircraft Short period mode was explained by comparing it to that of a torsional *spring-mass-damper* system. It was found that the spring coefficient, quantified by the C_{m_α} stability derivative, is influenced dramatically by the location of the aircraft centre of mass relative to the longitudinal neutral point. A consequence of moving the aircraft centre of mass aft of the statically stable location, is that the aerodynamic spring coefficient changes such that the aircraft becomes completely uncontrollable by a human pilot. Since the aerodynamic spring coefficient was linked to the aircraft Short period mode of motion, a control system was designed regulating the aircraft Short period mode in order to negate the effect of the changing spring coefficient and in doing so regain static stability for all centre of mass positions. To this end, the Short period mode was mathematically isolated from the rest of the aircraft dynamics.

The ideas presented in [15] provided the necessary modelling strategy to isolate the aircraft Short period mode from the rest of the aircraft dynamics through a normal specific acceleration interface. With the core of the variable stability problem isolated, the proposed stability augmentation control strategy was discussed conceptually in section 4.3. The analysis of the aircraft normal dynamics (encapsulating the Short period mode of motion) indicated that the normal specific acceleration control strategy proposed by [15] could not be implemented on the blended-wing-body aircraft used in this project. A *novel* control law was designed in section 4.4, using the concept of acceleration feedback control (a consequence of the work initially done by [15]) yielding an invariant dynamic response to aircraft parameters changing as a function of the centre of mass position.

The control law designed allows for the closed loop Short period mode poles to be placed arbitrarily, provided that the following conditions are met:

1. To enforce the timescale separation assumed between the normal dynamics and point mass kinematics, the Short period mode closed loop poles must be placed at a frequency at least five times higher than the closed loop frequency of the aircraft point mass kinematics.

2. The closed loop Short period mode poles must be placed at a frequency lower than the maximum response frequency of the servo actuators used.

Section 4.4.1 discussed the effect of delays on the resulting closed loop pole locations, and provided additional insight into the choice of the closed loop pole locations.

Through the implementation of the **NSA** control system, regulating the aircraft Short period mode dynamics, the variable stability aircraft becomes a conventional statically stable aircraft for all centre of mass positions. The control law developed ensures that the aircraft exhibits the same dynamic response regardless of the static stability margin for all centre of mass positions in the range investigated.

Chapter 5 continues with the design of further outer loop flight control systems, regulating the aircraft point mass kinematics states to allow for full autonomous flight.

Chapter 5

Aircraft Flight Control Architecture

This chapter is aimed at describing the design of further outer loop controllers allowing for full autonomous flight. With the aircraft specific dynamics controlled by the inner loop normal specific acceleration controller, the variable stability aircraft problem reduces to that of a conventional statically stable aircraft for all centre of mass positions.

Section 5.1 presents the design of a control system regulating the aircraft longitudinal point mass kinematics. Section 5.3 follows with the design of a *novel* control system capable of adjusting the static stability margin of the aircraft in flight and consequently commanding the desired aircraft trim elevator setting. Section 5.4 concludes the chapter with a brief overview of the conventional lateral flight control systems used.

5.1 Kinematic Linear Quadratic Regulator

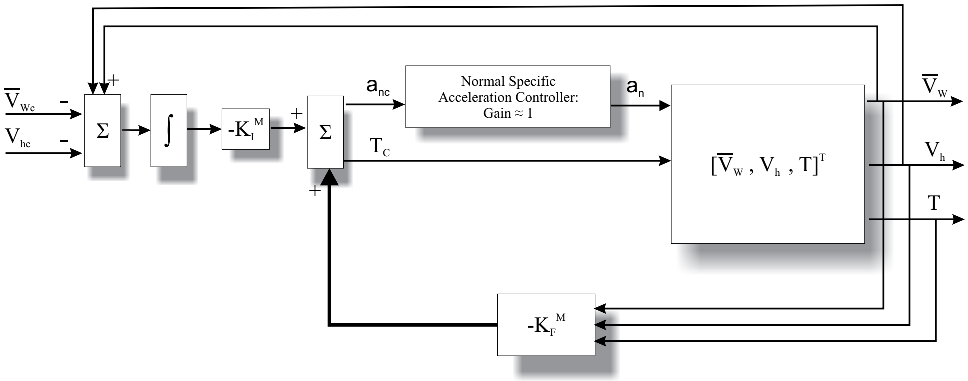

Figure 5.1: Airspeed and Climb rate **MIMO** control architecture

This section is aimed at discussing the design of a **M**ulti-**I**nput-**M**ulti-**O**utput (**MIMO**) **F**light **C**ontrol **S**ystem (**FCS**) regulating the aircraft's airspeed and climb rate. The control strategy is shown conceptually by figure 5.1. Here, V_{h_C} is the reference climb rate command, V_h the climb rate signal, $\overline{V}_{W_C}$ the airspeed command and T_C the thrust command. The **MIMO FCS** is designed using linear quadratic regulator theory, yielding optimal closed loop system poles. The **MIMO** integrator feedback gain matrix is denoted by $\mathbf{K}_I^M$ and the full-state feedback gain matrix is denoted by $\mathbf{K}_F^M$ as shown in figure 5.1. Furthermore, the **MIMO** control system will use a normal specific acceleration *virtual* actuator (a_{n_c}), driving into the normal specific acceleration (**NSA**) controller derived in the previous chapter. Since the **NSA** controller operates at a bandwidth much greater than the **MIMO** control system, it can be safely assumed that once a normal specific acceleration command is issued, that the **NSA** controller responds immediately and that the desired normal specific acceleration is obtained. Therefore, the **NSA** controller is modelled as a unity gain function with respect to the **MIMO** control system. With the control architecture briefly described, the derivation can be discussed in more detail. When substituting equation (4.3.7) into equation (4.3.2), the kinematic equations can be shown to be,

$$\dot{\theta}_W = -\frac{a_n}{\overline{V}_W} - \frac{g\cos\theta_W}{\overline{V}_W} \tag{5.1.1}$$

$$\dot{\overline{V}}_W = \frac{T - \overline{q}SC_D}{m} - g\sin\theta_W \approx \frac{T}{m} - g\sin\theta_W \tag{5.1.2}$$

Based on the work done by [15], the above equation for the velocity dynamics ignores drag by treating it as a disturbance acting on the system. Treating drag as a disturbance practically makes sense since drag is notoriously difficult to model with a reasonable degree of certainty. Since drag is a force acting on the system, the assumption is made [15] that the axial acceleration to axial velocity dynamics will naturally filter and remove high frequency drag disturbances. Lower frequency drag disturbances are removed by the feedback control system, and a compensator integrator providing infinite steady state gain will be augmented to the system to remove possible steady state drag disturbances.

Adding the propulsion model defined by equation (2.2.28) to the above dynamic equations and linearising the equations about the straight and level flight condition, the following results are obtained,

$$\begin{bmatrix} \dot{\overline{V}}_W' \\ \dot{\theta}_W' \\ \dot{T}' \end{bmatrix} = \begin{bmatrix} 0 & -g & \frac{1}{m} \\ \frac{2g}{\overline{V}_{W_0}^2} & 0 & 0 \\ 0 & 0 & -\frac{1}{\tau_T} \end{bmatrix} \begin{bmatrix} \overline{V}_W' \\ \theta_W' \\ T' \end{bmatrix} + \begin{bmatrix} 0 & 0 \\ -\frac{1}{\overline{V}_{W_0}} & 0 \\ 0 & -\frac{1}{\tau_T} \end{bmatrix} \begin{bmatrix} a_{n_c} \\ T_c \end{bmatrix} \tag{5.1.3}$$

where the following assumptions for the straight and level flight condition are made,

$$\sin\theta_{W_0} \approx 0 \tag{5.1.4}$$

$$\cos\theta_{W_0} \approx 1 \tag{5.1.5}$$

In the above equations, θ_{W_0} is the trim pitch angle of the wind axis system, which is zero for straight and level flight, and $\overline{V}_{W_0}$ is the trim airspeed as previously stated. The output equations are selected to extract climb rate and velocity magnitude, where equation (2.2.10) defined in chapter 2 is used to obtain the vehicle climb rate. The linearised output equations are given below,

$$\begin{bmatrix} \overline{V}'_W \\ V'_h \end{bmatrix} = \begin{bmatrix} 1 & 0 \\ 0 & \overline{V}_{W_0} \end{bmatrix} \begin{bmatrix} \overline{V}'_W \\ \theta'_W \end{bmatrix} \tag{5.1.6}$$

An obvious problem is encountered with equation (5.1.3) when it is desired to implement the proposed control strategy. As indicated by figure 5.1, the desired design strategy is a **LQR** controller regulating climb rate and airspeed. Unfortunately, **LQR** is a full state feedback solution, and climb rate is not present in the state vector. One option is to design an estimator capable of providing pitch attitude information and designing a **MIMO** pitch attitude and airspeed **LQR** full state feedback controller. However, the added complexity of designing the estimator with the additional computational strain the estimator will place on the embedded avionics is not warranted. These problems can be avoided entirely, if the state vector of equation (5.1.3) could be transformed to incorporate climb rate as a state instead of pitch attitude. This will allow for a full state feedback solution without the need for an estimator, as climb rate can be obtained from the mounted pressure sensors providing altitude information.

To aid in the derivation of the state transformation matrix, equations (5.1.3) and (5.1.6) are written as,

$$\dot{\mathbf{x}}_o = \mathbf{A}\mathbf{x}_o + \mathbf{B}\mathbf{u} \tag{5.1.7}$$

$$\mathbf{y} = \mathbf{C}\mathbf{x}_o \tag{5.1.8}$$

where $\mathbf{x}_o$ represents $\begin{bmatrix} \overline{V}'_W & \theta'_W & T' \end{bmatrix}^T$ with pitch attitude as a state, and $\mathbf{u}$ represents $\begin{bmatrix} a_{n_c} & T_c \end{bmatrix}^T$. Now, suppose that a state transformation matrix $\mathbf{T}$ exist such that,

$$\mathbf{x}_n = \mathbf{T}\mathbf{x}_o \Rightarrow \dot{\mathbf{x}}_n = \mathbf{T}\dot{\mathbf{x}}_o \tag{5.1.9}$$

where $\mathbf{x}_n$ represents $\begin{bmatrix} \overline{V}_W' & V_h' & T' \end{bmatrix}^T$ with climb rate as a state. Substituting the results of equation (5.1.9) into equations (5.1.7) and (5.1.8), the following useful results are obtained,

$$\begin{aligned} \dot{\mathbf{x}}_n &= \mathbf{TAT}^{-1}\mathbf{x}_n + \mathbf{TBu} && (5.1.10) \\ \mathbf{y} &= \mathbf{CT}^{-1}\mathbf{x}_n && (5.1.11) \end{aligned}$$

By noting that the output equations given by equation (5.1.6) relates the pitch attitude state to the climb rate state, the transformation matrix $\mathbf{T}$ is simply constructed by adding the propulsion source (thrust) state to equation (5.1.6). The result is shown below,

$$\begin{aligned} \mathbf{x}_n &= \mathbf{T}\mathbf{x}_o && (5.1.12) \\ \begin{bmatrix} \overline{V}_W' \\ V_h' \\ T' \end{bmatrix} &= \begin{bmatrix} 1 & 0 & 0 \\ 0 & \overline{V}_{W_0} & 0 \\ 0 & 0 & 1 \end{bmatrix} \begin{bmatrix} \overline{V}_W' \\ \theta_W' \\ T' \end{bmatrix} && (5.1.13) \end{aligned}$$

After the state vector is transformed, the system is augmented with integrators on airspeed and climb rate. The integrator states are given as,

$$\begin{aligned} \dot{E}_{\overline{V}_W} &= \overline{V}_W - \overline{V}_{W_c} && (5.1.14) \\ \dot{E}_{V_h} &= V_h - V_{h_c} && (5.1.15) \end{aligned}$$

and the complete augmented system with compensator integrator terms is given below,

$$\begin{aligned} \begin{bmatrix} \dot{\overline{V}}_W' \\ \dot{V}_h' \\ \dot{T}' \\ \dot{E}_{\overline{V}_W}' \\ \dot{E}_{V_h}' \end{bmatrix} &= \begin{bmatrix} 0 & -\frac{g}{\overline{V}_{W_0}} & \frac{1}{m} & 0 & 0 \\ \frac{2g}{\overline{V}_{W_0}} & 0 & 0 & 0 & 0 \\ 0 & 0 & -\frac{1}{\tau_T} & 0 & 0 \\ 1 & 0 & 0 & 0 & 0 \\ 0 & 1 & 0 & 0 & 0 \end{bmatrix} \begin{bmatrix} \overline{V}_W' \\ V_h' \\ T' \\ E_{\overline{V}_W}' \\ E_{V_h}' \end{bmatrix} + \begin{bmatrix} 0 & 0 \\ -1 & 0 \\ 0 & -\frac{1}{\tau_T} \\ 0 & 0 \\ 0 & 0 \end{bmatrix} \begin{bmatrix} a_{n_c} \\ T_c \end{bmatrix} \\ &+ \begin{bmatrix} 0 & 0 \\ 0 & 0 \\ 0 & 0 \\ -1 & 0 \\ 0 & -1 \end{bmatrix} \begin{bmatrix} \overline{V}_{W_c} \\ V_{h_c} \end{bmatrix} \qquad (5.1.16) \end{aligned}$$

5.1.1 LQR Design Methodology

Now that the linearised state equations are written in a form allowing for full state feedback without the need for an estimator, the **LQR** design methodology can be discussed in more detail. The **LQR** method specifically addresses the issue of achieving a balance between good system response and the control effort required. The method involves calculating the optimal control input to the system that minimises a cost function typically represented by,

$$\mathbf{J} = \int_0^\infty \left[\mathbf{x}^T\mathbf{Q}_1\mathbf{x} + \mathbf{u}^T\mathbf{Q}_2\mathbf{u}\right] dt \tag{5.1.17}$$

where $\mathbf{Q}_1$ is an $n \times n$ state weighting matrix, $\mathbf{Q}_2$ is an $m \times m$ control weighting matrix, and m is the number of control inputs in the **MIMO** system. The $\mathbf{Q}_1$ and $\mathbf{Q}_2$ weighting matrices must be positive definite and are usually diagonal, preferably containing non-zero elements. If one of the state weighting elements are zero, unstable results may be produced. For further information regarding **LQR** optimal control and the above equation, refer to [6].

To minimise the cost function given by equation 5.1.17, weights are applied to each state and control input in the matrices $\mathbf{Q}_1$ and $\mathbf{Q}_2$. By increasing a state's weighting, it is considered more important and the **LQR** algorithm calculates feedback gains to control the state more aggressively. One of the biggest draw-backs of using **LQR** is that complex coupling between states in large systems makes it extremely difficult to intuitively relate a weight back to a specific state. One would typically change a weighting by targeting a specific state with certain response characteristics in mind. The algorithm then returns optimal feedback gains, and although the actual closed loop dynamic response is stable, the response is not always what is desired. **LQR** design therefore becomes a very iterative process, especially when using larger systems. For this project, the weighting matrices $\mathbf{Q}_1$ and $\mathbf{Q}_2$ were chosen as,

$$\mathbf{Q}_1 = \text{diag}\left(\left[Q_{\overline{V}_W} \quad Q_{V_h} \quad Q_T \quad Q_{E_{\overline{V}_W}} \quad Q_{E_{V_h}}\right]\right) \tag{5.1.18}$$

$$\mathbf{Q}_2 = \text{diag}\left(\left[Q_{a_{n_c}} \quad Q_{T_c}\right]\right) \tag{5.1.19}$$

The weighting elements in the above matrices were chosen as the square of the inverse of the maximum desired deviation from the steady state value [18]. Therefore, each of the weighting elements contained in $\mathbf{Q}_1$ and $\mathbf{Q}_2$ were expressed as,

$$Q_{\sqsupset} = \frac{1}{(\text{Max Deviation in } \sqsupset)^2} \tag{5.1.20}$$

where ℶ represents a state or control input. Writing the weighting elements in the form given by equation (5.1.20), normalised the state or control input, and consequently allowed for a more intuitive selection of the weighting elements. The maximum deviation on the airspeed, climb rate and throttle states were set to 1 m/s, 1 m/s and 1 N respectively. For the actuation inputs, the normal specific acceleration actuator (a_{n_c}) was set to a maximum deviation of 0.2 m/s^2, and the throttle actuation state (T_c) to 0.5 N.

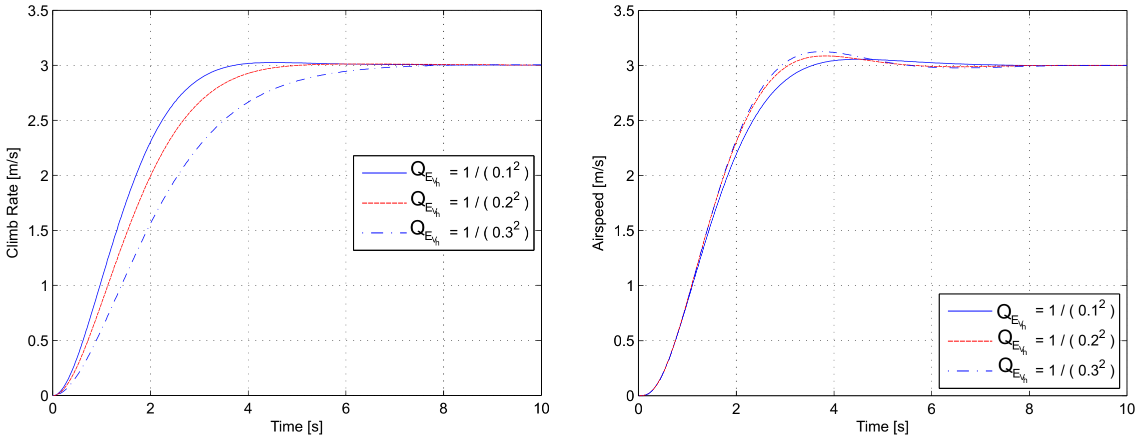

(a) (b)

Figure 5.2: (a) Climb Rate Step Response: Adjusting $Q_{E_{V_h}}$. (b) Airspeed Step Response: Adjusting $Q_{E_{V_h}}$.

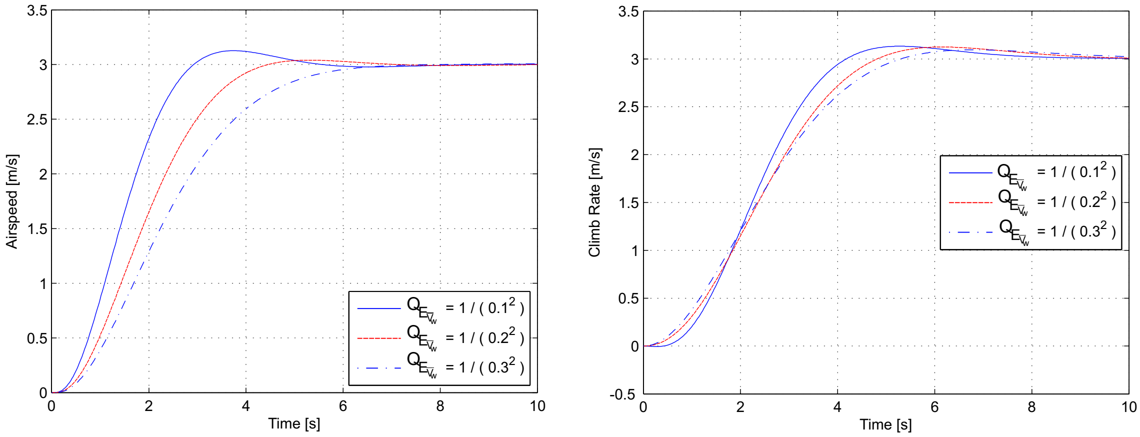

(a) (b)

Figure 5.3: (a) Airspeed Step Response: Adjusting $Q_{E_{\overline{V}_W}}$. (b) Climb Rate Step Response: Adjusting $Q_{E_{\overline{V}_W}}$.

Figures 5.2 and 5.3 show the closed loop step response for various values of $Q_{E_{V_h}}$ and $Q_{E_{\overline{V}_W}}$ respectively, when the unity gain block in figure 5.1 is replaced by the **NSA** controller designed in section 4.4. By decreasing the maximum desired deviation on the climb rate integrator state, the weighting on the state increases and the **LQR** algorithm returns feedback gains controlling the state more aggressively. The same is true for the airspeed integrator state. As shown by figures 5.2 and 5.3, when changing the weighting value of one state, the other state remains largely unaffected. This is because the coupling between airspeed and climb rate is weak for small pitch attitude angles. This allows the designer to select the desired response by changing only two variables, which underlines the advantage of using a reduced order model in the **LQR** design. With reference to figure 5.4, the weightings $Q_{E_{V_h}}$ and $Q_{E_{\overline{V}_W}}$ are chosen such that the timescale separation assumption between the rigid body dynamics and the point mass kinematics is enforced. Figure 5.4 shows that the closed loop poles end up in the allowable area, which is below the lower frequency bound discussed in section 4.4.1.

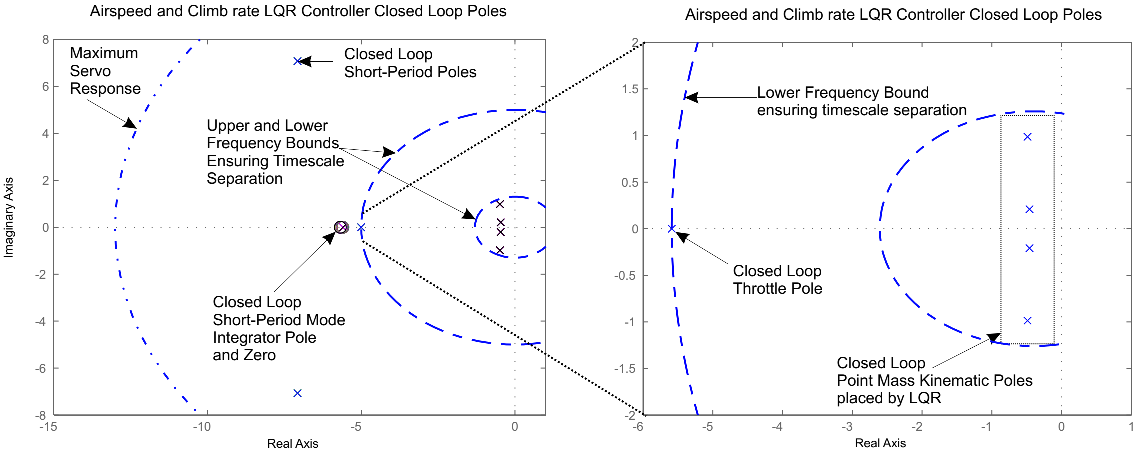

Figure 5.4: LQR design closed loop pole locations

For the purpose of this project, the speed of response of the airspeed and climb rate controller is not critical. It is desired to make the controller respond as quickly as possible, within the physical limitations of the aircraft, so as to provide maximum disturbance rejection without saturating the elevator or throttle, or violating the timescale separation assumption stated in section 4.3.2. Therefore, the climb rate rise time specification was chosen to be in the order of 5 seconds, and the airspeed rise time less than 10 seconds. A closed loop step response overshoot specification of less than 20% was imposed on both airspeed and climb rate. In a classic second order system, a 20% overshoot implies a phase margin of roughly 60°, providing sufficient additional phase lag at the gain crossover frequency [6]. Although phase and gain margins do not provide a complete indication about controller robustness for **MIMO** systems, the specifications are still used as guidelines when designing the control system since the **LQR** algorithm should provide robust enough feedback gains.

5.2 Altitude Controller

The altitude controller is the only longitudinal trajectory controller. The design approach is to generate a climb rate command from the altitude error signal, which means that only the extra integrator due to the height state need be stabilised by the feedback [14]. Before the height error signal is fed to the climb rate controller, it must be clipped at certain maximum and minimum values to ensure that it does not command climb rate signals in excess of ±3 [m/s], enforcing the assumption made during the linearisation of the aircraft outer loop model that the pitch angle is less than 10 degrees. The clipping of this command automatically ensures that the aircraft enters a constant climb when large altitude step commands are issued. The extra integrator, added naturally as a result of the height state, indicates that no additional compensator integrator is required to maintain zero steady state error, provided that there is no offset on the climb rate measurement.

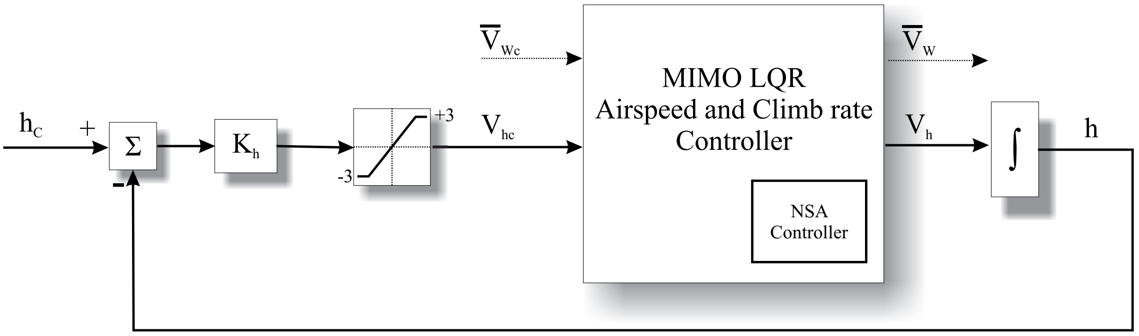

Figure 5.5: Altitude Control

After augmenting the dynamics given by equation (5.1.16) with the natural altitude integrator state h shown by figure 5.5, the altitude loop can be closed successively around the climb rate loop as shown. With reference to figure 5.5, h_c denotes an altitude command in meters (m), and K_h denotes the altitude feedback gain. Figure 5.6 (a) shows a root locus plot for the variation in the feedback gain K_h. Five poles are shown here, these being the four closed loop poles placed by the **LQR MIMO** control system, and one extra pole added by closing the altitude control loop.

A proportional gain of,

$$K_h = 0.1908 \tag{5.2.1}$$

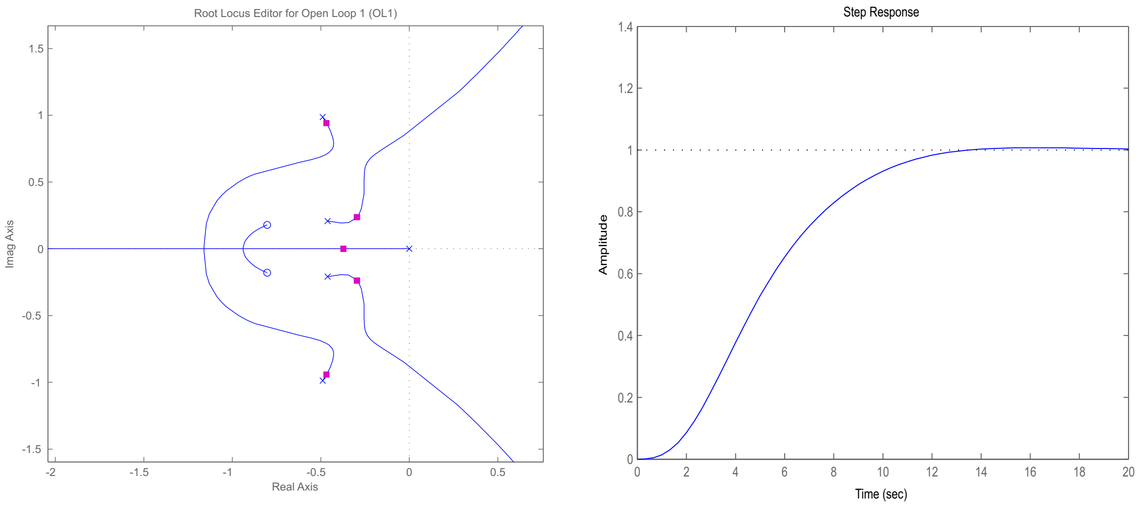

(a) (b)

Figure 5.6: (a) Altitude Controller Root Locus. (b) Altitude Controller Closed Loop Step Response.

is found to yield acceptable closed loop pole locations. The resulting closed loop step response is given by figure 5.6 (b), showing a less than 7 second rise time. The closed loop system response can be determined by,

$$\begin{bmatrix}\dot{x}\\ \dot{h}\end{bmatrix} = \begin{bmatrix}\mathbf{A} & -\mathbf{B}\begin{bmatrix}0 & K_h\end{bmatrix}^T \\ \mathbf{C} & 0\end{bmatrix}\begin{bmatrix}x\\ h\end{bmatrix} + \begin{bmatrix}\mathbf{B}\begin{bmatrix}0 & K_h\end{bmatrix}^T\\ 0\end{bmatrix} h_c \tag{5.2.2}$$

where **A** is the *closed loop* airspeed and climb rate state matrix, **B** is the climb rate input matrix defined by equation (5.1.16) and **C** is constructed to extract the altitude state h.

5.3 Aircraft Trim to Elevator Controller (ATEC)

The aircraft is equipped with an *actuator tray* that is adjusted in flight to move the aircraft centre of mass position, thereby adjusting the static stability margin. With reference to figure 5.7, a direct current (*DC*) motor is used to turn a screw thread, causing the actuator tray to displace linearly. Therefore, the first requirement of the **A**ircraft **T**rim to **E**levator **C**ontroller (**ATEC**) is to command and adjust the aircraft centre of mass position. The aircraft can be made statically stable, allowing for manual take off, after which the centre of mass can be shifted aft to evaluate the performance of the aircraft at the optimal centre of mass location specified by the aircraft designers.

The second requirement of the **ATEC** is to command and adjust the aircraft trim elevator setting in flight. This is useful if low-speed landings are desired. A positive trim

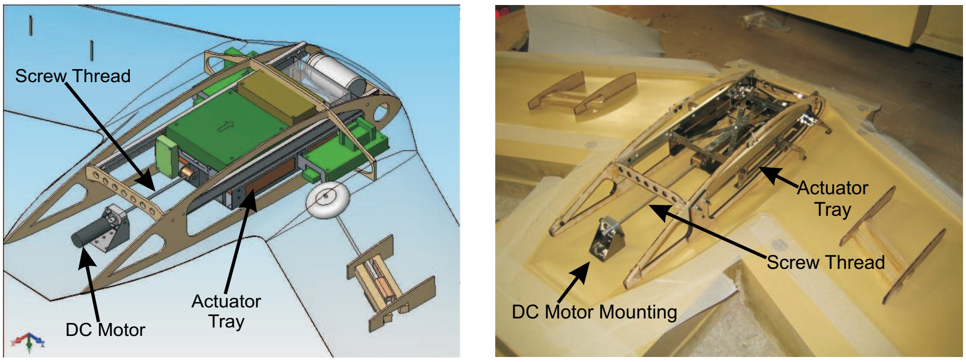

Figure 5.7: Actuator Tray and DC Motor

elevator value can be commanded, and the elevons can act as flaps reducing the aircraft's landing speed, enabling it to land on shorter runways. Although low-speed landings with positive elevon deflection are beyond the scope of this project, the **ATEC** is designed to cater for it. Section 5.3.1 starts by presenting the design of the aircraft centre of mass position controller, and section 5.3.2 follows with the design of a control system regulating the aircraft trim elevator setting.

5.3.1 Centre of Mass Position Control

The centre of mass position control architecture is shown conceptually by figure 5.8. A simple proportional feedback control system was designed, with feedback gain K_{cg}.

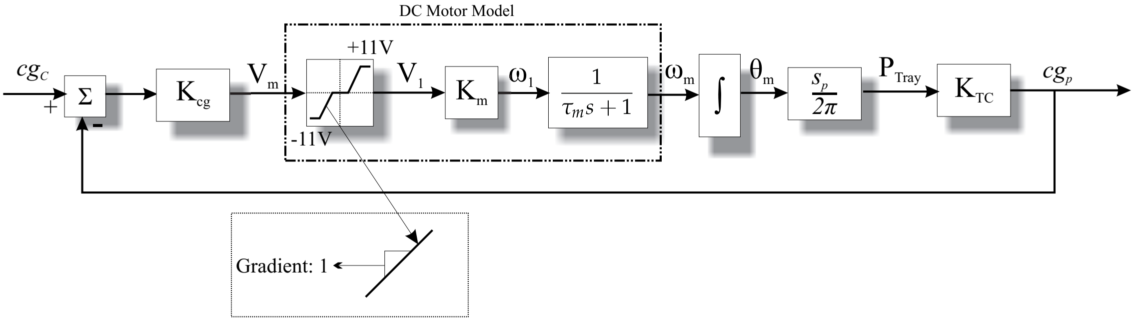

Figure 5.8: Centre of Mass Position Control

With reference to figure 5.8, V_m, ω_m and θ_m denotes the DC motor applied voltage, output speed (rad/s) and output angle (rad) respectively. The output angle θ_m is measured using an optical encoder mounted directly on the DC motor. The pitch of the screw thread attached to the DC motor is denoted by s_p, and the actuator tray position is denoted by P_{Tray}. The gain K_{TC} represents a linear relationship between the actuator tray position and aircraft centre of mass position, and is determined experimentally.

The DC motor model consists of two parts. The applied voltage enters a saturation block, also modelling the DC motor dead-band. The motor speed ω_1 is determined by multiplying the applied voltage V_m with the gain K_m. K_m, the motor DC gain, is 13.9 $[\frac{\omega_1}{V_1}]$ from the DC motor product data-sheet. The actual DC motor speed dynamic response is modelled with a low-pass filter, giving the output DC motor speed ω_m. When initially ignoring dead-band the DC motor model becomes,

$$\frac{\omega_m(s)}{V_m(s)} = \frac{K_m}{\tau_m s + 1} \tag{5.3.1}$$

where τ_m is the *no-load* motor mechanical time constant, and is given by $\tau_m = 7.28$ [ms] from the DC motor product data-sheet. In the above DC motor model, the motor armature inductance is considered negligibly small and is therefore ignored.

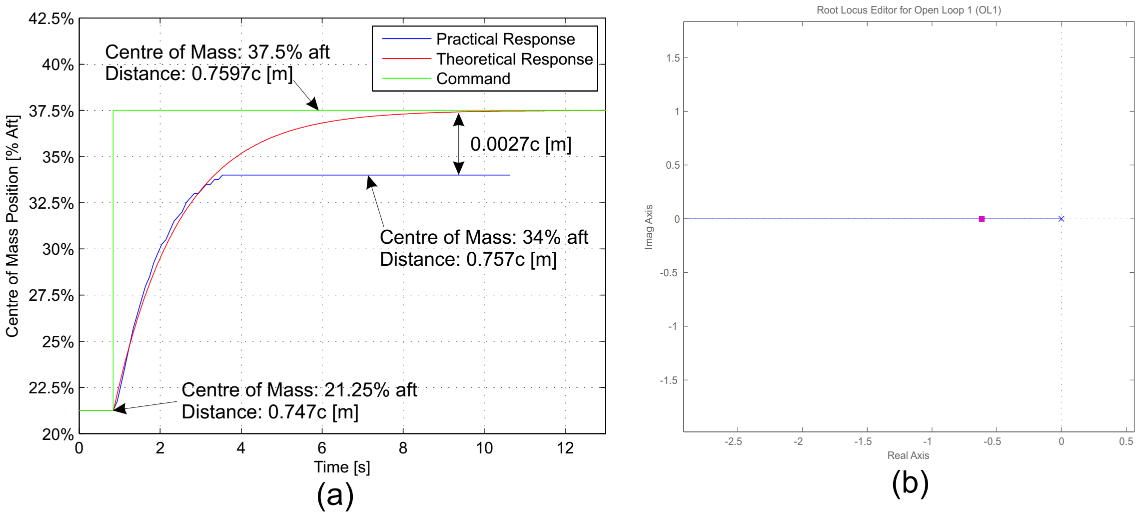

Figure 5.9: (a) Centre of Mass Position Controller Closed Loop Step Response. (b) Centre of Mass Position Controller Root Locus.

Figure 5.9 (b) shows a root locus plot for variations in the compensator gain K_{cg}. The DC motor dynamics (at 137 [rad/s]) operate at a frequency much higher than the dynamics of this control system, and consequently does not affect the centre of mass position dynamics. Note that the frequency of the DC motor dynamics is dictated by the *no-load* motor mechanical time constant, and that this time constant will not be 7.28 [ms] under load conditions. However, it is assumed that under typical load conditions concerning the actuator tray, that the DC motor dynamics is at a high enough frequency such that it does not influence the dynamics of the centre of mass position dynamics.

Recall that the assumption was made that the actuator tray dynamics operate at a frequency much lower than that of the rigid body rotational dynamics. With this assumption in place, the stability and control derivatives changing as a function of centre of mass position, and therefore actuator tray position, were considered parameters in the **NSA** control system designed in chapter 4. Therefore, the speed of response of the centre of mass position control system is not critical, as long as the aforementioned assumption is enforced. To this end, the gain K_{cg} is adjusted to provide a closed loop rise time of more than at least 1.5 seconds.

The centre of mass position closed loop step response is shown by figure 5.9 (a), where the commanded centre of mass position is expressed as a fraction of the aircraft chord length c. With reference to figure 5.9 (a), the practical closed loop step response of the centre of mass position control system shows a steady state error. The steady error is 0.0027c, which is 21.25% of the final value and therefore not acceptable.

The steady state error arises largely because of the inherent DC motor dead-band. When the voltage applied to the DC motor drops too low, the motor stops and consequently a steady state error is observed in the closed loop output response. This can be remedied to a certain extent by mathematically undoing the effect of the dead-band, thereby making the DC motor linear in its dead-band region. It was found experimentally that the DC motor enters its dead-band region when the applied voltage reaches $V_m \in [4.4, -4.4]$V. The following simple function performs a linear transformation, changing the applied voltage from $V_m \in \pm[0, 11]$V to $V_m \in \pm[4.4, 11]$V.

$$V_m = 0.6V_m \pm 4.4 \tag{5.3.2}$$

The practical closed loop step response is given by figure 5.10. Using the linear transformation function, the steady state error reduces to less than 0.15% of the final value.

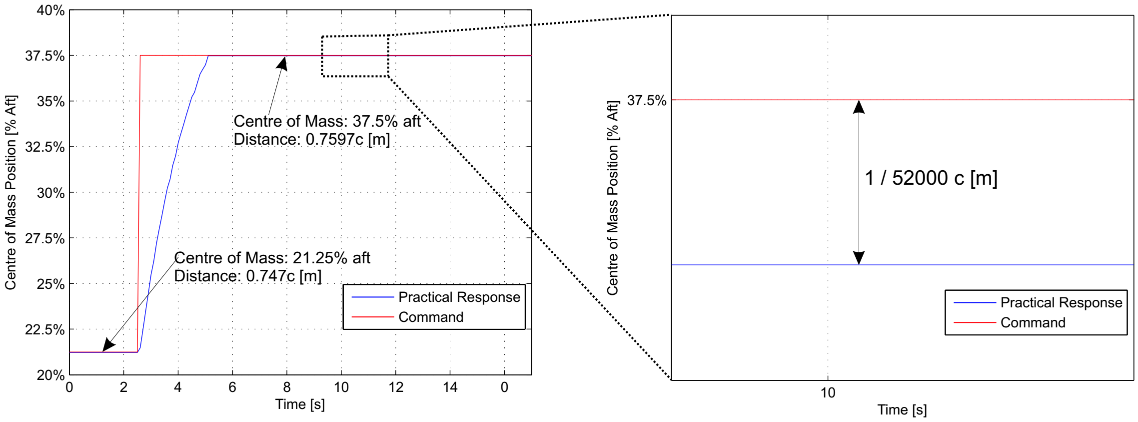

Figure 5.10: Centre of Mass Position Control Closed Loop Step Response after mathematically removing the DC motor dead-band

Unfortunately, reducing the steady state error by implementing the linear transformation function (5.3.2) is not a very elegant solution to the problem. Unmodelled effects such as static friction, motor backlash, backlash in the mechanical screw thread and aircraft orientation all act as disturbances to the system, inducing a steady state error on the commanded centre of mass position.

The following section briefly presents the design and associated practical response of an improved, more elegant, control system regulating centre of mass position with zero steady state error.

5.3.1.1 Proposed Improved Centre of Mass Position Control Design

It is desired to command centre of mass positions with zero steady state error. With reference to figure 5.11 (a), a pure integrator compensator removes steady state errors, but the closed loop response is unstable.

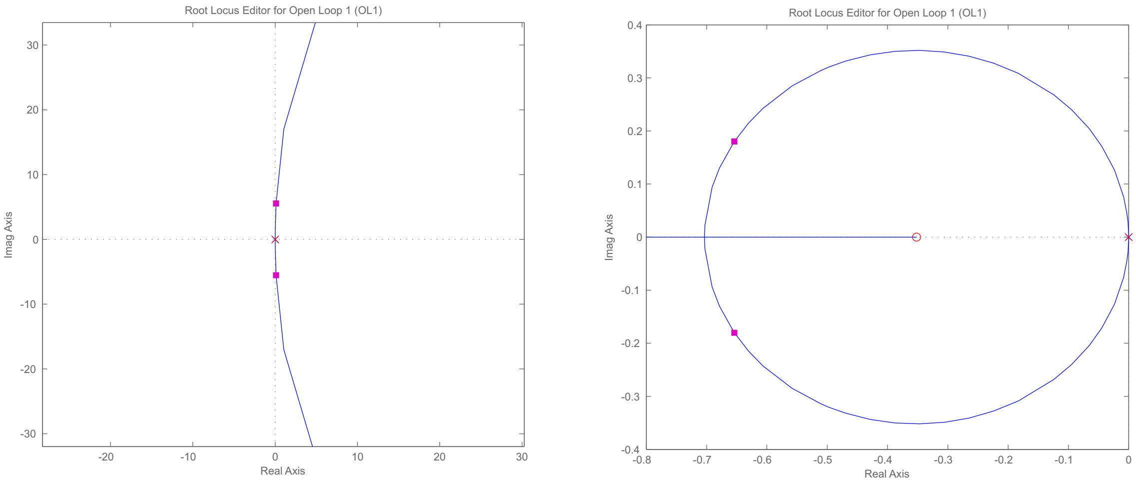

(a) (b)

Figure 5.11: (a) Integrator Compensator on Centre of Mass Position. (b) Lag Compensator on Centre of Mass Position

By designing a PI compensator, a zero is added in the left half plane and the closed loop response is stable (figure 5.11 (b)). The compensator is given by,

$$D(s) = \frac{K_p\left(s + \frac{K_I}{K_p}\right)}{s} \tag{5.3.3}$$

where K_I denotes the integrator gain and K_p the proportional gain. The integrator in the PI compensator provides infinite steady state gain and consequently removes steady state errors. As the frequency of the compensator zero approaches that of the compensator integrator, the phase margin improves (figure 5.12) but steady state reference following degrades. On the other hand, if the frequency of the compensator zero approaches the frequency of the closed loop poles, steady state errors are removed more promptly but at the expense of a degraded phase margin. Therefore, the frequency of the zero and associated compensator gain is selected such that sufficient steady state reference following is achieved with adequate phase margin.

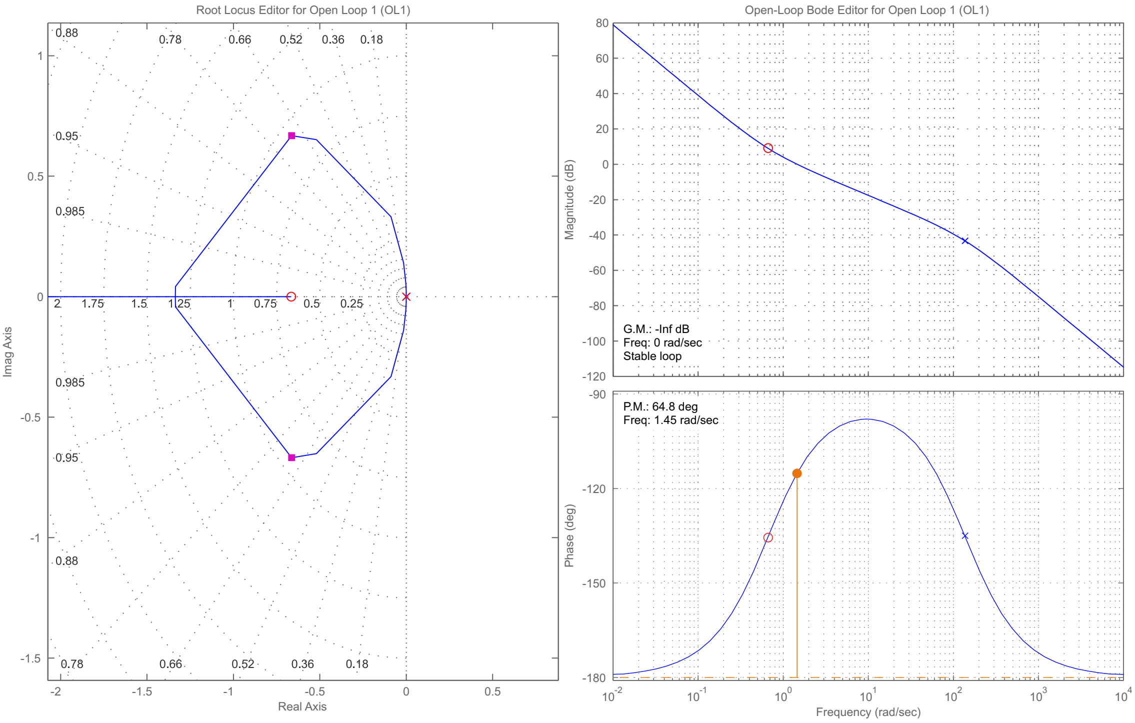

Figure 5.12: Lag Compensator Designed with Compensator Bode Plot

Figure 5.13 shows a bode plot of the resulting design, achieving a phase margin of 67.4°. Figure 5.14 shows the practical step response, with 20.5% overshoot. Note that although the rise time is very high, it is still well below the frequency of the rigid body rotational dynamics. Therefore, the validity of the timescale separation assumption made between the actuator tray and rigid body rotational dynamics is maintained.

As previously mentioned, the control system described here is an improvement to the proportional centre of mass position controller designed in the previous section, but was regrettably not implemented during any of the practical flight tests.

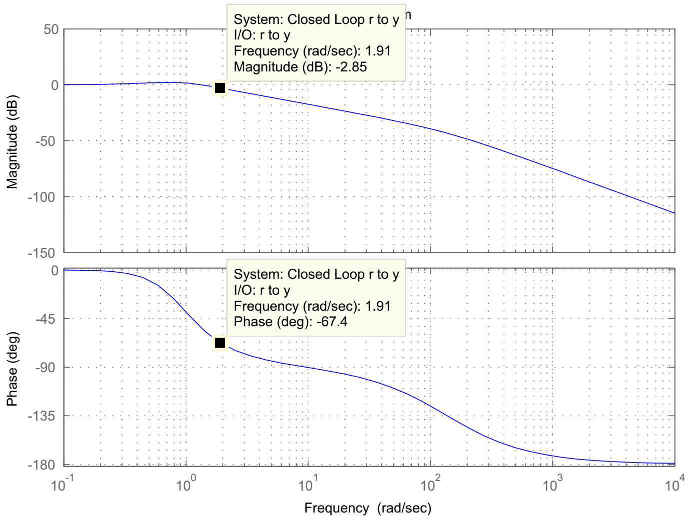

Figure 5.13: Closed Loop System Frequency Response

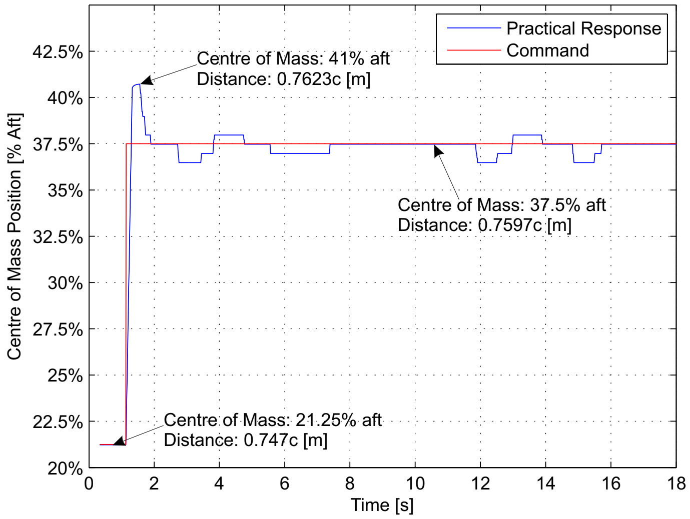

Figure 5.14: Practical Step Response of Improved Centre of Mass position control system

5.3.2 Trim Elevator setting Control

The aircraft trim elevator setting controller architecture is shown conceptually by figure 5.15.

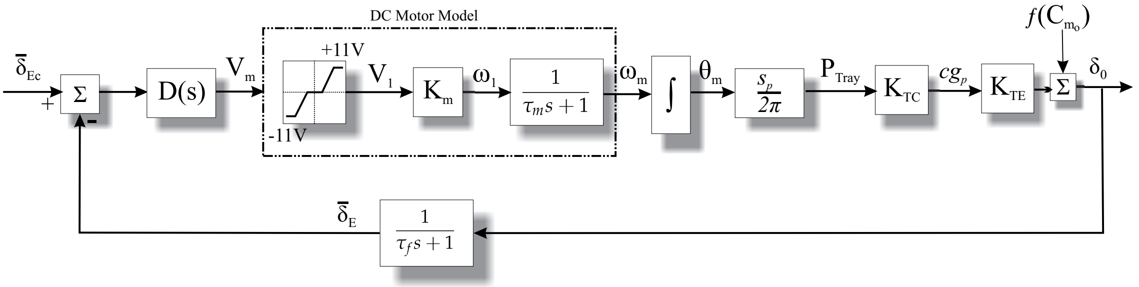

Figure 5.15: Trim Elevator Setting Controller conceptual overview

With reference to figure 5.15, the elevator signal commanded by the **NSA** control system is low-pass filtered to obtain the average elevator signal. The filtered elevator signal is fed back to allow for the average, or *trim* elevator setting angle to be commanded. The gain K_{TE} relates centre of mass position to elevator setting angle. K_{TE} is determined by solving the longitudinal rigid body rotational dynamics equations for the trim condition, and is given by [2],

$$K_{TE} = \frac{C_{m_\alpha} C_L - C_{m_\alpha} C_{L_0}}{C_{m_\alpha} C_{L_{\delta_E}} - C_{m_{\delta_E}} C_{L_\alpha}} \tag{5.3.4}$$

where C_{m_α}, $C_{L_{\delta_E}}$ and C_{L_α} are all linear functions of cg_p.

Figure 5.16 shows a root locus plot of the closed loop system when the compensator is only a proportional gain. The lower frequency pole visible is the natural integrator pole from ω_m to θ_m, and the higher frequency pole is the low-pass filter used to filter the elevator signal with time constant τ_f.

It is desired to command trim elevator setting angles with zero steady state error. With reference to figure 5.15, zero steady state error cannot be achieved through proportional feedback alone because of DC motor dead-band. Furthermore, the following factors are most likely to manifest into trim elevator setting errors over time:

- Errors in determining the gain K_{TC}.
- The presence of the zero lift pitching moment coefficient C_{m_0}[1], which was *assumed* to be zero due to the symmetrical camber of the wing of typical aircraft.

---

[1] The pitching moment at zero angle of attack. Typically aerofoil camber creates this moment.

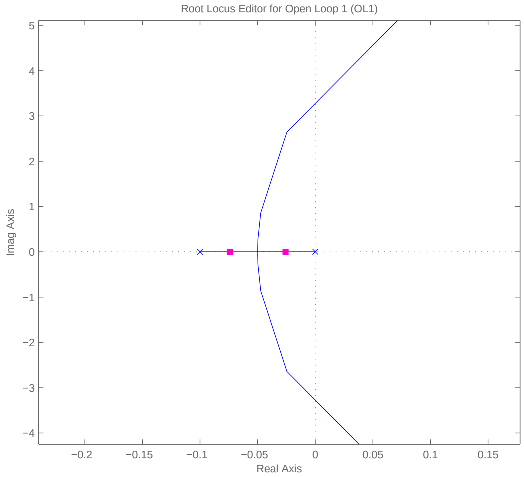

Figure 5.16: Trim Elevator Setting Controller: Root Locus Plot

- Errors in the stability derivatives given by equation (5.3.4).

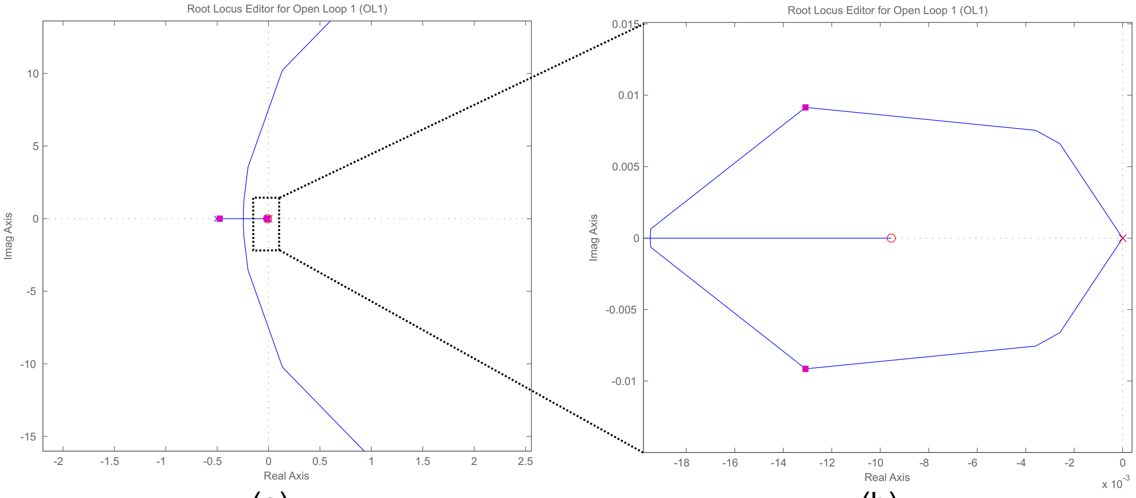

(a) (b)

Figure 5.17: Trim Elevator Setting Controller: Root Locus Plot with PI compensator

Therefore, to remove steady state modelling errors a PI control system was designed. With reference to figure 5.17 the low-pass filter cut-off frequency is selected at 0.5 [rad/s]. Considering that the Short period mode dynamics, controlled by the elevator, operate at a frequency greater than 7 [rad/s], the 0.5 [rad/s] cut-off frequency is low enough to provide a sufficiently averaged elevator signal over time. It was decided to design the trim elevator setting controller such that it reacts very slowly to changes in the trim elevator

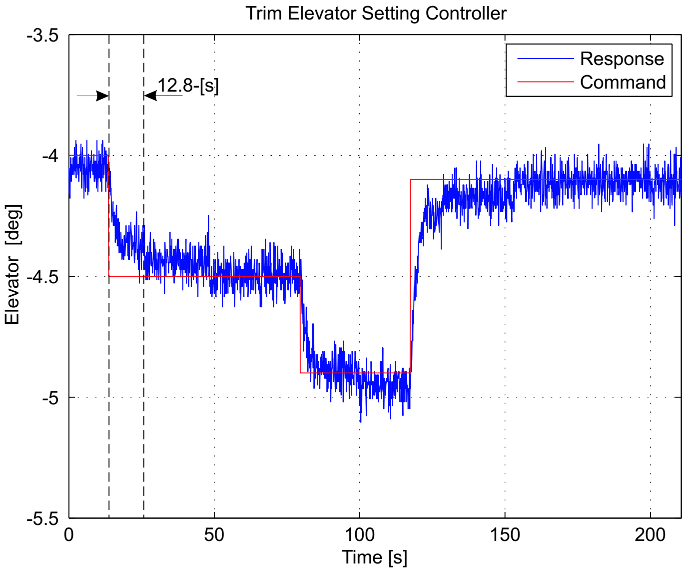

Figure 5.18: Trim Elevator Setting Controller Simulated Step Response

setting angle. Therefore, the trim elevator setting control system is designed with a rise time of about 13 seconds.

Figure 5.18 shows the closed loop step response of this controller when simulated in the hardware in the loop environment outlined in chapter 7. Note that the total elevator signal is shown by figure 5.18, *not* the low-pass filtered result. During the test flight phase of this project, the flight control systems were evaluated for various centre of mass positions rather than elevator trim angles. It is both more insightful and intuitive to describe the static stability margin using centre of mass position as opposed to using trim elevator setting angles. As the primary outcome of the project was to demonstrate control of a variable stability UAV, the centre of mass position controller was used during practical flight tests and not the trim elevator setting controller.

5.4 Simplified Lateral Flight Control System Design

This section provides a brief outline of the lateral flight control systems designed for this project. Since the variable stability aircraft problem manifests itself primarily in the aircraft longitudinal dynamics, conventional lateral flight control systems were designed. Refer to appendix A for the detailed designs.

With reference to figure 5.19, the lateral flight control system consists of a Dutch Roll damper, yaw rate controller, heading controller, cross track error controller (guidance controller) and a navigation algorithm respectively. A brief overview of the aforementioned systems is given here.

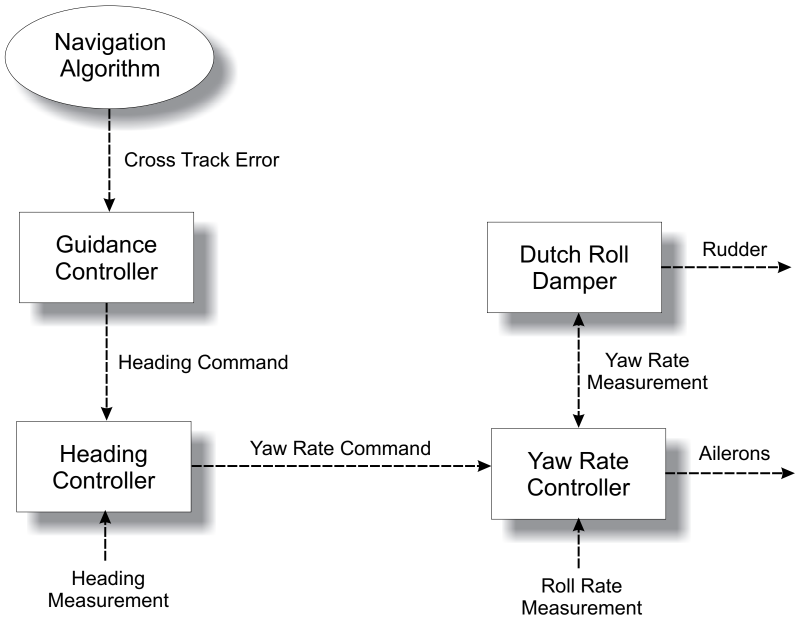

Figure 5.19: Lateral Flight Control System Conceptual Overview

Dutch Roll Damper: With reference to figure 5.19, a standard Dutch Roll damper is designed, as outlined in [2], by feeding a washed out yaw rate signal back to the rudder to suppress the typically lightly damped Dutch Roll mode. The washout filter ensures that the Dutch Roll damper does not counter the constant yaw rate experienced during steady turns.

Yaw Rate Controller: The yaw rate of the aircraft is well approximated as being linearly related to the roll angle in a steady state turn at low bank angles as argued by [14]. Therefore, the concept behind the lateral attitude controller is to feed back yaw rate to the ailerons instead of an estimated roll angle. A major advantage of this strategy is that significantly fewer calculations are required since no estimation takes place [14]. An integral type controller, using feedback from both the aircraft roll and yaw rates to the ailerons to improve lateral stability, is designed based on the ideas presented in [2]. This ensures that the commanded yaw rate is tracked with zero steady state error even when subject to constant steady state disturbances, such as those due to asymmetry in the actual aircraft.

Heading Controller: A simple proportional feedback controller, designed in the discrete time domain at 4Hz, is used since the natural integrator present in the heading dynamics ensures a zero steady state tracking error when no steady state disturbances are present, as outlined in [14]. It is responsible for converting a *heading error* signal into a yaw rate command, and regulates ground track heading.

Cross Track Error Controller: A simple proportional controller, designed in the discrete time domain at 4Hz, is responsible for regulating the lateral path tracking error by commanding an appropriate heading.

Navigation Algorithm: According to the specifications, the autopilot must be capable of autonomous way-point navigation. The designed cross track error trajectory controller is capable of guiding the aircraft along a given lateral path. However, the navigation algorithm is responsible for calculating a flyable path from one way-point to the next (*path planning*). Then between this path and the aircraft's current location, the cross track error is calculated. For the purposes of this project, a way-point is defined as a structure containing a three dimensional location and a destination heading. A detailed review of the entire navigation algorithm is available in appendix A.

5.5 Summary

Aircraft independent outer loop controllers were designed in this chapter, operating via inner loop controllers dynamically invariant to centre of mass position and therefore static stability margin. A **MIMO LQR** controller regulating airspeed and climb rate, was designed such that the timescale separation assumed between the rigid body rotational dynamics and point mass kinematics remained valid.

After the design of the altitude control system, the **ATEC** control strategy was developed. This entailed the design of two different control systems, one able to regulate the aircraft centre of mass position and another which regulates the trim elevator setting angle. It was shown that a PI compensator provided the best control solution for both the centre of mass position and trim elevator setting control systems.

With all of the flight control systems designed, it remained now to properly verify these designs through simulation. A hardware in the loop simulation environment was used to accomplish this task, and in doing so minimise risk during practical implementation on an actual aircraft. The hardware in the loop simulation environment will be discussed in chapter 7.

Chapter 6

Avionics and Ground Station

This chapter is aimed at presenting the avionics and associated subsystems developed for the project. The mass and volume design specifications of the avionics were determined by practical constraints imposed by the aircraft.

Recall from chapter 1, that one of the main design goals of Sekwa (the CSIR blended-wing-body aircraft) was to reduce drag at some optimal centre of mass location. A payload bay, shown by figure 6.1, was designed by the CSIR for the avionics systems. Consequently, an increase in the volume of the payload bay leads to an increase in the amount of drag created.

Furthermore, if the avionics and associated subsystems are found to add undesired mass to the vehicle, such that the total aircraft mass deviates from the optimal design specifications, unwanted drag will be created.

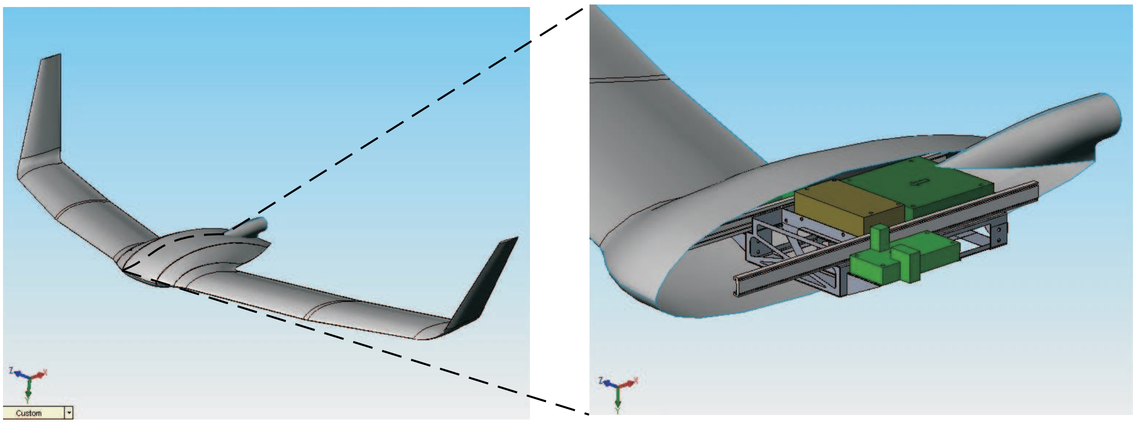

Figure 6.1: Aircraft Avionics Payload Bay

Therefore, during the course of the project close collaboration between the CSIR and SU (Stellenbosch University) played an important role in designing the main avionics system. The following design restrictions on the complete avionics system were agreed upon:

1. Maximum weight of less than 600g.
2. Maximum height of less than 64mm.
3. Maximum length of less than 190mm.
4. Maximum breadth of less than 100mm.
5. Desired operating time of 1 hour.

The Linux-based OBC (On-Board Computer) used at SU has a total mass of 600g [19], and when adding the remainder of the avionics subsystems the total avionics mass quickly accumulates to over 1.3kg, which is completely unacceptable. With the Linux-based OBC being the heaviest component in the existing SU avionics package, it was decided to replace this component with a smaller, lighter OBC, such that the complete avionics system (including sensor and actuator subsystems) adhere to the above physical constraints. Therefore, a new OBC system was designed specifically for this project to be as small as possible while maintaining crucial functionality, and the payload bay (more specifically the actuator tray) design underwent minor adjustments to achieve the most efficient design while accommodating the avionics. A practically feasible design solution was achieved within the specified constraints without excessively compromising either aerodynamic efficiency or avionics functionality.

This chapter begins by providing a conceptual overview of the avionics designed for this project (section 6.1). A high-level, block diagram approach is adopted to present the avionics development and outline the operation thereof. Section 6.2 follows with a brief overview of the ground station software developed.

6.1 Avionics

Figure 6.2 shows the conceptual layout of the complete avionics system. The entire avionics system consists of various nodes connected to one another by means of a CAN (Controller Area Network) bus. The complete avionics system consist of the following CAN nodes:

1. Main Avionics Node
2. DC Motor Control Node
3. Pressure Node
4. IMU (Inertial Measurement Unit) Node

5. Servo Control Node

The Pressure, IMU and Servo Control Nodes used in this project already exist as part of Stellenbosch University's standard avionics package, and have been applied to numerous UAV research projects at Stellenbosch University with great success. For detailed information regarding these nodes, refer to [20]. The nodes designed specifically for this project are the **DC Motor Control Node** and the **Main Avionics Node**, and are briefly discussed next.

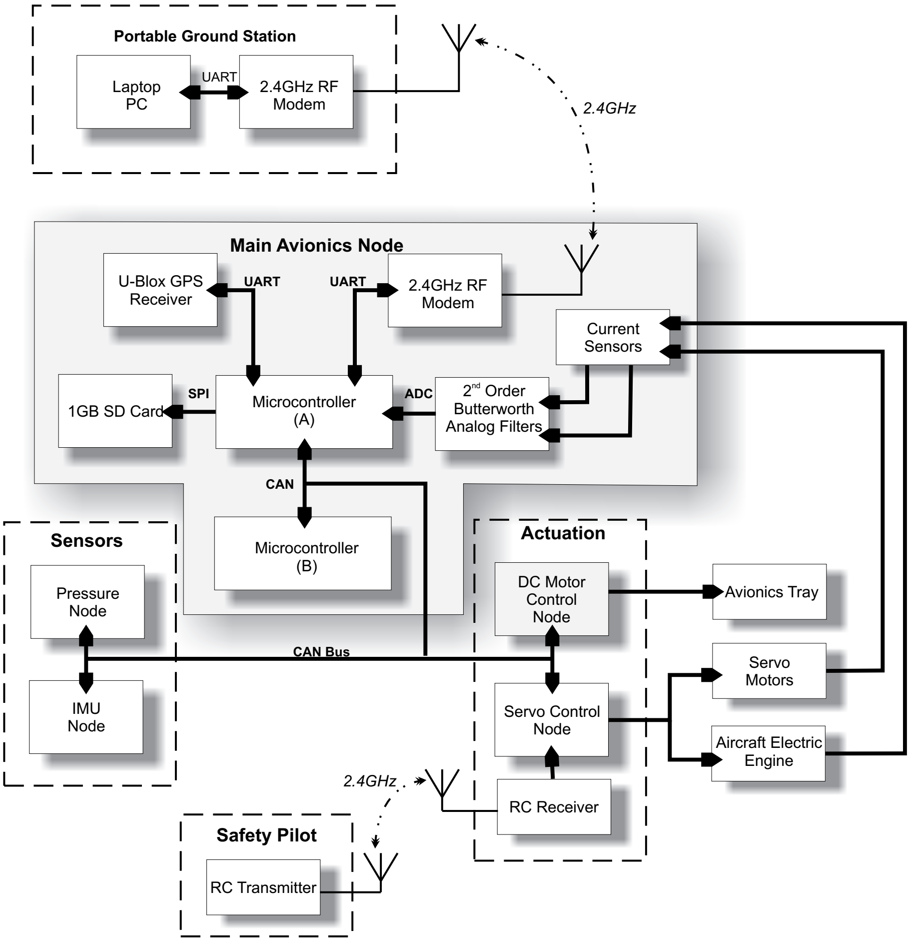

Figure 6.2: Avionics Conceptual Overview

6.1.1 DC Motor Controller CAN node

This node was designed to control the aircraft centre of mass position, using a DC motor to linearly displace the avionics *actuator tray*.

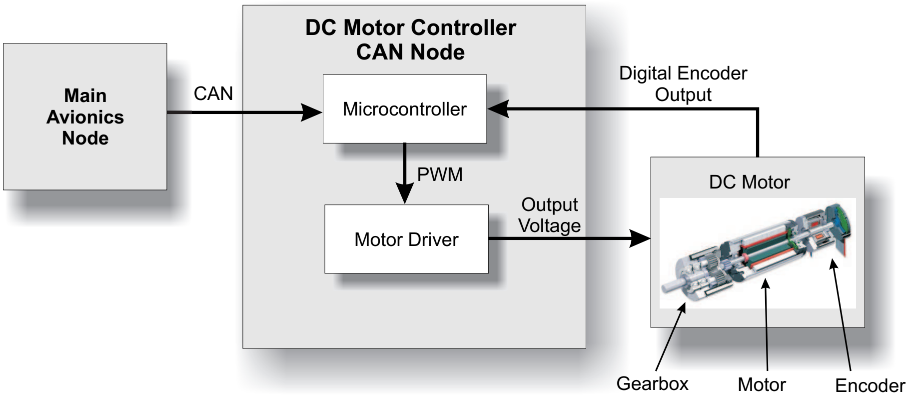

Figure 6.3: DC Motor Controller CAN Node Conceptual Overview

The **ATEC** controllers designed were implemented on this node, with centre of mass position and trim elevator setting commands received from the Main Avionics Node via the CAN bus network. The primary components of this system are:

- Microcontroller: dsPIC30F4011
- DC Motor Driver: LMD18200
- DC Motor: MAXON RE-MAX 17

The choice of microcontroller here is not critical. The dsPIC30F4011 was chosen to minimise development time, as this device supports PWM (Pulse Width Modulation), quadrature encoding and CAN modules.

The DC motor on the other hand was specifically chosen for its small size and weight characteristics. The lightest commercially available option at the time, the MAXON RE-MAX 17, is 17mm in diameter, has an integrated digital encoder and gearbox, and weighs only 27g. The encoder provides position feedback of the actuator tray, used in the control feedback loop. The following section investigates the choice of the DC motor gearbox in more detail.

6.1.1.1 DC Motor Gearbox Considerations

The DC motor, screw thread, actuator tray and avionics are shown in figure 6.4. The following practical considerations determined the type of DC motor gearbox used:

- The DC motor must provide enough torque in order to turn the screw thread and displace the actuator tray when the aircraft is pitched at extreme angles.
- The DC motor must be able to displace the actuator tray at a high enough rate in order to stabilise the aircraft during possible emergency situations.

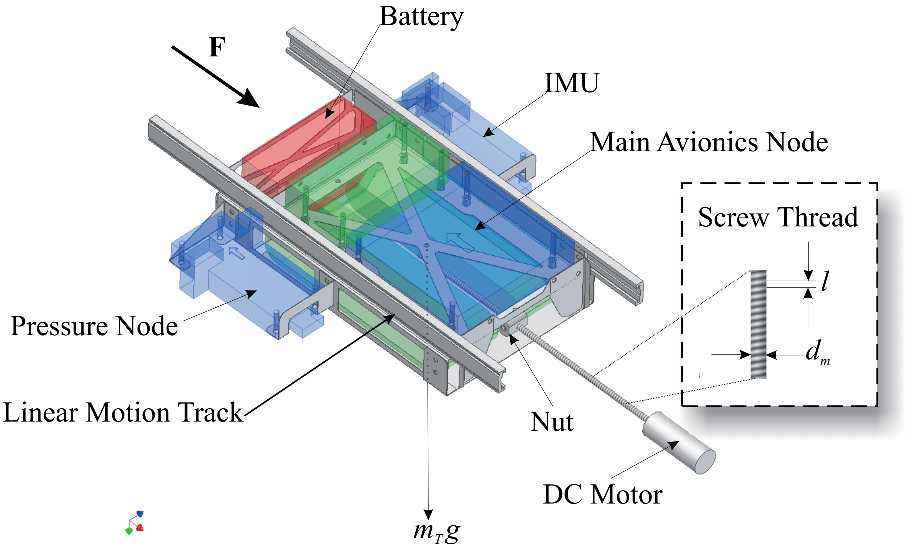

Figure 6.4: Actuator Tray With DC Motor and Screw Thread

The following analysis determines the torque required by the DC motor to move the actuator tray. Consider the case where the aircraft is pitched at 90°. It is assumed that the aircraft is not accelerating axially, and that the friction between the actuator tray and linear motion tracks is negligibly small. Under the aforementioned conditions, the axial compressive force **F**, shown by figure 6.4, can be written as,

$$\mathbf{F} = m_T g \tag{6.1.1}$$

where m_T is the mass of the actuator tray. Under this condition, the torque required (T_R) by the DC motor to raise the actuator tray load is given by [13] as,

$$T_R = \frac{\mathbf{F} d_m}{2} \left(\frac{l + \pi f d_m}{\pi d_m - f l} \right) \tag{6.1.2}$$

In the above equation, $d_m = 4$mm is the screw diameter, $l = 1$mm is the screw pitch and $f = 0.08$ is the friction coefficient [13] between the screw thread and the nut mounted on the actuator tray.

Assuming an absolute maximum actuator tray mass of 2kg, and that the aircraft is pitched at 90°, the force **F** amounts to 19.62 [N]. Evaluating equation (6.1.2) under the aforementioned conditions, 6.3 [mNm][1] is required by the DC motor to overcome the mass of the actuator tray. According to the DC motor product data sheet, the maximum

---

[1] mNm denotes milli-newton meter

continuous motor output torque is 3.34 [mNm], which is 2.96 [mNm] less than the maximum amount of torque required.

Therefore, a reduction gearbox was required to sufficiently increase the amount of DC motor output torque without excessively decreasing the output speed. The gearbox chosen was a 4.4:1 reduction planetary gearbox. This gearbox had the smallest reduction ratio of the available manufacturer options, and subsequently increased the maximum continuous motor torque to 14.7 [mNm].

However, by adding the gearbox, the nominal DC motor speed was reduced from 4180 [rpm] to 950 [rpm]. Assuming that, practically, only 600 [rpm] could be achieved due to friction and motor internal losses, the maximum possible actuator tray speed V_T can be calculated as follows,

$$V_T = 600\,[\mathrm{rev/min}] = 10\,[\mathrm{rev/s}] \tag{6.1.3}$$

$$V_T = 10\,[\mathrm{rev/s}] = 10 * l\,[\mathrm{mm/s}] \tag{6.1.4}$$

where l is the mechanical screw thread pitch. Expressing the actuator tray speed as a percentage of centre of mass position change ($\%_{cg}$), the maximum theoretical speed is given by,

$$V_T = 7.143\,[\%_{cg}/s] \tag{6.1.5}$$

The maximum speed that the DC motor can move the actuator tray is important, when it is desired to stabilise the vehicle as quickly as possible during emergency situations. According to the above results, the DC motor is theoretically capable of moving the actuator tray over the entire range in 14 [s]. Table 6.1 shows the practical results obtained when the DC motor was commanded to stabilise the aircraft from its most unstable position, at different pitch angles and at maximum speed.

Aircraft Pitch Angle	Time [s]
0°	14.2
45°	14.2
90°	14.5

Table 6.1: Time taken by DC motor to move Actuator Tray over entire range of motion

The practical results given in table 6.1 indicates that the DC motor was capable of moving the actuator tray over the entire range of motion in less than 15 seconds. Although the gearbox enables the DC motor to move the actuator tray very effectively, the overall speed needed to recover the stability margin is very low. Assuming that the pilot can control the aircraft when the centre of mass is in front of the AVL predicted neutral point, the centre of mass is required to move a distance of 16% from its most unstable position. Moving the centre of mass 16% with the chosen gearbox takes roughly 2.2 $[s]$. Considering that the primary stability problem is in the Short period mode dynamics, when the centre of mass is in the aft position, a recovery time of 2.2 $[s]$ is very slow when compared to the bandwidth of the Short period mode. The low recovery speed is the result of the classic design trade-off between torque and speed. For this project however, torque was favoured above speed, since it is more important to stabilise the vehicle, albeit slowly, as opposed to risking the possibility of the tray not moving at all. The resulting design was agreed upon by both the CSIR and SU.

Measurement Precision: The microcontroller quadrature encoder interface was configured to provide double count resolution. With the encoder situated on the high-speed side of the gearbox (figure 6.3), the centre of mass position could be measured to within 0.4%, providing excellent resolution when implementing the **ATEC** control systems.

6.1.1.2 Safety Features

When the DC motor controller node is switched on, the avionics tray is moved forward until a mechanical contact switch is pressed by the tray. This will zero the encoder position measurement, and the centre of mass is measured with the zeroed position as its absolute reference point. The DC motor controller CAN node only operates if it receives a synchronisation signal from the Main Avionics CAN node at 20ms intervals. If the synchronisation signal is not received, it is assumed that the Main Avionics CAN node entered a possible error state. This results in the DC motor controller CAN node automatically stabilising the aircraft by moving the actuator tray forward at full speed until the contact switch is pressed.

6.1.2 Main Avionics CAN Node

This node was designed such that it acts as a *drop-in* replacement for the OBC used at SU. It was designed to be as generic as possible, allowing for more of the same nodes to be added to the system should extra processing power be required. The Main Avionics Node consists of the following subsystems:

- Two 16 bit Embedded Microcontrollers operating in parallel
- GPS receiver
- RF (Radio Frequency) Modem
- Current Sensors

- Data Logging on a 1 gigabyte SD (Secure Digital) card

A brief conceptual outline of each of the aforementioned subsystems are given next.

6.1.2.1 Embedded Processing Power

Two 16 bit microcontrollers, communicating via a dedicated CAN bus, are responsible for all of the on-board calculations required to implement the complete autopilot system. The specific microcontroller device used was dictated by both *cost* and *development time*. Consequently, the dsPIC30F6014 microcontroller was chosen. These devices provide adequate processing power with low power consumption, and were already used extensively by the SU UAV research group, therefore sufficient device support and developed software was readily available. Furthermore, the device supports a CAN controller module, simplifying the interface designed between the various CAN sensor and actuator control nodes. The functionality of each microcontroller is outlined next.

Microcontroller (A): With reference to figure 6.2, Microcontroller (A) is responsible for the following operations:

- Receiving and Transmitting data via the RF link using the SU RF data parser (see [19]).
- Parsing the received GPS data string and extracting the relevant information.
- Sampling the current sensors.
- Executing the Navigation algorithms.
- Data logging and file management of sensor data received from the CAN nodes.

Microcontroller (B): This device is dedicated to executing the flight control routines, including the stability augmentation control system. Of all of the flight control systems designed, the **NSA** stability augmentation control system is the *most* important, and consequently was assigned the highest priority on microcontroller (B).

6.1.2.2 GPS Module

The GPS module is the u-Blox RCB-4H OEM Receiver with a 25 dB gain active antenna and 4Hz update rate. This low cost module has been used extensively in practical UAV research projects at SU and provides good measurement accuracy. The module provides the necessary state information for autonomous way-point navigation.

6.1.2.3 Radio Frequency Communication Module

The radio module consists of a MaxStream XStream 2.4GHz OEM Transceiver with a 2.1 dB gain active dipole antenna. The modules have been proven in a number of Stellenbosch University UAV projects to provide good, reliable line of sight communication. These transceivers provide addressed packets with full duplex communication at 9600 bps to be used for command and telemetry purposes.

6.1.2.4 Current Sensors

If drag is reduced at the optimal centre of mass location, it is expected that the aircraft will need less power to hold its trim airspeed. Therefore, a LEM HXS 50-NP current transducer (figure 6.5) is used to measure the main engine current dissipated throughout the flight. The LEM HXS 50-NP current transducer is a Hall effect sensor, with galvanic isolation[2] between the primary and secondary circuit. The primary circuit is the main current carrying conductor to the aircraft's electric engine.

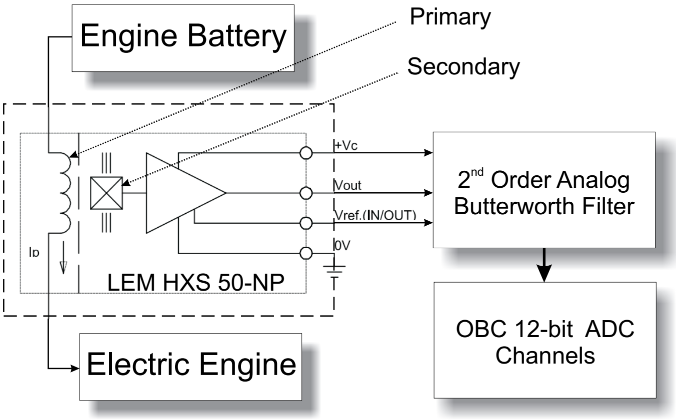

Figure 6.5: LEM HXS 50-NP

With reference to figure 6.5, since the primary and secondary circuits are isolated, the sensor is non-invasive and will therefore not cause the engine to stop in the event of accidental sensor failure. A similar sensor was used to obtain the current dissipated by the servo actuators. This allows for an additional measurement of the control effort required to stabilise the vehicle at unstable centre of mass locations, the possible applications of which are discussed further in chapter 9.

Furthermore, current measurements are extremely useful if longer flight times are desirable, as the amount of battery power used can be determined throughout the flight.

---

[2] Galvanic isolation is the principle of isolating functional sections of electric systems such that charge-carrying particles cannot move from one section to another, i.e. there is no electric current flowing directly from one section to the next.

The current sensors provide a voltage output proportional to the measured current. The voltage signal is filtered with a second order analog Butterworth filter before being sampled by the 12 bit analog to digital converters on the microcontroller. For detailed information regarding the Butterworth filters designed, refer to [12].

6.1.2.5 Data Storage

Two forms of data capturing were implemented, the first form involved streaming data to the ground station and the second involved on-board solid state storage.

It is desired to easily access and retrieve stored telemetry data, therefore Microsoft's FAT32 file system was implemented on a 1 gigabyte SD card with an SPI interface. This enables the extraction of telemetry data using any standard SD card reader. The data file is thereafter processed using MATLAB to obtain the relevant flight and diagnostic information. For detailed information regarding the FAT32 file system refer to [23], and on the SD card itself see [24].

To prevent telemetry data from being corrupted in the event of accidental power failure, or if the aircraft has a hard landing (or a possible crash), the file system was implemented slightly differently than it is usually implemented on a standard personal computer. Normally, a file is created and the file system along with the directory structure is dynamically updated as the file size increases. However, should an accidental power failure occur, the file system might be corrupted, preventing Windows from reading the data file. Therefore, during the initial power-up sequence, the OBC creates the entire file system and directory structure statically of one 30MB data file. Only the file system and the directory structure is written, with the file still containing *random* data. Telemetry data is written sequentially to the 30MB data file, with the amount of data logged transmitted to the ground station. With the amount of logged data known, MATLAB is then used to extract the data from the 30MB file. The 30MB file size can be easily increased if required, however for the purpose of this project, one 30MB data file proved to be more than what was required to successfully store all of the relevant data during a typical test flight.

In the event of temporary loss of telemetry link between the aircraft and ground station, the current amount of data stored will be received by the ground station once the link is restored since it is streamed to the ground station every second.

As a recommendation, the amount of data logged can be written on the data card as well. This could be written as a separate *status* file, which could be read by MATLAB to determine the relative file size before extracting the data from the data file. Storing the amount of data logged, rather than relying on the RF telemetry link, should provide adequate data retrieval capability during both RF telemetry link and power failure.

6.1.2.6 Power Management

The avionics system is powered by a three cell 11.1V Lithium-Polymer battery. A DC-DC converter is used to transform the 11.1V to 6.5V. The regulator used is the PT78HT265 series from Texas Instruments, boasting a 90% efficiency. Although DC-DC switching regulators are extremely efficient, they are notorious for producing noisy power outputs. Power bus noise interferes with the operation of various devices, as most digital circuitry are specified to operate with a stable, filtered power supply. For this reason, low voltage drop-out linear regulators were used to regulate the 6.5V down to 5V.

Placing switch-mode and linear regulators in series combined the efficiency of the switching regulator with the stable, filtered supply regulation ability of the linear regulator. To increase the life span of the linear regulators, each subsystem in the Main Avionics Node has its own linear regulator. This allows for better current, and therefore better heat, distribution.

To conserve power as far as possible without compromising avionics performance, the microcontrollers were programmed to operate at roughly 20MIPS (Million Instructions Per Second), using less than 200mA at 5V.

6.1.2.7 Safety and Reliability

Numerous safety features were employed on the Main Avionics Node to minimise risk during flight tests. Some of the features include:

- A Smooth Transition algorithm, adopted from [19], between Safety Pilot and Autopilot commands to the servo actuators. The smooth transition helps protect the aircraft by avoiding abrupt changes of the servo positions.

- Confirmation Message transmission to the ground station after successfully receiving a command. This provides confirmation that the avionics are operating as expected.

- Error Message transmission in the event of possible failures, including sensor failures. This aids in the debugging of hardware subsystems, low-level software subroutines and more high-level control system software routines.

- All actuators were limited to safe, realistic values in software. This prevents the autopilot from accidentally commanding excessively large actuation values, thereby protecting the aircraft. Typically, the servo actuation limits were set to 10°. The servo actuation limits can be adjusted from the ground station if required.

Software already exists for the Linux-based OBC developed at SU. The Linux-based software routines have been thoroughly tested and proven in a number of UAV projects.

Therefore, as much of the already proven software functionality designed for the Linux-based OBC was implemented on this new OBC. This decreased development time, while increasing system reliability.

6.1.3 Complete System

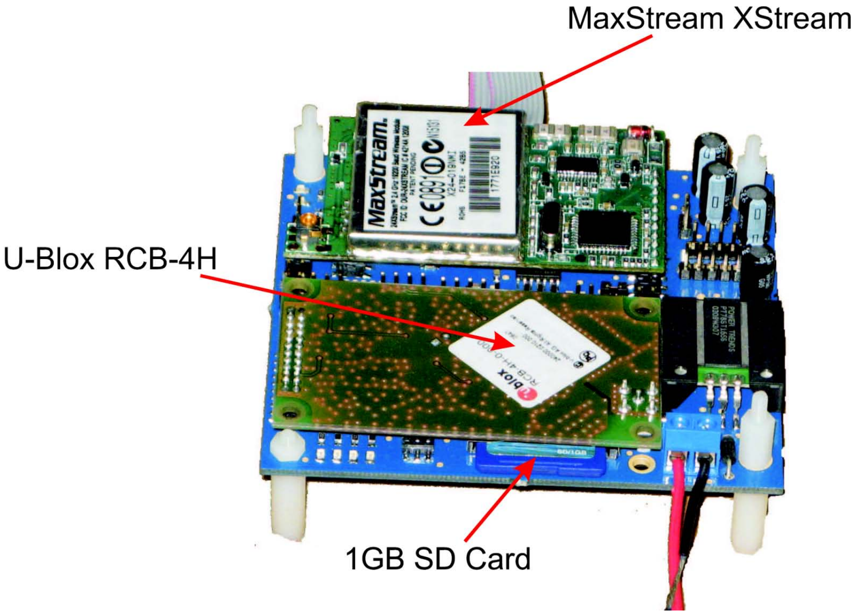

Figure 6.6: Main Avionics Node Designed

The final OBC design is shown in figure 6.6. The complete avionics system was designed to be highly modular. The modular design approach is capable of extending system functionality, as it allows for a second avionics system to be integrated into the primary system. Adding a second avionics system is useful if redundancy becomes a primary design objective, or if more processing power is required. Debugging and development time is also significantly reduced by adopting a modular systems design approach.

Table 6.2 summarises the complete avionics system mass. The final design is 48.3g lighter than required, thus adhering to the specifications agreed upon with the aircraft designers. Furthermore, the mechanical height, length and breadth constraints were all achieved ensuring smooth avionics integration into the aircraft.

To meet the flight time requirement of 1 hour, a 1800 [mAh] battery was selected. With the avionics continuously dissipating roughly 500 [mA], this allowed for about 140 [mA] of average current per servo for each of the nine servos used. The actual average servo current depends on factors such as wind disturbances. During flight tests however, it was found to be less than 140 [mA]. Therefore, the flight time requirement of 1 hour was achieved.

Component	Weight (g)
Main PCB with Maxstream, GPS and connectors	95.5
Servo Node	41.5
Pressure Node	39
IMU Node	41
DC Motor controller Node	11.5
DC Motor	27
Necessary Cables	23.6
RC Receiver	28
MaxStream Antenna	21
GPS Antenna	50
Battery	173.6
Total	**551.7**

Table 6.2: Avionics Mass Summary

6.2 Ground Station

A GUI (Graphical User Interface), based on the system initially designed by [19], was developed providing a user friendly environment through which the aircraft could be monitored. The software served as a communications interface between the on-board avionics and the ground station operator. The GUI software consists of seven functional pages, each of which are briefly discussed next.

6.2.1 Main Page

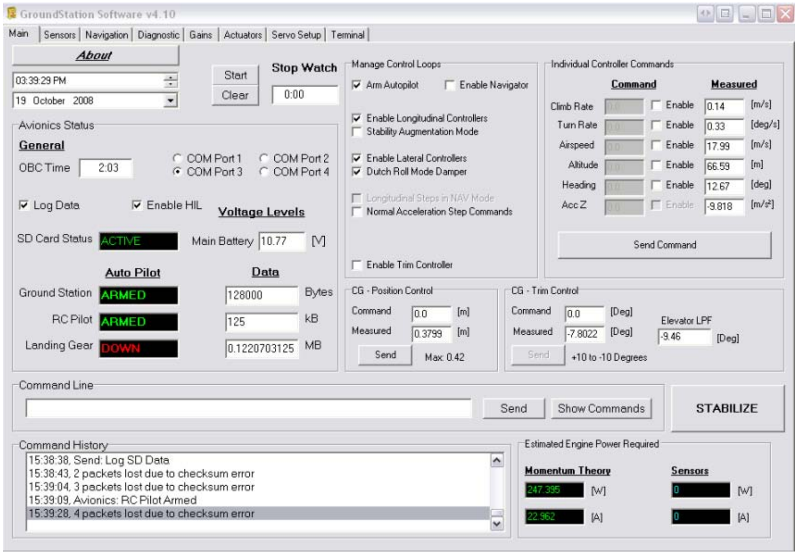

03:39:29 PM
19 October 2008

Stop Watch 0:00

Avionics Status

General
OBC Time 2:03
○ COM Port 1 ○ COM Port 2
● COM Port 3 ○ COM Port 4
☑ Log Data ☑ Enable HIL

Voltage Levels
Main Battery 10.77 [V]

SD Card Status ACTIVE

Auto Pilot		Data	
Ground Station	ARMED	128000	Bytes
RC Pilot	ARMED	125	kB
Landing Gear	DOWN	0.1220703125	MB

Manage Control Loops
☑ Arm Autopilot ☐ Enable Navigator
☑ Enable Longitudinal Controllers
☐ Stability Augmentation Mode
☑ Enable Lateral Controllers
☑ Dutch Roll Mode Damper
☐ Longitudinal Steps in NAV Mode
☐ Normal Acceleration Step Commands
☐ Enable Trim Controller

Individual Controller Commands

	Command		Measured	
Climb Rate	0.0	☐ Enable	0.14	[m/s]
Turn Rate	0.0	☐ Enable	0.33	[deg/s]
Airspeed	0.0	☐ Enable	17.99	[m/s]
Altitude	0.0	☐ Enable	66.59	[m]
Heading	0.0	☐ Enable	12.67	[deg]
Acc Z	0.0	☐ Enable	-9.818	[m/s²]

CG - Position Control
Command 0.0 [m]
Measured 0.3799 [m]
Max: 0.42

CG - Trim Control
Command 0.0 [Deg]
Measured -7.8022 [Deg]
+10 to -10 Degrees
Elevator LPF -9.46 [Deg]

Command History
```
15:38:38, Send: Log SD Data
15:38:43, 2 packets lost due to checksum error
15:39:04, 3 packets lost due to checksum error
15:39:09, Avionics: RC Pilot Armed
15:39:28, 4 packets lost due to checksum error
```

Estimated Engine Power Required

Momentum Theory		Sensors	
247.395	[W]	0	[W]
22.962	[A]	0	[A]

Figure 6.7: Ground Station Software Main Page

The main page of the ground station allows the user to arm or disarm the autopilot, arm or disarm individual control loops and send specific commands to any of the outer or inner control loops. From this page data logging on the SD data card can be toggled and engine battery power monitored. This page also displays the estimated engine power required by the aircraft engine, using measurements obtained from both the engine battery voltage and current.

This page allows the aircraft centre of mass to be commanded to any set point and has an emergency stabilisation button to stabilise the airframe should the operator deem it necessary. SD card status and the amount of SD telemetry data logged are also provided. This page prevents the user from issuing commands to controllers when they are disabled, prevents the operator from enabling navigation when lateral controllers are disarmed and serves as the main interface to the on-board avionics.

6.2.2 Sensors Page

This page displays all of the sensor data provided by the IMU node, pressure node and GPS. The following data is displayed,

- Aircraft Specific Accelerations.
- Aircraft Angular Rates.
- Airspeed, Climb rate and Altitude.
- Engine and Servo Currents.
- GPS Latitude, longitude, heading, height above mean sea level and velocities.
- Amount of GPS satellites used for navigation along with satellite relative signal strength.

It allows the operator to zero the aircraft position, altitude and inertial sensors before a flight test. Using this page the operator can request the amount of satellites seen and used by the GPS for navigation at any time allowing the operator to make an informed decision about whether to continue with the flight test or not. Comprehensive information regarding satellite signal strength is also made available to the operator. Various GPS setup controls allow for hot starts, cold starts or warm starts in either platform stationary, airborne 1 g or airborne 2 g operation modes.

6.2.3 Navigation Page

The navigation page enables the operator to upload, edit and delete a set of up to 15 way points. When the navigator is enabled, this page shows the aircraft's 2D flight path in real-time as viewed from above. This allows the operator to keep track of the vehicle if it becomes difficult to see against white cloud cover for example.

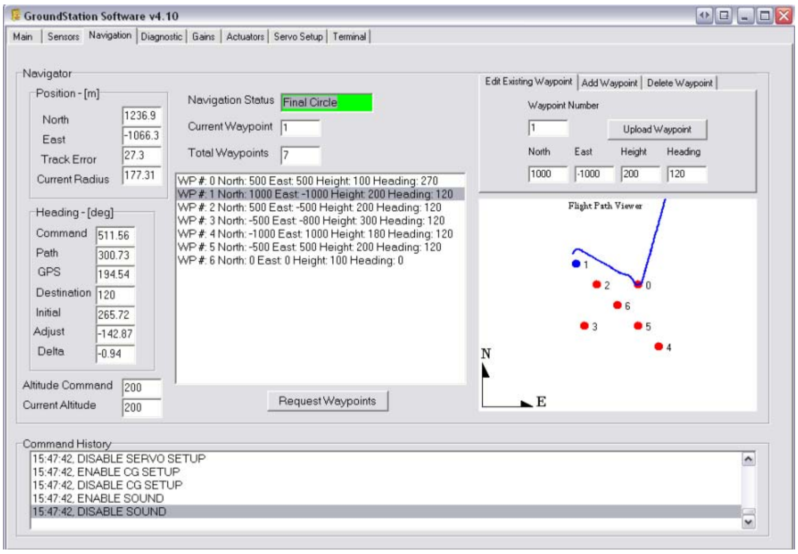

Position - [m]
North: 1236.9
East: -1066.3
Track Error: 27.3
Current Radius: 177.31

Heading - [deg]
Command: 511.56
Path: 300.73
GPS: 194.54
Destination: 120
Initial: 265.72
Adjust: -142.87
Delta: -0.94

Altitude Command: 200
Current Altitude: 200

Navigation Status: Final Circle
Current Waypoint: 1
Total Waypoints: 7

```
WP #: 0 North: 500 East: 500 Height: 100 Heading: 270
WP #: 1 North: 1000 East: -1000 Height: 200 Heading: 120
WP #: 2 North: 500 East: -500 Height: 200 Heading: 120
WP #: 3 North: -500 East: -800 Height: 300 Heading: 120
WP #: 4 North: -1000 East: 1000 Height: 180 Heading: 120
WP #: 5 North: -500 East: 500 Height: 200 Heading: 120
WP #: 6 North: 0 East: 0 Height: 100 Heading: 0
```

Waypoint Number: 1

North	East	Height	Heading
1000	-1000	200	120

Command History

```
15:47:42, DISABLE SERVO SETUP
15:47:42, ENABLE CG SETUP
15:47:42, DISABLE CG SETUP
15:47:42, ENABLE SOUND
15:47:42, DISABLE SOUND
```

Figure 6.8: Ground Station Software Navigation Page

6.2.4 Diagnostic Page

The diagnostic page lists the entire command history during the flight test. It also displays status, error and confirmation messages received from the avionics during normal operation. Some additional SD card status display boxes help to ensure that the on-board data logging function is fully operational at all times. Furthermore, this page aids in debugging as it displays the integrator states, along with the current **NSA** feedback gains calculated by the autopilot.

6.2.5 Gains Page

This page acts as a general engineering tool by providing the ability to adjust controller gains, filter cut-off frequencies and controller command limits. During calibration of the centre of mass position control system, this page is used to calibrate the centre of mass position relative to the actuator tray position.

6.2.6 Actuators Page

The received pilot commands are displayed here in particular units along with the specific commands issued to each of the sixteen servo motors connected to the servo board. After the actuators are calibrated, this page serves as a monitoring station used to confirm that the correct values are commanded to each of the individual servo actuators.

6.2.7 Servo Setup Page

This page is used when calibrating the servos. It allows the operator to setup mechanical offsets and gains to ensure that the control surfaces respond correctly. Firstly, offsets are removed to centre the actuators thereby compensating for mechanical offsets in the servo horns and push-rods. Secondly, gains are adjusted accordingly to ensure that the correct throw on all control surfaces are obtained.

6.3 Summary

The Main Avionics Node designed is an improvement over the existing Linux-based OBC used at SU with respect to size, mass and power consumption, providing a practically feasible solution to the Sekwa specifications stated earlier. Although the Linux-based SU OBC is significantly more powerful, the Main Avionics Node provides enough processing power to successfully implement all of the flight control software routines developed in this thesis.

A CAN bus, multi-master network protocol was implemented, along with the capability of logging up to 1GB of information. The generic nature of the Main Node allows it to be used in a variety of applications, such as an electronic flight control computer or stand-alone data logging CAN node. Therefore, if size and power consumption is not of primary concern, the Main Avionics CAN Node could be combined with the Linux-based OBC to create a powerful on-board computer with mass data storage capability.

With the flight control routines implemented on the Main Avionics Node, software was developed allowing a user to remotely monitor all of the aircraft systems from a portable ground station. The ground station software enables modular flight control testing, simplifying the evaluation of the various control systems designed.

The following chapter continues with a discussion of the hardware in the loop environment used to test the flight control systems, hardware and ground station software, to minimise as much risk as possible before practically implementing the entire system on the actual aircraft.

Chapter 7

Hardware in the loop Simulation

In order to minimise risk during practical implementation, the flight control system is evaluated in a **H**ardware **I**n the **L**oop (**HIL**) simulator. The hardware in the loop simulator proved to be of paramount importance to the success of the project. This chapter presents a basic overview of the **HIL** simulation environment, as well as the simulated performance and response of the aircraft under near *real-world* conditions. Factors such as wind, sensor noise and actuator slew are included to facilitate a more realistic simulation environment.

7.1 Conceptual Overview

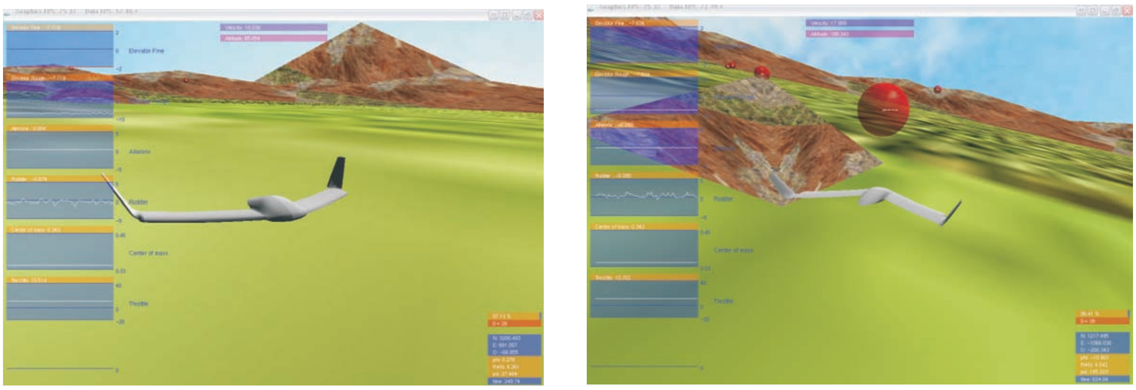

Figure 7.1: Hardware in the Loop Graphics Engine

The **HIL** simulator is shown conceptually by figure 7.2. The avionics designed (see chapter 6) has the capability of interfacing via a CAN bus with various CAN nodes. The **HIL** distribution board, developed by [19], acts as another node on the CAN bus and relays information between the simulation environment implemented on a PC and the on-board computer (OBC) designed for this project.

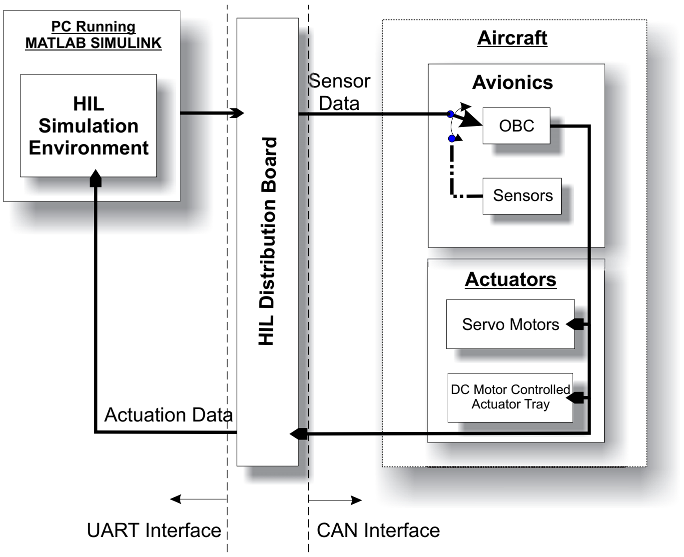

Figure 7.2: Hardware in the Loop Conceptual Overview

Sensor data, created in the simulation environment, is transmitted to the OBC via the **HIL** distribution board CAN interface. After the OBC executes the autopilot software routines, the OBC transmits actuation commands to the various aircraft actuators. These actuation commands in turn are also transmitted to the **HIL** simulation environment, where sensor, wind, engine, gravity, six degree of freedom and aerodynamic models simulate the aircraft dynamic response. Sensor data is created once again, transmitted to the OBC via the CAN interface and the process is repeated. This in turn allows for the evaluation of the aircraft flight control systems. The logical flow of the **HIL** simulator is given by algorithm 1.

An OpenGL graphics engine, shown by figure 7.1, aids in autopilot verification allowing the flight control systems to be visually inspected in a three dimensional environment.

Typically, **HIL** simulations were conducted in such a way that they mimic the likely course of events during a practical flight test. The simulation starts with the aircraft on the runway. After a manual take-off with the centre of mass in the most stable position, the autopilot system is engaged. The ground station software is then used to issue commands to individual controllers, and data is logged throughout the simulated flight. Telemetry data is analysed after the simulated test flight to verify that the flight control system was functioning properly. The simulation environment, implemented using MATLAB, is briefly outlined in the following section.

Algorithm 1: Simplified **HIL** Simulation Environment Conceptual Flow

```
while (HIL Simulation) do
    MATLAB Transmits Sensor Data to OBC
    if (OBC Received Sensor Data) then
        OBC Executes Autopilot Software Routines
        OBC Transmits Actuation Commands
    end
    while (MATLAB Receives No Actuation Commands) do
        MATLAB Waits for Actuation Commands
    end
    MATLAB Runs Aerodynamic Model
    MATLAB Runs Engine Model
    MATLAB Runs Gravity Model
    MATLAB Runs Wind Model
    MATLAB Runs Six Degree of Freedom Model
    MATLAB Runs Sensor Model
end
```

7.2 Simulation Environment

The simulation environment operates in MATLAB's SIMULINK, a tool that is particularly well suited for modelling, simulating and analysing dynamic systems. The *main* simulation environment, shown by figure 7.3, essentially consists of six parts outlined below,

1. **HIL subsection block:** This block arranges the sensor data in the correct order to be transmitted via the CAN bus interface. It also contains the **HIL** s-function responsible for data transmission to the **HIL** distribution board via the UART interface between the PC and **HIL** distribution board. After the OBC transmits the calculated actuator commands, this block provides the actuator commands in particular units used in the rest of the simulation environment. Before the actuator commands are sent to the aerodynamic model however, they are passed through an *actuator model* block.

2. **Aircraft/Earth Model Block:** This block contains the aerodynamic model (presented in chapter 2), a wind model, gravity model, engine model, runway model and six degree of freedom model. For detailed information regarding these models, refer to [14] and [19].

3. **Sensor Model Block:** This block takes data from the previously described block and converts it to sensor data, mimicking data from actual rate gyroscopes, accelerometers, pressure sensors and GPS by adding appropriate values of noise over time. Since the actual sensors are mounted on the actuator tray, and not on the air-

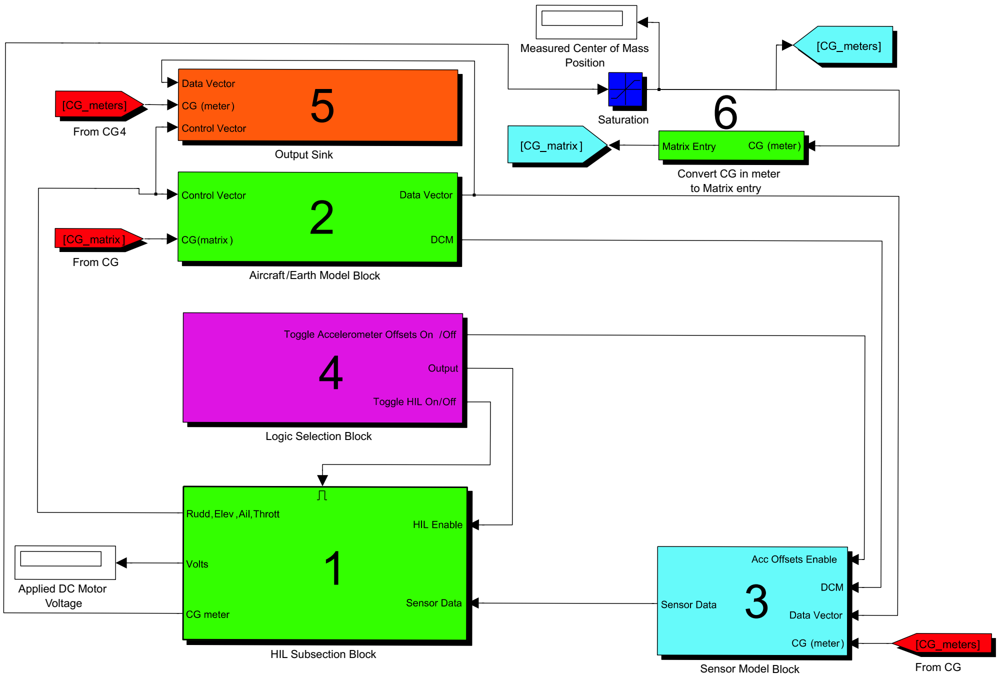

Figure 7.3: Hardware in the Loop Simulation Environment

craft centre of mass, this block also calculates offsets in accelerometers due to the motion of the actuator tray relative to the aircraft centre of mass position.

4. **Logic Selection Block:** This block is used to either enable or disable **HIL**, the simulation of accelerometer offsets and actuator failure.

5. **Output Sink:** This block handles the output to the OpenGL graphics engine. A User Datagram Protocol (UDP) connection is used to transmit aircraft position and attitude to the graphics engine. The engine interprets the information and displays the aircraft in a 3D environment, thereby simulating flight each time the information is updated by the simulation environment. For more information on the graphics engine refer to [22]. A secondary function of this block is to log data, which is extremely useful during testing of the flight control systems.

6. **Convert CG in meter to Matrix entry:** As previously mentioned, the aircraft is modelled in AVL and MATLAB is used to extract the stability and control derivatives as a function of centre of mass position into structures. The structure consist of a series of $n \times 1$ matrices, with each matrix containing the $n \times 1$ data set of a specific derivative over the centre of mass range investigated. This block therefore converts the centre of mass position measured by the digital encoder (in meters) to the relative matrix entry used to obtain the desired derivative. Consequently,

the aerodynamic model in block 2 is updated accordingly thereby simulating an aircraft with varying stability.

Realistic Evaluation: The mathematical models used in the **HIL** simulation environment, are complete non-linear models without the assumptions made during development of the control systems. This provides a higher fidelity simulation environment, as the full, coupled non-linear six degree of freedom equations of motion are implemented. Furthermore, the lateral stability and control derivatives are updated in the aerodynamic model as a function of centre of mass position, to verify the assumption made in chapter 3 that the lateral derivatives can be assumed constant for control design purposes.

Quantisation Effects: The avionics designed for this project adequately performs floating point calculations with high enough precision such that quantisation effects can be neglected in the simulation environment.

Code Conversion: All of the flight control systems were initially implemented in C-code using MATLAB s-functions. This approach comes highly recommended, and significantly reduces development time, since the flight control system C-code can be debugged in the simulation environment prior to implementation on the OBC.

7.2.1 Controller Robustness Evaluation

This section presents the disturbance, actuator and sensor models used in the simulation environment, providing the capability of creating realistic test conditions for the flight control systems before practically implementing the system on an actual aircraft.

7.2.1.1 Wind Model

The wind model used in this project was adopted from [19], and generates wind gusts by passing a white noise signal through a noise shaping filter. The block simulates wind gusts as well as constant wind disturbances. RMS wind gust disturbances of 2 [m/s], with constant wind disturbances of 5 [m/s], were typically used during **HIL** simulations and added to each of the aircraft body axis directions as velocity disturbances.

7.2.1.2 Sensor Noise Models

The sensor noise model adds a Gaussian distributed random signal to the relevant sensor signal to simulate the effect of sensor noise. The variance of the random Gaussian distributed signal was initially obtained using the data-sheets of the various sensors, after which it was adjusted using practical recorded sensor data. Table 7.1 gives the specific noise figures used.

Sensor	RMS Noise	Units
Angular Rate Gyroscopes	0.8	$^\circ/s$
Accelerometers	0.141	m/s^2
Differential and Absolute Pressure Sensors	0.5	Pa
GPS Position	$\frac{4\pi}{20e6}$	rad
GPS Altitude	4	m
GPS Velocity	0.5	m/s

Table 7.1: Sensor Noise Values Used in **HIL** Simulations

During practical tests, the GPS module used showed an absolute low frequency position drift of roughly 4 meters. Unfortunately, GPS position drift was not incorporated into the **HIL** simulation environment. For a higher fidelity **HIL** simulation environment, it is recommended that GPS position drift be incorporated into the GPS noise model.

7.2.1.3 Actuator Model

The actuator model, applying to the servo motors used in this project, essentially consist of three cascaded blocks. The actuator signal enters a slew rate limiter block, set up with a slew rate of $260^\circ/s$ (obtained from the product data-sheet of the specific servo motors used for the project). Next, the signal passes through a backlash block and quantizer, set up with 0.1° dead band width and quantization intervals respectively. The actual servos used performed better than this, but it was decided to test the flight control system under extreme conditions to minimise risk during practical implementation.

7.2.1.4 Accelerometer Offset Model

The analysis of section 2.2 assumed that the accelerations are measured in the aircraft body axes by sensors mounted at the aircraft centre of mass. However, the accelerometers are mounted on the actuator tray, and therefore do not measure the correct accelerations. When taking the IMU as a point within the aircraft, the following equations give the measured accelerations due to offsets in the tray position relative to the aircraft centre of mass [1],

$$a_x^{'} = -x(q^2 + r^2) \tag{7.2.1}$$

$$a_y^{'} = x(pq + \dot{r}) \tag{7.2.2}$$

$$a_z^{'} = x(pr - \dot{q}) \tag{7.2.3}$$

where x is the axial difference in distance between the actuator tray position and the centre of mass position. In the above equation, it is assumed that the centre of mass moves only in the aircraft longitudinal axis. The values $a_x^{'}$, $a_y^{'}$ and $a_z^{'}$ are consequently added to the accelerations sent to the sensor block. This allows the effect of offsets in the accelerometers, due the position of the IMU relative to the centre of mass, to be investigated.

With the simulation environment discussed, the following section presents the results of a typical **HIL** simulated test flight.

7.3 Flight Control System Evaluation

This section presents hardware in the loop simulation data for a typical simulated flight test. The *main* objective is to use the simulation environment to verify the assumptions made during the design of the flight control system. The longitudinal flight control system simulation results are given in section 7.3.1, followed by the simulation results of the lateral flight control system in section 7.3.2.

7.3.1 Longitudinal Flight Control System Evaluation

7.3.1.1 Normal Specific Acceleration Controller

The **NSA** control system step response for centre of mass positions 0% and 100% aft of the stable position are shown by figures 7.4 (a) and 7.4 (b) respectively. The control system was found to regulate normal specific acceleration very well regardless of the static stability margin.

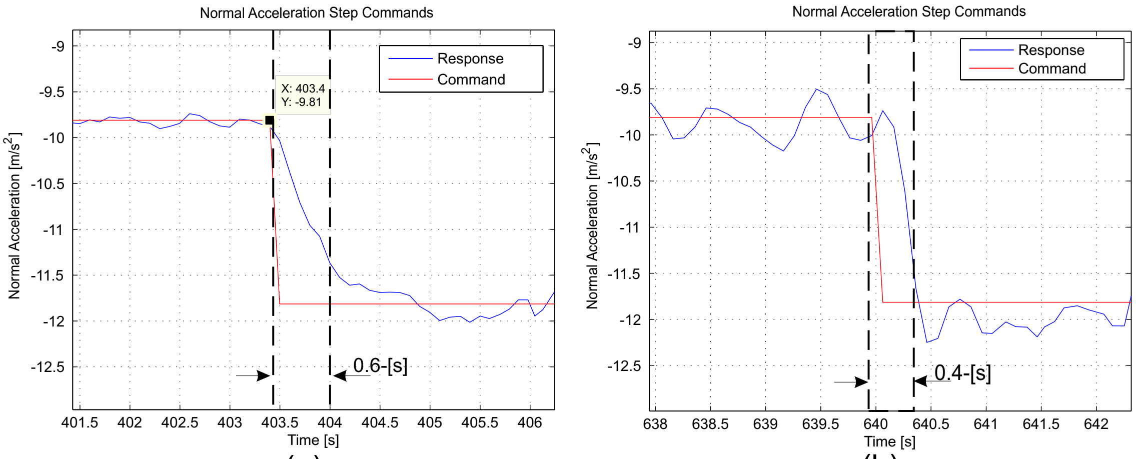

(a) (b)

Figure 7.4: Normal Specific Acceleration Step Response: (a) Centre of Mass 0% Aft. (b) Centre of Mass 100% Aft

Figures 7.5 (a) and 7.5 (b) show normal specific acceleration regulation, when the centre of mass is 0% and 100% aft of the stable position respectively. In both cases, the outer loop **LQR MIMO** control system commands normal specific acceleration. As expected, when a climb rate from 2 [m/s] to 0 [m/s] is commanded, the **LQR MIMO** controller commands more positive normal specific acceleration, resulting in the aircraft pitching in a nose-down manner. The aircraft's climb rate is consequently reduced, and less positive normal specific acceleration is commanded as the aircraft approaches the straight and level flight condition (0 [m/s] climb rate).

Furthermore, hardware in the loop simulations confirmed the validity of the assumption made in chapter 4 during the derivation of the **NSA** controller, stating that the velocity magnitude of the wind axis system is equal to the aircraft's airspeed.

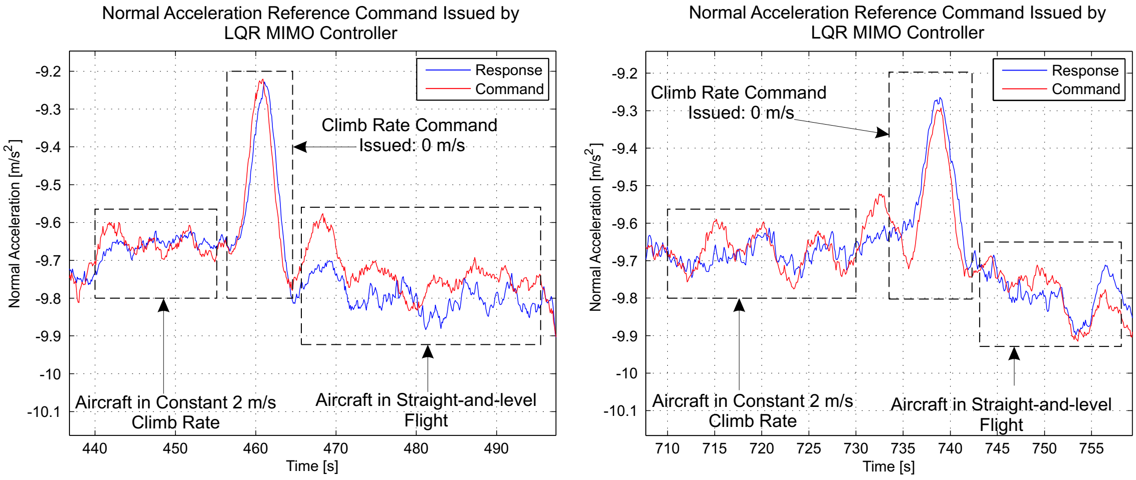

(a) (b)

Figure 7.5: Normal Specific Acceleration Regulation: (a) Centre of Mass 0% Aft. (b) Centre of Mass 100% Aft

7.3.1.2 Airspeed and Climb Rate Controller

With reference to figure 7.6, a 2 [m/s] climb rate step command is shown when the aircraft centre of mass is 0% and 100% aft of the most stable position respectively. The commanded response settles at 90% of its final value in about 7.7 seconds. Furthermore, note that the rise times shown by figures 7.6 (a) and 7.6 (b) are roughly the same. This indicates that the inner loop **NSA** controller is working properly and presents an invariant dynamic response to the outer loop **LQR MIMO** controller, thus producing the same dynamic response regardless of the static stability margin.

Continuing with the analysis of the outer loop **LQR MIMO** control system designed in chapter 5 (see section 5.1), the result of a -2 [m/s] airspeed step command is shown by figure 7.7. Figure 7.7 (a) is when the centre of mass is 0% aft, and figure 7.7 (b) is when the centre of mass is 100% aft of the stable position. The rise times are found to be roughly equal once again, confirming that the flight control systems produce an invariant dynamic response to centre of mass position changes.

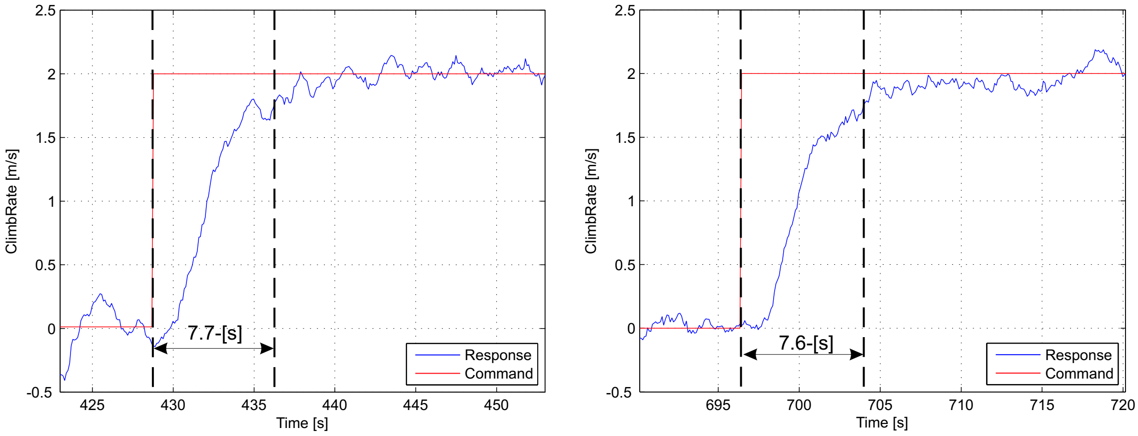

(a) (b)

Figure 7.6: Climb Rate Step Response: (a) Centre of Mass 0% Aft. (b) Centre of Mass 100% Aft

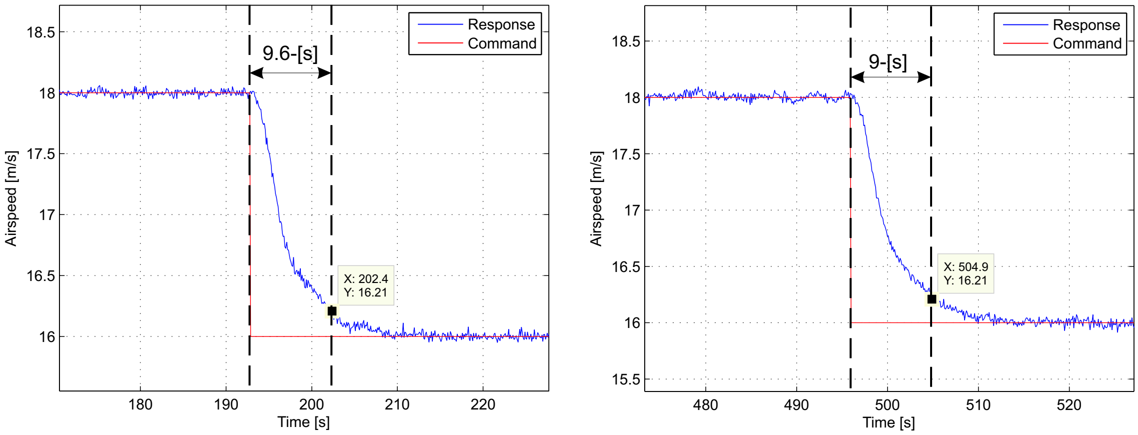

(a) (b)

Figure 7.7: Airspeed Step Response: (a) Centre of Mass 0% Aft. (b) Centre of Mass 100% Aft

7.3.1.3 Effect of Variations in Moment of Inertia as a function of Centre of Mass Position

With reference to figure 7.8, another test was conducted aimed at investigating the effect of errors in the moment of inertia values obtained. Recall from chapter 2, that the actuator tray was shown to change the I_{yy} moment of inertia by 28%. Therefore, a hardware in the loop simulation was carried out with a 28% error in I_{yy}, and the results are given by figure 7.8. It was found that, although the climb rate rise time increased by about 0.8 seconds, that the response remained stable. These results indicated that the control system designed was capable of handling fairly large errors in the moment of inertia values while still providing stable results. Therefore, it is not critical to know the *exact* moment of inertia values for control design purposes, as long as the moment of inertia values used are roughly within 30% of the actual values.

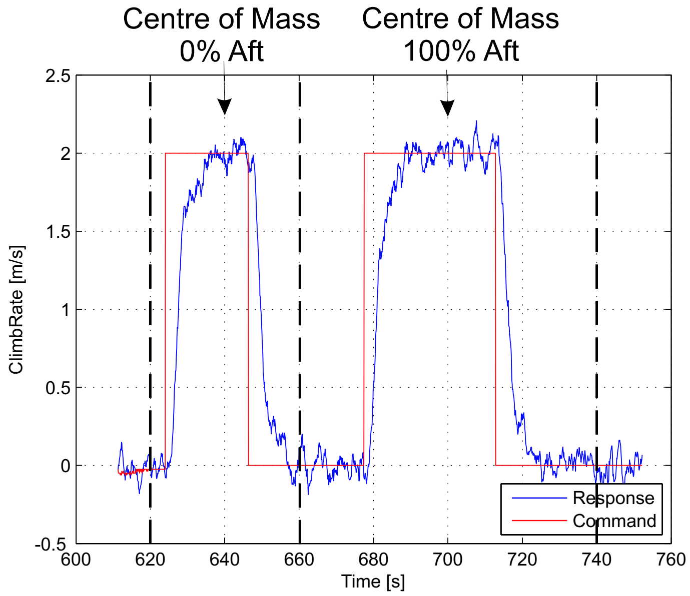

Figure 7.8: Climb Rate Response with 28% increase in I_{yy}

The results obtained makes intuitive sense, since a larger I_{yy} moment of inertia will make the aircraft more resistant to faster pitching motions, which leads to a slower closed loop climb rate step response. On the other hand, more overshoot will be observed with a reduction in I_{yy}. A reduction in I_{yy} however is not considered here, since the installation of the actuator tray leads to an increase in I_{yy} (see chapter 2 section 2.3).

7.3.2 Lateral Flight Control System Evaluation

7.3.2.1 Yaw Rate Controller

Figure 7.9 (a) and 7.9 (b) shows the yaw rate step response when the centre of mass is 0% and 100% aft of the stable position respectively. The results clearly confirm the assumptions made in chapter 3, stating that the lateral stability and control derivatives can be considered constant for variations in aircraft centre of mass along the vehicle longitudinal axis.

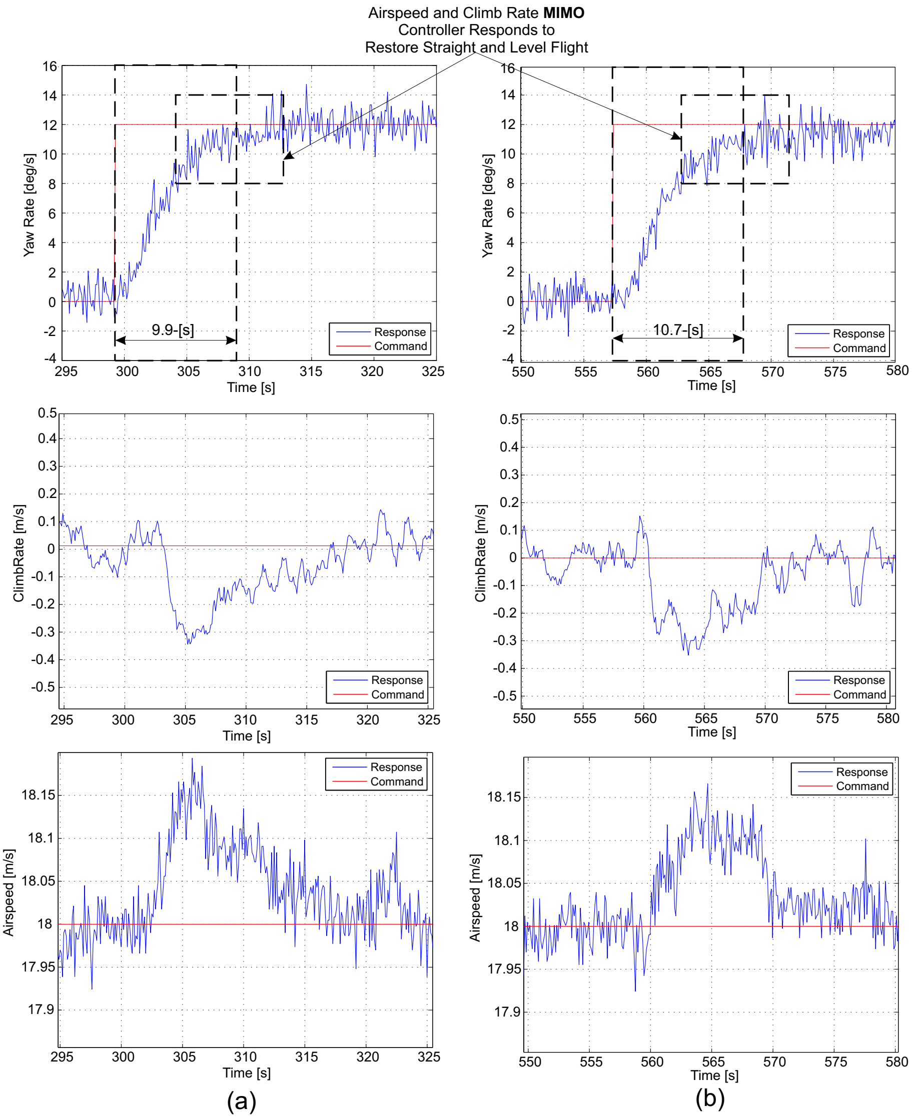

Figure 7.9: Yaw Rate Step Response: (a) Centre of Mass 0% Aft. (b) Centre of Mass 100% Aft

Note that, during a constant turn, the airspeed and climb rate **MIMO** controller responds to restore straight and level flight, leading to a slight deterioration in the yaw rate transient response as indicated on figures 7.9 (a) and 7.9 (b). Despite the slight deterioration in the yaw rate response, the controller was observed to perform well under coupled, non-linear simulation conditions, for various centre of mass locations.

7.3.2.2 Guidance and Navigation

Figure 7.10 shows the aircraft two-dimensional flight path during way point navigation. When the navigator was armed, the path planning algorithm generated a valid path between two way points. Next, the cross track error algorithm calculated the aircraft's lateral position track error from the desired path, and fed the error to the guidance controller. The guidance controller in turn issued heading commands to the heading controller (which issued yaw rate commands to the yaw rate controller), and the aircraft was regulated about the desired path. For details on the cross track error algorithm, guidance and heading controllers, refer to appendix A.

The path planning algorithm used [14] generates a desired path between two way points consisting of:

- Initial Circle: The initial turning circle required to fly in the direction of the next way point.
- Straight Line Section: The shortest path to the next way point.
- Approach Circle: The final turning circle required to fly through the second way point.

With reference to figure 7.10, the desired path is shown by the dashed line, and a way point is indicated by a cross.

To avoid clutter, the simulation was conducted for only two way points. The navigator was armed, and the aircraft approached the first way point at a heading of 90°. After it reached the first way point, the aircraft turned into the first turning circle (red). At this point, a constant feed forward yaw rate was commanded to prevent the aircraft from overshooting the initial turn. The feed forward yaw rate command issued was $\frac{\overline{V}_W}{R_c}$, where $\overline{V}_W$ was the current airspeed magnitude, and R_c the turning circle radius.

Next, the aircraft entered a straight line section (green), and the guidance controller issued heading commands to track back to the desired path. As the aircraft approached the second way point, it entered the approach turn (magenta), and again a yaw rate command was added in a feed forward manner. The aircraft turned, and passed through the second way point. After passing through the second way point, the navigator calculated the new path back to the first way point. The aircraft consequently made the initial turn (red), flew the straight line section (green), and then the navigator was disabled (blue).

The results obtained during **HIL** simulated flight tests confirmed that the autopilot was capable of successfully navigating way points.

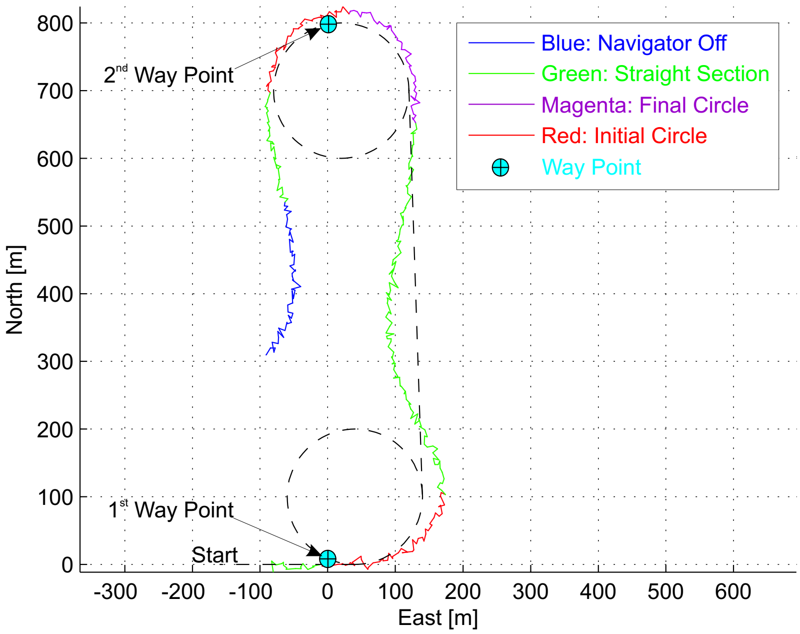

Figure 7.10: Way point Navigation

7.4 Summary

In order to save development time, and to minimise risk during practical flight tests, the hardware in the loop simulation environment proved to be an extremely useful engineering tool. The simulation environment provided invaluable insight into the flight control system, and allowed for further development and refinement.

The **HIL** simulation environment was fundamentally constructed using non-linear, coupled differential equations, describing the dynamics of the vehicle. Using the complete set of coupled equations, all of the assumptions made during the design of the flight control system could be verified.

HIL simulated flight tests confirmed the assumption made regarding the lateral stability and control derivatives, stating that these derivatives could be assumed to remain constant for variations in aircraft centre of mass position over the range investigated. This was done by updating the lateral stability and control derivatives as a function of aircraft centre of mass position, and observing that the control system designed based on fixed lateral parameters provided the same dynamic response for various centre of mass locations.

With all of the control systems thoroughly tested in the hardware in the loop simulation environment, under near *real-world* conditions, it remained now to demonstrate that the flight control system designed was capable of performing equally well in practice. The following chapter presents the results obtained during practical flight tests of the variable stability blended-wing-body aircraft.

Chapter 8

Practical Implementation

After the first design iteration of Sekwa, the BWB (blended-wing-body) aircraft developed by the CSIR, it was found that more detailed aerodynamic analyses were required before any practical flight tests could be conducted on the vehicle.

Figure 8.1: Stellenbosch University (SU) Variable Stability Aircraft (VSA)

However, to further minimise risk during practical implementation of the flight control system on the more expensive Sekwa UAV, a low-cost, off-the-shelf airframe was acquired to act as an initial test vehicle for the flight control system to be implemented. This BWB aircraft, shown in figure 8.1, was specifically constructed for the project so as to closely resemble Sekwa, enabling evaluation of the flight control system on a similar platform type.

The purpose of the Stellenbosch University (SU) Variable Stability Aircraft (VSA) was not to demonstrate drag reduction at a certain centre of mass location, as the vehicle was not designed for it. The sole purpose of the SU VSA was to practically verify that the flight control system was capable of controlling a statically unstable aircraft. After the flight control system was demonstrated to perform on the SU VSA, it could be applied with greater confidence on the Sekwa UAV.

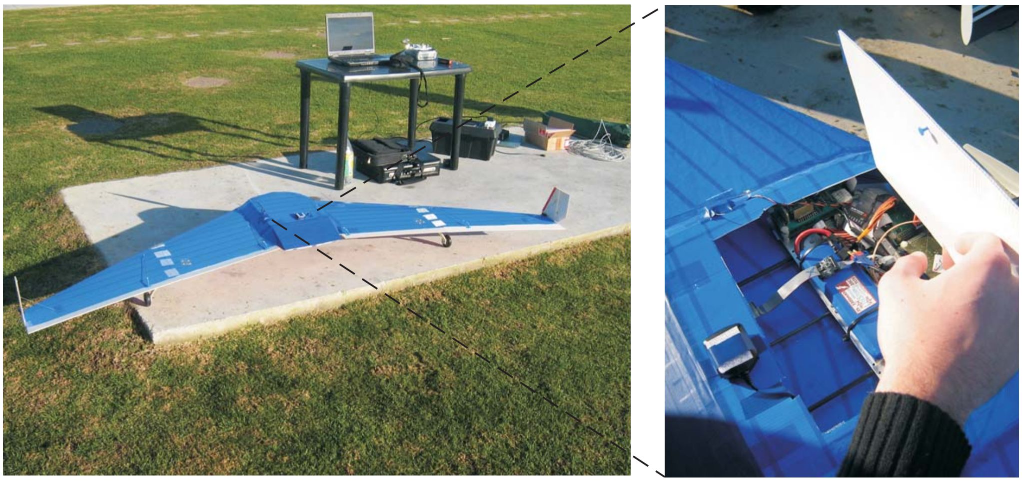

Figure 8.2: SU VSA During Test Flight Preparations.

The chapter presents the practical flight test results obtained, as tested on the SU VSA (Stellenbosch University Variable Stability Aircraft). The SU VSA, shown by figure 8.2, was equipped with static landing gear, an electric engine and an avionics pod. An actuator tray was constructed, consisting of a thin aluminium sheet for mounting the avionics, with the actuator tray sliding on carbon fibre rods inside the avionics pod.

8.1 Initial Considerations

8.1.1 Flight Control System Portability

The flight control system for the SU VSA was designed such that the closed loop dynamic response of the various SU VSA control systems were almost identical to the closed loop dynamic response of the control systems designed for Sekwa.

Since both SU VSA and Sekwa are blended-wing-body aircraft with varying static stability margins, only minor adjustments to the flight control system was required to implement the system on the SU VSA. The generic nature of the inner loop stability augmentation system was underlined during the re-design process, as only the coefficients of the linear and quadratic functions describing the stability and control derivatives were needed to implement the system on the new vehicle. The weighting parameters of the **LQR MIMO** control system regulating airspeed and climb rate were kept exactly the same for the new vehicle. Since a conventional lateral flight control system was designed, using a successive loop closure technique, it was the only component of the flight control system that required a complete re-design.

After the flight control system was adapted for the SU VSA, extensive hardware in the loop simulations were conducted to verify the correct operation of the flight control system. Due to the similarity in the closed loop dynamic response between the SU VSA and Sekwa vehicles, it is not necessary to provide hardware in the loop simulation data of the SU VSA. The practical results obtained in the chapter can thus be directly compared with the hardware in the loop simulation data presented in chapter 7.

Section 8.1.2 begins by introducing the modular flight control system testing procedure employed in this project.

8.1.2 Initial Modular Flight Test Approach

A number of manual flight tests, with lead weights to simulate the actual avionics, were initially conducted to test the aircraft itself. The lead weights were positioned to place the centre of mass at the stable position, and it was found that the pilot could control the aircraft very well with the centre of mass in the stable position.

To minimise risk, early flight tests involved partial autopilot control only. The partial autopilot control tests were aimed at individually testing the lateral and longitudinal flight control systems, before implementing the complete flight control system. The partial autopilot tests are described below:

- The first test involved the human pilot controlling the aircraft's longitudinal dynamics. The pilot was given control over the aircraft's throttle and elevator. The lateral flight control system was armed, and it was observed that the aircraft was capable of successfully flying a commanded yaw rate under lateral autopilot control.
- The second test involved the human pilot controlling the aircraft's lateral dynamics. The pilot was given control over the aircraft's rudders and ailerons. The longitudinal flight control system was armed, and it was observed that the aircraft was capable of flying a commanded climb rate and airspeed under longitudinal autopilot control.

The aforementioned tests were conducted with a statically stable centre of mass position. After the lateral and longitudinal flight control systems were individually tested, the full autopilot system could be safely evaluated. The following section continues with the results obtained during some of the practical flight tests conducted.

8.2 Practical Results and Flight Tests

This section presents the data obtained during practical implementation of the flight control system designed for the SU VSA.

Section 8.2.1 starts by presenting the practical data obtained during evaluation of the lateral flight control system, and shows that autonomous way point navigation was achieved practically. The airspeed and altitude (section 8.2.2) control systems are evaluated next, followed by practical step response data of the **NSA** stability augmentation control system. Section 8.3 follows by presenting the performance of the flight control system under the variable stability condition, with emphasis on the unstable case. Section 8.4 gives the most important results of the chapter, showing that the autopilot was capable of controlling the aircraft where the human pilot was unable to.

Each section starts by presenting a brief outline of the flight test procedure, followed by more specific details of the control system tested during the relevant flight test. All of the data presented here was obtained from the sensors mounted inside the aircraft. Since low-cost, off-the-shelf sensors were used, all of the data presented in the chapter are practical sensor measurement data and thus include the errors due to sensor noise.

8.2.1 Selected Lateral Control System Response

The primary objective of the lateral flight control system was to facilitate autonomous way point navigation, and to augment the low natural directional stability. This allowed for the aircraft stability augmentation control system to be tested without the interference of a human pilot, thereby ensuring greater consistency during evaluation of the longitudinal flight control system.

8.2.1.1 Test Procedure: Lateral Flight Control System

- After manual take-off, the aircraft reached an altitude of 80 [m], and the pilot adjusted the elevon trim setting such that the aircraft was flying straight and level.
- The full flight control system was engaged, and the aircraft was observed to hold its airspeed at the commanded value of 18 [m/s], with zero climb rate.
- **Yaw Rate Controller:** A yaw rate command of 14 [deg/s] was given until the aircraft completed a 360° turn.
- **Heading Controller:** The heading controller was armed, and a heading command of 20° was issued, followed by a 10° heading step command.
- **Way Point Navigation:** Next, the guidance controller was armed, and the aircraft performed autonomous way point navigation.

8.2.1.2 Flight Test Results: Yaw Rate Controller

The yaw rate controller, designed in appendix A, was observed to reach 90% of the final value commanded in approximately 4.8 seconds, as indicated by figure 8.3. Subsequent tests confirmed the assumption made that the lateral stability and control derivatives, are not affected by variations in the aircraft centre of mass position along the vehicle longitudinal axis, for the centre of mass position range investigated.

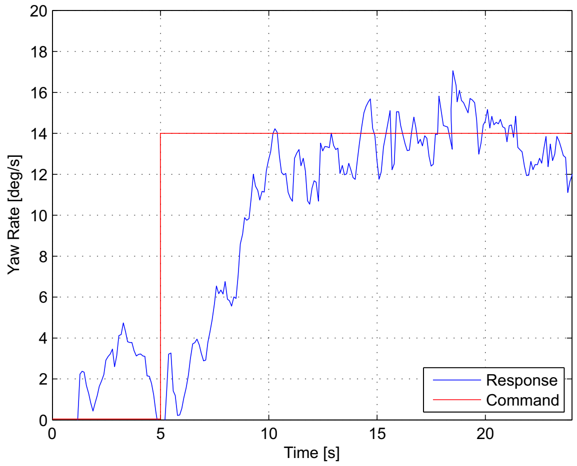

Figure 8.3: Yaw Rate Controller Step Response

8.2.1.3 Flight Test Results: Heading Controller

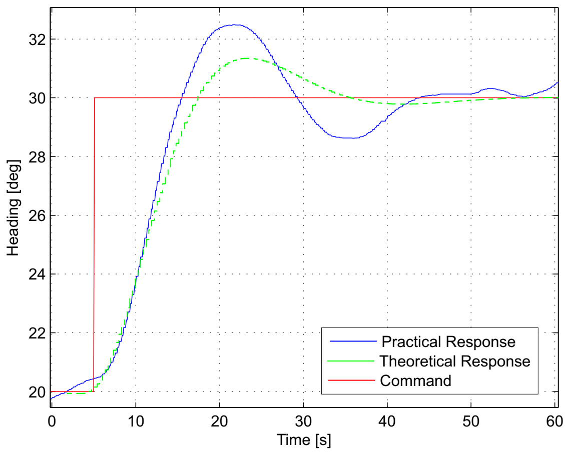

Figure 8.4: Heading Controller Step Response

The heading controller, designed in appendix A, was observed to reach 90% of the final value commanded in approximately 9.47 seconds, as indicated by figure 8.4. Note that the practical response is slightly faster, with more overshoot, than the theoretical response. This is because the theoretical response assumed a constant GPS delay of 0.25 seconds, but practically the GPS delay was found to be more in the order of 0.33 seconds. The higher GPS delay lead to more overshoot in the closed loop heading response.

8.2.1.4 Flight Test Results: Way Point Navigation

The aircraft was capable of fully autonomous way point navigation, under various centre of mass locations. The result of one such autonomous flight is given by figure 8.5, showing the aircraft's two-dimensional flight path as viewed from above.

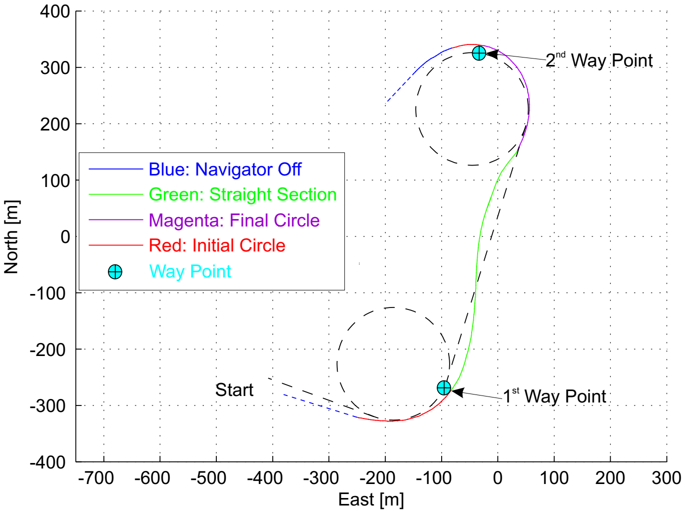

Figure 8.5: Flight Test Way point Navigation.

The flight path given by figure 8.5 shows that the two respective way points were very far apart, and provided very good results. However, for safety reasons, it was necessary to fly the aircraft well within visual range of the safety pilot, and therefore the majority of the way points chosen were much closer to each other than the way points shown on figure 8.5.

As previously mentioned, the purpose of the lateral flight control system in general was to remove the human pilot from the loop when evaluating the more important **NSA** stability augmentation control system. To obtain more consistent results during testing of the longitudinal controllers at various centre of mass positions, it was desired that the aircraft remain more or less wings-level during the course of a test flight (see appendix A). Therefore, the heading and guidance controllers were designed with very slow rise time specifications. The slow rise time specifications ensured that the aircraft banked more slowly during way point navigation, but unfortunately when the way points were chosen closer to each other (within roughly 250m of each other), the guidance controller performed very poorly. This was expected to be the case, as the slow rise time specification set on the guidance controller means that the aircraft takes a considerable amount of time to converge back to the desired path.

With the guidance controller designed with a theoretical rise time of 17 seconds, and with an airspeed magnitude of 18 m/s, the aircraft covers a theoretical straight-line distance of 306 m before converging to the desired path. When the way points were chosen within 250 m of each other, the aircraft was unable to completely converge back to the desired path before reaching the next way point, resulting in inconsistent results obtained during way point navigation.

Even though fully autonomous way point navigation was accomplished, the results were unsatisfactory. This was mainly due to the lateral inner loop yaw rate controller restricting the aircraft to small bank angles. To improve the aircraft's lateral performance, an estimator is suggested to obtain the aircraft's bank angle. A controller could then be designed regulating the aircraft's estimated bank angle, which would allow the aircraft to fly a smaller turn radius, thereby improving the response of the guidance controllers when the way points are chosen closer to each other.

However, way point navigation was not the primary focus of the project, and the heading and guidance controllers succeeded in their task of facilitating full autonomous flight without interference from a human pilot, and allowed for consistent evaluation of the longitudinal flight control system.

8.2.2 Airspeed and Altitude Control Systems

The results of two flight tests are given in this section. The first (**Test 1**) involves airspeed regulation about the trim velocity, and the second (**Test 2**) involves airspeed and altitude step commands. Both of the aforementioned flight tests started with the general flight test procedure outlined below.

8.2.2.1 General Test Procedure: Airspeed and Altitude Control Systems

- After manual take-off, the aircraft reached an altitude of 65 [m], and the pilot adjusted the elevon trim setting such that the aircraft was flying straight and level.
- The full flight control system was engaged, and the aircraft was observed to hold its airspeed at the commanded value of 18 [m/s], with zero climb rate.
- The guidance controller was armed, and the aircraft performed autonomous way point navigation.
- **Test 1 - Airspeed Regulation:** During way point navigation, the aircraft's ability to regulate the desired trim airspeed was recorded.

- **Test 2 - Airspeed and Altitude Step Response:** During way point navigation, the closed loop airspeed and altitude step response data was recorded.

8.2.2.2 Test 1 - Airspeed Regulation Flight Test Results

Figure 8.6 shows the recorded airspeed for the entire duration of the flight test conducted. With reference to figure 8.6, with the flight control system engaged, airspeed was regulated with an RMS error of 0.3 [m/s].

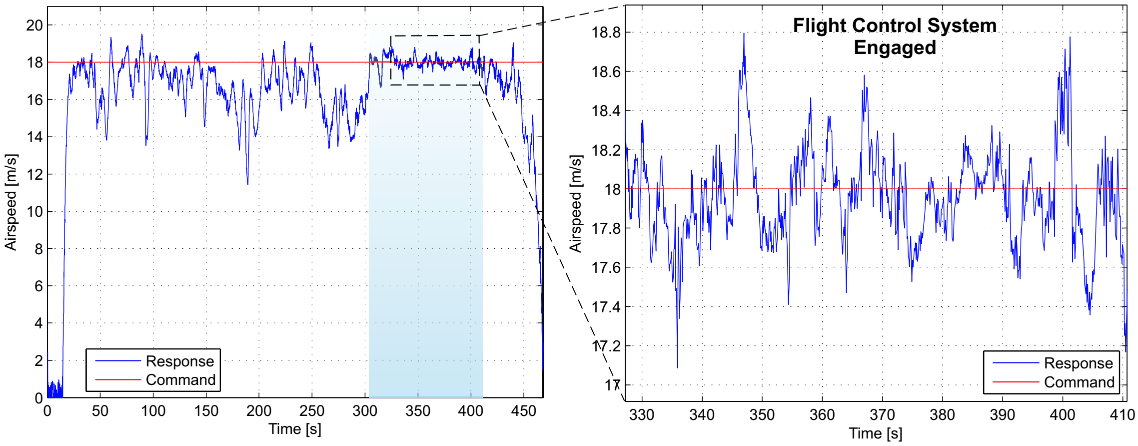

Figure 8.6: Regulating Airspeed

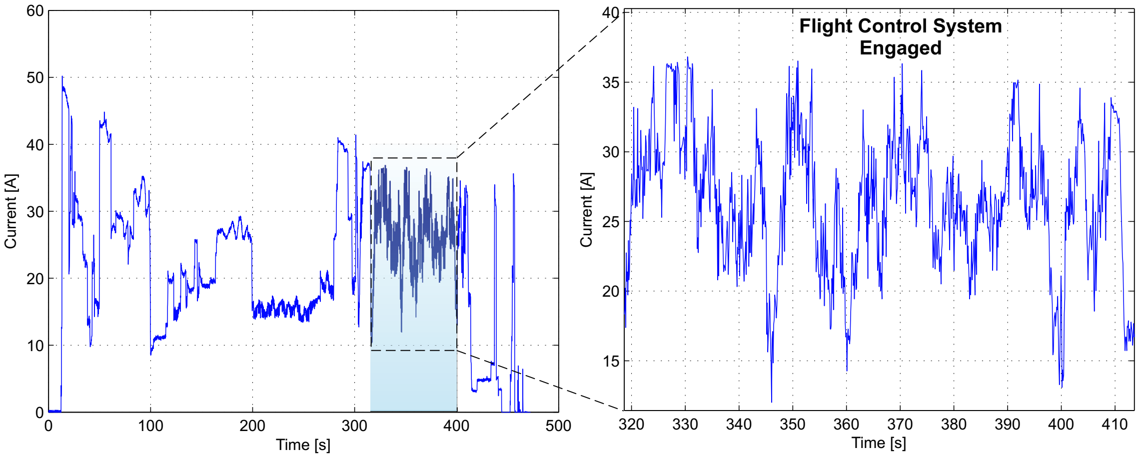

Figure 8.7: Engine Current During Flight Test

Since the purpose of the SU VSA was to test the flight control system to be implemented on Sekwa, Sekwa's trim airspeed of 18 [m/s] was used. With reference to figure 8.7, the electric engine required an average of 26.6 [A] to maintain an airspeed of 18 [m/s].

A 3300 [mAh] engine battery was used, resulting in an estimated flight time of 7 minutes. For the purpose of this project, a total flight time of approximately 7 minutes was deemed acceptable.

8.2.2.3 Test 2 - Airspeed and Altitude Step Response

Flight Test Procedure: For this test, during way point navigation an airspeed command of 16 [m/s] was issued, and after 35 seconds airspeed was commanded to the trim value of 18 [m/s] once again. Thereafter, an altitude step command of 35 [m] was given, and the flight test was terminated after the desired altitude was reached.

Flight Test Results: Figure 8.8 (a) shows that the control system reached 90% of the final value commanded in 5.32 [s], for a -2 [m/s] airspeed step command. The step response is slightly faster than what was observed during **HIL** simulations, which can be attributed to modelling errors in the engine model used during **HIL** simulated flight tests. To improve the airspeed transient response, more effort must be invested into obtaining a higher fidelity engine model. However, even with a slightly degraded practical response, the control system was observed to regulate airspeed satisfactorily.

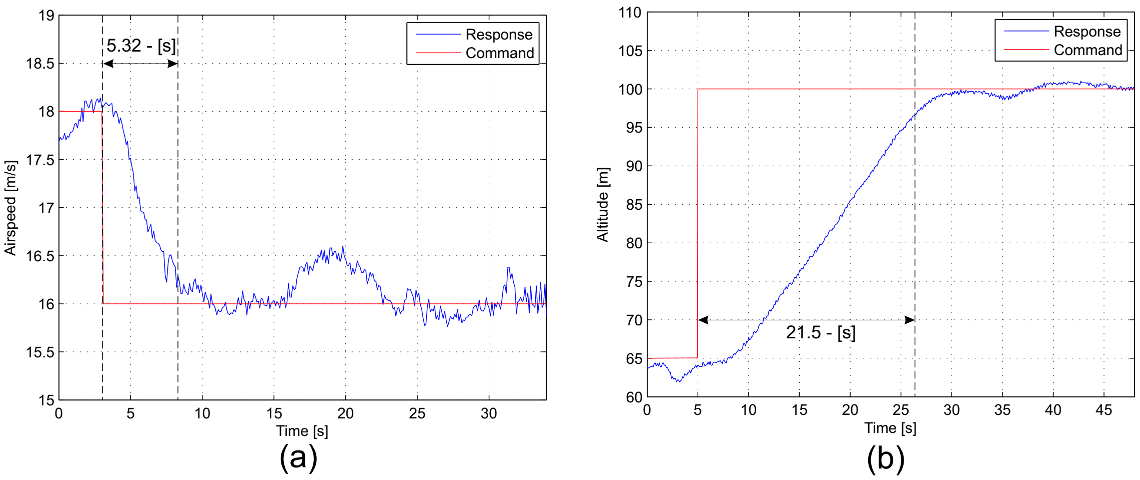

(a) (b)

Figure 8.8: (a) Airspeed Controller Step Response. (b) Altitude Controller Step Response.

Figure 8.8 (b) shows the practical altitude step response. Note however that a 35 m step was issued, resulting in the aircraft entering a constant climb rate. The time recorded for this response was 21.5 [s] to reach 90% of the final value commanded. Note how the the control system automatically entered the aircraft into a constant climb rate mode for the majority of the altitude step. The altitude controller was observed to regulate aircraft altitude with a RMS error of 1.0 [m].

8.2.3 Normal Specific Acceleration Control System

The objective of this test was to evaluate the **NSA** controller's practical step response.

8.2.3.1 Test Procedure: NSA Control System

- After manual take-off, the aircraft reached an altitude of 65 [m], and the pilot adjusted the elevon trim setting such that the aircraft was flying straight and level.
- The inner loop stability augmentation control system (**NSA** controller) was engaged, along with the lateral yaw rate controller.
- The **NSA** controller was commanded to regulate normal specific acceleration at -9.81 [m/s], and a $0°/s$ yaw rate command was issued.
- After the aircraft normal specific acceleration settled at -9.81 [m/s], a normal specific acceleration step command of -0.81 [m/s] was issued.

8.2.3.2 Flight Test Results

With reference to figure 8.9, the **NSA** closed loop step response showed a rise time of about 0.3 $[s]$, with the centre of mass placed 0% aft of the stable position. This corresponds very well to the 0.4 $[s]$ rise time observed during **HIL** simulation tests. The **NSA** control system was observed to work well in practice, delivering acceptable results.

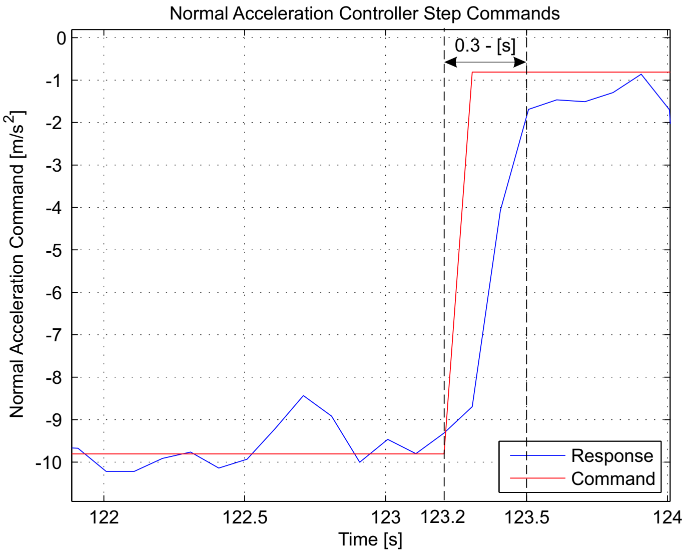

Figure 8.9: NSA Controller Step Response for the Statically Stable Case

8.3 Control System Evaluation for the Variable Stability Case

This section investigates the performance of the normal specific acceleration controller, and shows that it adequately stabilised the variable stability aircraft. Section 8.3.1 presents the results when the **LQR MIMO** control system was in control of the SU VSA. Next, section 8.3.2 shows that the pilot, when commanding normal specific acceleration through the **NSA** control system, was capable of flying the aircraft when it was *statically unstable*.

8.3.1 LQR MIMO Control System Commanding Normal Specific Acceleration

The following test was aimed at specifically evaluating the longitudinal flight control system under various centre of mass positions, and to show that the **NSA** control system succeeded in stabilising the vehicle regardless of the static stability margin.

8.3.1.1 Flight Test Procedure

- After manual take-off, the aircraft reached an altitude of 80 [m], and the pilot adjusted the elevon trim setting such that the aircraft was flying straight and level.
- The full flight control system was armed, and the aircraft entered way point navigation mode.
- During way point navigation, with the centre of mass 0% aft of the stable position, a 2 [m/s] climb rate command was issued. After the 2 [m/s] climb rate command, a zero climb rate command was issued.
- Next, the centre of mass was commanded aft of the AVL predicted neutral point, and a 2 [m/s] climb rate was commanded once again.
- After the desired climb rate was reached, the aircraft was stabilised and the test was terminated.

8.3.1.2 Flight Test Results

Over the course of the flight test, the centre of mass was moved as indicated by figure 8.10 (a). Figure 8.10 (b) shows how the aircraft trim elevator setting changed as a function of centre of mass position. At time 615 [s], the centre of mass was aft of the AVL predicted neutral point. Note how the elevator control effort increased (figure 8.10 (b)) when the centre of mass was aft of the neutral point. As mentioned in chapter 4, when the centre of mass is aft of the neutral point, C_{m_α} is positive, and acts as a spring pushing in the *same* direction as the applied disturbance, which explains the additional control effort applied by the **NSA** controller. The control system however proved to stabilise the vehicle very well at this point.

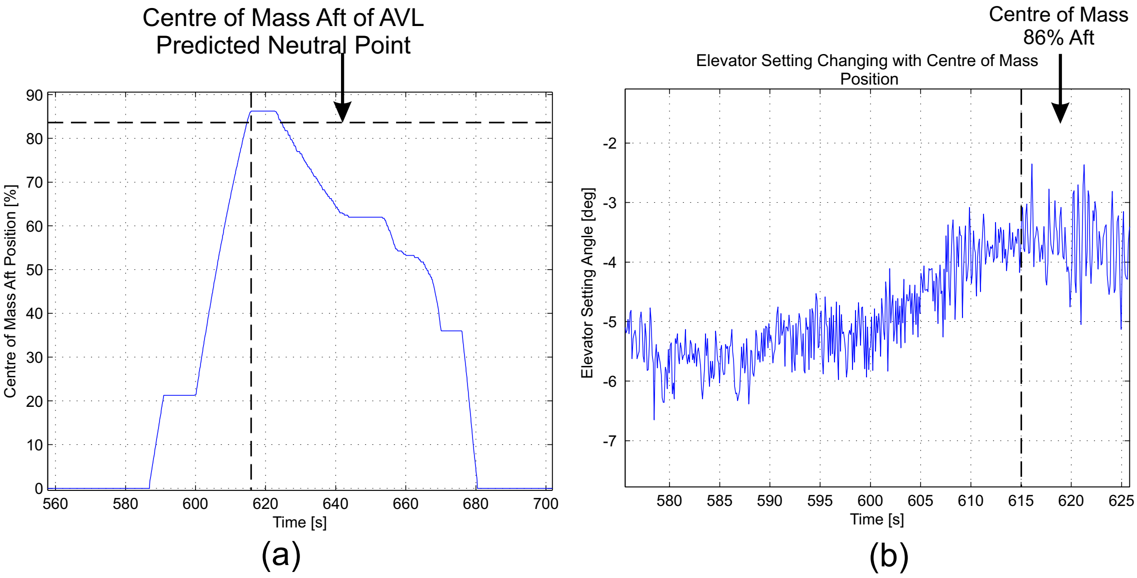

Figure 8.10: (a) Centre of Mass Position over Entire Flight. (b) Change in Elevator Trim Setting Angle with Centre of mass position.

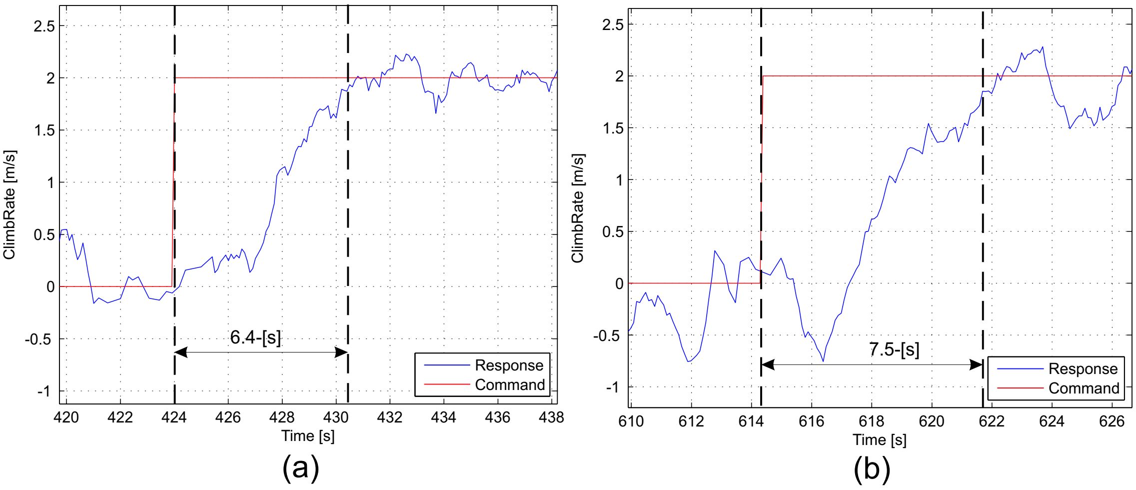

Figure 8.11: (a) Climb Rate Controller Step Response when aircraft is statically **stable**. (b) Climb Rate Controller Step Response when aircraft is statically **unstable**

Figures 8.11 (a) and 8.11 (b) shows the practical climb rate step response for a 2 [m/s] climb rate step command, when the aircraft was statically **stable** and statically **unstable** respectively. The results indicate that the aircraft was capable of performing a 2 [m/s] climb with the centre of mass *aft* of the AVL predicted neutral point. Note however that the rise times of the two respective climb rate step commands were not the same.

The difference can be attributed to both modelling errors in the Short period mode dynamics, and the inherent noise of the climb rate sensor which makes it difficult to identify the aircraft's true response to climb rate commands.

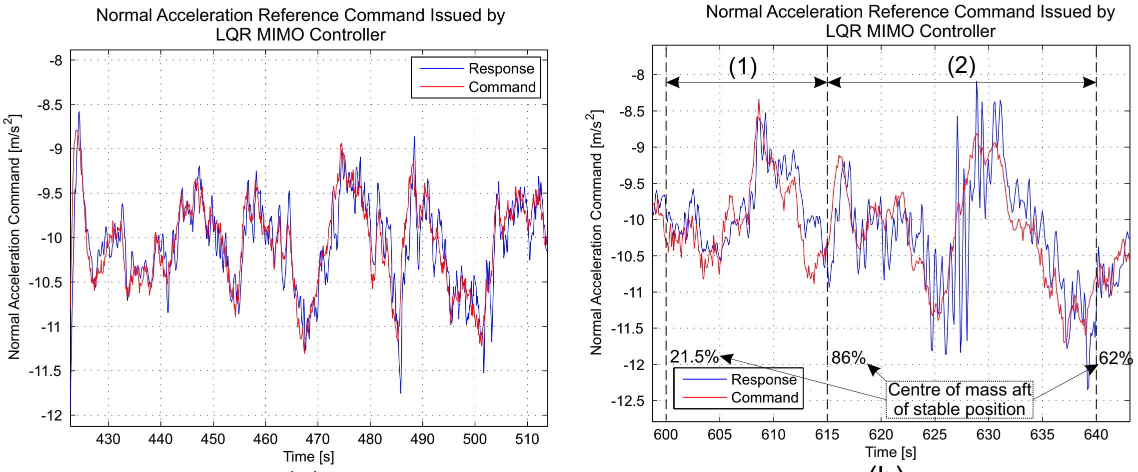

(a) (b)

Figure 8.12: (a) Specific Acceleration Controller Reference Following: Centre of Mass fixed in foremost position. (b) Specific Acceleration Controller Reference Following: Variable centre of mass position.

Figure 8.12 (a) shows how the designed **NSA** controller followed the normal specific acceleration reference command generated by the outer-loop **MIMO LQR** controller regulating airspeed and climb rate. The **NSA** controller seemed to follow the normal specific acceleration reference commands adequately, even when the aircraft's static stability margin was changed in flight. Figure 8.12 (b) (1) is when the centre of mass was moved from 21.25% aft to 86% aft of the stable position, which is aft of the AVL predicted aircraft neutral point. Figure 8.12 (b) (2) is when the centre of mass was moved from 86% aft to 62% of the stable position. The **NSA** control system was observed to regulate normal specific acceleration with a RMS error of 0.8 [m/s].

8.3.2 Human Pilot Commanding Normal Specific Acceleration

The purpose of this test was to illustrate that a human pilot could control the aircraft regardless of the centre of mass position, and therefore the static stability margin, using the stability augmentation controller in a *Fly-by-Wire* mode.

8.3.2.1 Flight Test Procedure: *Fly-by-Wire* Mode

- After manual take-off, the aircraft reached an altitude of 65 [m], and the pilot adjusted the elevon trim setting such that the aircraft was flying straight and level.
- The **NSA** stability augmentation control system was armed, and the *Fly-by-Wire* mode was activated. At this point, the pilot was commanding normal specific acceleration, instead of elevator.
- To allow the pilot to successfully fly the aircraft through the **NSA** controller, it was necessary to adjust the gain converting the pilot elevator commands to normal specific acceleration commands, such that the aircraft's pitch response remained unchanged when the stability augmentation controller was armed. After minor adjustments to the gain converting pilot elevator commands to normal specific acceleration reference commands, the pilot confirmed that the control system reacted as if the elevator was being commanded directly.
- After the pilot was comfortably in control of the aircraft, the centre of mass was shifted aft of the AVL predicted neutral point.
- The **NSA** controller's response was recorded, and after the controller's performance was tested over the entire centre of mass position range, the aircraft was stabilised and the test was terminated.

8.3.2.2 Flight Test Results: *Fly-by-Wire* Mode

Figure 8.13 shows how the **NSA** control system followed normal specific acceleration commands generated by the pilot.

In this test, the pilot was allowed to command ailerons, rudder, throttle and normal specific acceleration (through the **NSA** controller). The aircraft centre of mass was commanded to 34% aft of the neutral point. Then, it was moved 72% aft, after which it was moved 96% aft of the stable position. Therefore, the human pilot successfully controlled the aircraft when it was statically **unstable**.

Following the *Fly-by-Wire* flight test, the pilot indicated that the aircraft presented the same response during the course of the flight. This suggested that the **NSA** control system succeeded in its task, providing an invariant dynamic response over the centre of mass range investigated.

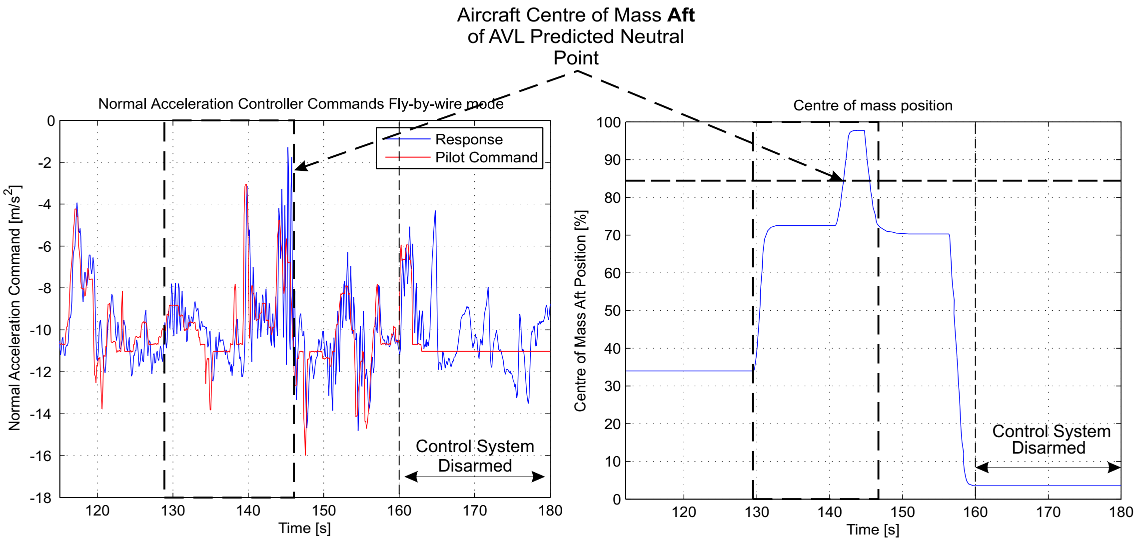

Figure 8.13: Fly-by-Wire Stability Augmentation control system with aircraft statically unstable

8.4 Practical Demonstration - The Lack of Natural Static Stability

Up to this point, throughout the flight tests conducted the pilot was only allowed *complete* control of the vehicle when the centre of mass was 0% aft of the stable position. However, following the completion of one particular flight test, the flight control system was mistakenly disarmed, when the aircraft centre of mass was 48.75% aft of the stable position, as indicated by figure 8.14 (a).

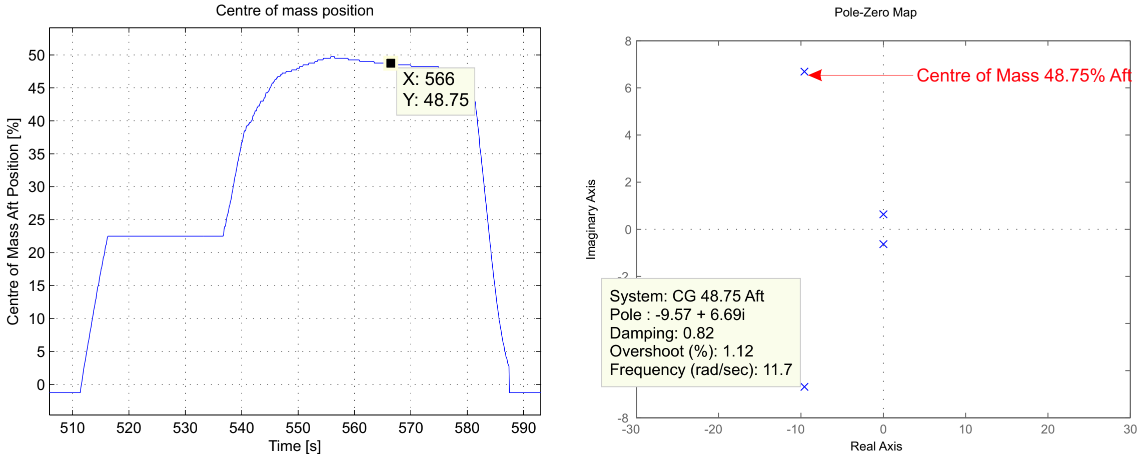

(a) (b)

Figure 8.14: (a) Centre of mass Position. (b) Pole-Zero Map of Aircraft Longitudinal dynamics when Centre of mass is 48.75% aft of the stable position

It was expected that disarming the flight control system at this point will not pose any significant problems, especially when considering the aircraft open-loop eigenvalues, indicated by figure 8.14 (b). With the centre of mass 48.75% aft of the stable position, the aircraft Short period mode exhibits an undamped natural frequency of 11.7 [rad/s] with a damping ratio of 0.82. These numbers indicate a well stable Short period mode, and therefore the pilot should be more than capable of controlling the aircraft at this point. Unfortunately, it was quickly discovered that the aircraft was *not* stable at this point.

8.4.1 Results of Accidental Autopilot De-activation

Data received from the pilot-controlled RC transmitter, figure 8.16 (a), confirmed that the autopilot system was disarmed at time 566 $[s]$.

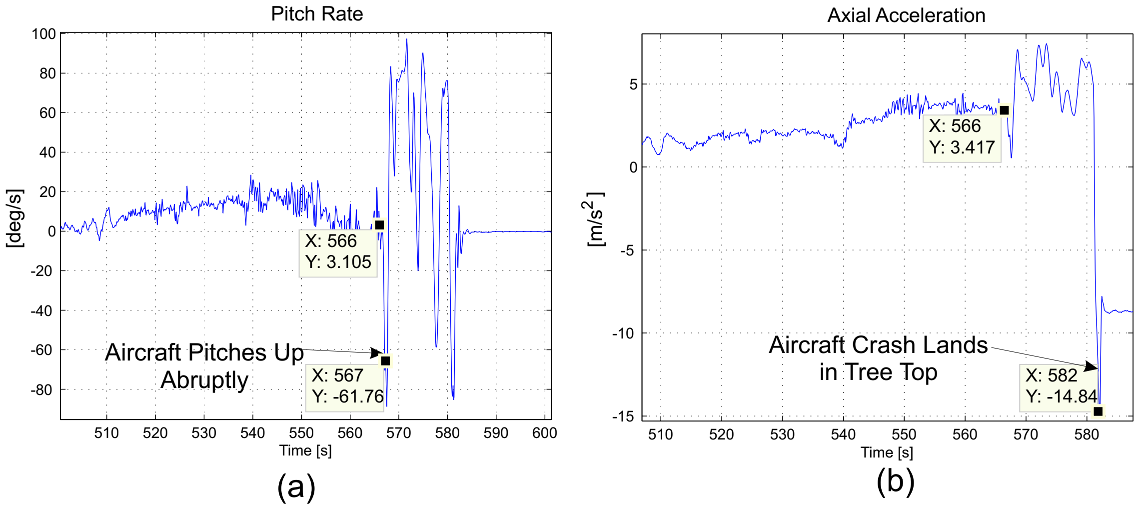

Figure 8.15: (a) Aircraft Pitch Rate [degrees/s]. (b) Axial Specific Acceleration [m/s^2]

At time 567 $[s]$, the aircraft abruptly entered an extreme nose-down pitching motion, with pitch rate in excess of $60^\circ/s$, as shown by figure 8.15 (a). The pilot consequently reacted only 0.7 $[s]$ later. As shown by figure 8.16 (b), the pilot commanded no elevator up to 0.7 $[s]$ *after* the aircraft suffered the abrupt nose-down pitching motion. The pilot instinctively pulled back on the elevator in an attempt to recover the aircraft. By the time the pilot reacted however, the aircraft had already entered a stall, and after a series of stalled spins and failed recovery attempts, crash-landed in a tree top. The axial acceleration measurement, given by 8.15 (b), suggested that the aircraft crashed at time 582 $[s]$.

Fortunately, the aircraft itself suffered no visible damage whatsoever, and the avionics remained completely intact.

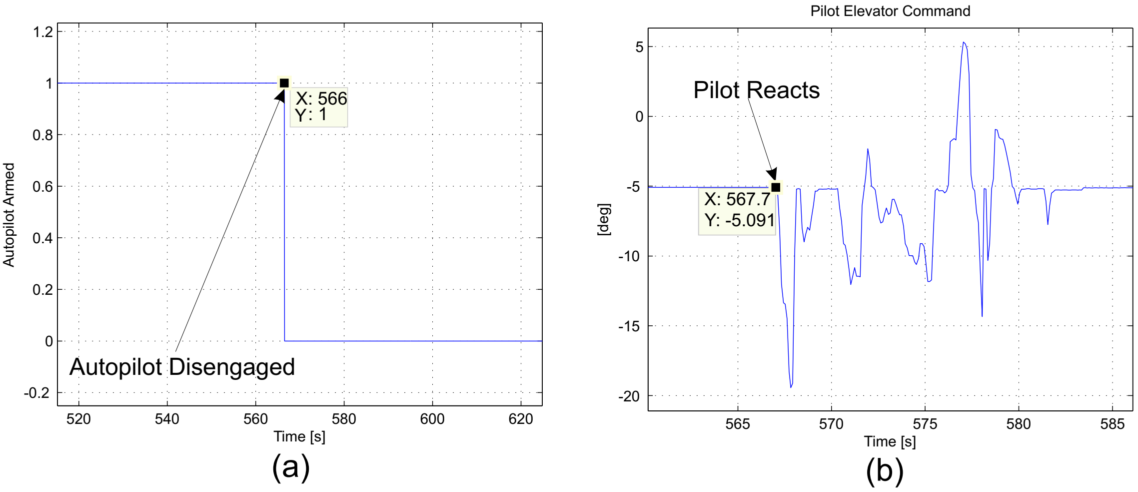

Figure 8.16: (a) Pilot RC Transmitter Autopilot Armed/Disarm Status. (b) Pilot Elevon Commands [degrees]

8.4.2 Crash Analysis

After the incident, the stability derivatives were analysed using AVL. With the centre of mass 48.75% aft of the stable position, it was found that the derivative quantifying the aircraft's aerodynamic *spring-stiffness* (C_{m_α}), was 2.3 times less at the 48.75% aft position than at the 0% aft position. Consequently, it was concluded that the natural restoring moment generated by the aircraft was roughly 2.3 times less as well. Assuming that the neutral point was accurately calculated by AVL, this might explain why the pilot lost control of the vehicle at this point.

However, the open loop eigenvalues with the centre of mass 48.75% aft of the stable position indicated that the aircraft was stable. This suggests that AVL provided an inaccurate estimate of C_{m_α}. Since even the slightest change in C_{m_α} can have a tremendous effect on the stability of the vehicle, errors during the centre of mass position measurement as well as slight AVL modelling errors could very well have contributed to the previously described chain of events, which lead to the crash. Considering the high centre of mass position measurement accuracy (see chapter 6, section 6.1.1), the conclusion was drawn that the C_{m_α} derivative was incorrectly calculated by AVL for centre of mass positions near the neutral point.

These results are arguably the *most* important results obtained during the entire project, proving that the flight control system was fully capable of controlling the aircraft where an experienced human pilot failed to do so.

As indicated by figure 8.13, the pilot controlled the aircraft for roughly 27 $[s]$ in *Fly-by-Wire* mode, when the centre of mass was placed at an aft position of 48.75%. This proves that the stability augmentation *Fly-by-Wire* mode successfully assisted the pilot in controlling the vehicle under an apparently dangerously low static stability margin. Furthermore, the full flight control system controlled the vehicle at and beyond the 48.75% aft point for roughly 1 min, as shown by figure 8.10 (a). This means that the autopilot successfully controlled the aircraft at a static stability margin which was proven to be extremely difficult to control by a human pilot.

8.5 Summary

The chapter introduced the SU VSA constructed for the project, acting as an initial robust test platform capable of demonstrating flight at unstable centre of mass locations. The modular design approach of the flight control systems simplified integration of these systems into the SU VSA.

The lateral flight control systems, along with way point navigation, were successfully demonstrated as the aircraft was capable of tracking the desired way point orientated flight path.

The chapter discussed the results obtained during practical flight tests, and proved through practical implementation that the flight control system was capable of controlling the SU VSA under various static stability margins. It was found that the control system was robust enough to adequately regain static stability, even when the centre of mass was placed aft of the AVL predicted neutral point.

Lastly, it was shown that an experienced human pilot failed to control the aircraft under a relaxed static stability margin, even when the eigenvalue analysis suggested that the aircraft should have been well controllable. However, the pilot was able to comfortably control the aircraft through the **NSA** *Fly-by-Wire* mode. These results emphasised the fact that the stability augmentation control system designed, was the key component in achieving a successful demonstration of the flight of a statically unstable aircraft.

Chapter 9

Summary and Recommendations

9.1 Summary

This thesis reported the investigation, design and practical implementation of a flight control system capable of successfully controlling a variable stability blended-wing-body aircraft.

The main purpose of the control system was to augment the natural stability of the aircraft. The focus was to restore the aircraft's nominal static stability and then furthermore, to regulate motion variables to facilitate full autonomous flight. Investigation into the aircraft dynamics, as the centre of mass is moved aft of the stable position, revealed that the primary stability problem was observed in the aircraft's **S**hort **P**eriod **M**ode (**SPM**) of motion.

The control strategy was thus to implement a closed form **SPM** controller with enough degrees of freedom to stabilise the **SPM** of motion, by fixing the **SPM** poles in state space. It was shown that, by regulating the aircraft's normal specific acceleration, that the aircraft **SPM** could be regulated independently of the remainder of the aircraft dynamics. The normal specific acceleration acts as a virtual actuator to an outer, largely kinematics based, airspeed and climb rate controller. Through the virtual actuator, this controller always perceived a stable airframe with invariant dynamic response for all centre of mass positions.

A single offline **L**inear **Q**uadratic **R**egulator (**LQR**) design was thus sufficient for control at this level with altitude regulation added through simple proportional feedback to the climb rate command. Conventional lateral controllers were designed in a successive loop closure fashion. These included a Dutch roll damper as well as turn rate, heading and cross track error controllers. Path planning and cross track error algorithms were implemented to facilitate autonomous way point navigation.

Finally, two low bandwidth controllers were designed to regulate the centre of mass position in flight. The first controller allowed the centre of mass position to be commanded directly while the second regulated the centre of mass such that a desired average trim elevon position was realised. All of the controllers were designed to be computationally inexpensive and could therefore be implemented on small cost-effective embedded microcontrollers. Performing all autopilot functions and calculations on-board the aircraft implies that the aircraft is not restricted to flying within communications range of the ground station. The avionics designed includes low cost angular rate gyroscopes, accelerometers, pressure sensors and a GPS receiver. The avionics was capable of **H**ardware **I**n the **L**oop (**HIL**) simulation which greatly reduced the risks of autopilot errors during flight tests.

Practical flight tests confirmed that the flight control system was capable of full autonomous flight, even when the aircraft's stability margin was adjusted in flight. The results obtained proved that the stability augmentation control system could regain static stability for all centre of mass positions, and allowed the human pilot to control the aircraft when it was statically unstable. It was also proven that the aircraft was extremely difficult to control even at a slightly relaxed stability margin.

The following contributions were made during the course of the project towards the development of future UAVs within the ESL autonomous flight research group:

- A control algorithm capable of controlling a variable stability aircraft. Note that the algorithm is not restricted to blended-wing-body aircraft, and could be applied to more conventional aircraft as well.
- An aircraft aerodynamic model, providing aerodynamic forces and moments as a function of aircraft centre of mass location.
- A smaller, light weight, modular, on-board computer (OBC) was developed, allowing for all of the necessary flight control system software routines to be implemented. The OBC was designed such that it could be effortlessly integrated into the existing SU avionics system.
- A DC motor controller CAN node was developed. This node implements both the centre of mass position and the trim elevator setting control systems, and can also act as a general control node for a small DC motor.
- Comprehensive ground station GUI software was developed, providing a user-friendly interface between the ground station operator and the aircraft avionics systems.
- Construction and Modification of a variable stability blended-wing-aircraft, to serve as both a demonstrator vehicle and as a test platform for future UAV projects.

9.2 Recommendations

Recommendations on how the current flight control system could be improved will now be discussed.

9.2.1 Automatically Determining the Optimal Centre of Mass Position

In theory, the CSIR DPSS Sekwa vehicle should deliver less drag at some optimal centre of mass location. Instead of commanding the centre of mass to a theoretically calculated value, which in turn relies heavily on measurement precision as well as the exact location of the aircraft neutral point, a control system could be designed that searches for the optimal centre of mass location.

The optimal centre of mass location could be found by designing a control system that attempts to find the point where the aircraft engine dissipates the least amount of power. Currently, the system provides the capability of measuring the power applied to the aircraft electric engine directly. The power measurement could be averaged over time, and used in a feedback loop that commands the centre of mass position until the measured engine power reaches some local minimum. In this way, the optimal centre of mass position could be found practically.

Control Effort and Drag Reduction: The current avionics system provides information about the amount of current dissipated by the servo actuators during the course of a flight. As the vehicle becomes less stable, more control effort is employed by the **NSA** controller to regain stability. As the amount of control effort is increased, the servo actuators will move more rapidly, drawing more current, and unwanted drag might be induced. This must be investigated further in future Sekwa research, as it seems that there is a possible trade-off between the engine power saved at the optimal centre of mass location, versus the amount of power dissipated by the actuators to stabilise the vehicle.

9.2.2 Improving the Lateral Flight Control System

A possible improvement to the current lateral flight control system is to design a roll angle controller. The roll angle measurement could be obtained from an estimator. With direct roll angle feedback, the aircraft would be able to fly at larger bank angles, and consequently smaller turning circles during way point navigation could be used. This is desired for safety reasons, as the aircraft must fly well within visual range of the safety pilot.

An improvement to the current navigation system is outlined in [17]. This system does not rely on a lateral track error to regulate back to a desired path, and is expected to be a better candidate for way point navigation as opposed to the system employed in this project.

9.2.3 Avionics System Redundancy

Hardware modularity is achieved by implementing a CAN bus network. As this is a multi-master network, any node can act as the primary node. Should the master node fail, any secondary node can become the master node and normal operation of the avionics is resumed without interruption. Furthermore, sensor nodes can operate in parallel, monitoring each other. Should the primary sensor node fail, the secondary sensor node can simply become the primary sensor node, thus enabling a redundant sensor system. Although system redundancy is outside the scope of this project, the avionics were designed to cater for it. Further research into hardware redundancy could improve and expand the overall functionality of the current avionics system tremendously.

Appendices

Appendix A

Control of Lateral Dynamics

The arguments presented in chapter 3 concluded that the stability and control derivatives most prominent in the lateral aircraft dynamics can be assumed to remain almost constant over the centre of mass position range investigated. Therefore, conventional lateral flight control systems are designed and discussed in this chapter.

The primary function of the lateral flight control systems is to allow for full autonomous flight within a non-aerobatic flight envelope. This will allow for the non-conventional longitudinal flight control system designed to be evaluated without human pilot intervention. The lateral control system design details presented in the chapter were initially based on the Sekwa vehicle, and after some minor adjustments were implemented on the SU VSA.

A.1 Aircraft Lateral Dynamics Analysis

This section is aimed at analysing the lateral aircraft dynamics by investigating the lateral eigenvalues, and in doing so prove the assumptions made in chapter 3 that the lateral dynamics remain almost unchanged during centre of mass variations along $\boldsymbol{i}^B$.

A prerequisite to the analysis however is that the lateral dynamics be formally stated in a linear form. As previously mentioned, the aircraft dynamics presented in chapter 2 can be decoupled into longitudinal and lateral dynamics respectively. When analysing the lateral dynamics exclusively, the longitudinal forces, moments, angles and angular velocities are set to zero. Equations (2.2.8), (2.2.24), (2.2.25), (2.2.29) and (2.2.30) are then used to create the non-linear, decoupled lateral dynamic equations of motion. These non-linear differential equations are linearised about the straight and level trim flight condition producing,

$$
\begin{aligned}
\begin{bmatrix} \dot{\beta} \\ \dot{p} \\ \dot{r} \\ \dot{\phi} \end{bmatrix} &= \begin{bmatrix} \frac{\bar{q}S}{m\overline{V}_W}C_{Y_\beta} & \frac{\bar{q}Sb}{2m\overline{V}_W^2}C_{Y_P} & \frac{\bar{q}Sb}{2m\overline{V}_W^2}C_{Y_R} - 1 & \frac{g}{\overline{V}_W} \\ \frac{\bar{q}Sb}{I_{xx}}C_{l_\beta} & \frac{\bar{q}Sb^2}{2I_{xx}\overline{V}_W}C_{l_P} & \frac{\bar{q}Sb^2}{2I_{xx}\overline{V}_W}C_{l_R} & 0 \\ \frac{\bar{q}Sb}{I_{zz}}C_{n_\beta} & \frac{\bar{q}Sb^2}{2I_{zz}\overline{V}_W}C_{n_P} & \frac{\bar{q}Sb^2}{2I_{zz}\overline{V}_W}C_{n_R} & 0 \\ 0 & 1 & 0 & 0 \end{bmatrix} \begin{bmatrix} \beta \\ p \\ r \\ \phi \end{bmatrix} \\
&+ \begin{bmatrix} \frac{\bar{q}S}{m\bar{V}_S}C_{Y_{\delta_A}} & \frac{\bar{q}S}{m\bar{V}_S}C_{Y_{\delta_R}} \\ \frac{\bar{q}Sb}{I_{xx}}C_{l_{\delta_A}} & \frac{\bar{q}Sb}{I_{xx}}C_{l_{\delta_R}} \\ \frac{\bar{q}Sb}{I_{zz}}C_{n_{\delta_A}} & \frac{\bar{q}Sb}{I_{zz}}C_{n_{\delta_R}} \\ 0 & 0 \end{bmatrix} \begin{bmatrix} \delta_A \\ \delta_R \end{bmatrix}
\end{aligned}
\tag{A.1.1}
$$

where $\begin{bmatrix} \beta & p & r & \phi \end{bmatrix}^T$ is the linearised lateral control state vector. Writing the lateral dynamics in the form given by equation (A.1.1) allows for the calculation of the lateral *eigenvalues* describing the aircraft lateral dynamic response. Equation (A.1.1) describes a fourth-order system, and therefore four distinct eigenvalues can be found, classically forming two real poles with one complex pole pair. The complex pole pair in turn describe the classically defined dutch-roll mode of motion, and the two real poles describe the spiral and roll modes of the aircraft. These are briefly discussed next.

A.1.1 Modal Analysis

This section analyses the lateral modes of motion in more detail using modal decomposition. For details on modal decomposition refer to [14].

	Roll	Dutch Roll	Spiral
	-13.9402	$-0.4527 \pm 5.8722i$	0.039
β	$0.0034\angle 0°$	$0.0884\angle -165.50°$	$0.0127\angle 0°$
p	$0.9974\angle 0°$	$0.8753\angle 0°$	$0.0343\angle 0°$
r	$0.0044\angle 180°$	$0.4516\angle 107.20°$	$0.4151\angle 0°$
ϕ	$0.0716\angle 180°$	$0.1486\angle -94.41°$	$0.8792\angle 0°$

Table A.1: Lateral Modes

Table A.1 shows the eigenvalues (poles) of equation (A.1.1), with the eigenvectors describing each of the individual eigenvalues. As expected, four eigenvalues are obtained describing the three lateral modes of motion mentioned earlier. The aircraft lateral modes are discussed next, with reference to the results given in table A.1, to gain additional insight into the lateral aircraft dynamics.

A.1.1.1 Roll Mode

The roll mode is a non-oscillatory lateral characteristic which is usually substantially decoupled from the spiral and dutch-roll modes of motion [1]. Due to its non-oscillatory nature, it is described by a single real root of the characteristic polynomial of equation (A.1.1), and classically manifests itself as an exponential lag characteristic in rolling motion about $\boldsymbol{i}^B$. Typically, for small aircraft with low roll inertia, the roll mode exhibits short time constants and is consequently the fastest of the three lateral modes of motion discussed in this thesis.

A time history plot of pure roll mode motion is shown in figure A.1, where the lateral state space system (equation (A.1.1)) state vector has been initialised with the roll mode eigenvector (table A.1). Note that sideslip and yaw rate are not even visible on the plot.

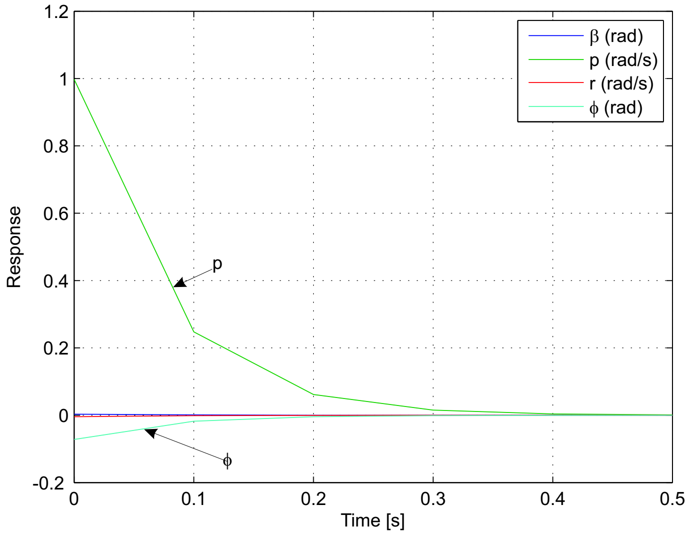

Figure A.1: Pure Roll Mode Response

A.1.1.2 Spiral Mode

The spiral mode is also non-oscillatory in nature [1] and is consequently determined by the other real root in the characteristic polynomial of equation (A.1.1). The mode classically describes the tendency of the aircraft to converge to or diverge from a wings level position after a disturbance. Assume that a disturbance acts on the aircraft such that a small positive bank angle ϕ develops. If left unchecked, this disturbance results in a small positive sideslip causing the aircraft to yaw into the direction of the sideslip velocity (fin effect). The yawing motion in turn produces differential lift across the main wing, resulting in a rolling motion being produced which increases the bank angle disturbance further, leading to a diverging motion. However, dihedral and quarter chord sweep back effects of the wing, tend to produce a negative roll moment in response to the sideslip which opposes the positive roll motion [1]. Therefore, the fin and dihedral effects act in opposition to create the spiral mode of motion. Since the fin and dihedral effects are typically similar in magnitude [1], the spiral mode classically exhibits a long time constant.

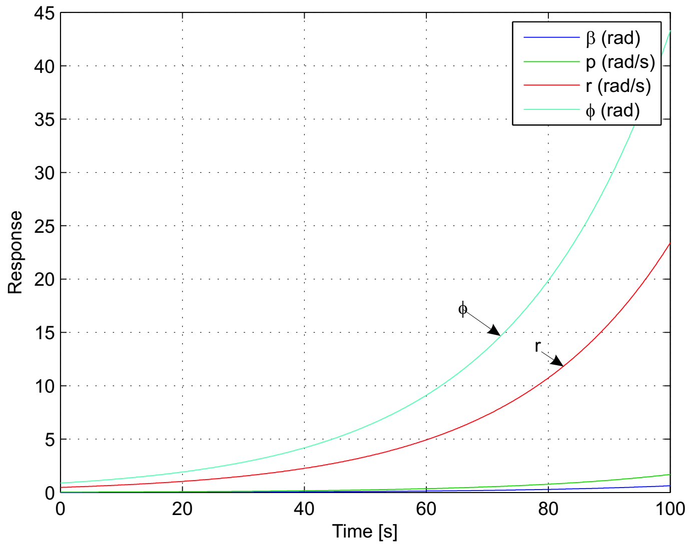

Figure A.2: Pure Spiral Mode Response

A time history plot of pure spiral mode motion is shown in figure A.2, where the lateral state space system (equation (A.1.1)) state vector has been initialised with the spiral mode eigenvector. Note that the aircraft used in this project has large vertical fins, which explains the unstable spiral mode.

A.1.1.3 Dutch Roll Mode

The dutch roll mode is a classical damped oscillation in yaw [1], about $\mathbf{k}^{B}$, which couples into roll. The mode can best be visualised by initially considering the aircraft to be restrained in yaw by a torsional "spring" acting about $\mathbf{k}^{B}$, where the spring stiffness is largely determined by the vertical fin. When a yaw disturbance acts on the aircraft, the vertical fin produces an aerodynamic "spring" force to produce a restoring yawing moment which results in a classical oscillatory motion [1]. However, the oscillation in yaw results in the airflow varying in an oscillatory manner across the main wing surface, leading to an oscillation in the differential lift generated and therefore an oscillation in the aircraft roll motion. According to [1], the oscillation in roll lags the oscillation in yaw by approximately 90°. This phase difference between the yawing and rolling motion implies that the forward moving wing is low and the aft moving wing is high, consequently leading to the wing tips tracing an elliptical path relative to the horizon in the $X_B Z_B$-plane [1].

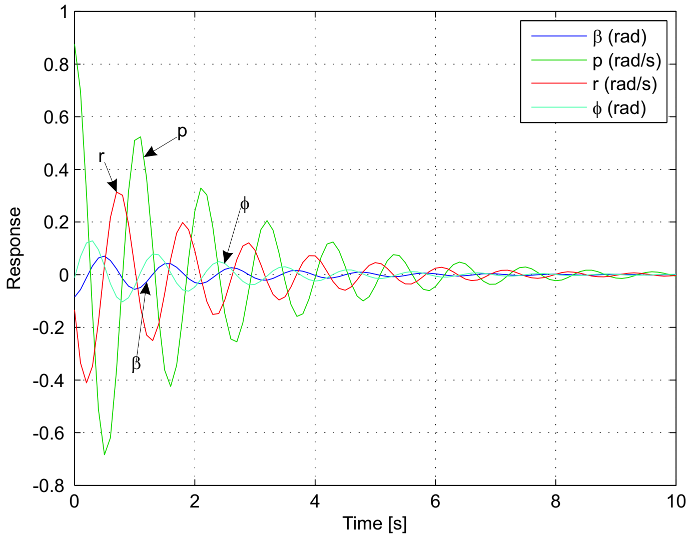

Figure A.3: Pure Dutch Roll Mode Response

Note that a large fin results in improved dutch roll mode damping, but unfortunately large vertical fins tend to degrade spiral stability. Therefore, it is expected that the resulting lateral aerodynamics will show a compromise between spiral stability and dutch roll mode damping, with a mildly stable (or even slightly unstable) spiral mode and a poorly damped dutch roll mode. The dutch roll mode poles are classically identified as a second order complex pole pair.

A time history plot of pure dutch roll mode motion is shown in figure A.3, where the lateral state space system (equation (A.1.1)) state vector has been initialised with the dutch roll mode eigenvector. Note that the oscillation in roll lags yaw by roughly 90° as mentioned earlier.

A.1.1.4 Relative Actuator Control Over Modes

Now that the lateral modes of motion are analysed, it remains to find which actuator best controls which mode of motion. This provides additional insight when designing the lateral flight control systems.

After the input matrix of equation (A.1.1) is transformed to modal form (see [14]), the relative control gains from the lateral actuators to each of the lateral modes of motion can be obtained. This provides an indication of which actuator controls which mode more effectively. The analysis provided the following results,

- Roll Mode: $\frac{AIL}{RUDD} = 3.6$

- Spiral Mode: $\frac{AIL}{RUDD} = 5.13$
- Dutch Roll Mode: $\frac{AIL}{RUDD} = 0.4$

indicating that the ailerons are more effective than the rudders to control both the roll and spiral modes of motion, whereas the rudders are more effective than the ailerons in controlling the dutch roll mode. The aforementioned results intuitively makes sense, and must be kept in mind when designing the various lateral control systems.

A.1.2 Eigenvalue Variation over Centre of Mass Position Range

Figure A.4 shows the aircraft lateral pole locations when evaluating the eigenvalues of equation (A.1.1) over the entire centre of mass range investigated.

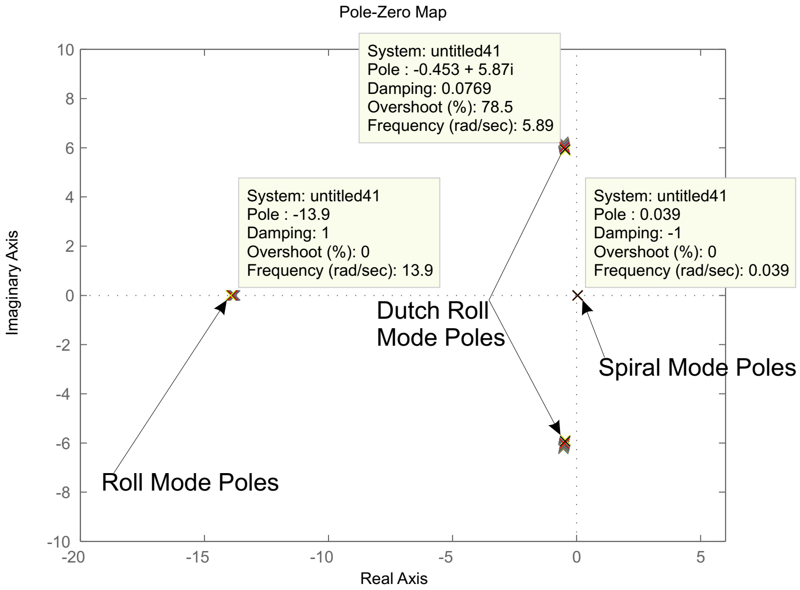

Figure A.4: Aircraft Open Loop Lateral Pole Locations over entire centre of mass range

As expected, a complex pole pair is found along with one real high and one real low frequency pole. The complex pole pair describes an oscillatory response, and is consequently identified as describing the dutch roll mode. On the other hand, the low frequency real pole describes the spiral mode and the high frequency real pole the roll mode of motion.

As shown by figure A.4, the poles most prominent in the aircraft *lateral* dynamics are acceptably invariant to variations in aircraft centre of mass position along the vehicle longitudinal axis. Therefore, the results given in chapter 3 are confirmed, and the lateral variable stability aircraft problem is observed to reduce to that of a conventional aircraft. For this reason, conventional lateral flight control systems, as described by [2] and [14], are designed, the purpose of which is to simply allow for full autonomous flight in order to successfully evaluate the non-conventional longitudinal controllers designed in chapter 4.

A.2 Lateral Flight Control System Design

The design and linear simulation of the lateral flight control system is considered in this section. Each controller design begins with a conceptual overview of the design before the details of the controller are considered and the results verified by means of linear simulation.

A.2.1 Dutch Roll Damper

Modal analysis showed that the dutch roll mode is poorly damped. Therefore, a dutch roll damper is designed to suppress the natural dynamics of the dutch roll made, and to provide artificial damping with respect to inertial space for wind gust disturbances.

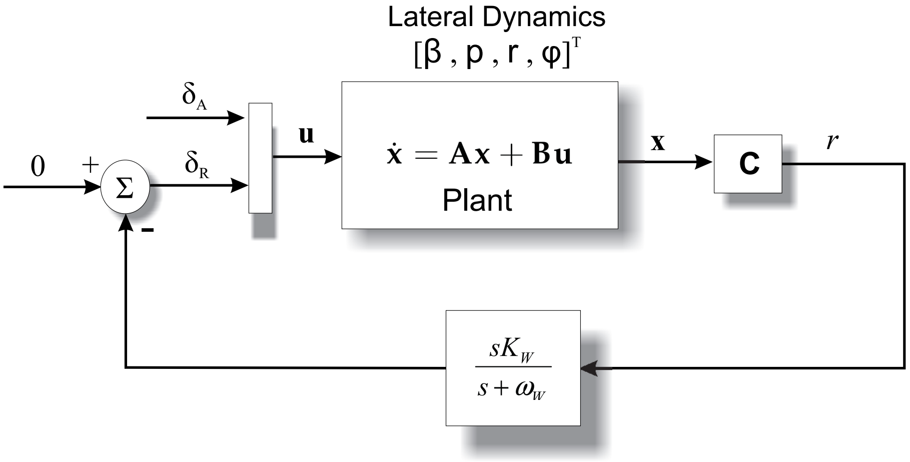

Figure A.5: Dutch Roll Damper Conceptual Overview

The dutch roll damper is implemented by feeding a yaw rate signal back to the rudder [2]. This is done because the rudder was shown (through modal analysis) to be more effective than the ailerons in controlling this mode. To prevent the damper from countering constant turn rate motions, the yaw rate signal is high pass filtered before being applied to the rudders. Furthermore, the high pass filter will negate the bias effects of low cost rate gyroscopes as an added advantage.

A.2.1.1 Design

The control system is given conceptually by figure A.5 where the plant dynamics are taken from equation (A.1.1). The output matrix (**C**) is set to extract the yaw rate state (r) in radians per second. This yaw rate signal moves through a washout[1] filter in the feedback loop. The washout filter cutoff frequency is chosen low enough to ensure the frequency of the dutch roll mode lies within its pass-band, and high enough to prevent the dutch roll damper from countering constant turn rates. A filter cutoff frequency of 1.14 [rad/s] was found to sufficiently damp the aircraft dutch roll mode.

Figure A.6 (a) shows a root locus plot of the lateral dynamics for variations in the filter feedback gain K_W. The five poles visible are the closed loop dutch roll mode poles, roll rate, spiral and washout state poles.

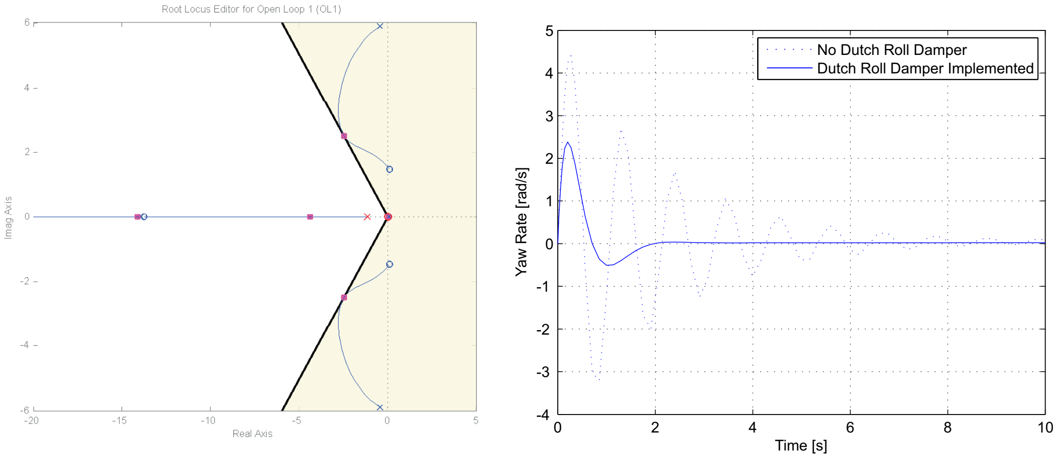

(a) (b)

Figure A.6: (a) Dutch Roll Damper Root Locus. (b) Closed Loop System Response With and Without the Dutch Roll Damper

The filter gain is increased to provide optimal damping (i.e. $\zeta = 0.707$) of the dutch roll mode for the chosen cutoff frequency. The washout filter designed is given as,

$$D_W(s) = \frac{-0.35s}{s+1.14} \tag{A.2.1}$$

The closed loop system dynamics with the augmented washout state (x_W) is given as [14],

---

[1] The high pass filter is also known as a washout filter

$$\begin{bmatrix} \dot{x} \\ \dot{x}_W \end{bmatrix} = \begin{bmatrix} \mathbf{A} - \mathbf{B}D_W\mathbf{C} & -\mathbf{B}C_W \\ B_W\mathbf{C} & A_W \end{bmatrix} \begin{bmatrix} x \\ x_W \end{bmatrix} + \begin{bmatrix} \mathbf{B} \\ 0 \end{bmatrix} \mathbf{u} \tag{A.2.2}$$

where A_W, B_W, C_W and D_W are the scalar state space representation of equation (A.2.1).

Linear Simulation: Figure A.6 (b) shows the aircraft yaw rate response with and without the dutch roll damper when the dutch roll mode is excited. It is clear that the dutch roll mode is well suppressed by the damper.

A.2.2 Lateral Attitude Control

It is shown by [14], for an aircraft in a steady, constant altitude, banked turn that the lateral acceleration can be written as,

$$a_L = \overline{V}\dot{\psi} = g\tan\phi \tag{A.2.3}$$

Therefore, if the pitch and roll angles are limited to small angles, the aircraft's yaw rate is found to be proportional to its roll angle,

$$\phi \approx \frac{\overline{V}}{g} r \tag{A.2.4}$$

This means that by controlling the aircraft yaw rate, the roll angle can also be regulated. The following observations must be kept in mind during design and implementation of the flight control systems if the roll angle is to be controlled by regulating yaw rate,

- Advantage: Roll angle control is achieved without the need to integrate a low-cost rate gyroscope.
- Disadvantage: Flight envelope is limited to small pitch and roll angles.

When evaluating equation (A.2.4) at the aircraft's trim airspeed, and for a $15^\circ/s$ yaw rate, the bank angle can be found to be,

$$\phi \approx \frac{\overline{V}}{g} r = \frac{18}{9.81} 15 = 27.5^\circ \tag{A.2.5}$$

Therefore, for the assumption that the roll angle can be approximated by the yaw rate to remain valid, the commanded yaw rate must not exceed $15^\circ/s$, and therefore the maximum allowable yaw rate command was limited to $15^\circ/s$.

A.2.2.1 Yaw Rate Controller

As explained earlier, by controlling yaw rate the aircraft roll angle can be regulated indirectly. Modal analysis showed that the ailerons are best suited to control the aircraft roll mode, thus a simple approach would be to simply feed back yaw rate to the ailerons to control the aircraft's roll attitude.

However, it is desired to command a certain yaw rate with zero steady error, therefore integral control must be employed to negate any steady state errors building up due to modelling errors. It is shown by [14] that the added integrator state drives the closed loop system unstable, a problem easily remedied by feeding back roll rate to the ailerons. This essentially counters the large aileron commands that the integrator generates over time and that drive the system unstable [14].

For the purpose of this project, the speed of response performance of this controller is not critical. The primary objective of this controller is to allow for full autonomous flight, which enables performance evaluation of the stability augmentation control system without interference from the human pilot.

A.2.2.2 Control System Design

The yaw rate controller architecture is given conceptually by figure A.7. The output matrix (**C**) is set to extract the roll and yaw rate states in radians per second, and the plant dynamics are obtained from equation A.2.2.

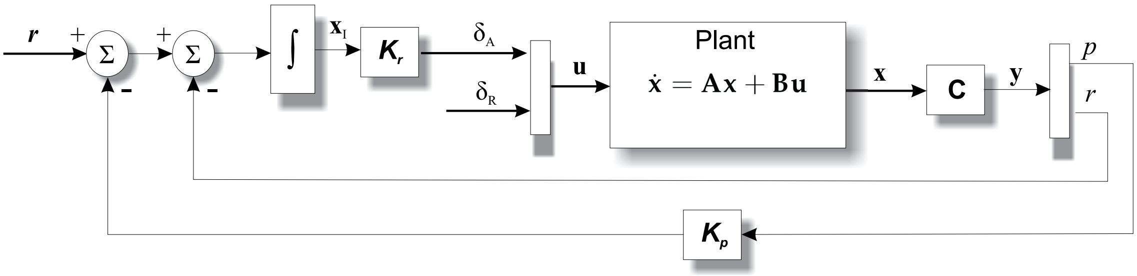

Figure A.7: Yaw Rate Controller Conceptual Overview

The design begins with the yaw rate loop. The integrator dynamics are described by,

$$\dot{x}_I = \mathbf{r} - [0 \quad 1]\mathbf{C}\mathbf{x} \tag{A.2.6}$$

where $\mathbf{r}$ is the reference yaw rate command and x_I is the integrator state. Figure A.8 (a) shows a root locus plot for the variation in the feedback gain $\mathbf{K}_r$, with the integrator dynamics included. Note how pure yaw rate feedback drives the system unstable. A higher feedback gain $\mathbf{K}_r$ increases the bandwidth of the system, but makes it more difficult for the roll rate loop to stabilise the system. The gain $\mathbf{K}_r$ is chosen iteratively with the roll rate feedback gain $\mathbf{K}_p$ to find the best solution.

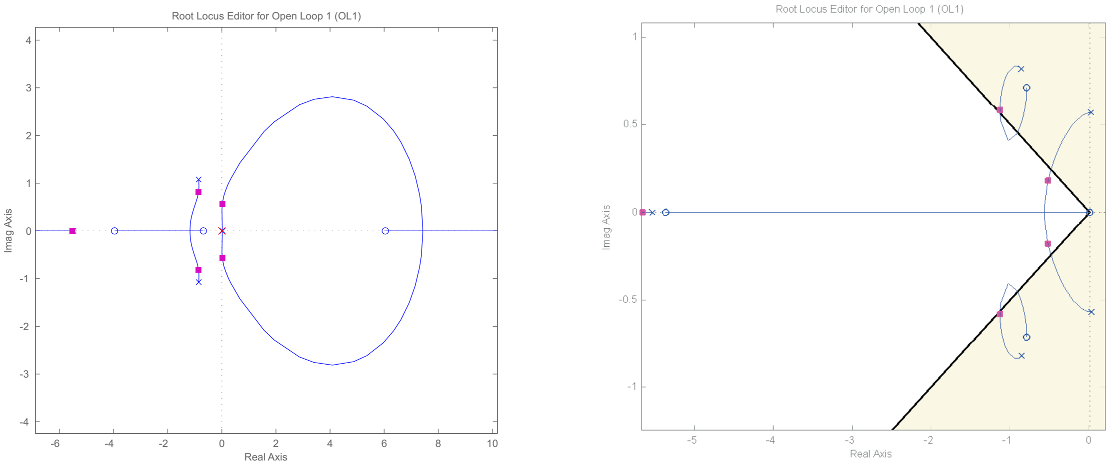

(a) (b)

Figure A.8: (a) Yaw Rate Loop Root Locus. (b) Roll Rate Loop Root Locus

The following feedback gains were consequently chosen,

$$\mathbf{K}_r = -0.12 \tag{A.2.7}$$

$$\mathbf{K}_p = 1.95 \tag{A.2.8}$$

With the above choice of feedback gains, the control system was observed to reach 90% of its commanded value in less than 4 seconds. With the integrator state augmented to the system, the closed loop dynamic equations are given [14] by,

$$\begin{bmatrix} \dot{\mathbf{x}} \\ \dot{x}_I \end{bmatrix} = \begin{bmatrix} \mathbf{A} & \mathbf{B}[K_r \quad 0]^T \\ -(\mathbf{C}_r + K_p\mathbf{C}_p) & 0 \end{bmatrix} \begin{bmatrix} \mathbf{x} \\ x_I \end{bmatrix} + \begin{bmatrix} 0 & \mathbf{B}[0 \quad 1]^T \\ 1 & 0 \end{bmatrix} \begin{bmatrix} \mathbf{r} \\ \delta_R \end{bmatrix} \tag{A.2.9}$$

where,

$$\mathbf{C}_p = [1 \quad 0]\mathbf{C} \tag{A.2.10}$$

$$\mathbf{C}_r = [0 \quad 1]\mathbf{C} \tag{A.2.11}$$

A.2.3 Heading Controller

The heading controller designed obtained its measurement information from the GPS receiver which has a maximum update rate of 4Hz, with a measurement delay on the order of 0.25 seconds (1 cycle) [14]. Therefore, because the update rate is not orders of magnitude larger than the bandwidth of the closed loop yaw rate controller, the heading controller was designed in the discrete time domain.

The design approach is to generate a yaw rate command from the heading error signal. This means that only the extra integrator added due the heading state needed to be stabilised by the feedback. This approach eases the design of the heading controller [14], since all of the dynamics specific to the aircraft are already encapsulated by the yaw rate control system.

The heading error command is sent through a saturation block, thereby ensuring that yaw rate commands of $\pm 15^\circ/s$ are not exceeded. As a result, when large heading steps are commanded the aircraft will simply enter a constant yaw rate for the majority of the turn.

A less than 20% overshoot specification was required to ensure a high enough phase margin. It was argued by [14], that if biases on the roll an yaw rate gyroscopes are ignored, then the heading state's natural integrator implies that no compensator integrator term is required to maintain a zero steady state heading error. However, if any biases do exist on either roll or yaw rate gyroscopes, to maintain a zero steady state heading error, it is required to add a heading compensator integrator term. However, it was shown by [14], that for typical angular rate gyroscope biases, that the steady state heading error made is negligibly small, and therefore biases on the roll and yaw rate gyroscopes are ignored. The same approach was adopted for this project, and proved to deliver acceptable results in practice.

A.2.3.1 Control System Design

The heading controller is shown conceptually by figure A.9, and the plant dynamics are taken from equation (A.2.9). The output matrix **C** is set to extract the yaw rate perturbation state in radians per second. After passing through the natural integrator, the yaw rate perturbation state becomes a heading perturbation state in radians.

MATLAB was used to incorporate the effect of the ZOH circuit, for a sample time of 0.25 seconds, into the continuous plant model. When augmenting the discrete equivalent

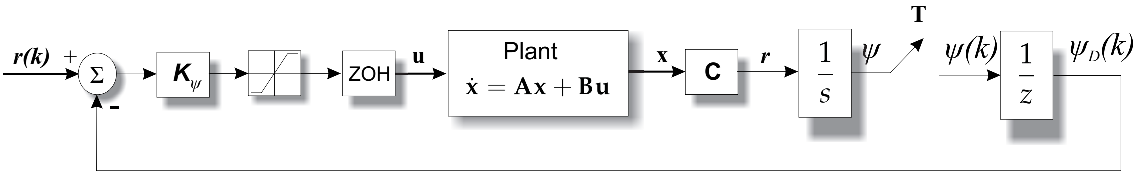

Figure A.9: Heading Controller Conceptual Overview

of the heading and delayed heading states into the model, the plant dynamics can be written as,

$$\begin{bmatrix} \mathbf{x}(k+1) \\ \psi(k+1) \\ \psi_D(k+1) \end{bmatrix} = \begin{bmatrix} \Phi & \mathbf{0} & \mathbf{0} \\ T\mathbf{C} & 1 & 0 \\ \mathbf{0} & 1 & 0 \end{bmatrix} \begin{bmatrix} \mathbf{x}(k) \\ \psi(k) \\ \psi_D(k) \end{bmatrix} + \begin{bmatrix} \Gamma \\ 0 \\ 0 \end{bmatrix} \mathrm{u}(k) \tag{A.2.12}$$

where $\mathbf{x}(k)$ is the discrete state vector, u(k) is the discrete yaw rate command input, Φ is the plant transition matrix, Γ is the discrete input matrix, $\psi(k)$ is the discrete heading state and $\psi_D(k)$ is the single cycle delayed discrete heading state.

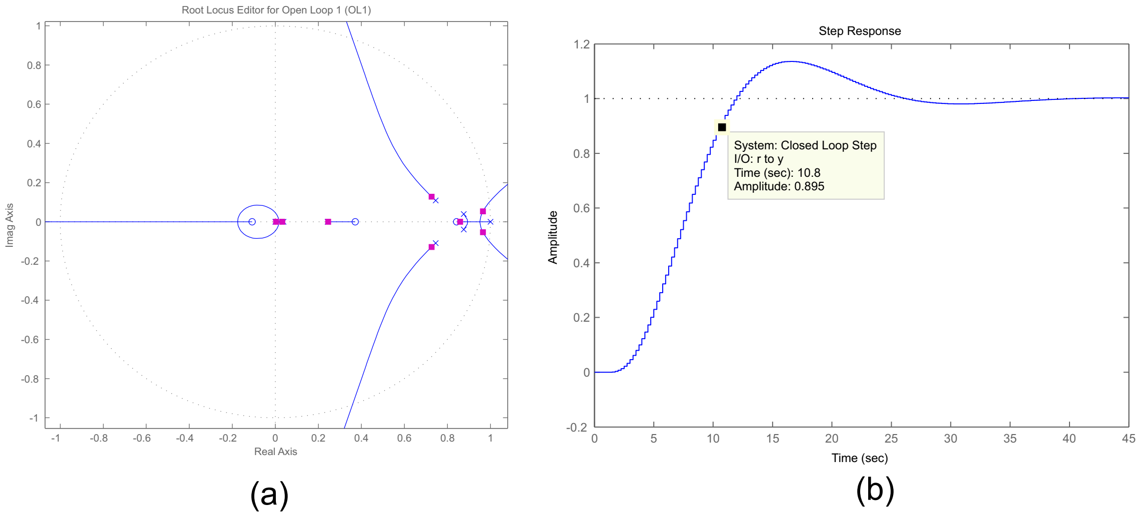

Figure A.10: (a) Heading Loop Root Locus. (b) Heading Controller Linear Simulation.

Figure A.10(a) shows a discrete root locus plot (plotted in the z-plane) for variations in the feedback gain K_ψ. Seven poles are visible on the plot. These are the five poles of figure A.8(b), the roll mode and heading state. From figure A.10(a) it is clear that simple proportional feedback can easily stabilise the system.

Note that practically, rather than a constant 0.25 seconds delay, the GPS delay was found to vary between 0.25 seconds and 0.33 seconds. Therefore, it was decided to design for a low rise time, in order to improve system robustness with respect to the uncertain GPS delay. Furthermore, a less than 20% overshoot specification was set to ensure a high enough phase margin. To accomplish this, a feedback gain of,

$$K_{\psi} = 0.16 \tag{A.2.13}$$

was found satisfactory. The linear step response is shown by figure A.10(b). The control system was designed to reach 90% of the final value commanded in less than 11 seconds. Because of the uncertain GPS delay, it is expected that practically more overshoot will be seen in the closed loop heading response.

The closed loop system is described [14] by,

$$\mathbf{x}(k+1) \quad = \quad \left[\Phi - \Gamma K_{\psi}\mathbf{C}\right]\mathbf{x}(k) + \left[\Gamma K_{\psi}\right] r(k) \tag{A.2.14}$$

where $\mathbf{x}$, Φ and Γ are the state vector, system matrix and input matrix of equation (A.2.12) respectively, and r(k) is the discrete heading command.

A.2.4 Guidance Controller

The guidance controller designed was adopted from [14], and involves generating a heading command from a cross track error signal. This means that only the extra integrator due to the cross track error state needs to be stabilised by the feedback. The cross track error signal is calculated from GPS position measurements, and is discussed in section A.3.

The lateral track state adds a natural integrator, ensuring zero steady state error under zero rate gyroscope biases. Like the heading controller, the guidance controller is also susceptible to biases in the angular rate gyroscopes. By adding a compensator integrator term on the heading controller, the effect of rate gyroscope biases can be removed. However, for the purpose of this project, it was found that any steady state errors introduced in the guidance controller due to rate gyroscope biases are acceptably small.

A.2.4.1 Control System Design

The guidance controller is shown conceptually by figure A.11, where the plant dynamics are given by equation (A.2.14). The output matrix $\mathbf{C}$ is set to extract the derivative of the track state in metres per second. The track state derivative moves through a natural integrator, and becomes the track state y in metres.

MATLAB was used to incorporate the effect of the ZOH circuit, for a sample time of 0.25 seconds, into the continuous plant model. When augmenting the discrete equivalent

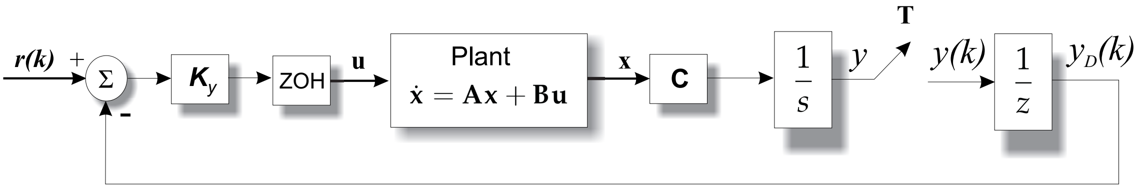

Figure A.11: Guidance Controller Conceptual Overview

of the lateral track and delayed lateral track states into the model, the plant dynamics can be written as,

$$\begin{bmatrix} \mathbf{x}(k+1) \\ y(k+1) \\ y_D(k+1) \end{bmatrix} = \begin{bmatrix} \Phi & \mathbf{0} & \mathbf{0} \\ T\mathbf{C} & 1 & 0 \\ \mathbf{0} & 1 & 0 \end{bmatrix} \begin{bmatrix} \mathbf{x}(k) \\ y(k) \\ y_D(k) \end{bmatrix} + \begin{bmatrix} \Gamma \\ 0 \\ 0 \end{bmatrix} \mathrm{u}(k) \tag{A.2.15}$$

where $\mathbf{x}(k)$ is the discrete state vector, u(k) is the discrete heading command input, Φ is the plant transition matrix, Γ is the discrete input matrix, $y(k)$ is the discrete cross track error state and $y_D(k)$ is the single cycle delayed discrete cross track error state.

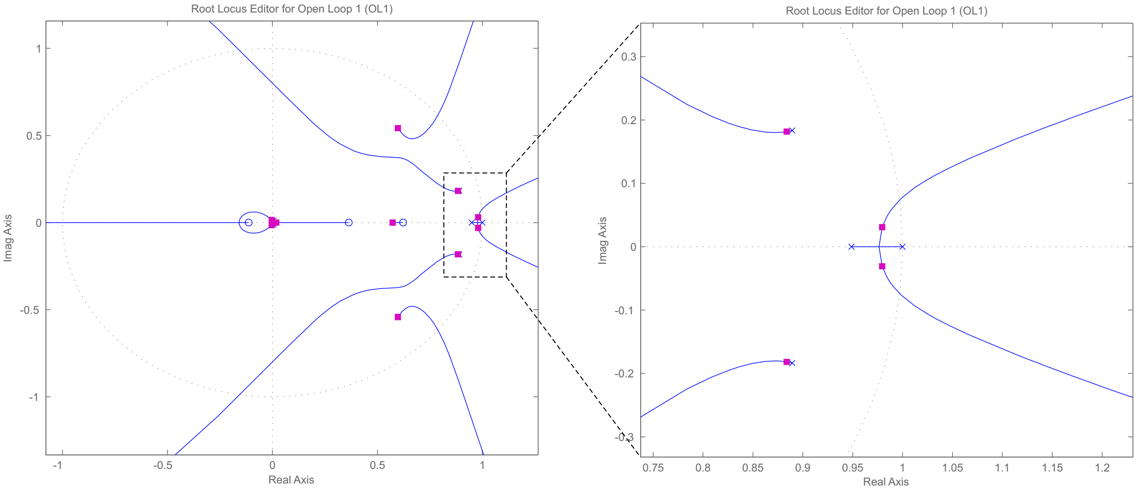

Figure A.12: Guidance Controller Root Locus

Figure A.12 shows a discrete root locus plot (plotted in the z-plane) for variations in the feedback gain K_y. The poles of figure A.10(a), along with the cross track error state are visible on figure A.12. A proportional feedback gain of,

$$K_y = 0.006 \tag{A.2.16}$$

was chosen, and the closed loop step response is shown by figure A.13. Because the lateral controllers were designed using a consecutive loop closure technique, the low rise time of the heading controller imposed a low rise time on the guidance controller as well. The guidance controller reaches 90% of the final commanded value in less than 17 seconds. To increase the speed of response, the heading controller rise time must be increased, which will allow for a faster guidance controller to be designed. The guidance controller however proved to work well in practice. It should be noted, that the purpose of the lateral flight control system in general was to remove the human pilot from the loop when evaluating the more important **NSA** stability augmentation control system. A low rise time specification on the heading and guidance controllers implies that the aircraft will bank less often and less aggressively, ensuring that the aircraft remains more or less wings-level during the course of the test flight. This essentially minimises the effect of the lateral flight control system on the longitudinal flight control system, enabling the **NSA** controller to be evaluated at various centre of mass positions without interference from either the lateral controller or the human pilot. Therefore, if it is desired to compare the dynamic step response characteristics of the longitudinal controllers at various centre of mass positions, more consistent data could be obtained.

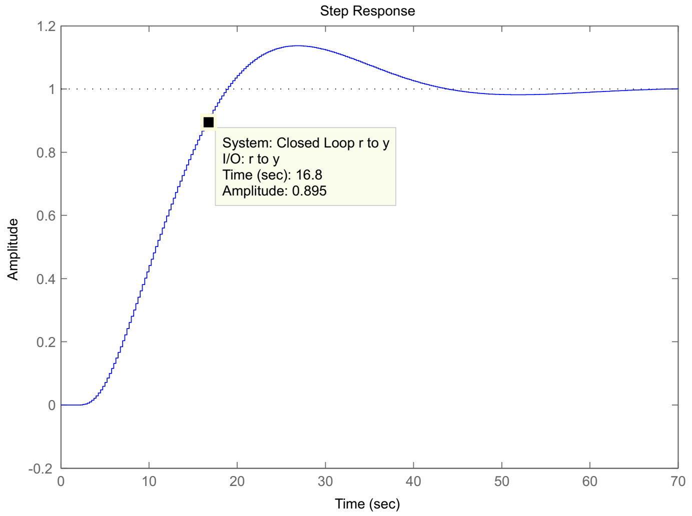

Figure A.13: Guidance Controller Linear Step Response

The closed loop system response can be written [14] as,

$$\mathbf{x}(k+1) \quad = \quad \left[\Phi - \Gamma K_y \mathbf{C}\right] \mathbf{x}(k) + \left[\Gamma K_y\right] r(k) \qquad \text{(A.2.17)}$$

where $\mathbf{x}$, Φ and Γ are the state vector, system matrix and input matrix of equation (A.2.15) respectively, and r(k) is the discrete lateral track command.

A.3 Navigation

This section presents the navigation algorithm capable of generating the cross track error required by the guidance controller. The navigation algorithm consist of two parts, a *path planning* algorithm and *cross track error* algorithm, both of which were adopted from [14] and used in the project. The path planning algorithm generates a valid path between two way points, and the cross track error algorithm calculates the error from the generated path. The aforementioned algorithms are discussed in more detail next.

A.3.1 Path Planning Algorithm

The path planning algorithm is responsible for generating a valid path between two way points, where a way point was defined for this project as,

- A 3D location in inertial space
- A heading

Given an initial and a destination way point, the algorithm finds the shortest path consisting of an initial circle, followed by a straight line section and ending with a final circle, that leads from the initial to the destination way point. The respective starting and ending course tangents are coincidental with the initial and destination headings. For more information on the path planning algorithm, refer to [14].

The turning circle radius can be set arbitrarily. It was shown that for small bank angles, that the aircraft roll angle can be approximated by its yaw rate. To maintain the validity of this assumption, the maximum allowable yaw rate was limited to $15^\circ/s$, resulting in a 28° bank angle. For the chosen trim velocity of 18 [m/s], when the aircraft experiences a $15^\circ/s$ yaw rate, the turning circle is 70 metres. However, to ensure that the maximum yaw rate of $15^\circ/s$ is not exceeded, the turning circle was set to 100 metres. This means that the a yaw rate command of roughly $10^\circ/s$ will be issued, and the aircraft will fly a coordinated turn with a 18° bank angle.

A typical path output is shown by figure A.14. The algorithm generates four possible path options, selects the shortest path and returns the necessary information required to completely describe the path. The path information is used by the cross track error algorithm, which is discussed next.

A.3.2 Cross Track Error Algorithm

With a valid path available between two way points, the cross track error calculates the aircraft's lateral track error from the generated path, so that it can be fed to the guidance controller. During navigation, the cross track error algorithm proceeds as follows:

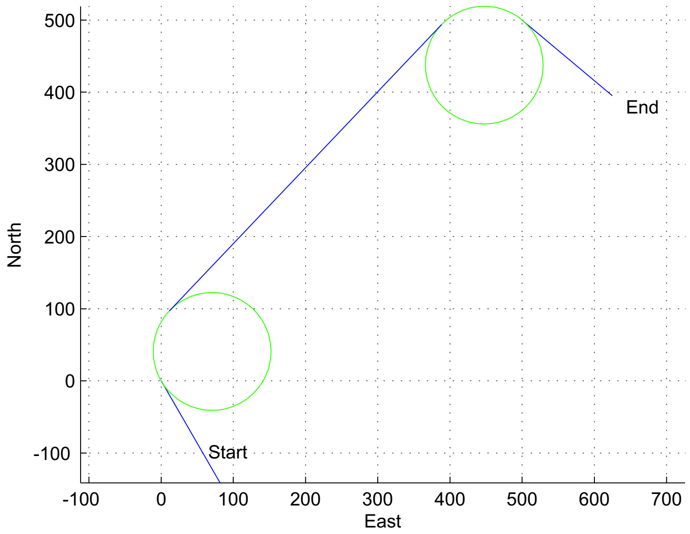

Figure A.14: Typical Path Planner Graphical Output

1. After a valid path is generated, the aircraft is on the initial turning circle section. The cross track error calculation for the circular section is obtained by subtracting the straight line distance between the current aircraft location and the circle centre location from the desired radius.

2. As the aircraft approaches the departure point from the initial turning circle to the straight line section, the aircraft's heading vector is compared to that of the straight line section to determine the point of departure. When the aircraft heading vector is within 10° of the path's straight line section heading, the algorithm transitions to cross track error regulation about the straight line section.

3. The cross track error for the straight line section is obtained by centreing the coordinate system at the start of the straight line and rotating it such that the straight line heading lies along the new inertial X-axis [14]. The cross track error is then the Y coordinate of the transformed aircraft location.

4. When the X coordinate of the transformed aircraft location exceeds the length of the straight line section, the algorithm transitions to cross track error regulation about the final circular section as described by point 2 above.

For detailed information concerning the cross track error algorithm, see [14].

A.3.3 Way-point Navigator

Autonomous navigation was accomplished by using both the path planning and cross track error algorithms, and is conceptually described by algorithm 2 below.

Algorithm 2: Way Point Navigation

```
while Navigation Activated do
    Retrieve the next way point in the flight plan
    Call Path Planning Algorithm
    while Initial turn incomplete do
        Calculate circular path cross track error
    end
    while Straight line section complete do
        Calculate straight line section cross track error
    end
    while Final turn incomplete do
        Calculate circular path cross track error
    end
end
```

The way point navigation algorithm allowed for the evaluation of the stability augmentation control system without the intervention from a human pilot, thereby ensuring more consistent results.

Appendix B

Vectors and Coordinate Transformations

B.1 Vectors and vector notation

The following is a quick overview of vector notation and the direction cosine matrix used in this project. This should serve as a reference only as more detailed information can be found in [15].

Unless otherwise indicated, vectors are represented by boldface, italic symbols such as $\boldsymbol{K}$. A vector in three dimensional space[1] not bound to any axis system may be expressed as the linear sum of three vectors that span three dimensional space. Three orthogonal unit vectors are chosen as basis vectors for axis system A such that $\boldsymbol{i}^A$,$\boldsymbol{j}^A$ and $\boldsymbol{k}^A$.The convention is to denote the coordinate variables with the superscript of the respective axis system. $\boldsymbol{K}$ is expressed as

$$\boldsymbol{K} = X^A\boldsymbol{i}^A + Y^A\boldsymbol{j}^A + Z^A\boldsymbol{k}^A = X^B\boldsymbol{i}^B + Y^B\boldsymbol{j}^B + Z^B\boldsymbol{k}^B \tag{B.1.1}$$

Equation B.1.1 shows that the vector coordinated in two different axis systems are equal.

Coordinate vector: A *coordinate vector* is defined as a matrix of coordinate values. A coordinate system on a set consists of a one-to-one mapping of the points in the set into $\Re^n$. This is another method of conveying the same information without having to tediously express the basis vectors. Note that a boldface, non-italic symbol is used to represent a coordinate vector.

$$\mathbf{K}_A = \begin{bmatrix} X^A \\ Y^A \\ Z^A \end{bmatrix} \tag{B.1.2}$$

---

[1] $\boldsymbol{K} \in \Re^3$

Note that, because the basis vectors are absent, two coordinate vectors of the same vector is not equal. This is because each coordinate vector now contains the *coordinates* relative to different coordinate grids or axis systems.

$$\mathbf{K}_A = \begin{bmatrix} X^A \\ Y^A \\ Z^A \end{bmatrix} \neq \begin{bmatrix} X^B \\ Y^B \\ Z^B \end{bmatrix} = \mathbf{K}_B \tag{B.1.3}$$

B.2 Derivative of a Vector

In deriving the equations of motion of an aircraft, it is useful to be able to write the derivative of a vector with respect to one axis system in terms of the derivative of the same vector with respect to another axis system. When taking the derivative of vector $\boldsymbol{K}$ coordinated in axis system B with respect to axis system A,

$$\left.\frac{d}{dt}\boldsymbol{K}\right|_A = \left.\frac{d}{dt}(X^B\boldsymbol{i}^B + Y^B\boldsymbol{j}^B + Z^B\boldsymbol{k}^B)\right|_A \tag{B.2.1}$$

Equation B.2.1 can be simplified as shown by [15] to,

$$\left.\frac{d}{dt}\boldsymbol{K}\right|_A = \left.\frac{d}{dt}\boldsymbol{K}\right|_B + \boldsymbol{\omega}^{BA} \times \boldsymbol{K} \tag{B.2.2}$$

where $\boldsymbol{\omega}^{BA}$ is the angular velocity of a basis unit vector with respect to axis system A. For detailed information on the derivation, refer to [15].

B.3 Coordinate Transformations

To transform a vector coordinated in axis system A to axis system B each unit vector of A is coordinated in B as in [15]. Typical examples are coordinating velocity into the Inertial axis system and body axis quantities into one of the aerodynamic axis system.

$$\begin{aligned} \boldsymbol{K} &= X^A\boldsymbol{i}^A + Y^A\boldsymbol{j}^A + Z^A\boldsymbol{k}^A \\ &= X^A\left[(\boldsymbol{i}^A\cdot\boldsymbol{i}^B)\boldsymbol{i}^B + (\boldsymbol{i}^A\cdot\boldsymbol{j}^B)\boldsymbol{j}^B + (\boldsymbol{i}^A\cdot\boldsymbol{k}^B)\boldsymbol{k}^B\right] + \\ &\quad Y^A\left[(\boldsymbol{j}^A\cdot\boldsymbol{i}^B)\boldsymbol{i}^B + (\boldsymbol{j}^A\cdot\boldsymbol{j}^B)\boldsymbol{j}^B + (\boldsymbol{j}^A\cdot\boldsymbol{k}^B)\boldsymbol{k}^B\right] + \\ &\quad Z^A\left[(\boldsymbol{k}^A\cdot\boldsymbol{i}^B)\boldsymbol{i}^B + (\boldsymbol{k}^A\cdot\boldsymbol{j}^B)\boldsymbol{j}^B + (\boldsymbol{k}^A\cdot\boldsymbol{k}^B)\boldsymbol{k}^B\right] \\ &= X^B\boldsymbol{i}^B + Y^B\boldsymbol{j}^B + Z^B\boldsymbol{k}^B \end{aligned} \tag{B.3.1}$$

Note that when vector $\boldsymbol{K}$ is transformed only its representation changes, the physical vector remains the same. As a matrix multiplication this is expressed as,

$$\begin{aligned}
\boldsymbol{K} &= \begin{bmatrix} \boldsymbol{i}^B & \boldsymbol{j}^B & \boldsymbol{k}^B \end{bmatrix} \begin{bmatrix} X^B \\ Y^B \\ Z^B \end{bmatrix} && \text{(B.3.2)} \\
&= \begin{bmatrix} \boldsymbol{i}^B & \boldsymbol{j}^B & \boldsymbol{k}^B \end{bmatrix} \begin{bmatrix} \boldsymbol{i}^A \cdot \boldsymbol{i}^B & \boldsymbol{j}^A \cdot \boldsymbol{i}^B & \boldsymbol{k}^A \cdot \boldsymbol{i}^B \\ \boldsymbol{i}^A \cdot \boldsymbol{j}^B & \boldsymbol{j}^A \cdot \boldsymbol{j}^B & \boldsymbol{k}^A \cdot \boldsymbol{j}^B \\ \boldsymbol{i}^A \cdot \boldsymbol{k}^B & \boldsymbol{j}^A \cdot \boldsymbol{k}^B & \boldsymbol{k}^A \cdot \boldsymbol{k}^B \end{bmatrix} \begin{bmatrix} X^A \\ Y^A \\ Z^A \end{bmatrix} \\
\therefore \quad & \mathbf{K}_B = [\mathbf{DCM}^{BA}]\mathbf{K}_A && \text{(B.3.3)}
\end{aligned}$$

Each element in the transformation matrix represents the angle between two basis vectors. This matrix is commonly referred to as the direction cosine matrix (DCM). According to [15] the inverse of the DCM is equal to its transpose[2]

$$\mathbf{K}_A = [\mathbf{DCM}^{BA}]\mathbf{K}_B = [\mathbf{DCM}^{BA}]^T\mathbf{K}_B \qquad \text{(B.3.4)}$$

Euler Angles: The difference between two axis systems can be described by using Euler angles [9]. To transform from axis system A to B as described in [18] the following rotations are performed, with $\boldsymbol{u}_i^A$ representing the i^{th} unit vector in the A axis system

1. Rotate A through angle ψ about unit vector $\boldsymbol{u}_u^A$. The resulting axis system is B_1.
2. Rotate B_1 through angle θ about unit vector $\boldsymbol{u}_v^{B_1}$. The new axis system is B_2.
3. Rotate B_2 through angle ϕ about unit vector $\boldsymbol{u}_w^{B_2}$. The final axis system is B.

To generate a different Euler sequence the values of u,v and w must be chosen correctly[3]. Care must be taken not to use the same basis vector twice [18].

Euler singularities occur when the second rotation causes the basis vectors of the first and third rotation to be the same. Euler 3-2-1 exhibits this singularity at $\theta = \pi/2$. For the purpose of this project however this singularity will never be reached since the flight envelope is non-aerobatic in nature.

To derive the DCM for Euler 3-2-1 the following transformation matrices given by [1] are used,

$$\mathbf{T}_\zeta^1 = \begin{bmatrix} 1 & 0 & 0 \\ 0 & \cos\zeta & \sin\zeta \\ 0 & -\sin\zeta & \cos\zeta \end{bmatrix} \quad \mathbf{T}_\zeta^2 = \begin{bmatrix} \cos\zeta & 0 & -\sin\zeta \\ 0 & 1 & 0 \\ \sin\zeta & 0 & \cos\zeta \end{bmatrix}$$

$$\mathbf{T}_\zeta^3 = \begin{bmatrix} \cos\zeta & \sin\zeta & 0 \\ -\sin\zeta & \cos\zeta & 0 \\ 0 & 0 & 1 \end{bmatrix}$$

---

[2] Sufficient condition for orthonormality [15]

[3] Commonly the sequence 3-2-1 is chosen translating to Yaw-Pitch-Roll

$\mathbf{T}^i_\zeta$ is the transformation matrix describing a rotation of ζ about the i^{th} unit vector. By combining the above single rotation transformation matrices, any Euler sequence can be constructed. The DCM transforming from the inertial axis system to the body axis system and from inertial axis system to wind axis system are given by,

$$\begin{aligned}[\mathbf{DCM}^{BI}_{321}] &= \mathbf{T}^1_\phi \mathbf{T}^2_\theta \mathbf{T}^3_\psi \\ &= \begin{bmatrix} C_\psi C_\theta & S_\psi C_\theta & -S_\theta \\ C_\psi S_\theta S_\phi - S_\psi C_\phi & S_\psi S_\theta S_\phi + C_\psi C_\phi & C_\theta S_\phi \\ C_\phi S_\theta C_\psi + S_\psi S_\phi & S_\psi S_\theta C_\phi - C_\psi S_\phi & C_\theta C_\phi \end{bmatrix}\end{aligned} \tag{B.3.5}$$

and

$$[\mathbf{DCM}^{WI}_{321}] = \mathbf{T}^1_{\phi_W} \mathbf{T}^2_{\theta_W} \mathbf{T}^3_{\psi_W} \tag{B.3.6}$$

respectively. Here the superscript denotes the transformation implied. For example, the superscript WI implies a transformation matrix transforming a coordinate vector in the inertial axis system to the wind axis system. Note that C_ζ and S_ζ represents $\cos\zeta$ and $\sin\zeta$ respectively.

Aerodynamic Axes: Similarly, transforming from the *wind* to body axis system:

$$\begin{aligned}[\mathbf{DCM}^{BW}] &= \mathbf{T}^2_\alpha \mathbf{T}^3_{-\beta} \\ &= \begin{bmatrix} C_\alpha C_\beta & -C_\alpha S_\beta & -S_\alpha \\ S_\beta & C_\beta & 0 \\ S_\alpha C_\beta & -S_\alpha S_\beta & C_\alpha \end{bmatrix}\end{aligned} \tag{B.3.7}$$

To transform from the *stability* to the body axis system:

$$\begin{aligned}[\mathbf{DCM}^{BS}] &= \mathbf{T}^2_\alpha \\ &= \begin{bmatrix} C_\alpha & 0 & -S_\alpha \\ 0 & 1 & 0 \\ S_\alpha & 0 & C_\alpha \end{bmatrix}\end{aligned} \tag{B.3.8}$$

Appendix C

Aircraft Parameters and Coefficients

This section provides additional information regarding the physical parameters of both aircraft analysed in this project.

C.1 Geometric and Inertial Properties

The geometric and inertial properties for the Sekwa UAV are given by tables C.1 and C.2 respectively.

Geometric Property	**Value**
Mass (m)	3.20 [kg]
Wing Area (S)	0.39 [m^2]
Wing Span (b)	1.70 [m]
Aspect Ratio (A)	7.41
Mean Aerodynamic Chord ($\bar{c}$)	0.248 [m]

Table C.1: Sekwa Geometric Properties

Inertial Property	**Value**
I_{xx}	0.192 [kgm^2]
I_{yy}	0.055 [kgm^2]
I_{zz}	0.251 [kgm^2]

Table C.2: Sekwa Inertial Properties

The geometric and inertial properties for the SU VSA UAV are given by tables C.3 and C.4 respectively.

The moment of inertia of the SU VSA was estimated based on the double pendulum setup shown in figure C.1, as suggested in [17].

Geometric Property	**Value**
Mass (m)	3.60 [kg]
Wing Area (S)	0.87 [m^2]
Wing Span (b)	2.50 [m]
Aspect Ratio (A)	7.18
Mean Aerodynamic Chord ($\bar{c}$)	0.33 [m]

Table C.3: SU VSA Geometric Properties

Inertial Property	**Value**
I_{xx}	0.783 [kgm^2]
I_{yy}	0.188 [kgm^2]
I_{zz}	0.706 [kgm^2]

Table C.4: SU VSA Inertial Properties

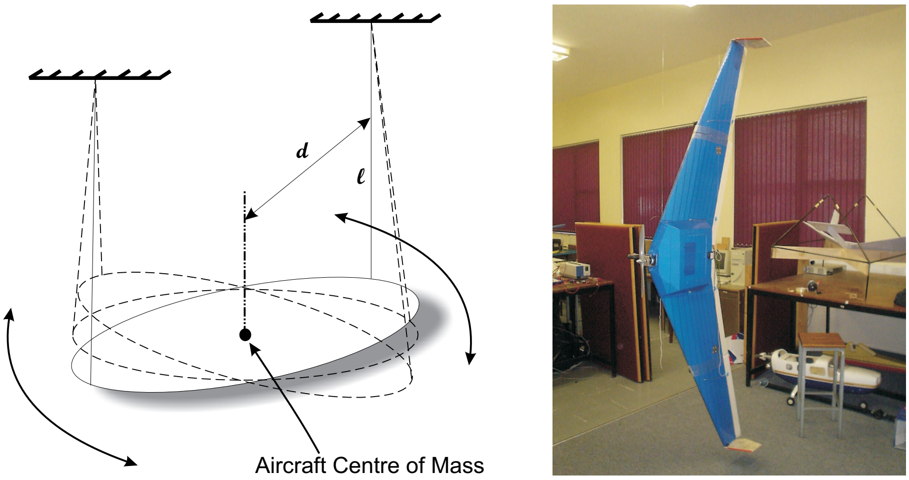

Figure C.1: Pendulum Setup for Estimation of Moment of Inertia

The aircraft is suspended by two equally long strings such that the strings are parallel to the moment of inertia axis of concern. The aircraft is then perturbed by applying a moment about the axis of concern and measuring the period of oscillation T. The equation relating the period of oscillation T to moment of inertia is given in [17] as,

$$I = \frac{mgd^2}{4\pi^2 l} T^2 \tag{C.1.1}$$

where T is the period of oscillation, l is the length of each string and d is the distance between each string and the moment of inertia axis of concern. Note that, for accurate results, the oscillation perturbations must be kept small (typically less than 10°) and $d \ll$

l.

The moment of inertia values for the Sekwa UAV was provided by the designers at the CSIR DPSS.

C.2 Propulsion and Thrust

C.2.1 Propulsion Sources and Propellers

The electric engines and propellers installed on both aircraft are given in table C.5. The engine/propeller combination for Sekwa was specified by the CSIR DPSS.

During the SU VSA flight tests, the pilot noted that the smaller E-Flite Power 25 electric engine will not provide enough thrust during windy conditions. As the majority of the flight tests were conducted in calm weather conditions however, the E-Flite Power 25 provided sufficient amounts of thrust for the purpose of the test flights. It should be noted that, as an improvement on the performance of the SU VSA, the E-Flite Power 32 electric motor must be used instead of the engine specified in table C.5.

Sekwa	SU VSA
AXi 2826/10 electric motor	E-Flite Power 25 electric motor
12 × 6 fixed pitch propeller	14 × 7 fixed pitch propeller

Table C.5: Propulsion Sources and Propellers

C.2.2 Static Thrust Values

For Sekwa, static thrust tests were conducted by mounting the aircraft engine on a load cell, and recording the thrust produced. With reference to figure C.2, a maximum amount of 20N static thrust was available.

With reference to figure C.3, the SU VSA static thrust was measured by attaching a strong, light weight string to the aircraft, which pulls a mass off a digital scale as the throttle is increased. By measuring the amount of mass lifted off the scale, the amount of static thrust could be calculated. The total amount of static thrust obtained was 17N.

C.3 AVL Modelling

Vortex Lattice method was extensively used in estimating the aerodynamic properties of both Sekwa and the SU VSA. More specifically, Athena Vortex Lattice (AVL) code was used. AVL employs the vortex lattice method, and basically takes the vehicle's geometric information and flight conditions, to compute lift, induced drag, stability derivatives and lift loading distribution. AVL provides a graphical output of the aircraft model, which

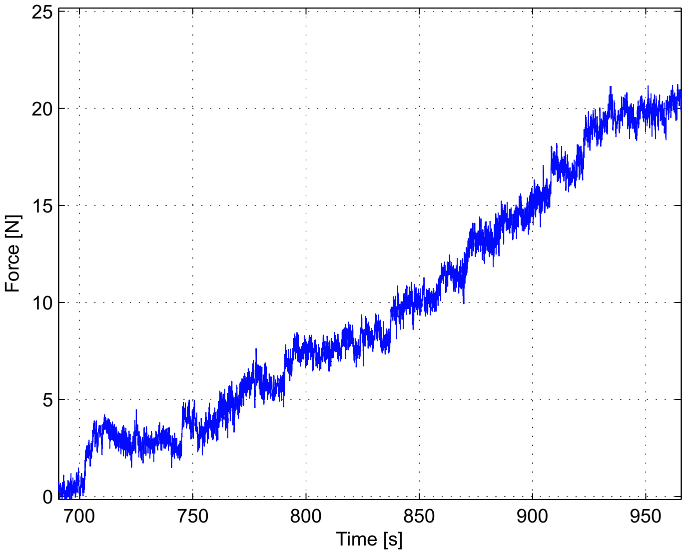

Figure C.2: Sekwa Static Thrust Test Results

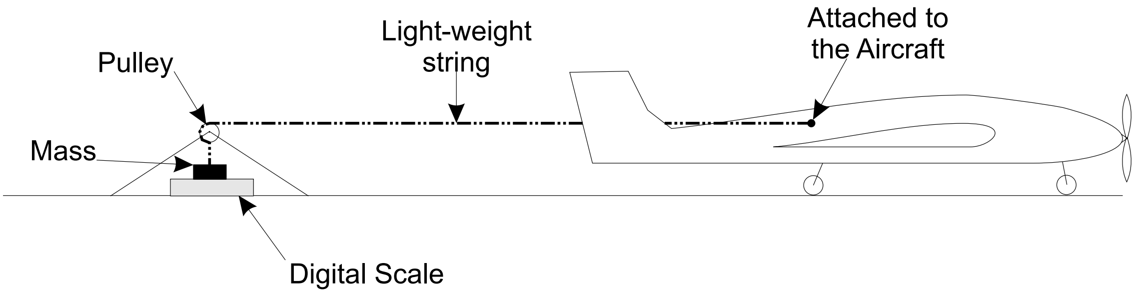

Figure C.3: SU VSA Static Thrust Test Procedure

can be used to verify that the model geometrically represents the actual vehicle. AVL graphical model outputs of Sekwa and the SU VSA are given by figures C.4 and C.5 respectively.

C.3.1 AVL Limitations

When dealing with any computational method, the limitations of the specific method employed must be kept in mind. AVL mentions three limitations. These are limitations on the airframe configuration, flow analysis and compressibility. These limitations are briefly discussed next. For more information, refer to [11].

C.3.1.1 AVL Limitations 1: Airframe Configuration

AVL is best suited for aerodynamic configurations consisting mainly of thin lifting surfaces, at small angles of attack and sideslip. AVL also provides the capability to model

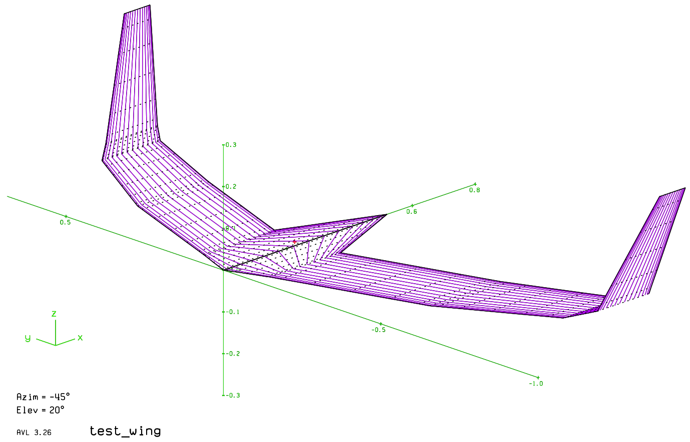

Figure C.4: Sekwa AVL Airframe Geometry Plot

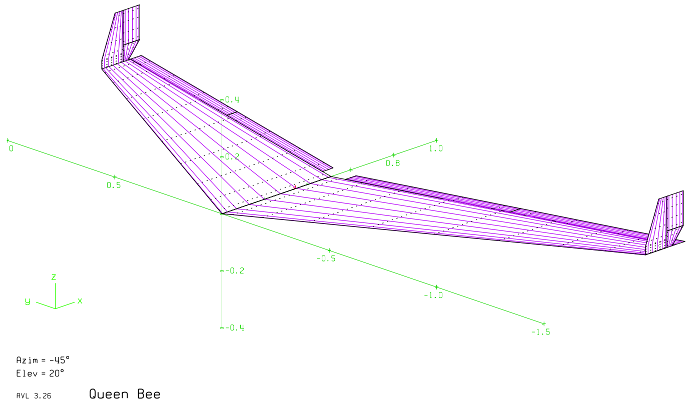

Figure C.5: SU VSA AVL Airframe Geometry Plot

slender bodies such as fuselages. However, according to [11], experience with slender-body theoretical models in AVL is still relatively limited. Therefore, if a fuselage is expected to have little influence on the aerodynamic loads, as is the case for blended-wing-body aircraft, it's recommended to omit the fuselage from the AVL model.

C.3.1.2 AVL Limitations 2: Unsteady Flow

AVL assumes quasi-steady flow, and avoids the analysis of unsteady flow by analysing the helix angles (flow angles) [11]. The roll, pitch and yaw rates used in the computations must be slow enough such that the resulting helix angles are small. For the helix angles to remain small, the dimensionless rotation rate parameters must fall within the following limits:

$$-0.10 < \frac{pb}{2V} < 0.10 \tag{C.3.1}$$

$$-0.03 < \frac{qc}{2V} < 0.03 \tag{C.3.2}$$

$$-0.25 < \frac{rb}{2V} < 0.25 \tag{C.3.3}$$

The flight envelope employed for this project is fairly conventional, and therefore the above constraints are well met.

C.3.1.3 AVL Limitations 3: Compressibility

To quantify compressibility effects in AVL, the Prandtl and Glauert factor must be used as defined in [11]. This factor is given by,

$$\frac{1}{B} = \frac{1}{\sqrt{1 - M_0^2}} \tag{C.3.4}$$

where $\frac{1}{B}$ is the Prandtl and Glauert factor, and M_0 is the free-stream Mach number. When the Prandtl and Glauert factor approaches 1.4, the AVL flow analysis becomes unreliable. Mach number is generally defined as,

$$M_0 = \frac{\overline{V}}{u_s} \tag{C.3.5}$$

where u_s is the velocity of sound in the medium, and $\overline{V}$ is the velocity of the object relative to the medium. At temperature 15 degrees Celsius and at sea level, the speed of sound is 340.3 m/s. For this project, the velocity $\overline{V}$ is the aircraft trim airspeed, which is 18 m/s. Evaluating the above equation, a Mach number of 0.05 is obtained, implying a Prandtl and Glauert factor of 1.0. Therefore, AVL compressibility limitations were not considered for the project.

C.3.2 Stability and Control Derivatives

AVL provides stability and control derivatives in both wind and geometry axes. The geometry axis system is defined with the X-axis pointing downstream, the Y-axis points out the starboard wing perpendicular to the X-axis, and the Z-axis is perpendicular to the XY-plane.

Equations (C.3.6) to (C.3.11) are used to transform the selected geometry-axes derivatives modelled with AVL to the wind axis system,

$$C^W_{D_\alpha} = -C^B_{X_w}(\cos\alpha)^2 + C^B_{Z_u}(\sin\alpha)^2 + (C^B_{X_u} - C^B_{Z_w})\sin\alpha\cos\alpha \tag{C.3.6}$$

$$C^W_{L_{\bar{V}_W}} = -C^B_{Z_u}(\cos\alpha)^2 + C^B_{X_w}(\sin\alpha)^2 + (C^B_{X_u} - C^B_{Z_w})\sin\alpha\cos\alpha \tag{C.3.7}$$

$$C^W_{D_{\bar{V}_W}} = -C^B_{X_u}(\cos\alpha)^2 - C^B_{Z_w}(\sin\alpha)^2 - (C^B_{X_w} + C^B_{Z_u})\sin\alpha\cos\alpha \tag{C.3.8}$$

$$C^W_{m_{\bar{V}_W}} = -C^B_{m_u}\cos\alpha - C^B_{m_w}\sin\alpha \tag{C.3.9}$$

$$C^W_{D_q} = -C^B_{X_q}\cos\alpha - C^B_{Z_q}\sin\alpha \tag{C.3.10}$$

$$C^W_{D_{\delta_E}} = -C^B_{X_{\delta_E}}\cos\alpha - C^B_{Z_{\delta_E}}\sin\alpha \tag{C.3.11}$$

where the superscripts W and B denote a stability or control derivative modelled in the wind axes and the geometry axes respectively. The above derivatives were used during analysis of the aircraft longitudinal dynamics, outlined in chapter 4.

C.3.2.1 Sekwa Longitudinal Stability and Control Derivatives

The Sekwa longitudinal stability and control derivatives are listed below as a function of centre of mass position, expressed in percentage aft of the stable position ($\Delta_{cg_{\%}}$):

$$C_{m_\alpha}(\Delta_{cg_{\%}}) = 34.106\times10^{-4}(\Delta_{cg_{\%}}) - 0.12875 \tag{C.3.12}$$

$$C_{m_{\delta_E}}(\Delta_{cg_{\%}}) = 12.828\times10^{-4}(\Delta_{cg_{\%}}) - 0.45827 \tag{C.3.13}$$

$$C_{L_q}(\Delta_{cg_{\%}}) = -69.946\times10^{-4}(\Delta_{cg_{\%}}) + 4.0543 \tag{C.3.14}$$

$$C_{L_{\delta_E}}(\Delta_{cg_{\%}}) = -1.9529\times10^{-7}(\Delta^2_{cg_{\%}}) + 1.3127\times10^{-4}(\Delta_{cg_{\%}}) + 1.6524 \tag{C.3.15}$$

$$C_{L_\alpha}(\Delta_{cg_{\%}}) = -3.4952\times10^{-7}(\Delta^2_{cg_{\%}}) + 2.5654\times10^{-4}(\Delta_{cg_{\%}}) + 4.3 \tag{C.3.16}$$

$$C_{m_q}(\Delta_{cg_{\%}}) = -5.3338\times10^{-6}(\Delta^2_{cg_{\%}}) + 33.094\times10^{-4}(\Delta_{cg_{\%}}) - 1.6945 \tag{C.3.17}$$

where $\Delta_{cg_{\%}} \in [0, 100]\,\%$. The specific centre of mass position in meter can be determined by:

$$cg_{meter} = 2\times10^{-4}\Delta_{cg_{\%}} + 0.22 \quad [m] \tag{C.3.18}$$

where the nose of the aircraft is taken as the reference point. The Oswald efficiency factor e and parasitic drag coefficient C_{D_0} are listed below as:

$$e = 0.85 \quad C_{D_0} = 0.0183 \tag{C.3.19}$$

C.3.2.2 SU VSA Longitudinal Stability and Control Derivatives

The SU VSA longitudinal stability and control derivatives are listed below as a function of centre of mass position, expressed in percentage aft of the stable position ($\Delta_{cg_{\%}}$):

$$
\begin{aligned}
C_{m_\alpha}(\Delta_{cg_{\%}}) &= 69.946\times10^{-4}(\Delta_{cg_{\%}}) - 0.64237 && \text{(C.3.20)}\\
C_{m_{\delta_E}}(\Delta_{cg_{\%}}) &= 14.094\times10^{-4}(\Delta_{cg_{\%}}) - 0.48838 && \text{(C.3.21)}\\
C_{L_q}(\Delta_{cg_{\%}}) &= -140.18\times10^{-4}(\Delta_{cg_{\%}}) + 4.3966 && \text{(C.3.22)}\\
C_{L_{\delta_E}}(\Delta_{cg_{\%}}) &= -1.9913\times10^{-8}(\Delta^2_{cg_{\%}}) + 1.5616\times10^{-5}(\Delta_{cg_{\%}}) + 0.93435 && \text{(C.3.23)}\\
C_{L_\alpha}(\Delta_{cg_{\%}}) &= -1.1793\times10^{-7}(\Delta^2_{cg_{\%}}) + 7.8086\times10^{-5}(\Delta_{cg_{\%}}) + 4.6149 && \text{(C.3.24)}\\
C_{m_q}(\Delta_{cg_{\%}}) &= -2.117\times10^{-5}(\Delta^2_{cg_{\%}}) + 85.918\times10^{-4}(\Delta_{cg_{\%}}) - 1.5964 && \text{(C.3.25)}
\end{aligned}
$$

where $\Delta_{cg_{\%}} \in [0, 100]\,\%$. The specific centre of mass position in meter can be determined by:

$$
cg_{meter} = 7.7\times10^{-4}\Delta_{cg_{\%}} + 0.343 \quad [m] \qquad \text{(C.3.26)}
$$

where the nose of the aircraft is taken as the reference point. The Oswald efficiency factor e and parasitic drag coefficient C_{D_0} are listed below as:

$$
e = 0.75 \quad C_{D_0} = 0.0193 \qquad \text{(C.3.27)}
$$

C.3.2.3 Lateral Stability and Control Derivatives

The lateral stability and control derivatives for both Sekwa and the SU VSA are listed in table C.6.

Derivative	**Sekwa**	**SU VSA**
C_{Y_β}	-0.54013	-0.14405
C_{l_β}	-0.23809	-0.058161
C_{n_β}	0.065812	0.017169
C_{Y_p}	-0.2114	0.022644
C_{l_p}	-0.48479	-0.47992
C_{n_p}	-0.002061	-0.015654
C_{Y_r}	0.24094	0.04191
C_{l_r}	0.17042	0.060848
C_{n_r}	-0.035424	-0.006349
$C_{Y_{\delta_A}}$	-0.093965	-0.0061879
$C_{l_{\delta_A}}$	-0.35203	-0.20661
$C_{n_{\delta_A}}$	0.0018335	-0.0036096
$C_{Y_{\delta_R}}$	0.36772	0.067609
$C_{l_{\delta_R}}$	0.1056	0.013407
$C_{n_{\delta_R}}$	-0.047785	-0.0099122

Table C.6: Lateral Stability and Control Derivatives

Appendix D

Aircraft Empirical Equations

This section provides additional information regarding the geometry of aircraft in general. The information presented here was used to calculate parameters such as the aircraft mean aerodynamic chord and wing reference area. For detailed information regarding these equations refer to [1].

D.1 Aerofoil Geometry Equations

The aircraft is divided into four major lifting surfaces, namely the wing (*W*), fuselage, horizontal tail plane (*T*) and vertical fin (*F*). With reference to figure D.1, the aircraft geometric parameters can be calculated as given in [14] and [21].

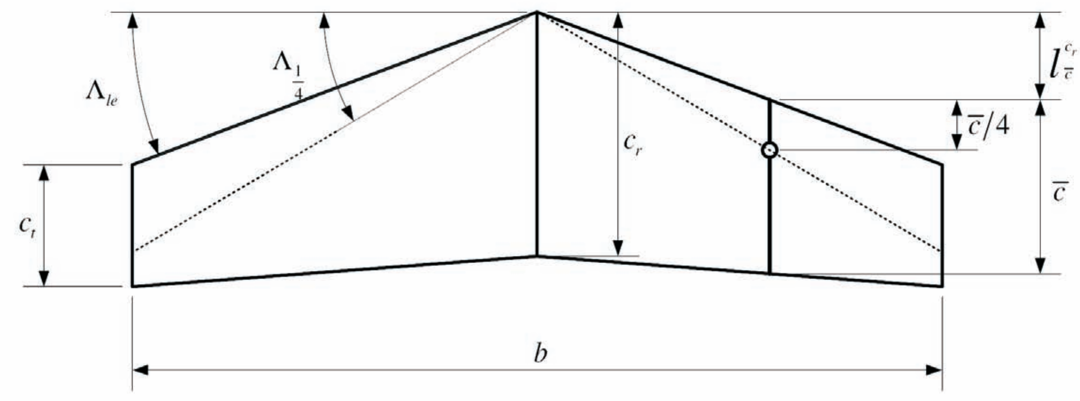

Figure D.1: Simplified Aerofoil Geometric Representation, derived from [21]

D.1.1 Reference Area

The reference are can be calculated with,

$$S = 2\int_0^s \left(c_r + \frac{2y}{b}(c_t - c_r)\right) dy \tag{D.1.1}$$

$$\therefore S = \frac{b}{2}(c_t + c_r) \tag{D.1.2}$$

where s, c_t and c_r denotes semi-span, tip chord and root chord lengths respectively.

D.1.2 Mean Aerodynamic Chord

The wing mean aerodynamic chord (mac) can be determined by,

$$\bar{c} = \frac{2}{S}\int_0^s \left(c_r + \frac{2y}{b}(c_t - c_r)\right)^2 dy \tag{D.1.3}$$

$$\therefore \bar{c} = \frac{2}{S}\left(c_r^2\frac{b}{2} + \frac{4}{b}c_r(c_t - c_r)\frac{b^2}{8} + \frac{4}{b^2}(c_t - c_r)^2\frac{b^3}{24}\right) \tag{D.1.4}$$

The distance that the mac lies behind the tip of the root chord can be calculated with,

$$l_{\bar{c}}^{c_r} = \frac{b}{2}\frac{c_r - \bar{c}}{c_r - c_t}\tan\Lambda_{le} \tag{D.1.5}$$

where Λ_{le} denotes the leading edge sweep angle. Furthermore, the height of the fin mac shown in figure D.3 relative to the centre line of the aircraft is determined by,

$$h_f = \frac{b}{2}\frac{c_r - \bar{c}}{c_r - c_t} + h_{c_r} \tag{D.1.6}$$

D.1.3 Aspect Ratio and Quarter Chord Sweep Angle

The aspect ratio (A) and quarter chord sweep angle ($\Lambda_{\frac{1}{4}}$) are calculated with,

$$A = \frac{b^2}{S} \tag{D.1.7}$$

$$\Lambda_{\frac{1}{4}} = \arctan\left(\tan\Lambda_{le} + \frac{1}{4}\frac{c_t - c_r}{s}\right) \tag{D.1.8}$$

D.2 Lift Curve Slope

The lift curve slope of an aerofoil $\frac{\partial C_L}{\partial \alpha}$ is calculated with,

$$\frac{\partial C_L}{\partial \alpha} = \frac{\left.\frac{\partial C_L}{\partial \alpha}\right|_{\infty}}{1+\frac{\left.\frac{\partial C_L}{\partial \alpha}\right|_{\infty}}{\pi A}} \tag{D.2.1}$$

$$\left.\frac{\partial C_L}{\partial \alpha}\right|_{\infty} = 1.8\pi\left(1+0.8\frac{t}{c}\right)\cos\Lambda_{le} \tag{D.2.2}$$

where t,c and Λ_{le} denote the aerofoil thickness, chord length and main wing sweep angle respectively. The term $\frac{\partial C_L}{\partial \beta}$ is obtained similarly where Λ_{le} denotes the leading edge sweep angle of the vertical tail plane.

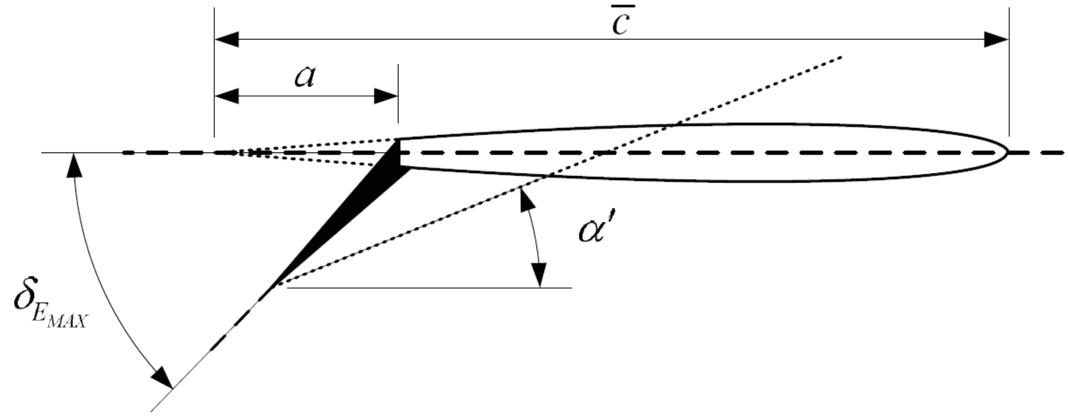

Figure D.2: Control Surface Deflection Approximation, derived from [21]

With reference to figure D.2, the elevator lift curve slope $\frac{\partial C_{L_T}}{\partial \delta_E}$ is calculated with,

$$\frac{\partial C_{L_T}}{\partial \delta_E} = \frac{\partial C_{L_T}}{\partial \alpha'}\frac{\partial \alpha'}{\partial \delta_E} \tag{D.2.3}$$

$$\frac{\partial \alpha'}{\partial \delta_E} = \frac{1}{\delta_{E_{max}}}\tan\left(\frac{a\sin\delta_{E_{max}}}{\frac{\bar{c}_t}{2}+a(\cos\delta_{E_{max}}-1)}\right) \tag{D.2.4}$$

where a is the elevator chord length assumed constant over the entire span. The parameter $\frac{\partial C_{L_T}}{\partial \alpha'}$ can be calculated with equation D.2.2 where Λ_{le} should be taken as the leading edge sweep angle of the horizontal tail plane.

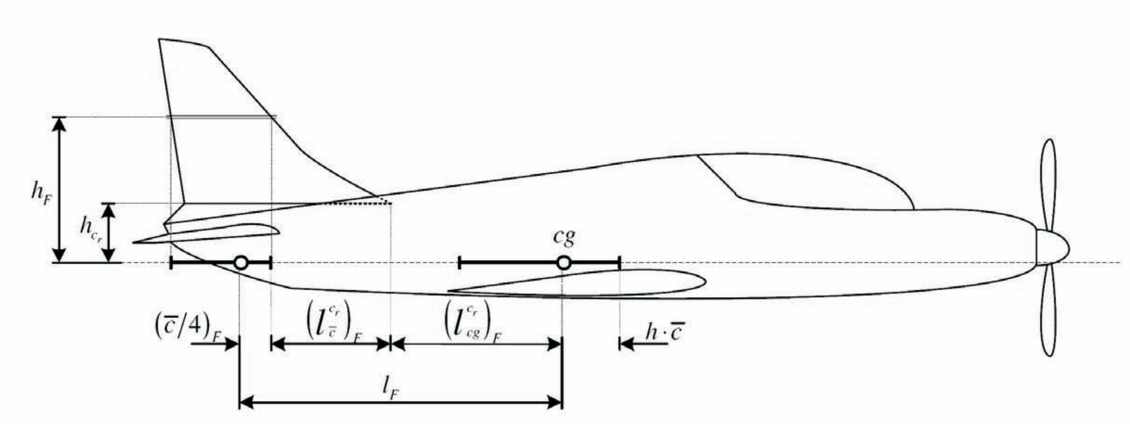

Figure D.3: Aircraft Geometry Side View, derived from [21]

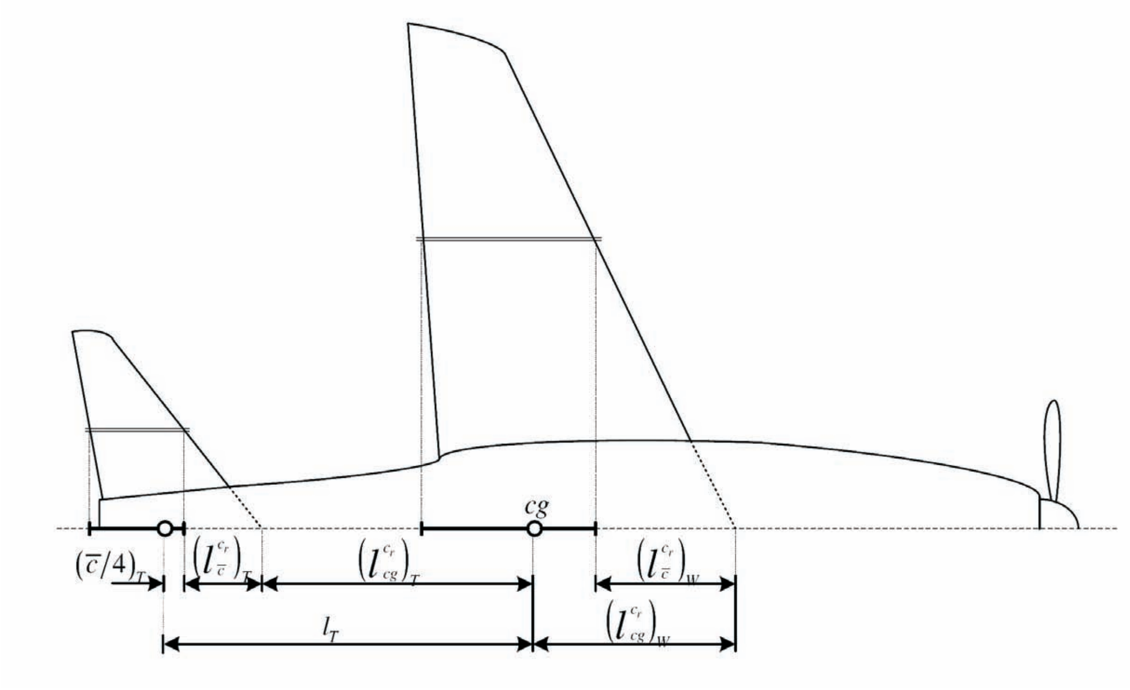

Figure D.4: Aircraft Geometry Top View, derived from [21]

D.3 Aircraft Geometric Equations

D.3.1 Centre of Gravity

The location of the centre of gravity is usually expressed as a fraction of the *mac* of the wing,

$$h = \frac{l_{cg}^{c_r} - l_{\bar{c}}^{c_r}}{\bar{c}} \tag{D.3.1}$$

For this project however, the centre of mass was practically measured.

D.3.2 Tail and fin moment arms

To determine the tail and fin moment arms (figures D.4 and D.3), the following equations are used,

$$l_T = l_{cg}^{c_r} + l_{\bar{c}}^{c_r} + \frac{\bar{c}}{4} \tag{D.3.2}$$

$$l_F = l_{cg}^{c_r} + l_{\bar{c}}^{c_r} + \frac{\bar{c}}{4} \tag{D.3.3}$$

where the parameters are taken to either the fin or tail plane reference geometries respectively.

Appendix E

Momentum Theory Power Calculation

E.1 Required Power

Often the amount of power dissipated by the engine is required in analysis, especially when factors such as airframe efficiency and estimated flight time are being evaluated.

Froude's momentum theory of propulsion as described in [7] is used to obtain an equation dependent on air density, velocity, propeller area and commanded thrust predicting the power required by the propeller. The following theory is based on the assumptions that,

1. The actuator is an infinitely thin disc with area S offering no resistance to air passing through it.
2. Air passing through the disc receives energy in the form of pressure energy being distributed evenly across the disc area.
3. Velocity of the air through the disc is constant over the entire disc area.
4. All energy supplied to the disc is transferred to the air.

Figure E.1 represents a disc actuator in rest in a fluid. A long way ahead of the disc the fluid moves at speed V_0 and has a pressure of ρ_0. As the fluid accelerates toward the disc between the streamlines it moves at a greater velocity V_1 and with decreased pressure ρ_1. Behind the disc fluid pressure becomes ρ_2 [1] and it moves at velocity V_2.

Arguing that the pressure differences between ρ_0, ρ_1 and ρ_2 are small the mass of fluid passing through the disc in unit time is $\rho_0 S V_1$. Since the increase of rearward momentum of this mass of fluid is the mass of fluid passing through the disc multiplied by the difference in fluid velocity between V_0 and V_2, the thrust on the disc is shown to be,

---

[1] Here $\rho_2 = \rho_0$

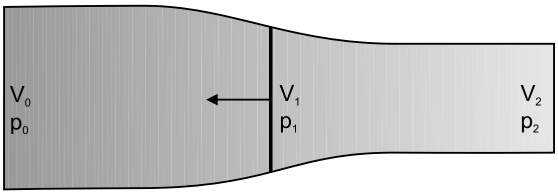

Figure E.1: Propeller Thrust [18]

$$T = \rho_0 S V_1 (V_2 - V_0) \tag{E.1.1}$$

Consequently, the fluid velocity passing through the disc can be expressed as

$$V_1 = V_0(1 + a) \tag{E.1.2}$$

where a is termed the *inflow factor* as given in [7]. Since the velocity V_1 is the average of V_0 and V_2 i.e. $V_1 = \frac{1}{2}(V_2 + V_0)$, it can be shown that

$$V_2 = V_0(1 + 2a) \tag{E.1.3}$$

The inflow factor, used to determine the power supplied to the actuator is determined by substituting equation E.1.2 and E.1.3 into E.1.1. The result is obtained as,

$$a = \sqrt{\frac{1}{4} + \frac{T}{2\rho_0 S V_0^2}} - \frac{1}{2} \tag{E.1.4}$$

As a result, it is shown by [7] that the minimum power[2] supplied to the propeller is,

$$P_S = T V_0 (1 + a) + c_c T V_0 (1 + a) \tag{E.1.5}$$

In practice however, the power supplied to the propeller will be about 10% to 20% greater than this, therefore the correction factor c_c must be obtained experimentally for every propeller/engine combination.

---

[2] Note that V_0 is the vehicle airspeed and ρ_0 the *free stream* air pressure

Bibliography

[1] M.V. Cook, *Flight Dynamics Principles*. Elsevier Butterworth-Heinemann, 1997.

[2] J.H. Blakelock, *Automatic Control of Aircraft and Missiles*. Wiley-Interscience, 1991.

[3] B. Etkin, L.D. Reid, *Dynamics of Flight Stability and Control,* 3^rd *ed*. John Wiley & Sons, 1996.

[4] M.C. Koen *Modelling and Simulation of an RPV for Flight Control System Design Purposes*. University of Pretoria, 2006.

[5] McRuer, Ashkenas and Graham, *Aircraft Dynamics and Automatic Control*. Princeton University Press, 1990.

[6] G.F. Franklin, J.D. Powell, A. Emama-Naeini, *Feedback Control of Dynamic Systems*. Addison-Wesely Publishing Company, 1994.

[7] N.B. Carruthers, E.L. Houghton, *Aerodynamics for Engineering Students,* 3^rd *ed*. Edward Arnold Publishers, 1982.

[8] G.F. Franklin, J.D. Powell, A. Emami-Naeini *Feedback Control of Dynamic Systems,* 4^{th} *ed*. Pearson Educational International, 2002.

[9] J. Diebel, *Representing Attitude: Euler Angles, Unit Quaternions and Rotation Vector*. Stanford University, 2006.

[10] K.J. Astrom, T. Hagglund, *PID Controllers*. Instrument Society of America

[11] M. Drela, *AVL 3.14 User Primer*. MIT Aero & Astro, 2004.

[12] Paul Horowitz, Winfield Hill, *The art of electronics*, 2^{nd} edition. Cambridge University Press 1995.

[13] Joseph E. Shigley, Charles R. Mischke, Richard G. Budynas, *Mechanical Engineering Design* 7^{th} *ed*. McGraw-Hill Companies Inc, 2004.

[14] I.K. Peddle, *Autonomous Flight of a Model Aircraft*, University of Stellenbosch, 2004.

[15] I.K. Peddle, *Acceleration Based Manoeuvre Flight Control System for Unmanned Aerial Vehicles*, University of Stellenbosch, 2007.

[16] I.K. Peddle, T. Jones, *Acceleration Based 3D Maneuver Flight Control System for UAVs: Strategy and Longitudinal Design*, Submitted to Automatica, January 2008.

[17] S. Park, *Avionics and Control System Development for Mid-Air Rendezvous of Two Unmanned Aerial Vehicles*, MASSACHUSETTS INSTITUTE OF TECHNOLOGY, 2004

[18] S.C. Kriel, *A Comparison of Control Systems for the Flight Transition of VTOL Unmanned Aerial Vehicles*, University of Stellenbosch, 2008.

[19] W. J. Hough, *Autonomous Aerobatic Flight of a Fixed Wing Unmanned Aerial Vehicle*, University of Stellenbosch 2007.

[20] J. Venter, *Development of an experimental Tilt-Wing VTOL Unmanned Aerial Vehicle*, University of Stellenbosch, 2005.

[21] M.M. Basson, *Aircraft Dynamics Tutor Software Design*, University of Stellenbosch, 2007.

[22] M.C. Silberbauer. *Simulation Visualisation System*, Undergraduate Final Year Project, University of Stellenbosch, 2005.

[23] Microsoft Corporation. *Microsoft Extensible Firmware Initiative FAT32 File System Specification*, Hardware White Paper Version 1.03, December 6, 2000.

[24] SanDisk. *SanDisk Secure Digital Card Product Manual*, Product Manual, Version 1.9, December 2003.

[25] NASA History web page,
`http://history.nasa.gov/SP-367/appendc.htm`. 2006.